SATHYABAMA
INSTITUTE OF SCIENCE AND TECHNOLOGY
(DEEMED TO BE UNIVERSITY)
Accredited "A" Grade by NAAC | 12B Status by UGC | Approved by AICTE
www.sathyabama.ac.in

SCHOOL OF MECHANICAL ENGINEERING
DEPARTMENT OF AERONAUTICAL ENGINEERING

UNIT – I –LOW SPEED AERODYNAMICS – SAEA1403

UNIT 1

REVIEW OF AERODYNAMICS

1.1 Forces on an Aircraft

1.1.1 Types of forces

The forces acting on an aircraft can be separated into:

Gravitational: The gravitational force is the aircraft's weight, including all of its contents (i.e. fuel, payload, passengers, etc.). We will generally denote it **W**.

Propulsive: The propulsive force, referred to as the thrust, is the force acting on the aircraft generated by the aircraft's propulsion system. We will generally denote it **T**.

Aerodynamic: The aerodynamic force is defined as the force generated by the air acting on the surface of the aircraft. We will generally denote it **A**.

In reality, the propulsive and aerodynamic forces are often not easy to separate since the propulsive system and rest of the aircraft interact. For example, the thrust generated by a propellor, even placed at the nose of an aircraft, is different depending on the shape of the aircraft. Similarly, the aerodynamic forces generated by an aircraft are impacted by the presence of the propulsive systems. So, while we will use this separation of propulsive and aerodynamic forces, it is important to recognize the thrust generated by the propulsive system depends on the aircraft and the aerodynamic force acting on the aircraft depends on the propulsive system. The entire system is coupled.

1.2.2 Force and velocity for an aircraft

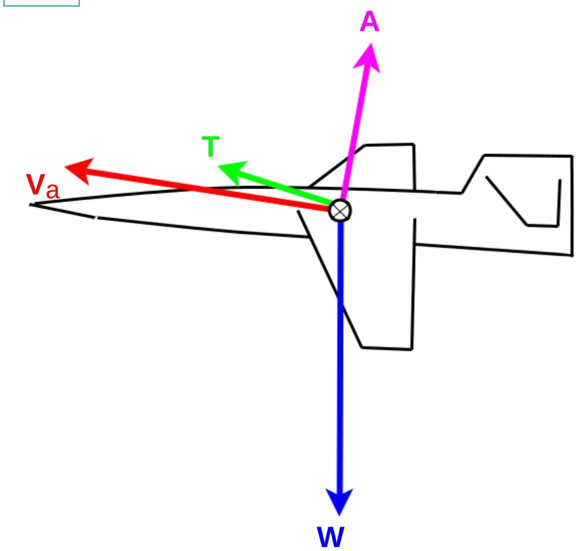

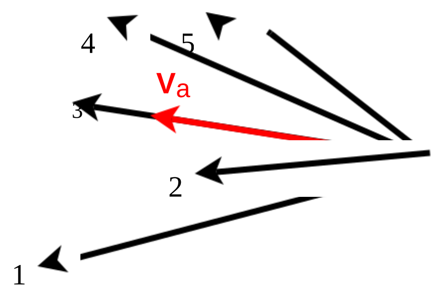

As shown in the above figure, the center of mass of an aircraft is moving with velocity $\mathbf{V}_a$. At that instant, the weight of the aircraft is **W**, the thrust is **T**, and the aerodynamic force is **A**. Which of the black arrows shown could be the velocity a short time later? Note the red arrow is the original velocity.

1.2.3 Aerodynamic forces

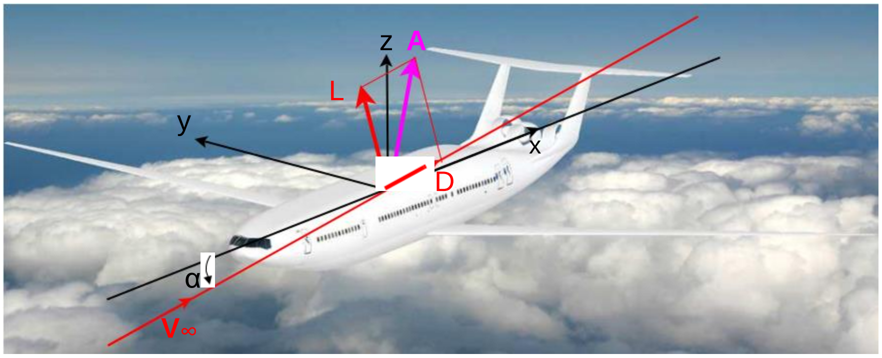

Figure 1.1: Aerodynamic forces for symmetric body without sideslip (the yaw force, Y is assumed zero and not shown).

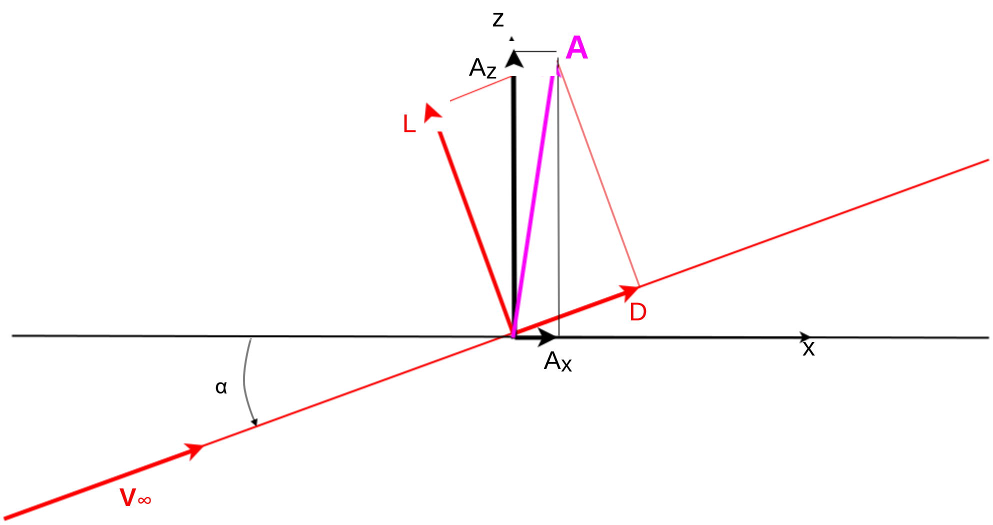

Figure 1.2: Lift and drag forces viewed in x-z plane.

In aerodynamics, the flow about an aircraft is often analyzed using a coordinate system attached to the aircraft, i.e. in the aircraft's frame of reference, often referred to as the geometry or body axes. Suppose in some inertial frame of reference, the velocity of the aircraft is $\mathbf{V}_a$ and the velocity of the wind far ahead of the aircraft is $\mathbf{V}_W$. In the aircraft's frame of reference, the velocity of the wind far upstream of the aircraft is $\mathbf{V}_\infty = \mathbf{V}_w - \mathbf{V}_a$ where $\mathbf{V}_\infty$ is commonly referred to as the freestream velocity and defines the freestream direction. Pilots and people studying the motion of an aircraft often refer to this as the relative wind velocity since it is the wind velocity relative to the aircraft's velocity.

Figure 1.1 shows an aircraft in this frame of reference. The y = 0 plane is usually a plane of symmetry for the aircraft with the y-axis pointing outward from the fuselage towards the right wing tip. The distance, b, between the wing tips is called the span and the y-axis is often referred to as the spanwise direction. The x-axis lies along the length of the fuselage and points towards the tail, thus defining what is often referred to as the longitudinal direction. Finally, the z-axis points upwards in such a way that the xyz coordinate system is a right-handed frame.

We will assume that the airplane is symmetric about the y = 0 plane. We will also assume that the freestream has no sideslip (i.e. no component in the y-direction). The angle of attack,

α, is defined as the angle between the freestream and the z = 0 plane. It is important to note that the specific location of the z = 0 plane is arbitrary. In many cases, the z = 0 plane is chosen to be parallel to an important geometric feature of the aircraft (e.g. the floor of the passenger compartment) and can be chosen to pass through the center of gravity of the aircraft (not including passengers, cargo, and fuel).

As shown in Figure 1.1, the aerodynamic force is often decomposed into:

Drag: The drag, D, is the component of the aerodynamic force acting in the freestream direction.

Lift: The lift, L, is the component of the aerodynamic force acting normal to the freestream direc-tion. In three-dimensional flows, the normal direction is not unique. However, the situation we will typically focus on is an aircraft that is symmetric such that the left and right sides of the aircraft (though control surfaces such as ailerons can break this symmetry) are the same, and the freestream velocity vector is in this plane of symmetry. In this case, the lift is the defined as the force normal to the freestream in the plane of symmetry as shown in Figure 1.1.

Side: The side force, Y , (also referred to as the yaw force) is the component of the aerodynamic force perpendicular to both the drag and lift directions: it acts along the span-wise direction. For the discussions in this course, the side force will almost always be zero (and has not been shown in Figure 1.1).

For clarity, the lift and drag forces are shown in the x-z plane in Figure 1.2. Also shown are the x and z components of the aerodynamic force whose magnitudes are related to the lift and drag magnitudes by

$$A_x = D\cos\alpha - L\sin\alpha \tag{1.1}$$

$$A_z = D\sin\alpha + L\cos\alpha \tag{1.2}$$

or equivalently

$$D = A_x\cos\alpha + A_z\sin\alpha \tag{1.3}$$

$$L = -A_x\sin\alpha + A_z\cos\alpha\,. \tag{1.4}$$

In other words, (D, L) are related to (A_x, A_z) by a rotation of angle α around the y-axis.

1.2.4 Aerodynamic force, pressure, and viscous stresses

The aerodynamic force acting on a body is a result of the pressure and friction acting on the surface of the body. The pressure and friction are actually a force per unit area, i.e. a stress. At the molecular level, these stresses are caused by the interaction of the air molecules with the surface.

The pressure stress at a point on the surface acts along the normal direction inward towards the surface and is related to the change in the normal component of momentum of the air molecules when they impact the surface. Consider a location on the surface of the body which has an outward pointing normal (unit length) as shown in Figure 1.3. If the pressure at this location is p, then the pressure force acting on the infinitesimal area dS is defined as,

$$-p\hat{\mathbf{n}}\,dS \equiv \text{pressure force acting on surface element } dS\,. \tag{1.5}$$

Additional information about pressure can be found in Section 1.2.4.

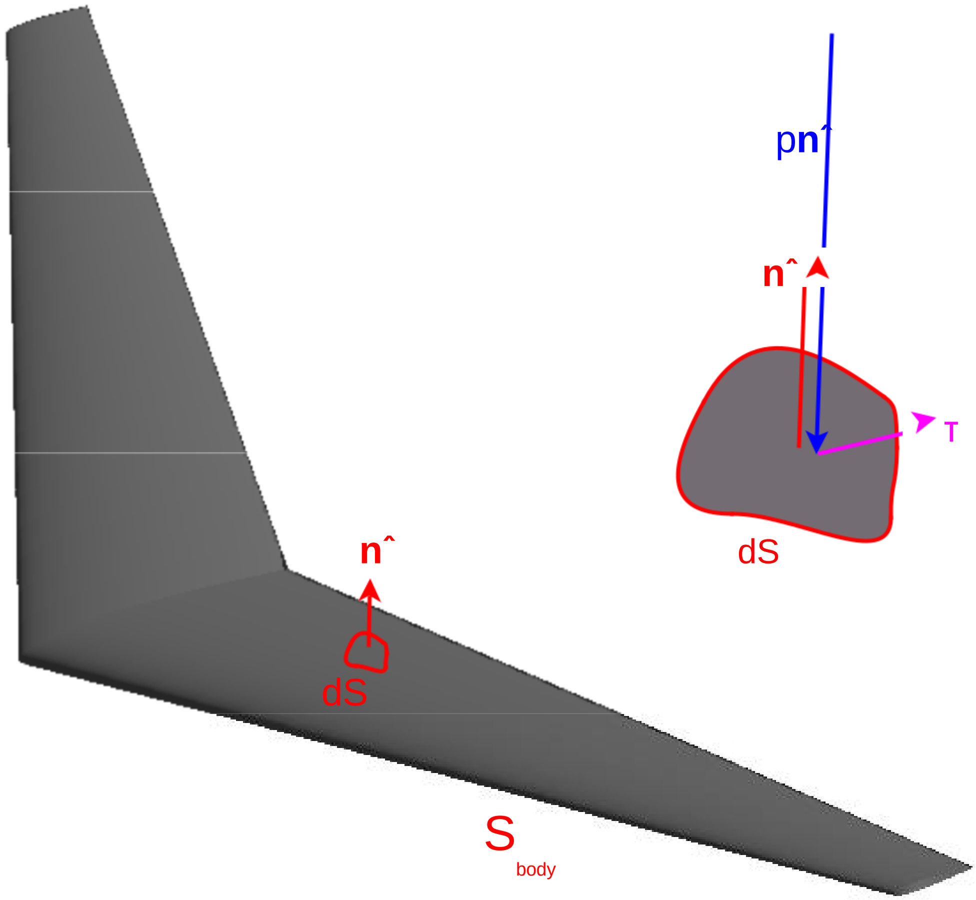

Figure 1.3: Pressure stress $-p\hat{\mathbf{n}}$ and viscous stress τ acting on an infinitesimal surface element of area dS and outward normal $\hat{\mathbf{n}}$ (right figure) taken from a wing with total surface S_{body} (left figure).

The frictional stress is related to the viscosity of the air and therefore more generally is referred to as the viscous stress. Near the body, the viscous stress is largely oriented tangential to the surface, however, a normal component of the viscous stress can exist for unsteady, compressible flows (though even in that case, the normal component of the viscous stress is typically much smaller than the tangential component). To remain general, we will define a viscous stress vector, τ (with arbitrary direction) such that the viscous force acting on dS is,

$$\tau \, dS \equiv \text{viscous force acting on } dS \, . \qquad (1.6)$$

The entire aerodynamic force acting on a body can be found by integrating the pressure and viscous stresses over the surface of the body, namely

$$\mathbf{A} = \iint_{S_{\text{body}}} (-p\hat{\mathbf{n}} + \tau)\, dS. \qquad (1.7)$$

In the following video, we apply this result to show how the differences in pressure between the upper and lower surfaces of a wing result in a z-component of the aerodynamic force, and discuss how this force is related to the lift.

1.3 Wing and Airfoil Geometry

1.3.1 Wing geometric parameters

In Figure 1.4, the planforms of three typical wings are shown with some common geometric parameters highlighted. The wing-span b is the length of the wing along the y axis. The root chord is labeled c_r and the tip chord is labeled c_t. The leading-edge sweep angle is Λ. Though not highlighted in the figure, $S_{planform}$ is the planform area of a wing when projected to the xy plane.

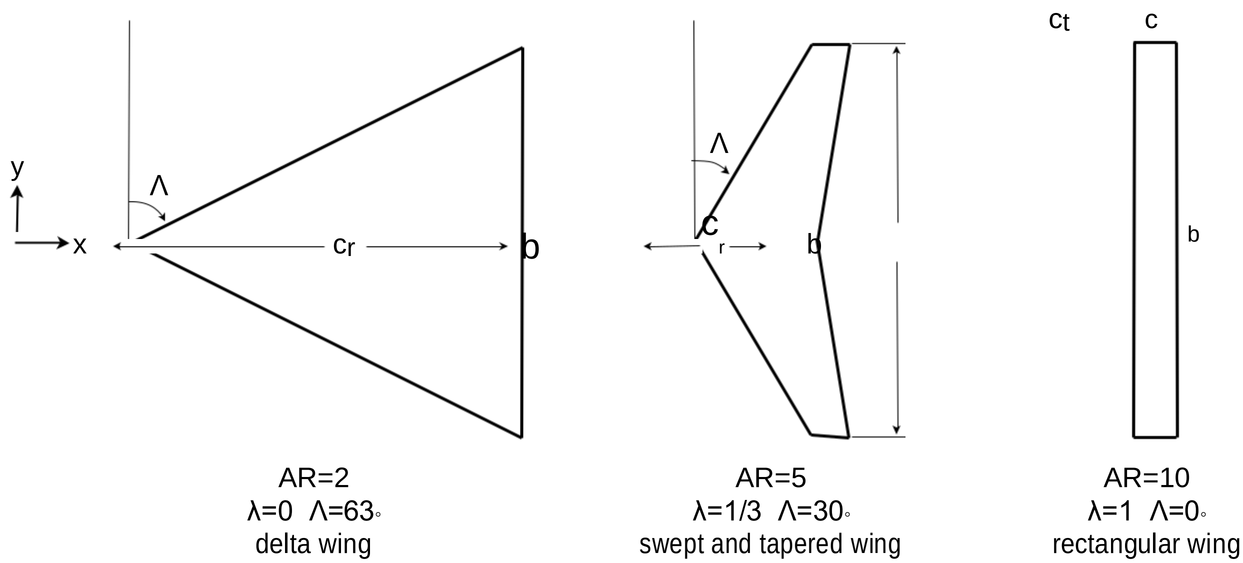

Figure 1.4: Planform views of three typical wings demonstrating different aspect ratios (AR), wing taper ratio (λ), and leading-edge sweep angle (Λ).

A geometric parameter that has a significant impact on aerodynamic performance is the aspect ratio AR which is defined as,

$$AR = \text{aspect ratio} \equiv \frac{b^2}{S_{ref}} \tag{1.8}$$

where S_{ref} is a reference area related to the geometry. As we will discuss in Section 1.4.1, the wing planform area is often chosen as this reference area, $S_{ref} = S_{planform}$.

Figure 1.4 shows wings with three different aspect ratios (choosing $S_{ref} = S_{planform}$): a delta wing with AR = 2; a swept, tapered wing with AR = 5; and a rectangular wing with AR = 10. As can be seen from the figure, as the aspect ratio of the wing increases, the span becomes longer relative to the chordwise lengths.

Another geometric parameter is the taper ratio defined as,

$$\lambda = \text{taper ratio} \equiv \frac{c_t}{c_r} \tag{1.9}$$

For the delta wing, $c_t = 0$ giving $\lambda = 0$, while for the rectangular (i.e. untapered, unswept) wing, $c = c_t = c_r$ giving $\lambda = 1$. The AR = 5 wing has a taper ratio of $\lambda = 1/3$.

1.3.2 Airfoil thickness and camber

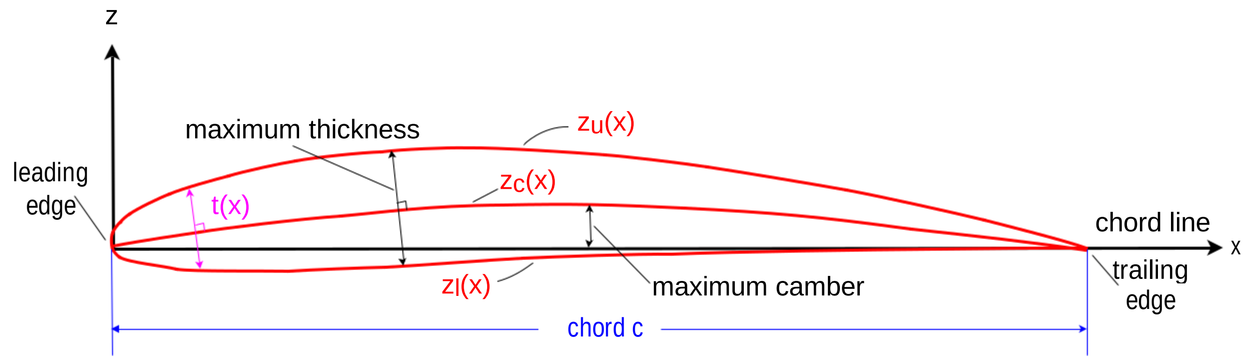

Figure 1.5: Airfoil geometry definition

The cross-section of the wing at a span location produces an airfoil. The common terminology associated with the geometry of airfoils is shown in Figure 1.5. Specifically, we define,

chord line: the chord line is a straight line connecting the leading and trailing edge of the airfoil. In a body-aligned coordinate system, the x-axis is chosen to lie along the chord line.

mean camber line: $z_c(x)$ is the mean camber line and is defined as the curve which is midway between the upper and lower surface measured normal to the mean camber line. The maximum camber is the maximum value of $z_c(x)$.

thickness distribution: $t(x)$ is the thickness distribution and is defined as the distance between the upper and lower surface measured normal to the mean camber line. The maximum thick-ness is the maximum value of $t(x)$.

Defining the angle of the mean camber line as θ_c such that,

$$\tan\theta_c = \frac{dz_c}{dx} \tag{1.10}$$

then the coordinates of points on the upper surface are,

$$x_u = x - \frac{t}{2}\sin\theta_c \tag{1.11}$$

$$z_u = z_c + \frac{t}{2}\cos\theta_c \tag{1.12}$$

and on the lower surface are,

$$x_l = x + \frac{t}{2}\sin\theta_c \tag{1.13}$$

$$z_l = z_c - \frac{t}{2}\cos\theta_c \tag{1.14}$$

We now introduce two other common terms by which airfoils are referred:

uncambered/symmetric airfoil: an airfoil with zero camber, i.e. $z_c(x) = 0$, is known as an uncambered or symmetric airfoil. Both terms are used interchangeably since an uncambered airfoil has an upper and lower surface which is symmetric about the z-axis, i.e. $z_l(x) = -z_u(x)$.

cambered airfoil: a cambered airfoil is one for which $z_c(x) = 0$ (at least for some portion of the chord).

1.3.3 NACA 4-digit airfoils

The NACA 4-digit series of airfoils are used throughout aerodynamics. These airfoils were developed by the National Advisory Committee for Aeronautics (NACA) which was a forerunner to NASA. The four digits of the airfoil are denoted as M P T T , e.g. for the NACA 4510 M = 4, P =5,TT =10.

The last two digits T T give the maximum thickness of the airfoil as a percent of the chord, specifically,

$$t_{max} = \frac{TT}{100} c \tag{1.15}$$

The thickness distribution of this series of airfoils is given by,

$$t = t_{max} \left[2.969 \sqrt{\frac{x}{c}} - 1.260 \frac{x}{c} - 3.516 \left(\frac{x}{c}\right)^2 + 2.843 \left(\frac{x}{c}\right)^3 - 1.015 \left(\frac{x}{c}\right)^4 \right] \tag{1.16}$$

It can be shown that the maximum thickness for these 4-digit airfoils occurs at x/c = 0.3. Also, the radius of curvature at the leading edge,

$$\frac{r_{LE}}{c} = 1.102 \left(\frac{t_{max}}{c}\right)^2 \tag{1.17}$$

Also, note that the thickness for these airfoils is actually non-zero at x/c = 1. Occasionally, the thickness definition is modified so that the thickness at the trailing edge is exactly zero. A common approach is to change the last coefficient from −1.015 to −1.036 which has neglible effects on the thickness distribution except in the immediate neighborhood of the trailing edge.

The M and P values are related to the mean camber line. Specifically, M gives the maximum camber as a percent of the chord,

$$z_{cmax} = \frac{M}{100} c \tag{1.18}$$

P gives the location of the maximum camber as a tenth of the chord. In other words, $z_{cmax} = z_c(x_{cmax})$ where

$$x_{cmax} = \frac{P}{10} c \tag{1.19}$$

Defining m = M/100 and p = P/10, then the formula for the mean camber line for the 4-digit series airfoils is given by,

$$\frac{z_c}{c} = \begin{cases} \dfrac{m}{p^2}\dfrac{x}{c}\left(2p - \dfrac{x}{c}\right), & \text{for } 0 \le \dfrac{x}{c} \le p \\[2ex] \dfrac{m}{(1-p)^2}\left[1 - 2p + 2p\dfrac{x}{c} - \left(\dfrac{x}{c}\right)^2\right], & \text{for } p \le \dfrac{x}{c} \le 1 \end{cases} \tag{1.20}$$

For example, the NACA 4510 airfoil has a maximum thickness which is 10% of the chord, a maximum camber which is 4% of the chord, and the location of maximum camber is at 50% of the chord. Figure 1.6 shows the NACA 0012 and 4412 airfoils. The NACA 0012 is a symmetric airfoil (in fact, all NACA 00T T airfoils are symmetric), while the NACA 4412 is a cambered airfoil.

Figure 1.6: Symmetric 12% thick airfoil (NACA 0012) on left and cambered 12% thick airfoil (NACA 4412) on right

1.4 Non-dimensional Parameters and Dynamic Similarity

1.4.1 Lift and drag coefficient definition

Common aerodynamic practice is to work with non-dimensional forms of the lift and drag, called the lift and drag coefficients. The lift and drag coefficients are defined as,

$$C_L \equiv \frac{L}{\frac{1}{2}\rho_\infty V_\infty^2 S_{ref}} \quad (1.21)$$

$$C_D \equiv \frac{D}{\frac{1}{2}\rho_\infty V_\infty^2 S_{ref}} \quad (1.22)$$

where ρ_∞ is the density of the air (or more generally fluid) upstream of the body and S_{ref} is a reference area that for aircraft is often defined as the planform area of the aircraft's wing.

The choice of non-dimensionalization of the lift and drag is not unique. For example, instead of using the freestream velocity in the non-dimensionalization, the freestream speed of sound (a_∞) could be used to produce the following non-dimensionalizations,

$$\frac{L}{\frac{1}{2}\rho_\infty a_\infty^2 S_{ref}}, \quad \frac{D}{\frac{1}{2}\rho_\infty a_\infty^2 S_{ref}}. \quad (1.23)$$

Or, instead of using a reference area such as the planform area, the wingspan of the aircraft (b) could be used to produce the following non-dimensionalizations,

$$\frac{L}{\frac{1}{2}\rho_\infty V_\infty^2 b^2}, \quad \frac{D}{\frac{1}{2}\rho_\infty V_\infty^2 b^2}. \quad (1.24)$$

A key advantage for using $\rho_\infty V_\infty^2 S_{ref}$ (as opposed to those given above) is that the lift tends to scale with $\rho_\infty V_\infty^2 S_{ref}$. While we will learn more about this as we further study aerodynamics, the first hints of this scaling can be seen in the video in Section 2.2.4. In that video, we saw that the lift on a wing is approximately given by,

$$L \approx \overline{p_l - p_u} \times S_{planform} \quad (1.25)$$

Since the lift on an airplane is mostly generated by the wing (with smaller contributions from the fuselage), then choosing $S_{ref} = S_{planform}$ will tend to capture the dependence of lift on geometry for an aircraft. Also, the average pressure difference $p_l - p_u$ tends to scale with $\rho_\infty V_\infty^2$ (again, we will learn more about this latter). Thus, this normalization of the lift tends to capture much of the parametric dependence of the lift on the freestream flow conditions and the size of the body. As a result, for a wide-range of aerodynamic applications, from small general aviation aircraft to large transport aircraft, the lift coefficient tends to have similar magnitudes, even though the actual lift will vary by orders of magnitude.

While aerodynamic flows are three-dimensional, significant insight can be gained by considering the behavior of flows in two dimensions, i.e. the flow over an airfoil. For airfoils, the lift and drag are actually the lift and drag per unit length. We will label these forces per unit length as L' and D'. The lift and drag coefficients for airfoils are defined as,

$$c_l \equiv \frac{L'}{\frac{1}{2}\rho_\infty V_\infty^2 c} \quad (1.26)$$

$$c_d \equiv \frac{D'}{\frac{1}{2}\rho_\infty V_\infty^2 c} \quad (1.27)$$

where c is the airfoil's chord length (its length along the x-body axis, i.e. viewed from the z-direction). In principle, other lengths could be used (for example, the maximum thickness of the airfoil). However, since the lift tends to scale with the airfoil chord (analogous to the scaling of lift with the planform area of a wing), the chord is chosen exclusively for aerodynamic applications.

1.4.2 Lift coefficient comparison for general aviation and commer-cial transport aircraft

Determine the lift coefficient at cruise for (1) a propellor-driven general aviation airplane and (2) a large commercial transport airplane with turbofan engines given the following characteristics:

		General aviation	Commercial transport
Total weight	W	2,400 lb	550,000 lb
Wing area	S_{ref}	180 ft^2	4,600 ft^2
Cruise velocity	V_∞	140 mph	560 mph
Cruise flight altitude		12,000 ft	35,000 ft
Density at cruise altitude	ρ_∞	1.6×10^{-3} slug/ft^3	7.3×10^{-4} slug/ft^3

Note that the total weight includes aircraft, passengers, cargo, and fuel. The air density is taken to correspond to the density at the flight altitude of each airplane in the standard atmosphere.

What is the lift coefficient for the general aviation airplane? Provide your answer with two digits of precision (of the form X.YeP).

1.4.3 Drag comparison for a cylinder and fairing

The drag on a cylinder is quite high especially compared to a streamlined-shape such as an airfoil. For situations in which minimizing drag is important, airfoils can be used as fairings to surround a cylinder (or other high drag shape) and reduce the drag. Consider the cylinder (in blue) and fairing (in red) shown in the figure.

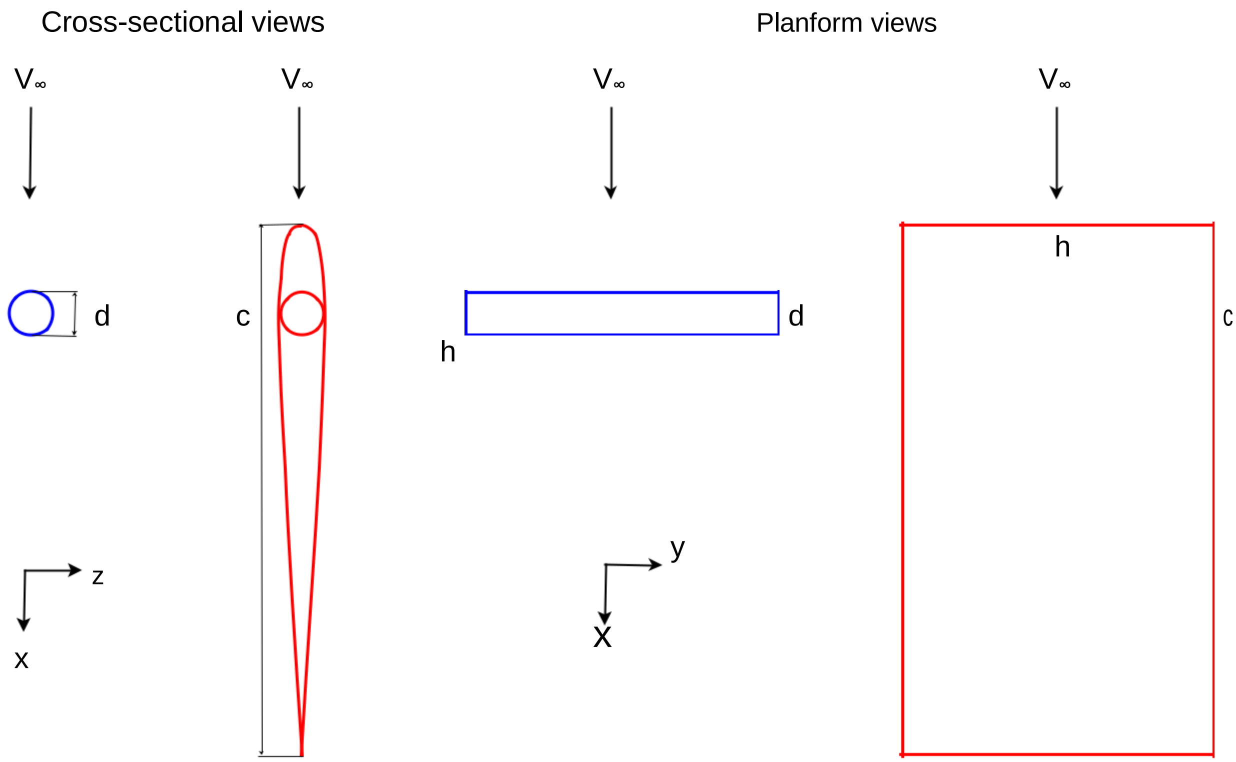

For the flow velocity of interest, the drag coefficient for the cylinder is $C_{D_{cyl}} \approx 1$ using the streamwise projected area for the reference area, i.e. S_{cyl} = dh.

Similarly, consider a fairing with chord c = 10d. For the flow velocity of interest, the drag coefficient for the fairing is $C_{D_{fair}} \approx 0.01$ using the planform area for the reference area, i.e. S_{fair} = ch.

What is D_{cyl}/D_{fair}, i.e. the ratio of the drag on the cylinder to the drag on the fairing?

1.5 Aerodynamic Performance

1.5.1 Aerodynamic performance plots

The variation of the lift and drag coefficient with respect to angle of attack for a typical aircraft (or for a typical airfoil in a two-dimensional problem) is shown in Figure 1.10. For lower values of angle of attack, the lift coefficient depends nearly linearly on the angle of attack (that is, the C_L-α curve is nearly straight). As the angle of attack increases, the lift eventually achieves a maximum value and is referred to as C_{Lmax}. This maximum lift is often referred to as the stall condition for aircraft. The value of C_{Lmax} is a key parameter in the aerodynamic design of an aircraft as it directly impacts the take-off and landing performance of the aircraft (see e.g. Problem 1.5.2).

Also shown on the C_L plot is the angle at which the lift is zero, $\alpha_{L=0}$. This angle is often used in describing the low angle of attack performance since given this value and the slope a_0 a reasonable approximation to C_L-α dependence is

$$C_L \approx a_0(\alpha - \alpha_{L=0}). \tag{1.37}$$

Finally, as the angle of attack decreases beyond $\alpha_{L=0}$, lift also achieves a minimum value. This negative incidence stall is less critical for aircraft, however, it does play a critical role in the performance of blades in axial-flow turbomachinery (setting one limit on the operability of these type of turbomachinery).

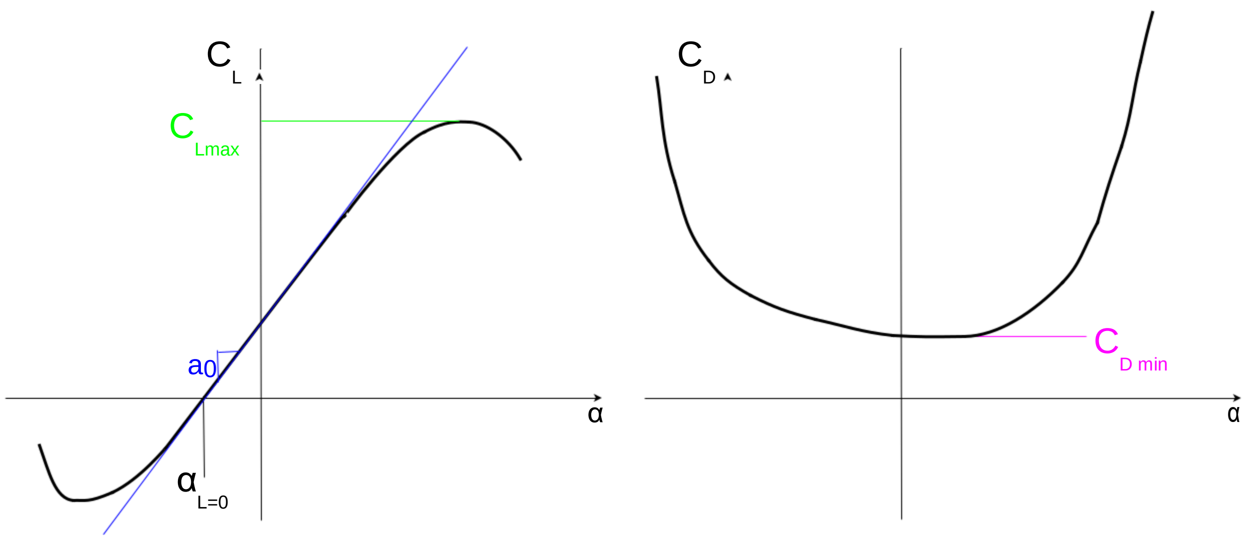

Figure 2.10: Typical lift and drag coefficient variation with respect to angle of attack for an aircraft

C_D is shown to have a minimum value C_{Dmin} which will typically occur in the region around which the lift is linear with respect to angle of attack. As the angle of attack increases, C_D also increases with rapid increases often occuring as C_{Lmax} is approached. Similar behavior also occurs for the negative incidence stall.

A useful method of plotting the drag coefficient variation is not with respect to angle of attack but rather plotting $C_D(\alpha)$ and $C_L(\alpha)$ along the x and y axis, respectively. This type of plot is commonly referred to as the drag polar and emphasizes the direct relation between lift and drag. It is indeed often more important to know how much drag one needs to "pay" to generate a given lift (or equivalently to lift a given weight).

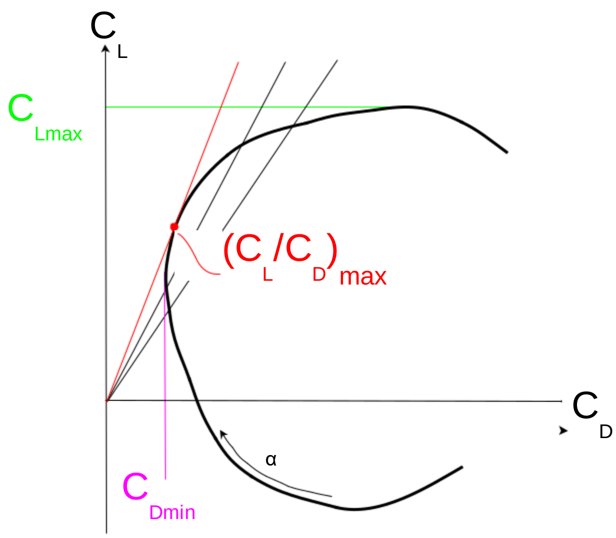

Figure 1.11: Typical drag polar for an aircraft

A typical drag polar is shown in Figure 1.11. In this single plot, the minimum drag and maximum lift coefficients can be easily identified. Also, shown in the plot is the location (the red dot) on the drag polar where C_L/C_D is maximum. Note that constant C_L/C_D occurs along lines passing through $C_D = C_L = 0$ and having constant slope. A few of these lines are shown in the plot. The maximum C_L/C_D line (the red line) must be tangent to the drag polar at its intersection (if not, C_L/C_D could be increased by a small change in the position along the polar).

To help gain further understanding of the magnitude and behavior of c_l and c_d, we consider two airfoils specifically the NACA 0012 and the NACA 4412 previously shown in Figure 1.6. The variation of c_l versus α is shown in Figure 1.12 for these airfoils at two different Reynolds numbers, $Re_\infty = 10^6$ and 10^7. Since the NACA 0012 is symmetric, the lift coefficients at α and $-\alpha$ have the same magnitude (but opposite sign) and $\alpha_{L=0} = 0$. Note that the slope in the linear region is not dependent on Reynolds number, and that $a_0 \approx 0.11$ per degree, or equivalently, 6.3 per radian. The same lift slope is observed for the NACA 4412, but in this case the camber of the airfoil causes $\alpha_{L=0} \approx -4^\circ$, making the lift coefficient higher for a given angle of attack compared to the NACA 0012. Finally, we note that the maximum c_l is dependent on the Reynolds number, with higher c_{lmax} occurring for higher Re_∞. During the course of this subject, we will discuss these various behaviors in detail.

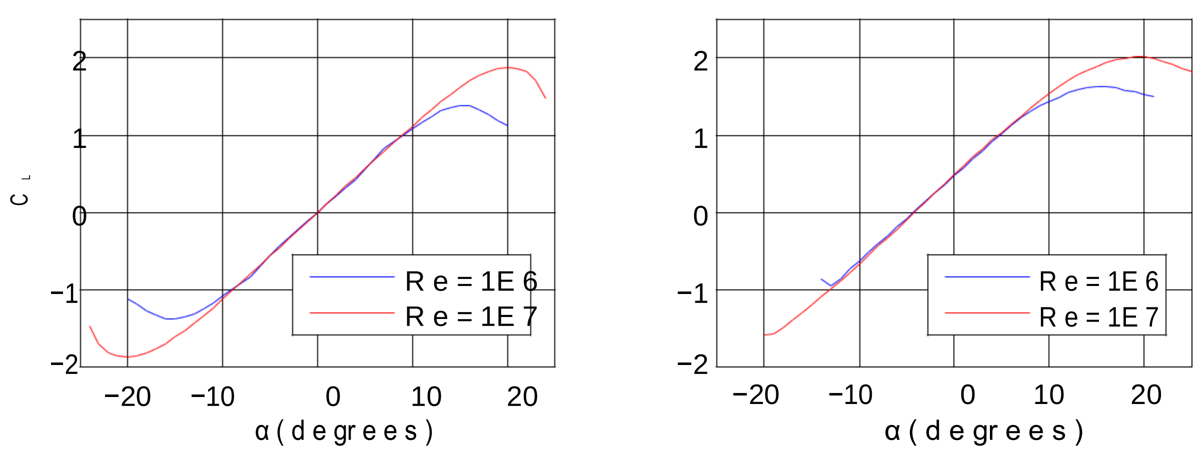

Figure 1.12: c_l versus α for NACA 0012 on left and NACA 4412 on right at $Re_\infty = 10^6$ and 10^7

The drag polars for these airfoils at the two Reynolds numbers are shown in Figure 2.13. Note that the drag coefficient is multiplied by 10^4, which is a frequently used scaling for the drag coefficient. In fact, a c_d increment of 10^{-4} is known as a **count** of drag and is commonly used to report drag coefficients in aerodynamics. Increasing the Reynolds number lowers the drag coefficient at these high Reynolds numbers. The minimum drag for the symmetric airfoil occurs at $c_l = 0$. However, for the cambered airfoil, the minimum drag occurs at $c_l \approx 0.5$. Thus, the maximum lift-to-drag ratio is larger and occurs for a higher c_l for the cambered airfoil. It is this result that leads to almost all aircraft with subsonic and transonic flight speeds to have cambered airfoils.

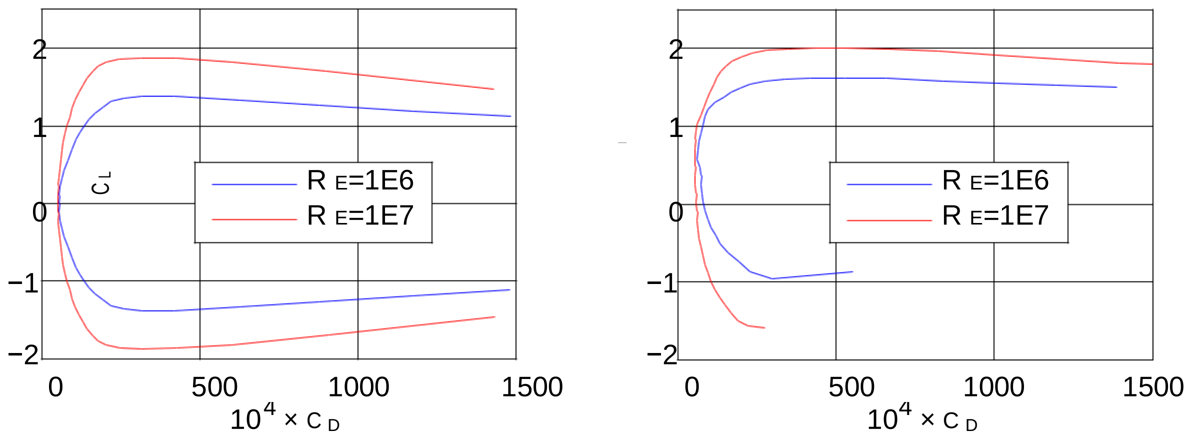

Figure 1.13: Drag polar for NACA 0012 on left and NACA 4412 on right at $Re_\infty = 10^6$ and 10^7

1.6 Potential Flow Modeling

1.6.1 Governing equations and the velocity potential

In the next two modules, we will assume that the flow around a body can be approximated as,

- Steady: the properties of the flow do not depend on time
- Inviscid: viscous stresses are assumed negligible
- Incompressible: the density is assumed constant
- Uniform freestream flow: the flow properties far upstream of the body are uniform
- Irrotational: the vorticity is zero **essentially everywhere** in the flow

In this section on Potential Flow Modeling, we will remain general to both two-dimensional and three-dimensional as the basic governing equations, boundary conditions, and modeling approach do not change between two- and three-dimensional flows. In the rest of this module and the next, we will solely focus on two-dimensional flows.

As you can see in the list of assumptions, the statement of irrotationality is qualified as the vorticity being zero **essentially everywhere**. This qualification is because we will allow vorticity at boundaries, which are not technically within the flow field, and in the three-dimensional flows we consider in the next module, along infinitely thin lines or sheets. In summary, we will use the term **irrotational** to describe flows that have zero vorticity almost everywhere, and proceed with caution.

The flow variables that we wish to determine are the pressure field p(x, y, z) and the velocity field **V**(x, y, z). Far upstream of the body, the uniform conditions will be p_∞ for the pressure and,

$$\mathbf{V}_\infty = V_\infty \cos\alpha\, \hat{\mathbf{i}} + V_\infty \sin\alpha\, \hat{\mathbf{k}} \tag{1.24}$$

for the velocity vector where α is the angle of attack. We assume density ρ is constant and given.

With the assumptions stated, we can now determine p(x, y, z) and **V**(x, y, z) using the state-ments of conservation of mass and momentum. Recall that the conservation of mass for an incom-pressible flow is,

$$\nabla \cdot \mathbf{V} = 0 \tag{1.25}$$

Since the flow has zero vorticity (because of our irrotational assumption), this means that the velocity vector field can be written as the gradient of a scalar function. This is a general result from vector calculus, that is a vector field with zero curl can always be written as the gradient of a scalar field. Using this, we can define a scalar field, φ(x, y, z), as,

$$\mathbf{V} = \nabla\varphi \tag{1.26}$$

which we will call the velocity potential, or just the potential for short. Substituting this into Equation (8.25) produces the conservation of mass in terms of the velocity potential,

$$\nabla \cdot (\nabla\varphi) = 0 \tag{1.27}$$

$$\nabla^2\varphi = 0 \tag{1.28}$$

where this partial differential equation for φ is known as Laplace's equation, and ∇^2 is called the Laplacian and is defined as,

$$\nabla^2 \equiv \frac{\partial^2}{\partial x^2} + \frac{\partial^2}{\partial y^2} + \frac{\partial^2}{\partial z^2} \tag{1.29}$$

The conservation of momentum reduces to the Bernoulli equation, as derived in Equation (1.22), and repeated here,

$$p + \frac{1}{2}\rho V^2 = p_\infty + \frac{1}{2}\rho V_\infty^2 \tag{1.30}$$

The basic process for determining **V** and p then is

1 Solve Equation (1.28) for φ

2 Determine the velocity from Equation (1.26)

3 Find the pressure from Bernoulli's equation, Equation (1.30)

1.6.3 Boundary conditions

In order to solve Equation (1.28), boundary conditions are needed on φ. The boundaries of concern in our application will be on the surface of the body and far away from the body (in what we will refer to as the farfield). Mathematically, Laplace's equation allows only one boundary condition to be set on φ at any point on the boundary of the domain.

At a solid surface, we will require that the flow must be tangent to the surface, that is, the flow cannot enter the surface. Thus, flow tangency on a stationary surface requires that the component of the velocity normal to the surface is zero,

$$\mathbf{V} \cdot \hat{\mathbf{n}} = 0 \tag{1.31}$$

where $\hat{\mathbf{n}}$ is the normal to the surface. Substituting in the potential, the flow tangency boundary condition becomes,

$$\nabla\varphi \cdot \hat{\mathbf{n}} = \frac{\partial \varphi}{\partial n} = 0 \text{ at a solid surface.} \tag{1.32}$$

In the farfield (as $|\mathbf{x}|\ !\ \infty$), we will assume that the flow velocity in the freestream direction returns to $\mathbf{V}_\infty$,

$$\mathbf{V} \cdot \mathbf{t}_\infty = V_\infty \quad \text{as } |\mathbf{x}|\ !\ \infty \tag{1.33}$$

where $\mathbf{t}_\infty \equiv \mathbf{V}_\infty / V_\infty$ is the unit vector in the direction of the freestream. In terms of the potential, this boundary condition is,

$$\nabla\varphi \cdot \mathbf{t}_\infty = V_\infty \quad \text{as } |\mathbf{x}|\ !\ \infty \tag{1.34}$$

This farfield boundary condition permits non-zero velocity perturbations in the plane normal to the freestream direction. However, in two-dimensional steady potential flows on unbounded domains, all components of the velocity perturbations can be shown to approach zero in the farfield (we will see this in the Embedded Question in Section 1.5.3 of the next module). In three-dimensional flows, perturbations can exist normal to the freestream and are an important feature of these flows. Specifically, a physical example of how these velocity perturbations can be non-zero is the vortex wake system downstream of a lifting body in three-dimensional flows (often associated with the wing tip vortex). In this case, the vortical motion far downstream of the body will be swirling about the freestream direction.

1.6.4 Equipotential lines and flow tangency

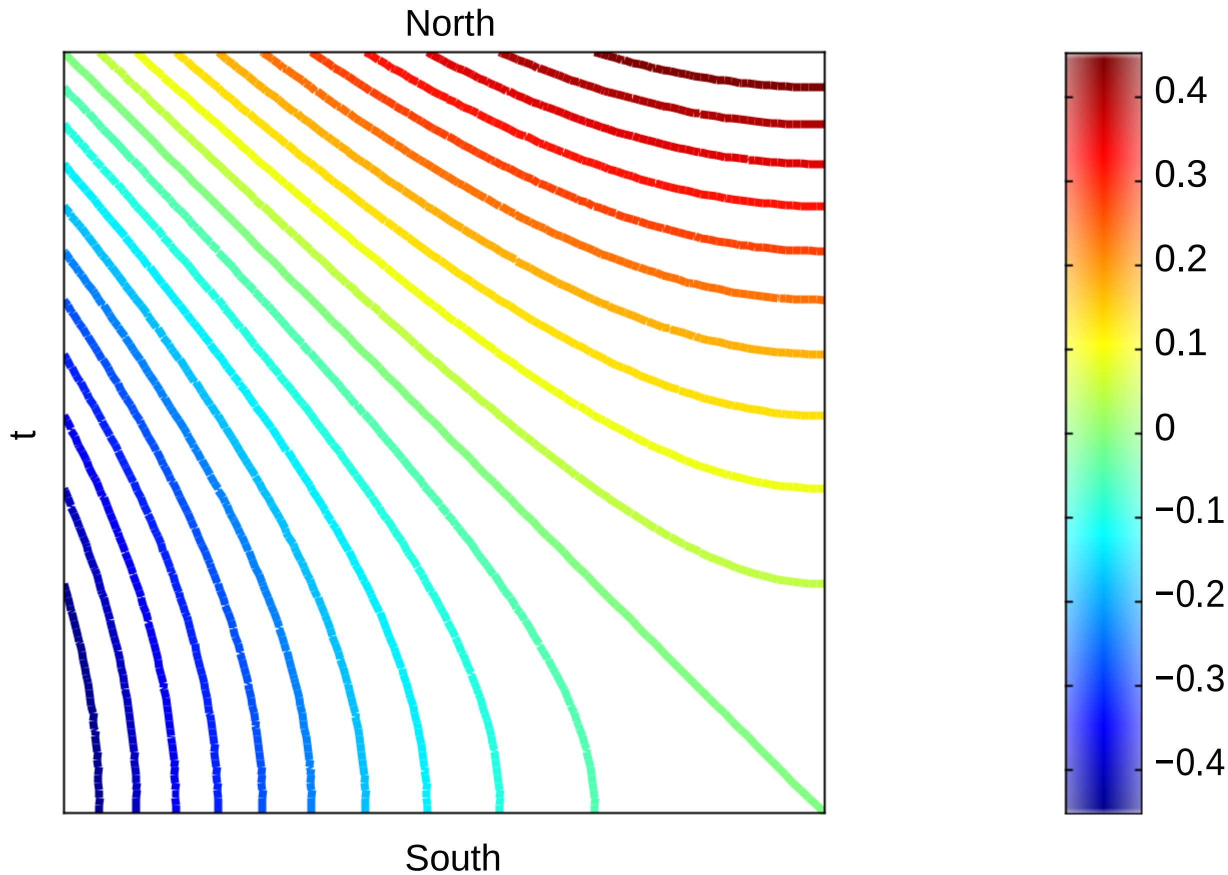

The figure above shows equipotential lines (i.e. lines along which φ is constant) for a two-dimensional incompressible potential flow. In this problem, you must use the equipotential lines to determine which boundaries the flow is entering the domain, tangent to the boundary, or exiting the domain.

1.6.6 Modeling approach

The approach used in potential flow modeling in aerodynamics is based on the principle of linear superposition. Let's consider two different potentials φ_1 and φ_2 both of which satisfy the conservation of mass (i.e. Laplace's equation),

$$\nabla^2\varphi_1 = 0 \tag{1.37}$$

$$\nabla^2\varphi_2 = 0 \tag{1.38}$$

Now, let us add these two potentials together including an arbitrary weighting to each, to define a new potential,

$$\varphi_{new} = c_1\varphi_1 + c_2\varphi_2 \tag{1.39}$$

where c_1 and c_2 are arbitrary constants. This new potential can be shown to satisfy the conservation of mass as well,

$$\begin{aligned}
\nabla^2\varphi_{new} &= \nabla^2(c_1\varphi_1 + c_2\varphi_2) && (1.40)\\
&= \nabla^2(c_1\varphi_1) + \nabla^2(c_2\varphi_2) && (1.41)\\
&= c_1\nabla^2\varphi_1 + c_2\nabla^2\varphi_2 && (1.42)\\
&= 0 && (1.43)
\end{aligned}$$

This generalizes to an arbitrary number of potentials such that if φ is defined as,

$$\varphi = \sum_{i=1}^{N} c_i\varphi_i \tag{1.44}$$

where $\nabla^2\varphi_i = 0$ for all i, then $\nabla^2\varphi = 0$. This means that the flow field arising from any linear combination of φ_i will satisfy conservation of mass.

Let's get a little more specific and introduce our first (and simplest) potential flow. That is, the potential for a uniform velocity of $\mathbf{V}_\infty$. We will label this velocity potential as φ_∞,

$$\varphi_\infty \equiv xV_\infty \cos\alpha + zV_\infty \sin\alpha \tag{1.45}$$

Then, taking the gradient of φ_∞, the velocity of this potential is,

$$\mathbf{V} = \nabla\varphi_\infty = V_\infty \cos\alpha\,\hat{\mathbf{i}} + V_\infty \sin\alpha\,\hat{\mathbf{k}} \tag{1.46}$$

Thus, φ_∞ represents a uniform flow at an angle α and speed V_∞.

Now, we consider the following linear combination of potentials,

$$\varphi = \varphi_\infty + \sum_{i=1}^{N} c_i\varphi_i \tag{1.47}$$

And, as before we assume that $\nabla^2\varphi_i = 0$. Further, we assume that the φ_i also satisfy,

$$\nabla\varphi_i \cdot \mathbf{t}_\infty = 0 \text{ as } |\mathbf{x}| \to \infty \tag{1.48}$$

In other words, the φ_i do not perturb the farfield velocity along the freestream direction. If we can find such φ_i, then the φ defined by Equation (1.47) will satisfy the farfield boundary condition (given by Equation 1.34) for any values of c_i (you might try to do this proof yourself!). This means that the c_i values can then be freely chosen to satisfy the flow tangency condition at the solid boundaries for the body of interest.

These φ_i are the building blocks for approximating our aerodynamic flows. The key then to this modeling approach is to find the φ_i which satisfy Laplace's equation and the farfield boundary condition in Equation (1.48). We consider this in the next section for two-dimensional flows and along the way encounter some classic potential flows.

1.7.4 Two-dimensional Nonlifting Flows

1.7.4.1 Introduction to nonlifting flows

1.1.

In this section, we will consider potential flows in which the lift is zero. Then, in the next section, we introduce the additional concepts required to model lifting flows.

1.7.4.2 Cylindrical coordinate system

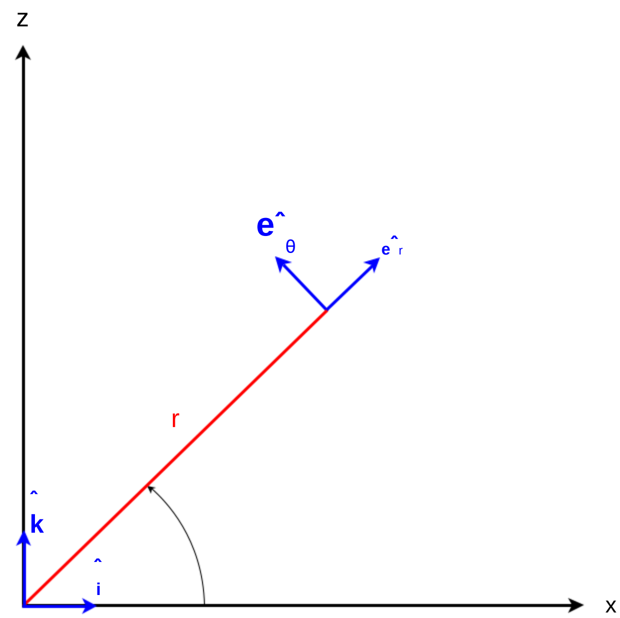

Figure 1.7.1: Two-dimensional cylindrical coordinate system

Many of the basic potential flows we will use as the building blocks of our aerodynamic models are easier to represent and analyze in cylindrical coordinates. As the two-dimensional coordinate system for our main application to airfoils is in the (x, z) plane (refer to Figure 1.5), we define the cylindrical coordinate system as shown in Figure 1.7.1. This gives the following relationship between (x, z) and (r, θ)

$$x = r\cos\theta \tag{1.52}$$

$$z = r\sin\theta \tag{1.53}$$

The unit vectors in the r and θ direction are,

$$\hat{\mathbf{e}}_r = \cos\theta\,\hat{\mathbf{i}} + \sin\theta\,\hat{\mathbf{k}} \tag{1.54}$$

$$\hat{\mathbf{e}}_\theta = -\sin\theta\,\hat{\mathbf{i}} + \cos\theta\,\hat{\mathbf{k}} \tag{1.55}$$

The radial and θ velocity components are related to u and w by,

$$u_r = u\cos\theta + w\sin\theta \tag{1.56}$$

$$u_\theta = -u\sin\theta + w\cos\theta \tag{1.57}$$

The gradient operator in cylindrical coordinates can be applied to φ to find u_r and u_θ,

$$u_r = \frac{\partial \varphi}{} \tag{1.58}$$

$$u_\theta = \frac{1}{r}\frac{\partial \varphi}{\partial \theta} \tag{1.59}$$

The divergence and curl of the velocity vector in cylindrical coordinates are,

$$\nabla\cdot\mathbf{V} = \frac{1}{r}\frac{\partial}{\partial r}(r u_r) + \frac{1}{r}\frac{\partial u_\theta}{\partial \theta} \tag{1.60}$$

$$\nabla\times\mathbf{V} = \left(\frac{1}{r}\frac{\partial u_r}{\partial \theta} - \frac{1}{r}\frac{\partial}{\partial r}(r u_\theta)\right)\hat{\mathbf{j}} \tag{1.61}$$

Finally, we note that Laplace's equation for φ in cylindrical coordinates is,

$$\nabla^2\varphi = \frac{1}{r}\frac{\partial}{\partial r}\left(r\frac{\partial \varphi}{\partial r}\right) + \frac{1}{r^2}\frac{\partial^2 \varphi}{\partial \theta^2} = 0 \tag{1.62}$$

1.7.4.3 Source

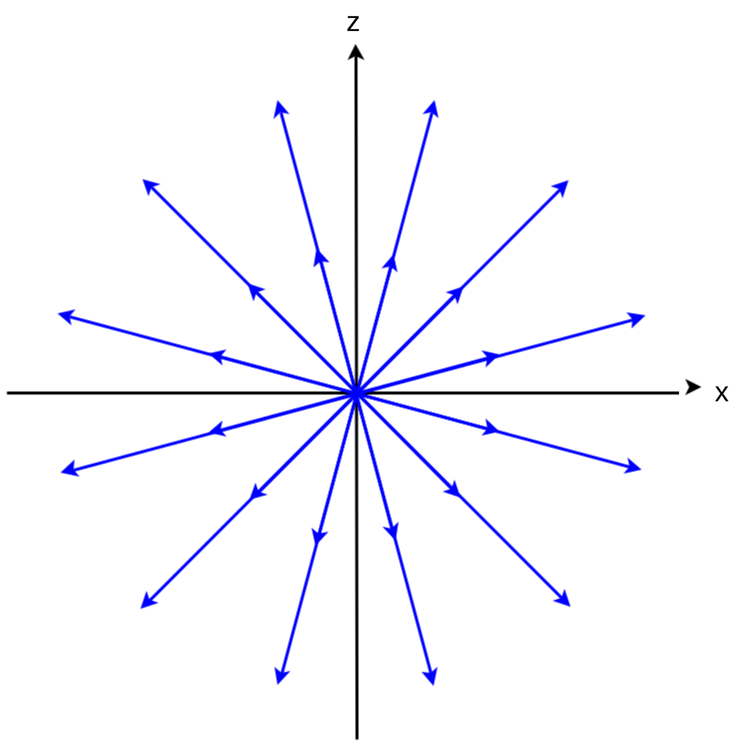

Figure 1.7.2: Streamlines for a point source

The first of our building blocks in two-dimensional potential flows is called a source and has the following potential and velocity field,

$$\varphi = \frac{\Lambda}{2\pi}\ln r \tag{1.63}$$

$$u_r = \frac{\Lambda}{2\pi r} \tag{1.64}$$

$$u_\theta = 0 \tag{1.65}$$

where Λ is a scaling constant called the **source strength**. Note that the units of Λ are (length)^2/time. As shown in Figure 1.7.2, the streamlines for the point source emit from the origin and are purely radial (since $u_\theta = 0$). Clearly, this means that the source emits mass at its origin. When $\Lambda < 0$, then the flow is drawn into the origin and in this case can be refered to as a **sink**.

The fact that a source produces mass would appear to be a violation of the conservation of mass. In the following video, we will explore this issue and a few others as we consider the source flow in more detail.

Summarizing the main results of this video, we see that:

- A source emits mass at a rate of $\rho\Lambda$ per unit span.
- A source satisfies the conservation of mass except at its origin. That is $\nabla \cdot \mathbf{V} = 0$ everywhere in the flow expect at its origin. And, at the origin, $\nabla \cdot \mathbf{V}$ is infinite.

In some situations, it is useful to have the potential and velocity for a source in (x, z) coordinates. For completeness, we include those expressions here.

$$\varphi = \frac{\Lambda}{2\pi} \ln \sqrt{x^2 + z^2} \tag{1.66}$$

$$u = \frac{\Lambda}{2\pi} \frac{x}{x^2 + z^2} \tag{1.67}$$

$$w = \frac{\Lambda}{2\pi} \frac{z}{x^2 + z^2} \tag{1.68}$$

1.7.4.4 Calculating mass flow rate for a source

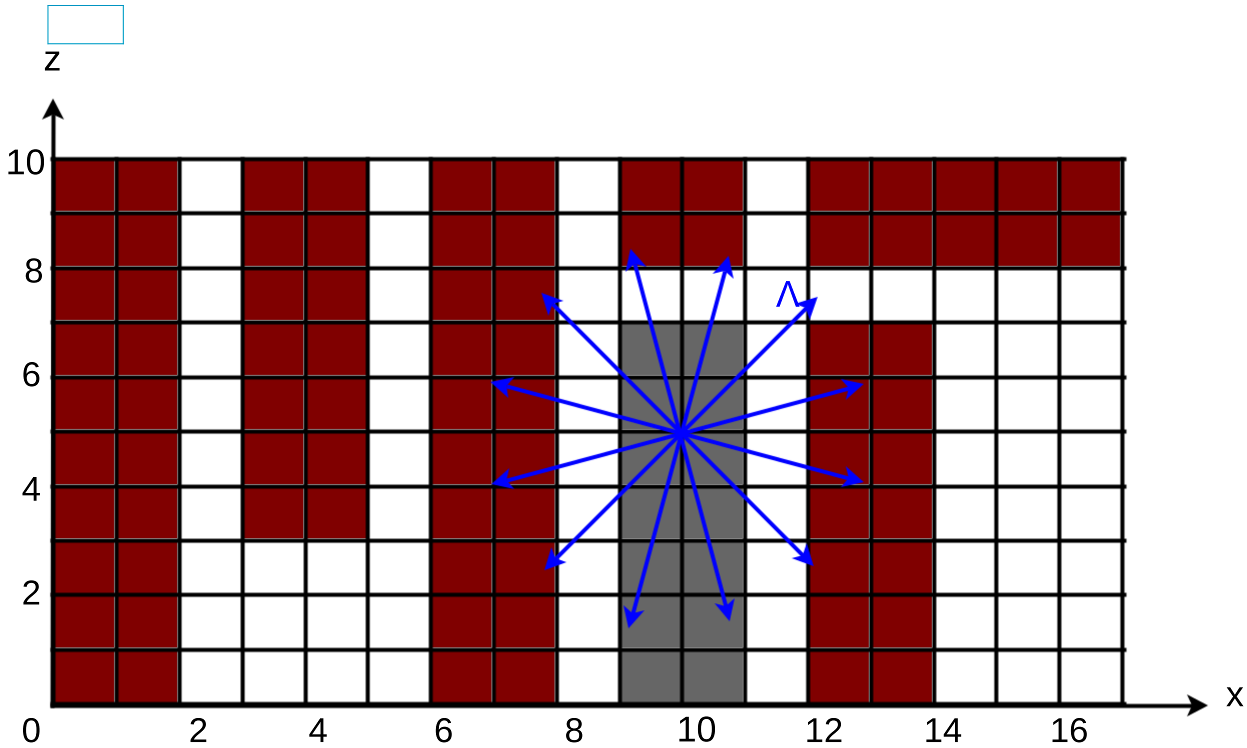

Consider the flow created by a source with strength $\Lambda = 11$ smoot^2/s as shown in the above figure. Note that a **smoot** is a unit of length occasionally used at MIT and the coordinate system in the figure is in smoots. (If you want to know more about smoots, do an Internet search). The fluid has a density of 7 kg/smoot^3. Determine the net mass flow rate (per span) out of the surfaces of the rectangular control volumes shown in the figure (in other words, determine $\rho\mathbf{V} \cdot \hat{\mathbf{n}}\, dS$ for each control volume, where $\hat{\mathbf{n}}$ is an outward point normal). Provide your answers in units of kg/smoot-s and use two significant digits.

What is the net mass flow rate out of the control volume with corners at (0, 0) and (2, 10)?

What is the net mass flow rate out of the control volume with corners at (3, 3) and (5, 10)?

What is the net mass flow rate out of the control volume with corners at (6, 0) and (8, 10)?

What is the net mass flow rate out of the control volume with corners at (9, 0) and (11, 7)?

What is the net mass flow rate out of the control volume with corners at (9, 8) and (11, 10)?

What is the net mass flow rate out of the control volume with corners at (12, 0) and (14, 7)?

What is the net mass flow rate out of the control volume with corners at (12, 8) and (17, 10)?

1.7.4.5 Flow over a Rankine oval

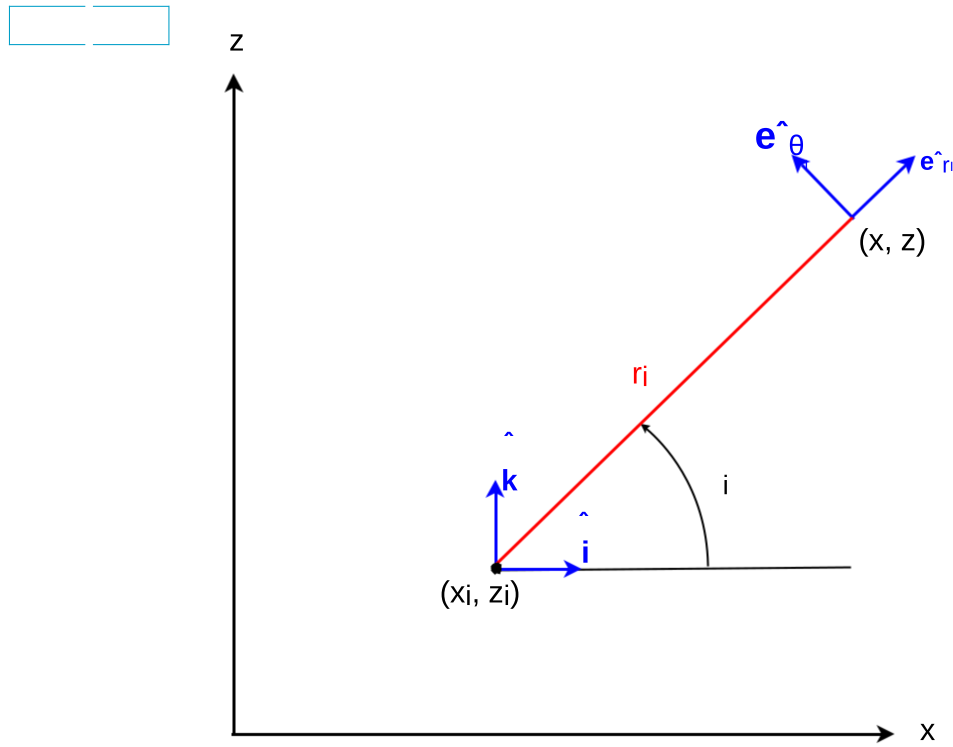

Figure 1.7.3: Two-dimensional cylindrical coordinate system about a point (x_i, z_i).

In this section, we describe the potential flow over a shape known as the Rankine oval. It will be our first potential flow in which we combine multiple potentials. In this case, we will combine a freestream at zero angle of attack with two sources. A source with positive strength Λ will be located at $(-l, 0)$ and a source with negative strength $-\Lambda$ (in others words, this is a sink) will be located at $(l, 0)$. To do this, we will need to translate the source potentials from the origin as they are given in Equations (1.63)-(1.65), to $(\pm l, 0)$. We define the coordinate system about a point (x_i, z_i) as shown in Figure 1.7.3, where

$$r_i = \sqrt{(x - x_i)^2 + (z - z_i)^2} \tag{1.69}$$

$$\theta_i = \arctan \frac{z - z_i}{x - x_i} \tag{1.70}$$

Using this coordinate system, a source of strength Λ_i located at point (x_i, z_i) has the following potential and velocity,

$$\varphi = \frac{\Lambda_i}{2\pi} \ln r_i \tag{1.71}$$

$$u_{r_i} = \frac{\Lambda_i}{2\pi r_i} \tag{1.72}$$

$$u_{\theta_i} = 0 \tag{1.73}$$

To emphasize, these radial and circumferential velocity components are in the $\hat{\mathbf{e}}_{r_i}$ and $\hat{\mathbf{e}}_{\theta_i}$ directions, not the radial and circumferential directions about the origin (in otherwords, not about $\hat{\mathbf{e}}_r$ and $\hat{\mathbf{e}}_\theta$).

The x and z velocity component expressions for these translated sources are,

$$\varphi = \frac{\Lambda_i}{2\pi} \ln \sqrt{(x - x_i)^2 + (z - z_i)^2} \tag{1.74}$$

$$u = \frac{\Lambda_i}{2\pi} \frac{x - x_i}{(x - x_i)^2 + (z - z_i)^2} \tag{1.75}$$

$$w = \frac{\Lambda_i}{2\pi} \frac{z - z_i}{(x - x_i)^2 + (z - z_i)^2} \tag{1.76}$$

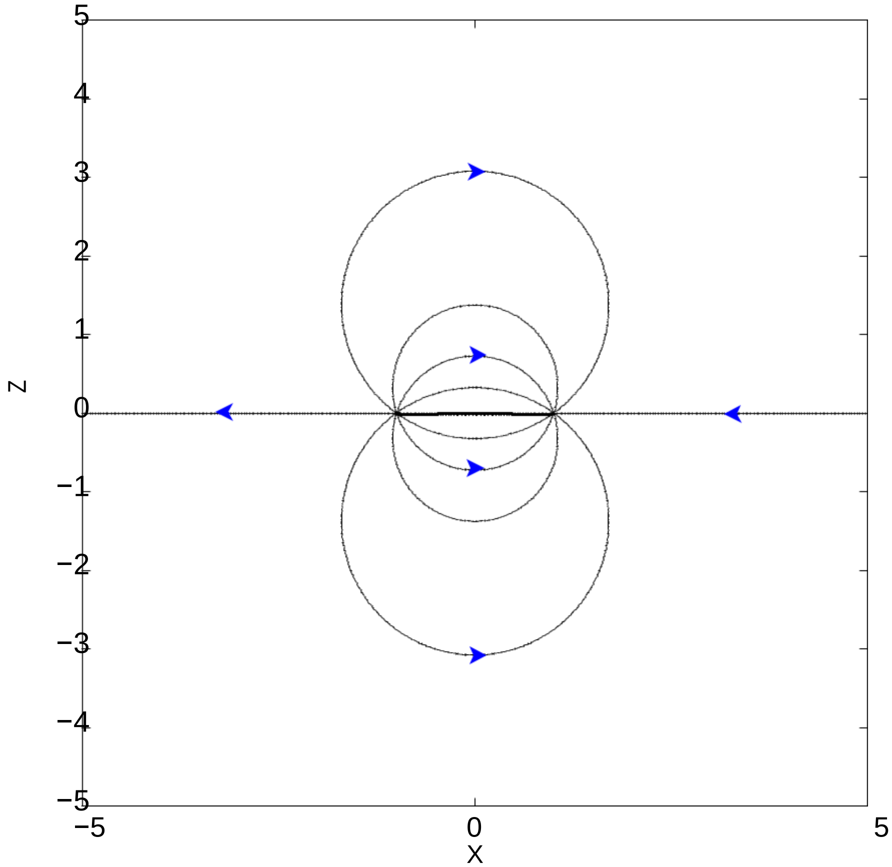

Figure 1.7.4: Streamlines for sources of strength $\Lambda = \mp 4$ located at $(\pm 1, 0)$.

Let's consider first the flow due to just the two sources. We will consider the specific case in which $\Lambda/(V_\infty l) = 4$. Non-dimensionalizing the velocities by V_∞ and the spatial coordinates by l, we will place the sources at $x = \pm 1$ (and $z = 0$) with strengths of ∓ 4. Figure 1.7.4 shows the flow induced only by the two sources. We can see that the flow is emitted from the source at $x = -1$ and is drawn into the source (which is acting as a sink) at $x = 1$.

Then, adding the freestream velocity produces the flow about a Rankine oval as shown in Figure 1.7.5. In the following video, we discuss this Rankine flow in more detail.

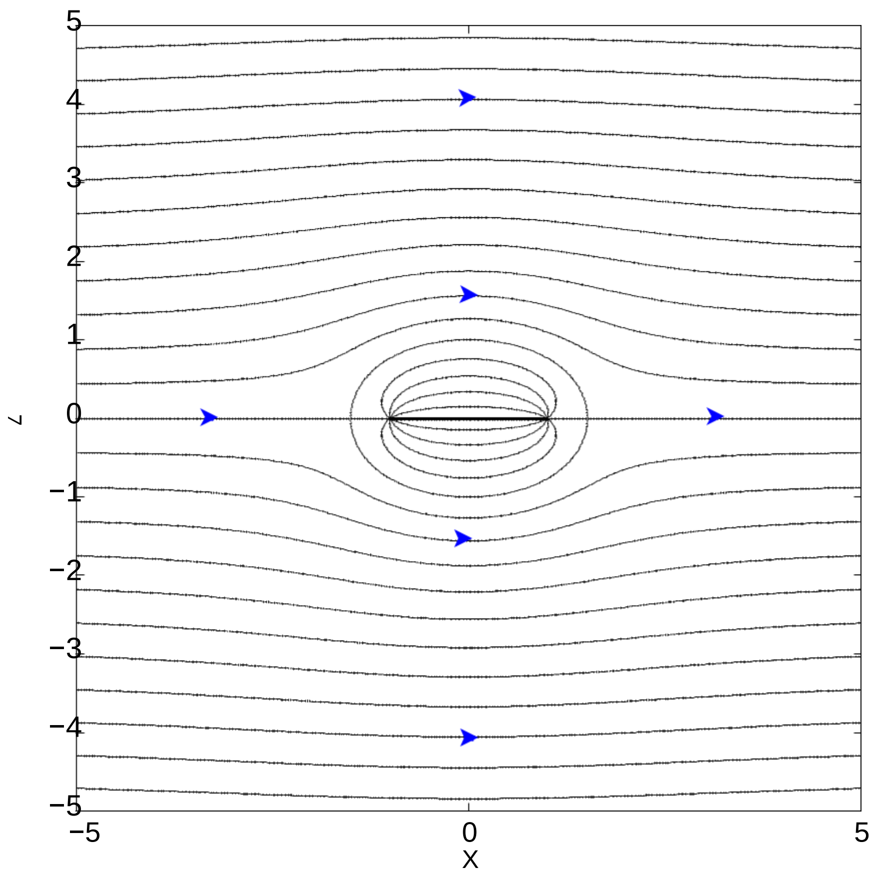

Figure 1.7.5: Streamlines for Rankine oval produced by a freestream flow and sources of strength $\Lambda = \mp 4$ located at $(\pm 1, 0)$.

Plot A

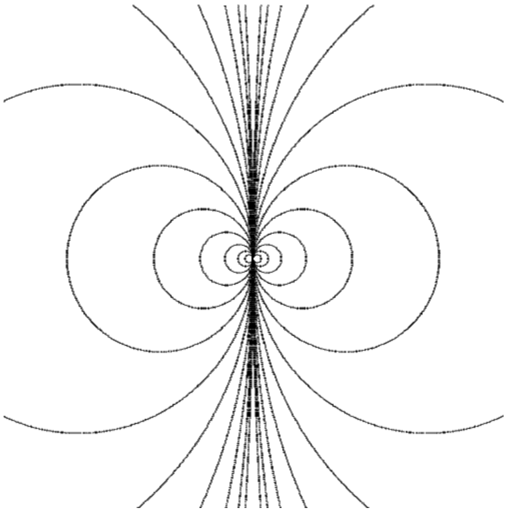

Plot B

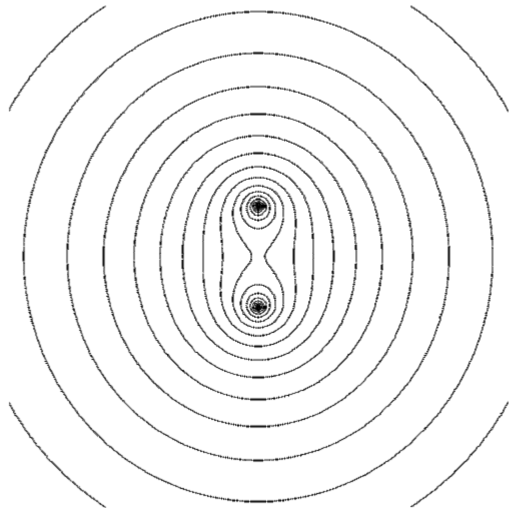

Plot C

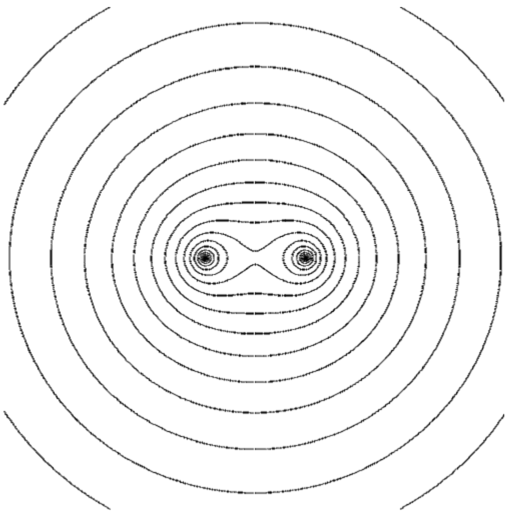

Plot D

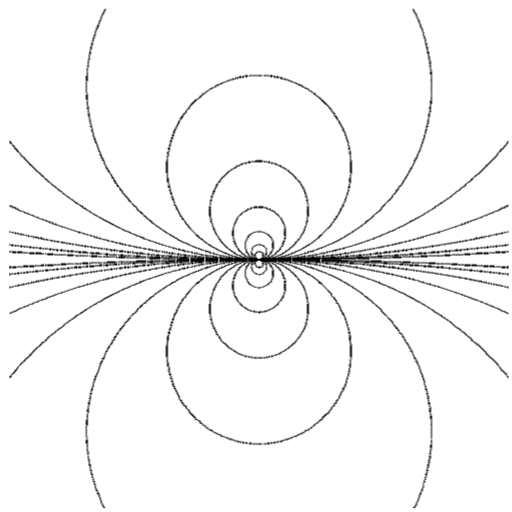

1.7.4.7 Doublet

Another building block potential flow is the doublet which has the following potential and velocities,

$$\phi = \frac{\kappa}{2\pi}\frac{\cos\theta}{r} = \frac{\kappa}{2\pi}\frac{x}{x^2+z^2} \tag{1.85}$$

$$u_r = -\frac{\kappa}{2\pi}\frac{\cos\theta}{r^2} \tag{1.86}$$

$$u_\theta = -\frac{\kappa}{2\pi}\frac{\sin\theta}{r^2} \tag{1.87}$$

$$u = \frac{\kappa}{2\pi}\frac{z^2-x^2}{(x^2+z^2)^2} \tag{1.88}$$

$$w = \frac{\kappa}{2\pi}\frac{-2xz}{(x^2+z^2)^2} \tag{1.89}$$

A common way that the doublet flow can be derived is by combining two sources at ($\pm l$, 0) with strengths $\mp\Lambda$ (which is identical to the source-sink combination in the Rankine oval flow from

Section 8.4.5), and taking the limit as l ! 0 while holding κ ≡ 2Λl = constant. The potential for this flow is,

$$\varphi = \lim_{l \to 0} \frac{\kappa}{4\pi l} \left[\ln \sqrt{(x+l)^2 + z^2} - \ln \sqrt{(x-l)^2 + z^2} \right] \tag{1.90}$$

Then, note that,

$$\lim_{l \to 0} \frac{1}{2l} \left[\ln \sqrt{(x+l)^2 + z^2} - \ln \sqrt{(x-l)^2 + z^2} \right] = \frac{\partial}{\partial x} \ln \sqrt{x^2 + z^2} = \frac{x}{x^2 + z^2} \tag{1.91}$$

Substituting this into Equation (8.90) gives the final result,

$$\varphi = \frac{\kappa}{2\pi} \frac{x}{x^2 + z^2} = \frac{\kappa}{2\pi} \frac{\cos\theta}{r} \tag{1.92}$$

The streamlines of the doublet flow are shown in Figure 8.6.

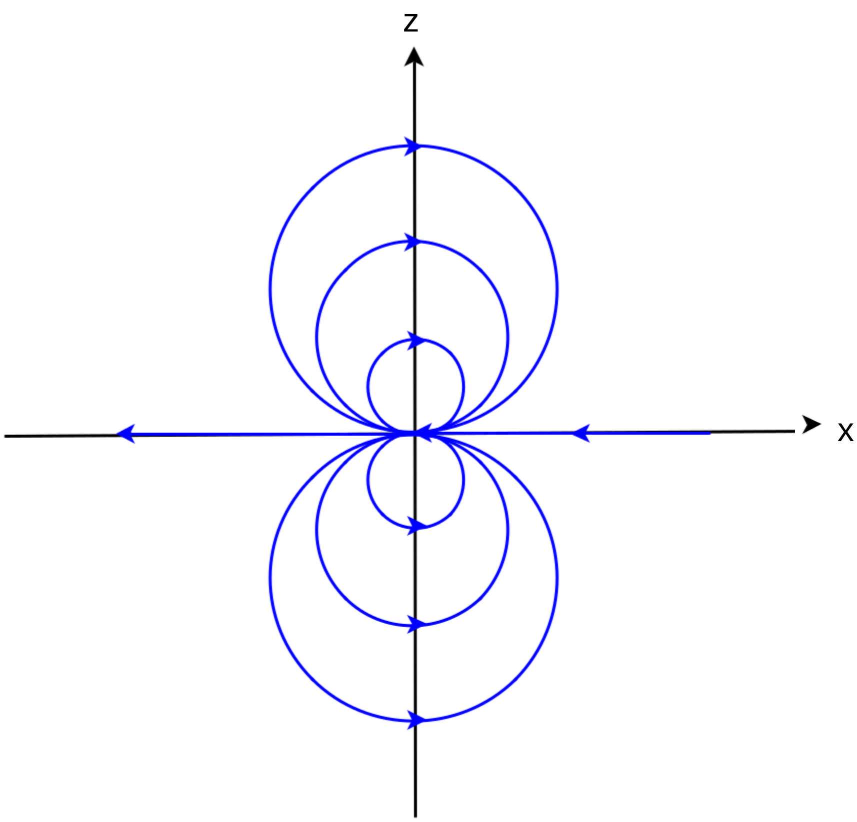

Figure 1.7.6: Streamlines for a doublet

1.7.4.8 Flow over a nonlifting cylinder

By combining a freestream (in the x-direction) with a doublet, the potential flow over a cylinder can be determined. First, we begin by determining the relationship between the doublet strength (κ), the freestream velocity (V_∞), and the radius of the cylinder (R). The potential and velocity for this flow are,

$$\varphi = V_\infty r \cos\theta + \frac{\kappa}{2\pi}\frac{\cos\theta}{r} \tag{1.93}$$

$$u_r = V_\infty \cos\theta - \frac{\kappa}{2\pi}\frac{\cos\theta}{r^2} \tag{1.94}$$

$$u_\theta = -V_\infty \sin\theta - \frac{\kappa}{2\pi}\frac{\sin\theta}{r^2} \tag{1.95}$$

On the surface of the cylinder, flow tangency requires $u_r(R, \theta) = 0$. Evaluating u_r at $r = R$ and enforcing $u_r = 0$ gives the doublet strength in terms of V_∞ and R,

$$u_r(R, \theta) = V_\infty \cos\theta - \frac{\kappa}{2\pi}\frac{\cos\theta}{R^2} = 0 \Rightarrow \kappa = 2\pi R^2 V_\infty \tag{1.96}$$

Thus, the potential and velocity for the flow around a cylinder of radius R in a freestream of velocity V_∞ are,

$$\varphi = V_\infty R \cos\theta \left(\frac{r}{R} + \frac{R}{r}\right) \tag{1.97}$$

$$u_r = V_\infty \cos\theta \left(1 - \frac{R^2}{r^2}\right) \tag{1.98}$$

$$u_\theta = -V_\infty \sin\theta \left(1 + \frac{R^2}{r^2}\right) \tag{1.99}$$

The streamlines for this potential flow are shown in Figure 1.7.7.

On the surface of the cylinder where r = R, the velocity components and velocity magnitude are,

$$u_r = 0 \tag{1.100}$$

$$u_\theta = -2V_\infty \sin\theta \tag{1.101}$$

$$V = 2V_\infty |\sin\theta| \tag{1.102}$$

The pressure on the surface can then be determined using Bernoulli's equation,

$$p(R, \theta) = p_\infty + \frac{1}{2}\rho V_\infty^2 - \frac{1}{2}\rho V^2 \tag{1.103}$$

$$= p_\infty + \frac{1}{2}\rho V_\infty^2 \left(1 - 4\sin^2\theta\right) \tag{1.104}$$

The corresponding pressure coefficient on the surface is,

$$C_p(R, \theta) = \frac{p(R, \theta) - p_\infty}{\frac{1}{2}\rho V_\infty^2} = 1 - 4\sin^2\theta \tag{1.105}$$

A plot of the surface velocity and pressure are shown in Figure 1.7.8. The velocity begins and ends at stagnation points and reaches a maximum speed which is $2V_\infty$ at the apex of the cylinder. The C_p has the corresponding behavior with $C_p = 1$ at the high pressure stagnation points and $C_p = -3$ at the low pressure apex.

We can see from the symmetry of the flow field that the lift and drag for this potential flow will be zero. For the lift, the flow is symmetric so that the pressure on the upper surface at some x is equal to the pressure on the lower surface at the same x. Thus, the net pressure force in the z direction will be zero as the upper and lower surface contributions will be equal magnitude but opposite directions. For the drag, the flow is also symmetric about the z axis (in otherwords, the pressure at x and −x are the same). Thus, due to this front-to-back symmetry, the net pressure force in the x direction (which is the drag) will also be zero. We will derive these results in detail once we include the possibility of lift (by allowing for the cylinder to rotate) in the next module.

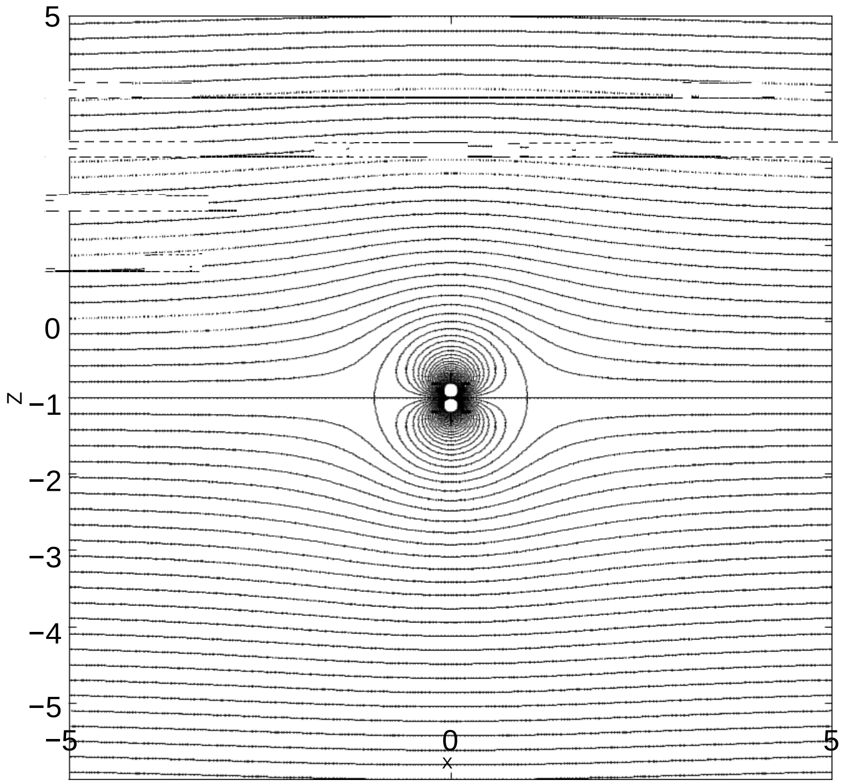

Figure 1.7.7: Streamlines for nonlifting flow over a cylinder

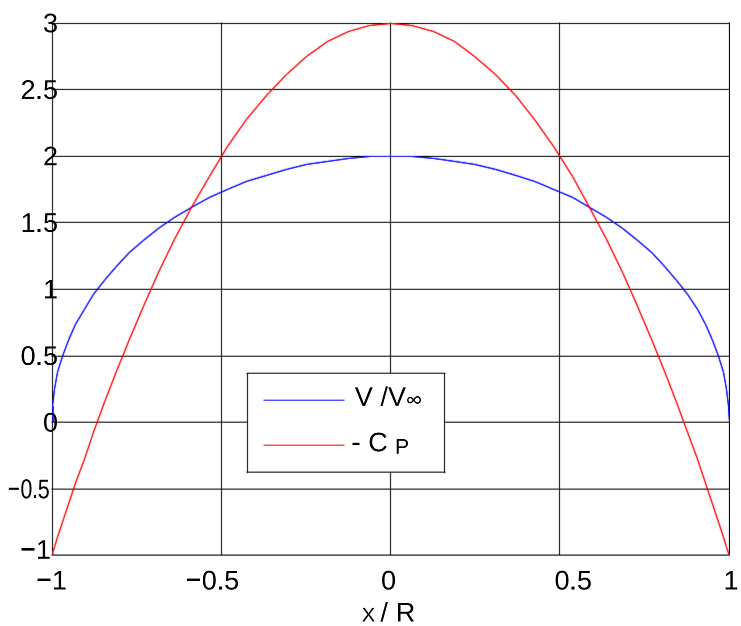

Figure 1.7.8: Surface V/V_∞ and C_p on a nonlifting cylinder.

1.8.5 Two-dimensional Lifting Flows

1.8.5.1 Point vortex

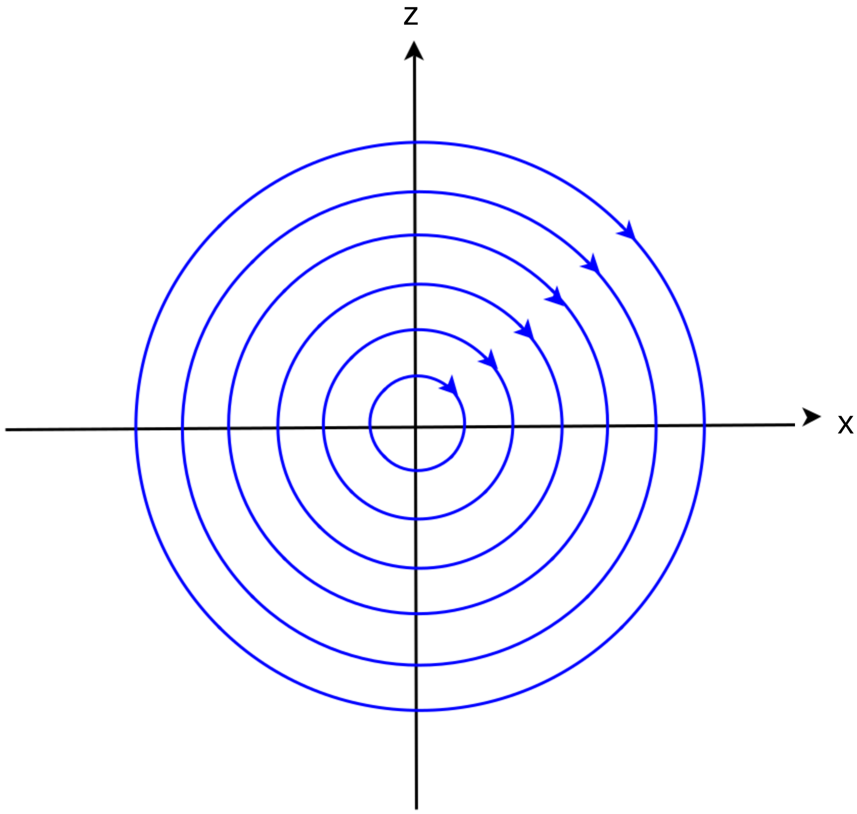

Figure 1.8.9: Streamlines for a point vortex

The last of our building block two-dimensional potential flows is called a point vortex and has the following potential and velocity field,

$$\varphi = -\frac{\Gamma}{2\pi}\theta \tag{1.106}$$

$$u_r = 0 \tag{1.107}$$

$$u_\theta = -\frac{\Gamma}{2\pi r} \tag{1.108}$$

where Γ is a scaling constant called the **circulation** of the vortex. Note that the units of Γ are $(\text{length})^2/\text{time}$. As shown in Figure 1.8.9, the streamlines of the point vortex are circles about the origin. The velocity becomes infinite as r ! 0.

The point vortex has zero vorticity everywhere except at its center where the vorticity is infinite. This is analogous to how $\nabla \cdot \mathbf{V}$ is infinite at the center of a point source, though everywhere else is equal to zero. The infinite vorticity at the origin of the point vortex can be derived using Stokes theorem. Stokes theorem applied to a two-dimensional velocity field (in the (x, z) plane) states that,

$$\oint_C \mathbf{V} \cdot d\mathbf{l} = -\iint_S (\nabla \times \mathbf{V}) \cdot \hat{\mathbf{j}}\, dS \tag{1.109}$$

where C is a contour surrounding an area S and the direction of integration around C is taken so

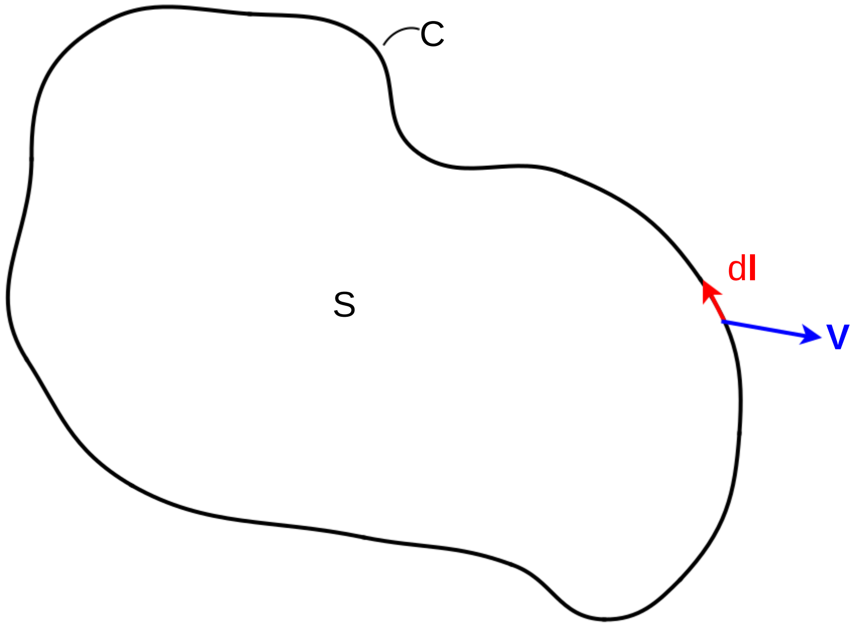

Figure 1.8.10: Contour integration used in applying Stokes Theorem

that the area is to the left of $d\mathbf{l}$ (see Figure 1.8.10). In the following video, we apply Stokes Theorem to a point vortex to show that

- $\oint_C \mathbf{V} \cdot d\mathbf{l} = -\Gamma$ for any contour surrounding the origin and $\oint_C \mathbf{V} \cdot d\mathbf{l} = 0$ for any contour that does not surround the origin.
- the vorticity is infinite at the origin.

1.8.5.2 Lifting flow over a rotating cylinder

Since the vortical flow does not perturb the radial velocity, we may add a point vortex to the nonlifting cylinder flow and the flow will still be tangent to the cylinder. The resulting flow will produce lift. We can think of this flow as being a model for the flow around a spinning cylinder. The potential and velocity for the lifting cylinder flow is,

$$\varphi = V_\infty R \cos\theta \left(\frac{r}{R} + \frac{R}{r}\right) - \frac{\Gamma}{2\pi}\theta \tag{1.110}$$

$$u_r = V_\infty \cos\theta \left(1 - \frac{R^2}{r^2}\right) \tag{1.111}$$

$$u_\theta = -V_\infty \sin\theta \left(1 + \frac{R^2}{r^2}\right) - \frac{\Gamma}{2\pi r} \tag{1.112}$$

The streamlines for the flow with $\Gamma/(2\pi V_\infty R) = \frac{1}{2}$ and 1 are shown in Figures 1.8.11 and 1.8.12, respectively.

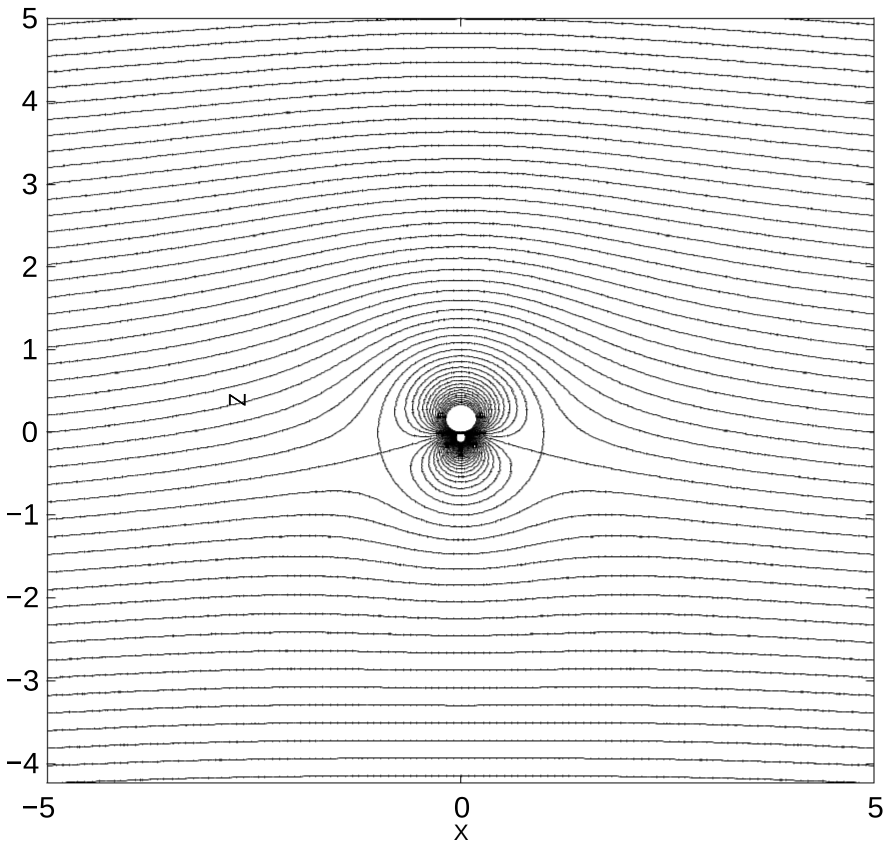

Figure 1.8.11: Streamlines for lifting cylinder flow for $\Gamma/(2\pi V_\infty R) = \frac{1}{2}$.

On the surface of the cylinder, the velocity components and velocity magnitude are,

$$u_r = 0 \tag{1.113}$$

$$u_\theta = -2V_\infty \sin\theta - \frac{\Gamma}{2\pi R} \tag{1.114}$$

$$V = 2V_\infty \sin\theta + \frac{\Gamma}{2\pi R} \tag{1.115}$$

$$\tag{1.116}$$

From this, we can determine the location of the stagnation points by determining the angles θ_{stag} at which $V = 0$, specifically,

$$2V_\infty \sin\theta_{stag} + \frac{\Gamma}{2\pi R} = 0 \tag{1.117}$$

$$\sin\theta_{stag} = -\frac{\Gamma}{4\pi V_\infty R} \tag{1.118}$$

Thus, there will be two stagnation points on the surface as long as $|\Gamma/(4\pi V_\infty R)| < 1$. For higher values, the stagnation point occurs off of the surface in the middle of the flow. We also note that $\sin\theta_{stag} = z_{stag}/R$ is the z location of the stagnation points. For the $\Gamma/(2\pi V_\infty R) = \frac{1}{2}$ case shown in Figure 8.11, the stagnation points are located at,

$$\frac{z_{stag}}{R} = -\frac{1}{4} \quad \text{or, equivalently} \quad \theta_{stag} = 194.5^\circ \text{ and } 345.5^\circ \tag{1.119}$$

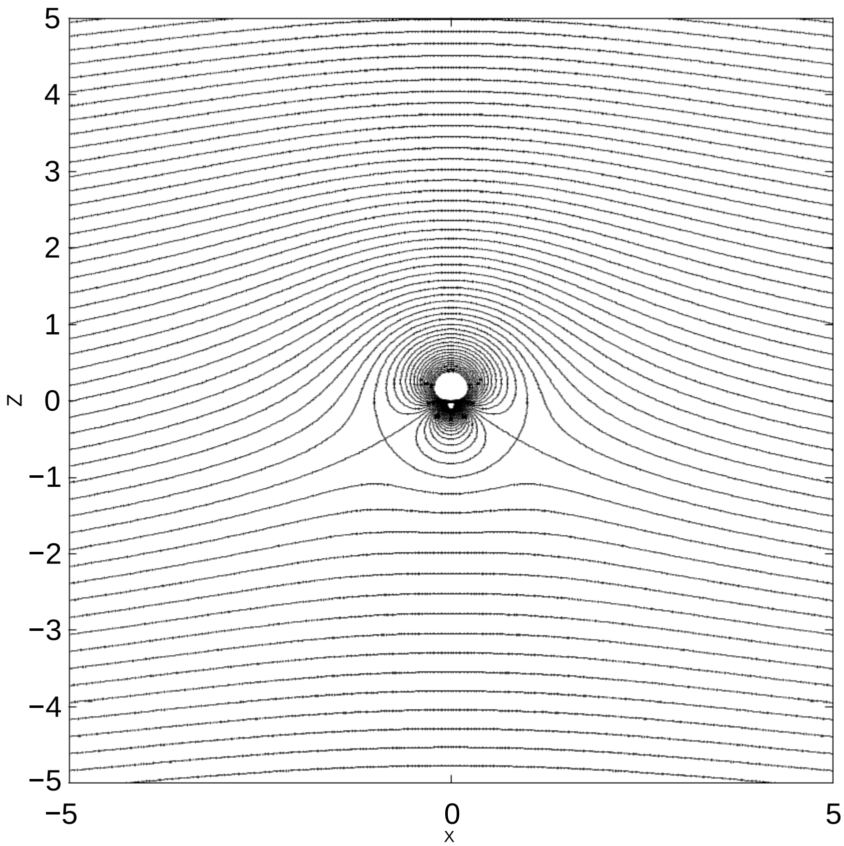

Figure 1.8.12: Streamlines for lifting cylinder flow for $\Gamma/(2\pi V_\infty R) = 1$.

For the $\Gamma/(2\pi V_\infty R) = 1$ case shown in Figure 1.8.12, the stagnation points are located at,

$$\frac{z_{stag}}{R} = -\frac{1}{2} \quad \text{or, equivalently} \quad \theta_{stag} = 210^\circ \text{ and } 330^\circ \tag{1.120}$$

The corresponding pressure coefficient on the surface is,

$$C_p(R, \theta) = \frac{p(R, \theta) - p_\infty}{\frac{1}{2}\rho V_\infty^2} = 1 - 4\sin^2\theta - \left(\frac{\Gamma}{2\pi V_\infty R}\right)^2 - \frac{2\Gamma}{\pi V_\infty R}\sin\theta. \tag{1.121}$$

In Figure 1.8.13, V and C_p on the cylinder surface are shown for $\Gamma/(2\pi V_\infty R) = 1$. The difference between the lower surface and upper surface C_p means that lift will be generated (since the pressures on the lower surface are higher than the pressures on the upper surface).

In the following video, we integrate the pressures around the surface of the cylinder to determine the lift and drag. The results of this analysis show that,

$$L' = \rho V_\infty \Gamma \quad \text{(Kutta-Joukowsky Theorem)} \tag{1.122}$$

$$D' = 0 \quad \text{(d'Alembert's Paradox)} \tag{1.123}$$

Thus, we see that the lift is directly related to the circulation and the drag is always zero on the cylinder for any values of Γ. In fact, both of these results are more general and apply to any shape in two-dimensional incompressible potential flows. The result that $L' = \rho V_\infty \Gamma$ is known as the Kutta-Joukowsky Theorem and we generalize it to other shapes.

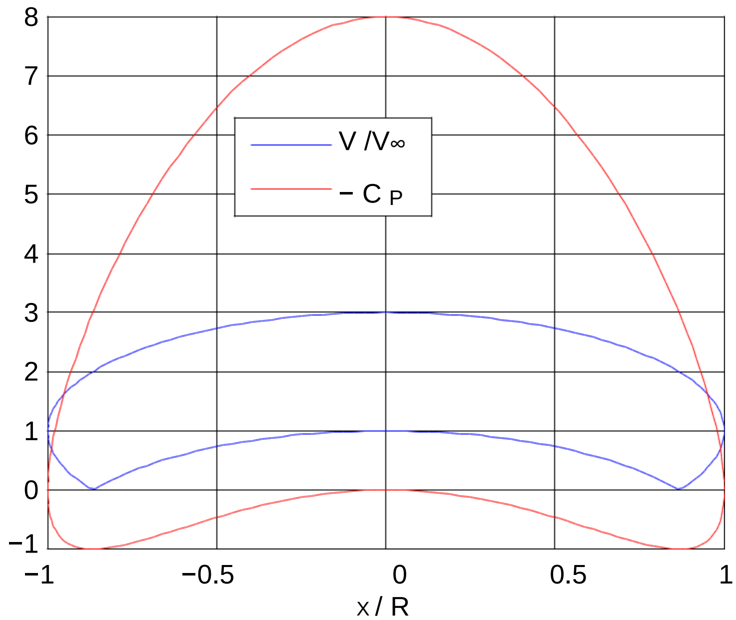

Figure 1.8.13: Surface V/V_∞ and C_p on a lifting cylinder for $\Gamma/(2\pi V_\infty R) = 1$.

1.8.5.4 Circulation

As we have seen for the lifting flow on a cylinder, the strength of the point vortex Γ is called the circulation of the vortex and is directly related to the lift. The circulation is a more general concept than just the strength of the point vortex. The general definition of the circulation is,

$$\Gamma \equiv -\oint_C \mathbf{V} \cdot d\mathbf{l} \qquad (1.127)$$

Suppose we have a point vortex with strength Γ_i. As we have seen in Section 1.8.5.1, $-\oint_C \mathbf{V} \cdot d\mathbf{l} = \Gamma_i$
for any contour containing the point vortex. Hence, the strength of the point vortex is equal to the circulation for a contour containing the vortex, i.e., $\Gamma \equiv -\oint_C \mathbf{V} \cdot d\mathbf{l} = \Gamma_i$.

1.8.5.5 Kutta-Joukowsky Theorem

For an incompressible steady two-dimensional potential flow with a uniform freestream, the lift on a body can be related to the circulation on a contour surrounding the body using the Kutta-Joukowsky Theorem,

$$\text{Kutta-Joukowsky Theorem: } L' = \rho V_\infty \Gamma \qquad (1.128)$$

where Γ is the circulation defined by Equation (1.127) for a contour C surrounding the body. This result is true for any shape.

In the following video, we derive the Kutta-Joukowsky Theorem.

1.8.5.6 d'Alembert's Paradox

For an incompressible steady two-dimensional potential flow with a uniform freestream, the drag on a body is zero:

$$\text{d'Alembert's Paradox: } D' = 0 \qquad (1.129)$$

As with the Kutta-Joukowsky Theorem, this result is true for any shape. This proof relied on the fact that the perturbation of the velocity (from $\mathbf{V}_\infty$) decays as x_w^{-1} downstream of the body. While we will not prove this rigorously in this course (though it can be proven), we observe that all of the fundamental solutions in two-dimensional flow decay at least as fast as x_w^{-1}. Specifically, the velocity for a source and vortex are proportional to r^{-1}. The velocity for the doublet is proportional to r^{-2}. The result is that the wake contributions to the drag integral will all be zero in two-dimensional incompressible flow.

SATHYABAMA
INSTITUTE OF SCIENCE AND TECHNOLOGY
(DEEMED TO BE UNIVERSITY)
Accredited "A" Grade by NAAC | 12B Status by UGC | Approved by AICTE
www.sathyabama.ac.in

SCHOOL OF MECHANICAL ENGINEERING
DEPARTMENT OF AERONAUTICAL ENGINEERING

UNIT – II –LOW SPEED AERODYNAMICS – SAEA1403

UNIT 2

LOW SPEED FLOW

2.1 Overview

2.1.1 Measurable outcomes

In this module, we introduce the fundamental concept of control volume analysis in which we analyze the behavior of a fluid or gas as it evolves inside a fixed region in space, i.e. a control volume. In particular, we will consider how the mass and momentum of the flow can change in a control volume. Then, we apply this control volume statement of the conservation of mass and momentum to a variety of problems with an emphasis on aerospace applications.

Specifically, students successfully completing this module will be able to:

2.1. Describe a continuum model for a fluid and utilize the Knudsen number to support the use of a continuum model for typical atmospheric vehicles.

2.2. Define the density, pressure, and velocity of a flow and utilize a field representation of these (and other) fluid states to describe their variation in space and time. Define the difference between a steady and unsteady flow.

2.3. Define pathlines and streamlines and describe their relationship for unsteady and steady flow.

2.4. Describe an Eulerian and Lagrangian control volume. State the conservation of mass and momentum for an Eulerian control volume.

2.5. Explain the physical meaning of the terms of the integral form of mass conservation.

2.6. Apply the integral form of mass conservation to typical problems in aerospace engineering.

2.7. Explain the physical meaning of the terms of the integral form of momentum conservation.

2.8. Apply the integral form of momentum conservation to typical problems in aerospace engineer-ing.

2.2 Continuum Model of a Fluid

2.2.1 Continuum versus molecular description of a fluid

We use the term fluid for both liquids and gases. Liquids and gases are made up of molecules. Is this discrete nature of the fluid important for us? In a liquid, molecules are in contact as they slide past each other, and overall act like a uniform fluid material at macroscopic scales.

In a gas, the molecules are not in immediate contact. So we must look at the **mean free path**, which is the distance the average molecule travels before colliding with another. Some known data for the air at different altitudes:

Altitude in km	Mean free path in m
0 (sea level)	10^{-7}
20 (U2 flight)	10^{-6}
50 (balloons)	10^{-5}
150 (low orbit)	1

Thus, the mean free path is vastly smaller than the typical dimension of any atmospheric vehicle. So even though the aerodynamic force on a wing is due to the impingement of discrete molecules, we can assume the air is a continuum for the purpose of computing this force. In contrast, computing the slight air drag on an orbiting satellite requires treating the air as discrete isolated particles since the mean free path and the size of satellite are similar. Even in the atmosphere, if the device has very small dimensions, for example if we are interested in a nanoscale device, we may have to consider the discrete nature of air.

As this discussion indicates, it is not the mean free path alone which is important to consider, but rather the ratio of the mean free path (l_{mfp}) to the reference length (l_{ref}). This ratio is known as the Knudsen number,

$$Kn \equiv \frac{l_{mfp}}{l_{ref}} \quad . \tag{2.1}$$

Thus, when the Knudsen number is small, i.e. $Kn \ll 1$, we do not need to analyze the motion of individual molecules around the vehicle. Instead, we can model the aggregate behavior of the molecules. In particular, instead of modeling each molecule and estimating how each molecule's velocity varies as it interacts with other molecules, we will model the gas as a continuum substance. This approach is called a continuum model and the study of continuum models of substances (solids, liquids, or gasses) is known as continuum mechanics.

The molecular modeling and continuum modeling approaches can be related to each other. This connection can be made by considering the statistical behavior of a population of molecules and determining how the molecular statistics evolve. The study of the statistical behavior of the motion of molecules is known as statistical mechanics. Statistical mechanics can be used to derive the governing equations for a continuum model of a gas. Our approach will be to assume the continuum model is valid and derive governing equations by applying the conservation principles of mass, momentum, and energy to this continuum model. We will however use some understanding of the molecular motion to motivate various assumptions in the derivation of our continuum model.

2.2.2 Solids versus fluids Continuum mechanics can be used to model both solids and fluids (with fluids including both liquids and gasses). However, when applying the continuum model to solids and fluids, a key distinction is made with respect to how the solid and fluid responds to the application of a stress. Figure 2.1 shows how an initially square-shaped portion of a solid and fluid responds when a shear stress τ is applied on its upper surface. The solid will deform to a new sheared shape at some angle θ, where θ is commonly refered to as the strain, and will maintain that shape unless the shear stress τ is changed. A fluid will also shear under the action of τ but will do so continually at a strain rate $\dot{\theta}$ and will never achieve a new fixed shape.

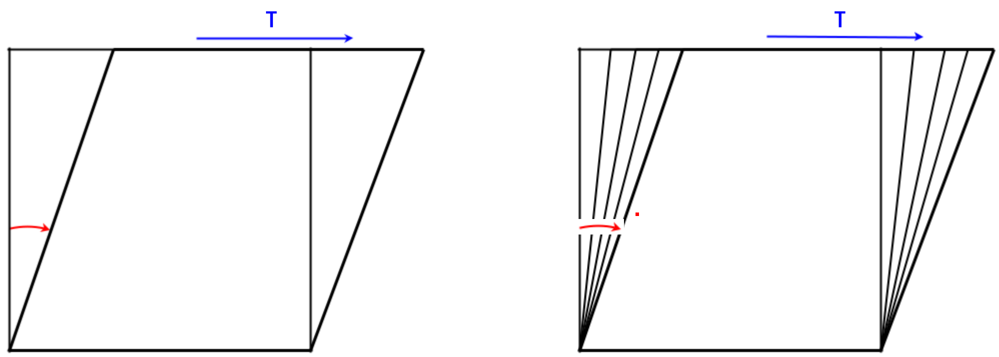

(a) Solid (b) Fluid

Figure 2.1: Relation between shear and strain motion in a solid and fluid

The simplest relationships between τ and θ for a solid, or τ and $\dot{\theta}$ for a fluid are linear relation-ships. For a solid, this linear relationship would be,

$$\tau = G\theta \tag{2.2}$$

where the constant of proportionality G is called the **elastic modulus** , and has the units of force/area. For a fluid, this linear relationship would be,

$$\tau = \mu\dot{\theta}, \tag{2.3}$$

where the constant of proportionality μ is the **dynamic viscosity** (introduced in Sections 2.4.4 and 2.4.6), and has the units of force×time/area.

2.2.3 Density

The fluid density ρ is defined as the mass/volume of the fluid for an infinitesimally small volume δV,

$$\rho \equiv \lim_{\delta V \to 0} \frac{\delta m}{\delta V} \tag{2.4}$$

The density can vary in space and possibly also time, so we write the density as the function $\rho(x, y, z, t)$. A scalar quantity such as the density that varies in space and time is a called time-varying scalar field.

The density can also be defined from a molecular view. In the molecular case, we would consider a small volume (though large enough to contain many molecules) at one instant in time and count the number of molecules of the volume at that instant. The density would then be the number of molecules multiplied by molecular mass of a single molecule, and finally divided by the volume.

2.2.4 Pressure

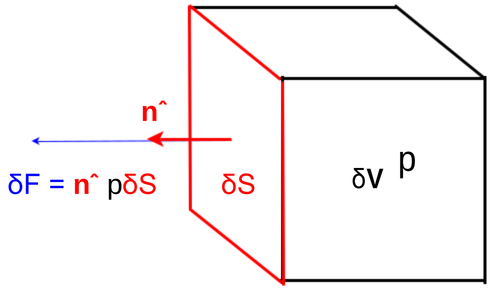

Figure 2.2: A cube-shaped infinitesimal volume with pressure p and volume δ**V**. The volume exerts an infinitesimal force δF on neighboring matter through the face δS in the outward normal direction **n**ˆ.

The pressure p is defined as the magnitude of the normal force/area that an infinitesimal volume of fluid exerts on neighboring fluid (or on the neighboring material if at the surface of a body). Specifically, consider an infinitesimal volume of fluid δ**V** and an infinitesimal region, δS, of the surface of the volume. Let the outward-pointing normal of δS be **n**ˆ. For example, Figure 3.2 shows a cube-shaped infinitesimal volume with square face. Then, the infinitesimal volume exerts an infinitesimal force on the neighboring matter (fluid or otherwise) given by,

$$\delta F = \hat{\mathbf{n}}\, p\, \delta S. \tag{2.5}$$

Equivalently, defining δF_n as the infinitesimal force in the direction of **n**ˆ, then the pressure is defined as,

$$p \equiv \lim_{\delta S \to 0} \frac{\delta F_n}{\delta S} \tag{2.6}$$

Like the density, the pressure is a time-varying scalar field, that is, p(x, y, z, t).

At the molecular level, the pressure in a gas can be interpreted as the normal force/area exerted when molecules collide (more accurately, the molecules interact and repel each other prior to actually colliding) as they pass between neighboring regions in space through δS.

2.2.5 Velocity

In our continuum model of a fluid, we can consider the fluid to be composed of infinitesimal volumes that move with the fluid, such that the volumes always contain the same matter. We will refer to these infinitesimal volumes that move with the fluid as **fluid elements**. Figure 2.3 shows the paths of four fluid elements as they move around an airfoil.

The velocity in our continuum model is defined as,

$$\mathbf{V} \text{ at a point } = \text{velocity of fluid element as it passes that point} \tag{2.7}$$

This velocity is a vector, with three separate components, and will in general vary between different points and different times,

$$\mathbf{V}(x, y, z, t) = u(x, y, z, t)\, \hat{\mathbf{i}} + v(x, y, z, t)\, \hat{\mathbf{j}} + w(x, y, z, t)\, \hat{\mathbf{k}}. \tag{2.8}$$

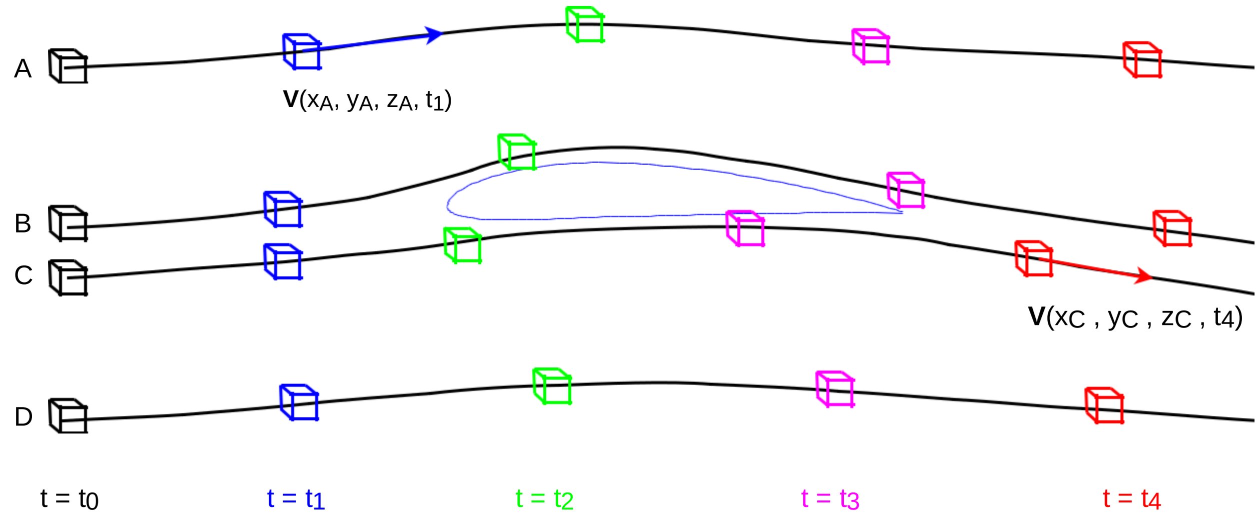

Figure 2.3: Motion of four fluid elements showing their locations at $t = t_0$, t_1, t_2, t_3, and t_4. Velocity vectors shown for fluid element A at t_1 and fluid element C at t_4.

So **V** is a time-varying vector field, whose components are three separate time-varying scalar fields u, v, w. We will also use index notation to denote the components of the velocity such that,

$$u_1 = u, \quad u_2 = v, \quad u_3 = w. \tag{2.9}$$

A useful quantity to define is the **speed** , which is the magnitude of the velocity vector.

$$V\,(x, y, z, t) = |\mathbf{V}| = \sqrt{u^2 + v^2 + w^2} \tag{2.10}$$

In general this is a time-varying scalar field. Note that the speed can also be written compactly using index notation as,

$$V = \sqrt{u_i u_i} \tag{2.11}$$

where the repeated index using Einstein's index notation convention expands to a summation over all values of the index, i.e. $u_i u_i = u_1 u_1 + u_2 u_2 + u_3 u_3$.

At the molecular level, the molecules in the vicinity of point (x, y, z) at time t generally do not have the continuum model velocity **V**(x, y, z, t). This is because the molecules have random motion associated with the temperature. Thus, the continuum velocity **V**(x, y, z, t) represents the average velocity of the molecules around (x, y, z) at time t.

As an example of this random molecular motion, consider the air in a room that does not have a fan, vent, or other source of motion. We observe that the air does not have any velocity, **V** = 0 everywhere. This is in fact a continuum view of air, which is often how we naturally think about air. In reality, the molecules in the air are moving, and at speed that depends on the temperature in the room. So, unless you are in a room with the temperature being absolute zero, the molecules in the room are moving, even though their average velocity is zero.

2.2.6 More on the molecular view of pressure and frictional forces on a body

Let's take a brief pause in our development of a continuum model of fluid motion to look a bit more closely at how the "actual" molecular motion gives rise to forces on a body.

2.2.8 Steady and unsteady flows

If the flow is **steady**, then ρ, p, **V** (and any other states of the flow) do not change in time for any point, and hence can be given as ρ(x, y, z), p(x, y, z), **V**(x, y, z). If the flow is **unsteady**, then these quantities do change in time at some or all points.

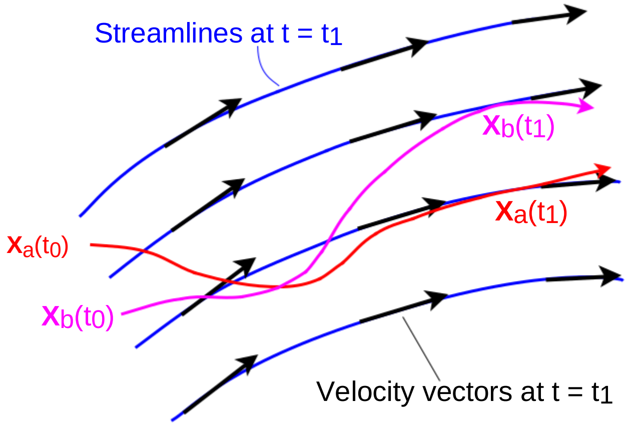

Figure 2.4: Illustration of pathlines and streamlines in an unsteady flow.

2.2.10 Pathlines and streamlines

As we analyze flows, we often sketch the direction the flow travels. In this section, we make this concept more precise and define pathlines and streamlines.

Pathlines: A pathline is the line along which a fluid element travels. The time rate of change of the position of the fluid element is the velocity,

$$\frac{d\mathbf{X}}{dt} = \mathbf{V}(\mathbf{X}, t) \tag{2.12}$$

Then, given an initial position of a fluid element, $\mathbf{X}_0$ at time t_0, the pathline can be found by integrating the velocity field,

$$\mathbf{X}(t) = \mathbf{X}_0 + \int_{t_0}^{t} \mathbf{V}(\mathbf{X}, \tau)\, d\tau \tag{2.13}$$

Streamlines: A streamline is a line which is everywhere tangent to the velocity field at some time. If the velocity field is time dependent (i.e. the flow is unsteady) then the streamlines will be a function of time as well. For a steady flow, the pathlines and streamlines are identical.

Figure 2.4 demonstrates the difference between pathlines and streamlines. The figure shows the pathlines for two fluid elements $\mathbf{X}_a(t)$ and $\mathbf{X}_b(t)$. Also shown are the velocity vectors and streamlines at $t = t_1$. Note that while the pathlines appear to cross each other, in fact the pathlines cannot intersect the same location at the same instant in time. Also note that the pathlines are tangent to the streamlines at $t = t_1$.

2.3 Introduction to Control Volume Analysis

2.3.1 Control volume definition

In developing the equations governing aerodynamics, we will invoke the physical laws of con-servation of mass, momentum, and energy. However, because we are not dealing with isolated point masses, but rather a continuous deformable medium, we will require new conceptual and mathematical techniques to apply these laws correctly.

One concept is the **control volume**, which is an identified volume of space containing fluid to which we will apply the conservation laws. In principle, the volume could be chosen to move and deform its shape as time evolves. However, in many cases, the control volume is stationary in an appropriately chosen frame of reference. This type of control volume which is fixed in space is frequently refered to as an **Eulerian control volume**. Figure 2.5 shows an Eulerian control volume. In this example, the flow travels freely through the control volume boundaries. In other situations, a portion of the control volume boundary may correspond to a solid surface (e.g. the surface of a wing) through which flow cannot pass.

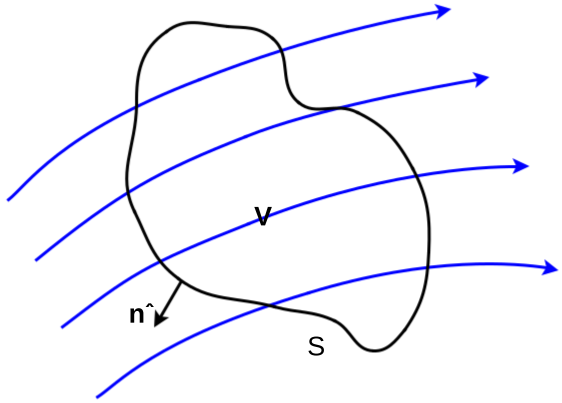

(a) Eulerian control volume

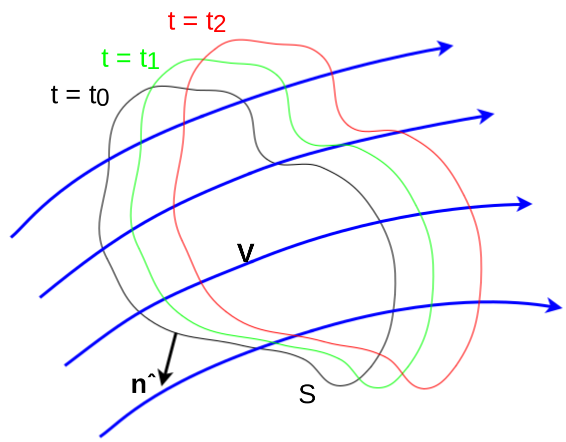

(b) Lagrangian control volume

Figure 2.5: Examples of an Eulerian control volume and Lagrangian control volume (i.e. control mass). In either case, the volume is denoted **V** with its boundary surface denoted S and the outward pointing normal at some location on the surface is $\hat{\mathbf{n}}$.

A closely related concept is the **control mass**, which is an identified mass of the fluid to which the conservation principles are applied. The control mass though will move with the fluid and deform it shape. In fact, a control mass is equivalent a control volume which is defined to follow the fluid. Often, a control mass is refered to as a **Lagrangian control volume**. An example of a Lagrangian control volume (i.e. control mass) is shown in Figure 2.5.

2.3.2 Conservation of mass and momentum

Before deriving the mathematical statements of the conservation of mass and momentum applied to Eulerian control volumes, we will first state these laws.

Conservation of mass: The conservation of mass requires that mass cannot be created or de-stroyed. In terms of an Eulerian control volume, mass can enter or leave the control volume at its boundaries. However, since mass cannot be created or destroyed, this means that the mass in the control volume must change to account for the flow of mass across its boundaries. Specifically, stating the conservation of mass as a rate equation applied to an Eulerian control volume, we could say,

$$\frac{d}{dt}\,(\text{mass in }\mathbf{V}) = (\text{flow of mass into }\mathbf{V})\ . \qquad (2.14)$$

However, common convention is to combine the terms and state the conservation of mass as,

$$\frac{d}{dt}\,(\text{mass in }\mathbf{V}) + (\text{flow of mass out of }\mathbf{V}) = 0 \qquad (2.15)$$

If the two terms on the left were not in balance (i.e. their sum was non-zero), then this would mean that rate of change of mass in the control volume did not equal the flow of mass into the control volume. In other words, mass would have been created (or destroyed). Thus, the sum of the terms on the left-hand side represents the rate at which mass is created within the control volume, and Equation (3.15) states that the rate of mass creation is zero within the control volume.

Conservation of momentum: The conservation of momentum states that the rate of change of momentum in a system is equal to the sum of the forces applied to the system. Using the same convention as for the conservation of mass, conservation of momentum applied to an Eulerian control volume gives,

$$\frac{d}{dt}\,(\text{momentum in }\mathbf{V}) + (\text{flow of momentum out of }\mathbf{V}) = \quad (\text{forces acting on }\mathbf{V}) \qquad (2.16)$$

As opposed to mass, momentum can be created (or destroyed) in a control volume **if** the sum of the forces on the control volume is non-zero.

2.4 Conservation of Mass

2.4.1 Rate of change of mass inside a control volume

In this section, we will express the rate of change of mass inside the control volume mathematically in terms of the fluid states. Since the density is the mass/volume, we may integrate the density throughout the control volume to determine the mass in the control volume,

$$\text{mass in } \mathbf{V} = \int_{\mathbf{V}} \rho \, d\mathbf{V} \qquad (2.17)$$

Then, the time rate of change can be found by differentiating with respect to time,

$$\frac{d}{dt}(\text{mass in } \mathbf{V}) = \frac{d}{dt}\int_{\mathbf{V}} \rho \, d\mathbf{V}. \qquad (2.18)$$

For a control volume that is fixed in space, the time derivative can also be brought inside the spatial integral to give,

$$\frac{d}{dt}(\text{mass in } \mathbf{V}) = \int_{\mathbf{V}} \frac{\partial \rho}{\partial t} \, d\mathbf{V}. \qquad (2.19)$$

2.4.2 Mass flow leaving a control volume

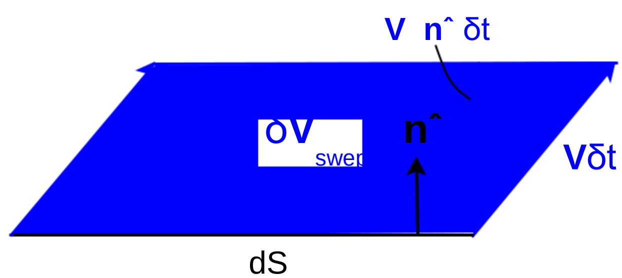

Figure 2.7: Volume of fluid, $\delta \mathbf{V}_{swept}$, that crosses an infinitesimal surface patch dS in time δt. (Note: side view shown)

Consider an infinitesimal patch of the surface of the fixed, permeable control volume. As shown in Figure 2.7, the patch has area dS, and normal unit vector $\hat{n}$. The plane of fluid particles which are on the surface at time t will move off the surface at time t + δt, sweeping out an infinitesimal volume given by,

$$\delta \mathbf{V}_{swept} = \mathbf{V} \cdot \hat{\mathbf{n}} \, \delta t \, dS, \qquad (2.20)$$

where $\mathbf{V} \cdot \hat{\mathbf{n}}$ is the component of the velocity vector normal to the patch.

The mass of fluid in this swept volume can be found by multiplying by the density to give,

$$\delta m_{swept} = \rho \, \mathbf{V} \cdot \hat{\mathbf{n}} \, \delta t \, dS. \qquad (2.21)$$

The total mass that flows out of the entire control volume in time δt can then be found by integrating over the entire surface,

$$\delta m_{swept,\,total} = \delta t \int_S \rho \, \mathbf{V} \cdot \hat{\mathbf{n}} \, dS \qquad (2.22)$$

where δt is taken outside of the integral since it is a constant.

The time rate at which the mass leaves the control volume, called the **mass flow rate** is then

$$\text{mass flow rate} = \lim_{\delta t \to 0} \frac{\delta m_{\text{swept, total}}}{\delta t} = \iint_S \rho\, \mathbf{V} \cdot \hat{\mathbf{n}}\, dS. \tag{2.23}$$

Another commonly used quantity is the **mass flux** and is defined simply as mass flow per area,

$$\text{mass flux} \equiv \rho \mathbf{V} \cdot \hat{\mathbf{n}} \tag{2.24}$$

At a solid surface, $\mathbf{V} \cdot \hat{\mathbf{n}} = 0$ since the flow cannot enter the solid. So the portion of a control volume boundary at a solid surface does not contribute to the mass flow. This result is frequently used when performing control volume analysis, and is an important consideration when choosing a control volume.

2.4.3 Conservation of mass in integral form

The conservation of mass for a control volume fixed in space as expressed in Equation (3.15) can be written mathematically using the results in Equations (3.18) and (3.23),

$$\frac{d}{dt} \iiint_V \rho\, d\mathcal{V} + \iint_S \rho\, \mathbf{V} \cdot \hat{\mathbf{n}}\, dS = 0. \tag{2.25}$$

Or, alternatively, using Equation (3.19),

$$\iiint_V \frac{\partial \rho}{\partial t}\, d\mathcal{V} + \iint_S \rho\, \mathbf{V} \cdot \hat{\mathbf{n}}\, dS = 0. \tag{2.26}$$

2.4.4 Application to channel flow (mass conservation)

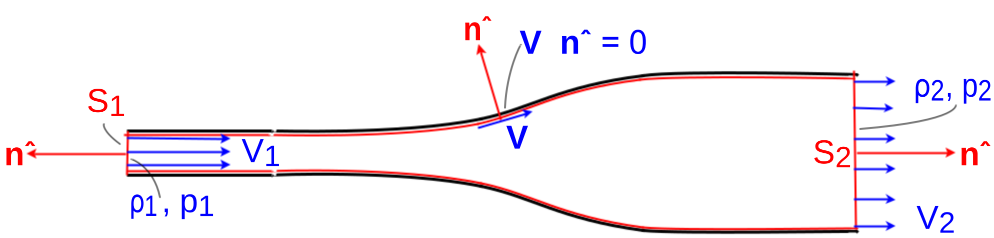

Figure 2.8: Channel control volume and flow conditions

Now, let's apply the integral form of conservation of mass to the channel flow shown in Figure 2.8. The flow is assumed to have uniform velocity, density, and pressure at its inlet (V_1, ρ_1, and p_1) and outlet (V_2, ρ_2, and p_2). Further, we will assume that the flow in the channel is steady. As we will derive in the following video, conservation of mass requires that,

$$\rho_1 V_1 S_1 = \rho_2 V_2 S_2 \tag{2.27}$$

Thus, when there is no unsteadiness, the mass flow leaving the outlet is the same as the mass flow entering the inlet. Further, we can re-arrange this expression to show that the mass flux varies inversely with the area,

$$\frac{\rho_2 V_2}{\rho_1 V_1} = \frac{S_1}{S_2} \tag{2.28}$$

Thus, when the area increases (as drawn in this figure), the mass flux decreases (or vice-versa when the area decreases the mass flux increases). For flows where the density is essentially constant (which would be true for water or for low Mach number air flows), this can be simplified further to,

$$\frac{V_2}{V_1} = \frac{S_1}{S_2} \text{ when } \rho = \text{constant} \tag{2.29}$$

Thus, when the area increases, the velocity decreases (and vice-versa).

2.5 Conservation of Momentum

2.5.1 Rate of change of momentum inside a control volume

In this section, we will express the rate of change of momentum inside the control volume mathematically in terms of the fluid states. This section is an extension of the results in Section 2.4.1. The momentum/volume is given by $\rho\mathbf{V}$, which we may integrate throughout the control volume to determine the momentum in the control volume,

$$\text{momentum in } \mathbf{V} = \iiint_{V} \rho\mathbf{V} \, d\mathbf{V} \tag{2.30}$$

Then, the time rate of change can be found by differentiating with respect to time,

$$\frac{d}{dt}(\text{momentum in } \mathbf{V}) = \frac{d}{dt} \iiint_{V} \rho\mathbf{V} \, d\mathbf{V}. \tag{2.31}$$

For a control volume that is fixed in space, the time derivative can also be brought inside the spatial integral to give,

$$\frac{d}{dt}(\text{momentum in } \mathbf{V}) = \iiint_{V} \frac{\partial}{\partial t}(\rho\mathbf{V}) \, d\mathbf{V}. \tag{2.32}$$

We can also consider a specific component of the momentum, as opposed to the entire momentum vector. For example, the time rate of change for the j-momentum component in the control volume is,

$$\frac{d}{dt}(\text{j-momentum in } \mathbf{V}) = \frac{d}{dt} \iiint_{V} \rho u_j \, d\mathbf{V} = \iiint_{V} \frac{\partial}{\partial t}(\rho u_j) \, d\mathbf{V}. \tag{2.33}$$

2.5.2 Momentum flow leaving a control volume

Following the same approach as in Section 2.4.2, the flow of momentum out of the entire control volume

$$\text{momentum flow} = \iint_{S} \rho\mathbf{V}\, \mathbf{V} \cdot \hat{\mathbf{n}} \, dS, \tag{2.34}$$

and the momentum flux is,

$$\text{momentum flux} \equiv \rho\mathbf{V}\, \mathbf{V} \cdot \hat{\mathbf{n}} \tag{2.35}$$

Considering only the j-component of momentum gives,

$$\text{j-momentum flow} = \iint_{S} \rho u_j \, \mathbf{V} \cdot \hat{\mathbf{n}} \, dS, \tag{2.36}$$

and the j-momentum flux is,

$$\text{j-momentum flux} \equiv \rho u_j \, \mathbf{V} \cdot \hat{\mathbf{n}} \tag{2.37}$$

As with the mass flow, since at a solid surface, $\mathbf{V} \cdot \hat{\mathbf{n}} = 0$ then the portion of a control volume boundary at a solid surface does not contribute to the momentum flow out of the control volume.

2.5.4 Forces acting on a control volume

We will consider two types of forces that act on the control volume:

Body force: a force acting within the volume. In our case, the body force will be gravity.

Surface force: a force acting on the surface of the control volume. In our case, the surface forces arising from the fluid will be due to pressure and viscous stresses. In addition, we will oc-casionally include surface forces arising from structures that are cut by the control volume surface.

A common difficulty with this distinction of body and surface forces is that, in fact, the pressure and viscous stresses which give rise to the surfaces forces are present inside the volume. However, within the control volume, these forces are balanced between neighboring fluid elements. For example, consider two neighboring fluid elements, element A and element B. The pressure force applied by element A on element B is exactly the opposite of the pressure force applied by element B on element A. Thus, the result is no net force within the volume. However, at the surface of the volume, the pressure produces a non-zero force acting on the fluid that is inside the control volume. The same argument also applies to viscous forces.

The body force due to gravity can be found by integrating the gravitational force/volume over the entire control volume. The gravitational force/volume is given by $\rho\mathbf{g}$ where $\mathbf{g}$ is the gravitational acceleration. Thus, the body force due to gravity acting on the control volume is,

$$\text{gravitational force on } \mathbf{V} = \int_V \rho\mathbf{g}\, d\mathbf{V} \tag{2.38}$$

The pressure and viscous force acting on the surface of a control volume can be determine in the same manner as the pressure and viscous force acting on the surface of the body in Equation (2.7). Thus, the pressure and viscous forces acting on the control volume are,

$$\text{pressure force on } \mathbf{V} = -\int_S p\,\hat{\mathbf{n}}\, dS, \tag{2.39}$$

$$\text{viscous force on } \mathbf{V} = \int_S \tau\, dS, \tag{2.40}$$

The forces can also be broken into individual components. Doing this give the force in the j-direction as,

$$\text{j-component of gravitational force on } \mathbf{V} = \int_V \rho g_j\, d\mathbf{V} \tag{2.41}$$

$$\text{j-component of pressure force on } \mathbf{V} = -\int_S p\,\hat{n}_j\, dS, \tag{2.42}$$

$$\text{j-component of viscous force on } \mathbf{V} = \int_S \tau_j\, dS, \tag{2.43}$$

where $g_j = \mathbf{g} \cdot \hat{\mathbf{e}}_j$, $\hat{n}_j = \hat{\mathbf{n}} \cdot \hat{\mathbf{e}}_j$, and $\tau_j = \tau \cdot \hat{\mathbf{e}}_j$ and $\hat{\mathbf{e}}_j$ is the unit vector in the j-coordinate direction. Occasionally, we are interested in including forces that act on the control volume that do not arise. To denote this possibility, we will include $\mathbf{F}_{ext}$ to represent external forces applied to the control volume. Here, we use the word **external** to represent forces acting on the control volume that are not part of the fluid. When this situation occurs, some region of the control volume must be of non-fluid substance, i.e. there is a region in the control volume that is outside the fluid. Thus, all of the forces which could be included in a control volume analysis are,

$$\rho \mathbf{g}\, d\mathbf{V} - p\, \hat{\mathbf{n}}\, dS + \tau\, dS + \mathbf{F}_{ext} \tag{1.44}$$

When using a control volume that includes not only the fluid but also other materials, if the mass or momentum of the other materials are changing inside the control volume, then that must be accounted for in the application of the conservation law. In the equations we develop, we will assume that the only dynamics occur in the fluid portions of the control volume.

2.5.6 When are viscous contributions negligible?

An important, often subtle, part of control volume analysis is determining when viscous contri-butions are negligible on a surface of the control volume. Understanding how to choose a control volume such that viscous contributions have negligible impact on the analysis is critical.

2.5.7 Conservation of momentum in integral form

The conservation of momentum for a control volume fixed in space as expressed in Equa-tion (2.16) can be written mathematically using the results in Equations (2.31) (2.34), (2.38), (2.39), and (2.40),

$$\frac{d}{dt}\iiint_V \rho \mathbf{V}\, dV + \iint_S \rho \mathbf{V}\, \mathbf{V}\cdot\hat{\mathbf{n}}\, dS = \iiint_V \rho \mathbf{g}\, dV - \iint_S p\, \hat{\mathbf{n}}\, dS + \iint_S \tau\, dS + \mathbf{F}_{ext}. \tag{2.45}$$

Or, alternatively, using Equation (3.32),

$$\iiint_V \frac{\partial}{\partial t}(\rho \mathbf{V})\, dV + \iint_S \rho \mathbf{V}\, \mathbf{V}\cdot\hat{\mathbf{n}}\, dS = \iiint_V \rho \mathbf{g}\, dV - \iint_S p\, \hat{\mathbf{n}}\, dS + \iint_S \tau\, dS + \mathbf{F}_{ext}. \tag{2.46}$$

Considering only the j-component of momentum gives,

$$\iiint_V \frac{\partial}{\partial t}(\rho u_j)\, dV + \iint_S \rho u_j\, \mathbf{V}\cdot\hat{\mathbf{n}}\, dS = \iiint_V \rho g_j\, dV - \iint_S p\, \hat{n}_j\, dS + \iint_S \tau_j\, dS + F_{ext_j}. \tag{2.47}$$

For many aerodynamics applications, the gravitational forces are very small compared to pres-sure and viscous forces. Thus, unless we specifically mention to include gravitational forces, we will employ the following forms of the momentum conservation equation,

$$\iiint_V \frac{\partial}{\partial t}(\rho \mathbf{V})\, dV + \iint_S \rho \mathbf{V}\, \mathbf{V}\cdot\hat{\mathbf{n}}\, dS = -\iint_S p\, \hat{\mathbf{n}}\, dS + \iint_S \tau\, dS + \mathbf{F}_{ext}. \tag{2.48}$$

or, considering only the j-component of momentum,

$$\iiint_V \frac{\partial}{\partial t}(\rho u_j)\, dV + \iint_S \rho u_j\, \mathbf{V}\cdot\hat{\mathbf{n}}\, dS = -\iint_S p\, \hat{n}_j\, dS + \iint_S \tau_j\, dS + F_{ext_j}. \tag{2.49}$$

2.5.9 Application to channel flow (momentum conservation)

Now, let's apply the integral form of conservation of momentum to the channel flow shown in Figure 3.8. Previously, in Section 3.4.4, we applied the integral form of the conservation of mass. As before, the flow is assumed to have uniform velocity and density at its inlet (V_1 and ρ_1) and outlet (V_2 and ρ_2). Further, the flow in the channel is assumed to be steady.

As is described in the following video, applying the x-momentum equations gives,

$$\dot{m}\,(V_2 - V_1) = p_1 S_1 - p_2 S_2 + \int_{S_{wall}} p\, dS_x + \int_{S_{wall}} \boldsymbol{\tau}\cdot\hat{\mathbf{i}}\, dS, \tag{2.50}$$

where $\dot{m} = \rho_1 V_1 S_1 = \rho_2 V_2 S_2$ is the mass flow in the channel.

The video discusses an alternative control volume which does not include the boundary layers, and therefore viscous forces are negligible in this alternative control volume. Using this alternative control volume, we show that if the boundary layers in the channel are small (compared to the diameter of the channel), then the viscous forces can be neglected. The resulting inviscid application of the conservation of x-momentum produces,

$$\dot{m}\,(V_2 - V_1) = p_1 S_1 - p_2 S_2 + \int_{S_{wall}} p\, dS_x. \tag{2.51}$$

2.6 Sample Problems

2.6.1 Lift generation and flow turning

In this example problem, we will apply conservation of y-momentum to relate the lift generated by an airplane (or other body) to the turning of the flow. We will use the control volume shown in Figure 2.9.

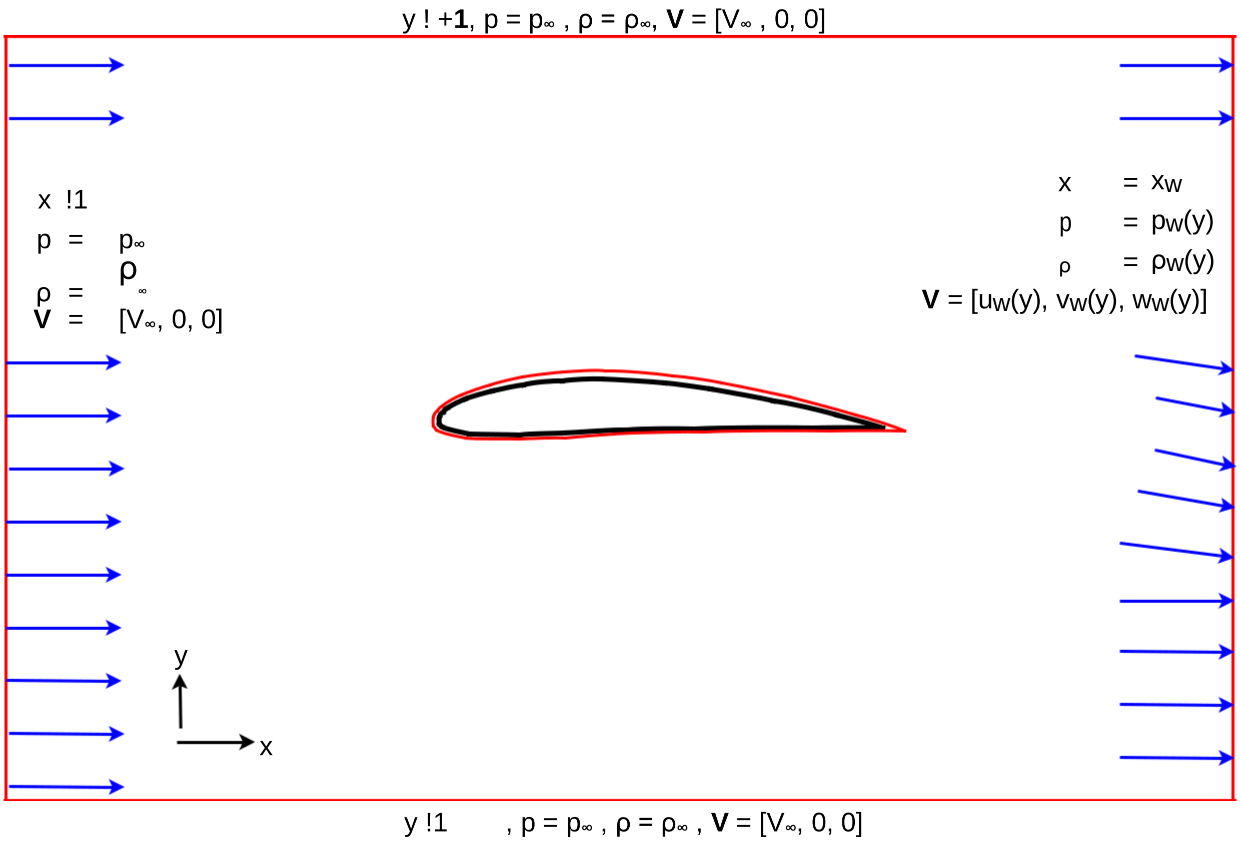

Figure 2.9: Control volume for sample problems.

The lift can be related to an integral of the flow properties in the downstream wake boundary of the form,

$$L = \int_{S_w} \text{integrand}\ dS. \tag{2.52}$$

Determine the integrand required to calculate the lift.

edXsolution

The key result we will derive in the video below is,

$$L = -\int_{S_w} \rho_w v_w u_w\ dS. \tag{2.53}$$

This result shows clearly that by turning the flow downward (so that in the wake $v_w \leq 0$), a positive lift force is generated. Thus, we can think of lift generation as the process of an aircraft turning a flow downward (in an efficient manner of course)!

As we will see later in the class (specifically, see Section 8.5.5), in two-dimensional flows we actually need to account for the fact that the flow upstream of the lifting body is infinitessimaly perturbed from the freestream. Thus, the two-dimensional result for the lift using the control volume for this problem would give,

$$L' = \int \rho_u v_u u_u\ dS - \int \rho_w v_w u_w\ dS. \tag{2.54}$$

$S_u S_w$

where S_u is the control volume boundary far upstream of the lifting body, and ρ_u, u_u and v_u are the density and velocity components on that boundary. In other words, we need to account for the fact the $v_u = 0$ in two-dimensional flows.

2.2.4 Bernoulli equation

Assuming the flow is incompressible and steady, the momentum equation as written in Equa-tion (2.11) can be simplified to,

$$\nabla\left(p + \frac{1}{2}\rho V^2\right) = \rho \mathbf{V} \times \omega + \mathbf{f}^{\tau} \tag{2.18}$$

The left-hand side is the gradient of the incompressible form of the total pressure, $p_0 \equiv p + \frac{1}{2}\rho V^2$ (see the discussion in Section 4.4.7) . Thus, we see that the total pressure in incompressible steady flow will not vary (i.e. the gradient is zero) when the flow is irrotational and the viscous effects are neglible. As discussed in Section 8.2.2, for flows with uniform freestream velocity, the vorticity is zero unless the fluid element enters a region (such as boundary layers or wakes) in which viscous effects are important. Thus, the conditions required for total pressure to be constant are the same as required for the flow to be approximated as irrotational, namely, viscous effects must be negligible.

We note that even when the vorticity is non-zero, if viscous effects are negligible then the total pressure along a streamline is constant. To see this, consider the inviscid form of Equation (2.18),

$$\nabla\left(p + \frac{1}{2}\rho V^2\right) = \rho \mathbf{V} \times \omega \tag{2.19}$$

The component of this equation along the streamwise direction can be found by taking the dot product of the equation along the streamwise direction. Since $\mathbf{V} \times \omega$ is perpendicular to $\mathbf{V}$ (and to ω) then the right-hand side is zero along the streamwise direciton. Thus, we have

$$\frac{\partial}{\partial s}\left(p + \frac{1}{2}\rho V^2\right) = 0 \Rightarrow p + \frac{1}{2}\rho V^2 = \text{constant along a streamline} \tag{2.20}$$

in steady, inviscid, incompressible flow. Further, when a steady, inviscid, and incompressible flow has no vorticity (e.g. if the freestream has uniform velocity) then,

$$\nabla\left(p + \frac{1}{2}\rho V^2\right) = 0 \Rightarrow p + \frac{1}{2}\rho V^2 = \text{constant everywhere} \tag{2.21}$$

In particular, for this problem we can evaluate the total pressure in the freestream and we have,

$$p + \frac{1}{2}\rho V^2 = p_\infty + \frac{1}{2}\rho V_\infty^2 \tag{2.22}$$

Equations (2.20)-(2.22) are refered to Bernoulli's equation after its originator Daniel Bernoulli who published this classic result in 1738. Commonly, the term $\frac{1}{2}\rho V^2$ is refered to as the **dynamic pressure** while p is the static pressure (or simply the pressure).

2.2.5 Pressure coefficient and Bernoulli's equation

In the situation in which viscous effects are negligible and the freestream velocity and pressure are uniform, then Bernoulli's equation can be used to relate the C_p to the local flow speed, giving,

$$C_p = 1 - \left(\frac{V}{V_\infty}\right)^2 \tag{2.23}$$

We note that at a stagnation point $C_p = 1$ since $V = 0$. Refering back to Figure 2.9, we can see the presence of the stagnation point.

SATHYABAMA
INSTITUTE OF SCIENCE AND TECHNOLOGY
(DEEMED TO BE UNIVERSITY)
Accredited "A" Grade by NAAC | 12B Status by UGC | Approved by AICTE
www.sathyabama.ac.in

SCHOOL OF MECHANICAL ENGINEERING
DEPARTMENT OF AERONAUTICAL ENGINEERING

UNIT – III –LOW SPEED AERODYNAMICS – SAEA1403

UNIT 3

AIRFOIL AND CONFORMAL TRANSFORMATION

3.1 Overview

3.1.1 Measurable outcomes

In this Module, we specifically develop models for the potential flow around airfoils. These models are quite powerful allowing quantiative estimates of the lift and pressure distribution over airfoils.

Specifically, students successfully completing this module will be able to:

3.1. Describe how the potential flow around a body has infinitely many solutions, each with a different circulation. State and apply the Kutta condition to determine the specific potential flow that represents the physically-observed behavior of the flow at a sharp trailing edge.

3.2. Describe a vortex sheet including how it is a linear combination of infinitesimal-strength point vortices and how the lift generated by the vortex sheet is related to the integral of its circulation distribution.

3.3. Describe a linear-varying vortex panel method including (1) the number and meaning of the unknowns representing the vortex distribution, (2) the imposition of the flow tangency boundary condition, (3) the imposition of the Kutta condition, (4) the structure and meaning of the influence coefficient matrix, and (5) the calculation of the lift from the vortex panel solution.

3.4. (1) Describe the assumptions of thin airfoil theory and (2) apply thin airfoil theory to estimate the forces and moments on airfoils in two-dimensional incompressible flow.

3.5. Describe the basic trends of lift and drag with respect to geometry and angle of attack observed in applying two-dimensional potential flow analysis of airfoils and, in particular, how these trends differ from actually-observed (viscous) flows.

3.2 Airfoil Flows

3.2.1 Lifting airfoils and the Kutta condition

For any body, there are actually infinitely many potential flow solutions that satisfy the boundary conditions. The appearance of an infinite number of solutions is demonstrated in the cylinder flows in Section 1.8.5.2. Any value of circulation still produces a valid solution for the flow around the cylinder.

For the case of an airfoil, infinitely many solutions also exist and again depend on the circulation. Figures 3.1 , 3.2, and 3.3 show the potential flow over an airfoil with three different circulation values. The question is which of the infinitely many flows best corresponds to the flow observed in reality?

The key feature to determine this is the behavior of the flow at the trailing edge. For $\Gamma/(V_\infty c) = 0$, the flow wraps around the trailing edge from the lower surface to the upper surface. For $\Gamma/(V_\infty c) = 0.9$, the flow leaves smoothly from the trailing edge. For $\Gamma/(V_\infty c) = 1.8$, the flow wraps around the trailing edge from the upper surface to the lower surface. However, flow wrapping around a sharp edge would require the pressure to be infinitely low due to the vanishing radius of curvature. Through Bernoulli this implies the velocity is infinitely high. Thus, in the actual physical flow (not the potential flow model), the flow at a sharp trailing edge leaves smoothly without wrapping around such is observed for the $\Gamma/(V_\infty c) = 0.9$ flow.

This observation gives rise to the **Kutta condition**: the potential flow that leaves smoothly off a sharp trailing edge is an appropriate model for the actual flow observed in nature. Thus, the Kutta condition can be used to pick the physically-realistic potential flow out of the infinitely many that exist for a given body. In the airfoil examples above, enforcing the Kutta condition would result in the $\Gamma/(V_\infty c) = 0.9$ flow being chosen.

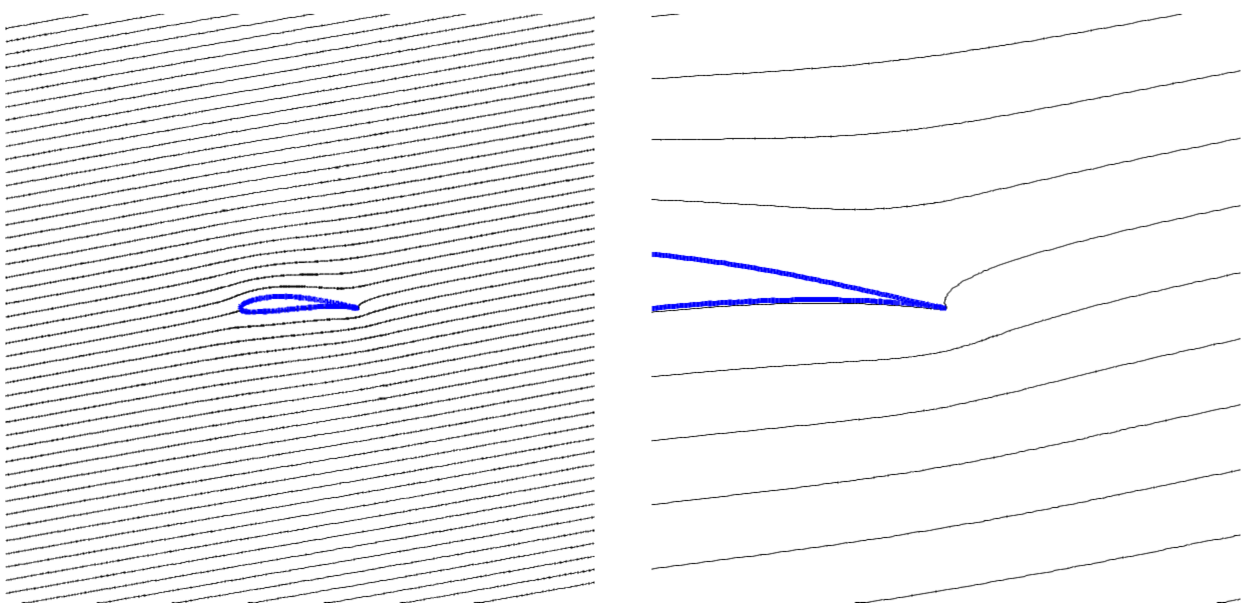

Figure 3.1: $\frac{\ }{V_\infty c}$ = 0 flow over airfoil

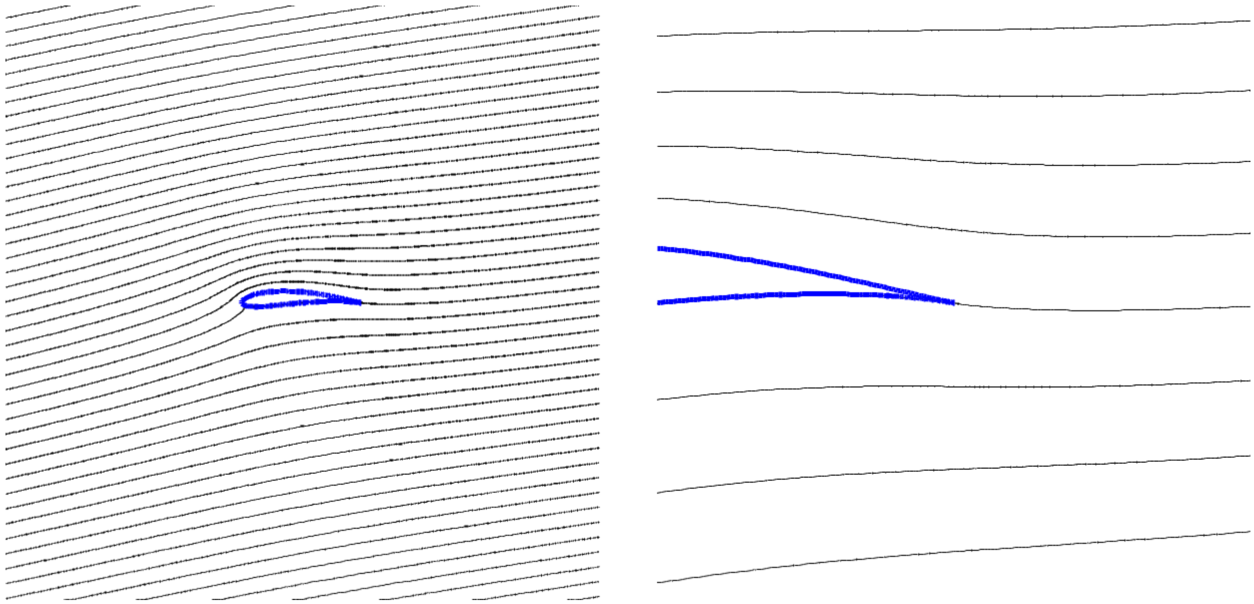

Figure 3.2: $V_\infty c$ = 0.9 flow over airfoil

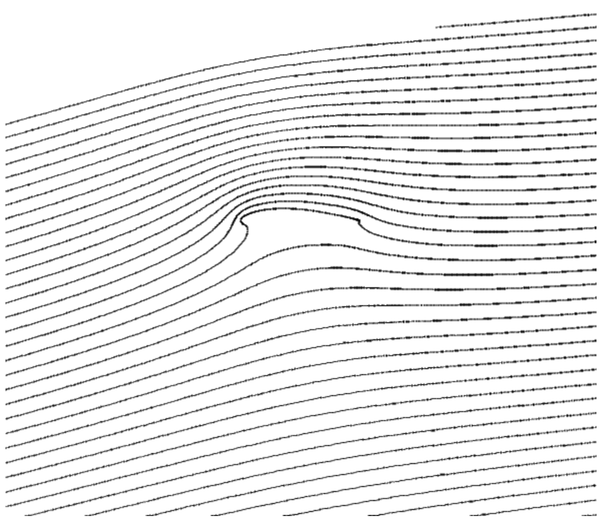

Figure 3.3: $V_\infty c$ = 1.8 flow over airfoil

3.2.3 Lift coefficient for a flat plate

The exact solution of the potential flow around airfoils requires conformal mapping techniques. In practice, conformal mapping techniques are difficult to extend to arbitrary geometries, as a result, numerical methods known as panel methods are used to model potential flows around general airfoil shapes. However, the variation of the lift for a flat plate is a result is useful to understand, and in particular, for comparison to approximate methods.

Specifically, the circulation that satisfies the Kutta condition for a flat plate of chord c is,

$$\Gamma = \pi V_\infty c \sin \alpha \tag{3.1}$$

Thus, the lift generated (using the Kutta-Joukowsky Theorem) is,

$$L' = \rho V_\infty \Gamma = \pi \rho V_\infty^2 c \sin \alpha \tag{3.2}$$

The lift coefficient is

$$c_l = 2\pi \sin \alpha \tag{3.3}$$

For small angles of attack the lift slope is

$$\frac{dc_l}{d\alpha} \approx 2\pi \tag{3.4}$$

and the lift coefficient can then be approximated as,

$$c_l \approx 2\pi\alpha \tag{3.5}$$

Note: α is in radians.

A very important point is that this potential flow result suggests that c_l will continue to rise until $\alpha = 90^\circ$. In the actual flow observed in nature, this will not happen since the boundary layer will separate at the leading edge at very low angles of attack for a flat plate. The neglect of boundary layer behavior places a limit to the applicability of potential flow models. While potential flow models will continue to predict increasing lift as the angle of attack increases (until the angle of attack approaches 90°), the actual viscous flows will stall at much lower angles. Specifically, as the boundary layer thickens and, in particular, when the boundary layer separates, potential flow models will no longer provide an accurate description of the flow.

And, finally, do not forget that the drag for this two-dimensional potential flow is zero according to d'Alembert's Paradox. So, $D' = 0$ and $c_d = 0$. Again, this is not true and is a reflection that viscous effects have not been included.

3.3 Vortex panel methods

3.3.1 Introduction to vortex panel methods

Thus far, our potential flow modeling has been for relatively simple geometric shapes. Now, we turn our attention to developing a potential flow modeling approach that can be applied to airfoils of any shape. The approach is founded upon the same ideas of applying linear superposition of basic building block solutions to Laplaces equation (i.e. conservation of mass), satisfying flow tangency on the body surface, utilizing the Kutta condition to select a potential flow that is physically-realistic at sharp trailing edges, and then using Bernoulli's equation and the Kutta-Joukowsky Theorem to determine the pressure distribution and the lift. So, while the mathematics will get a bit more involved, please keep in mind that the basic principles are no different than the simpler flows we have already studied in this module.

3.3.2 Vortex sheet model

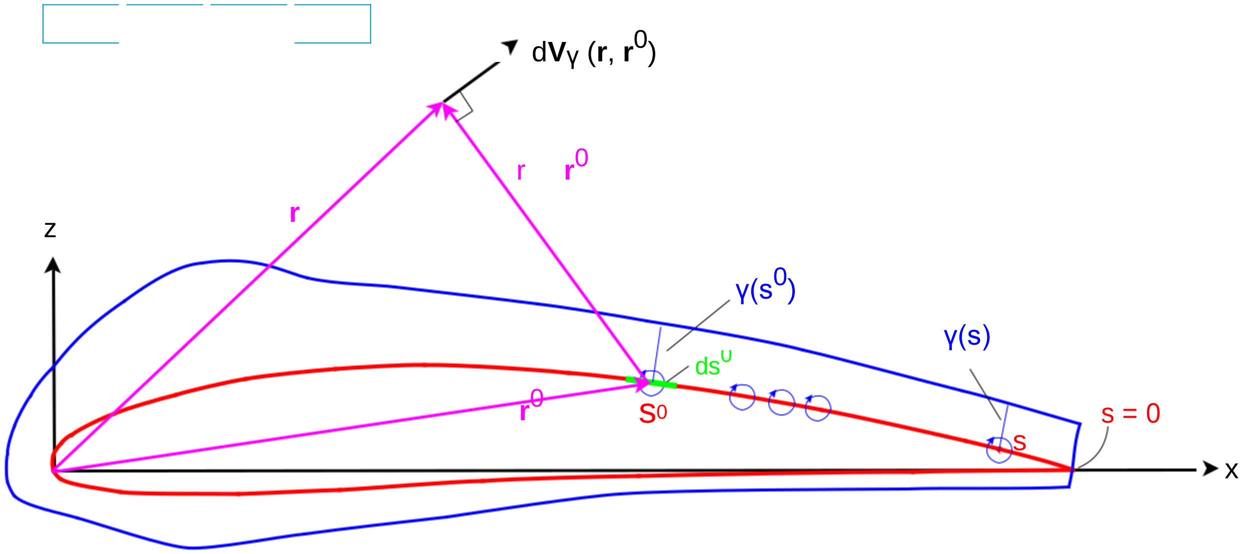

Figure 3.4: Vortex sheet on the surface of an airfoil and the infinitesimal velocity contribution $d\mathbf{V}_\gamma(\mathbf{r}, \mathbf{r}')$ at $\mathbf{r}$ induced by the point vortex at $\mathbf{r}'$ with strength $\gamma(s')ds'$.

The basis of the vortex panel model is a vortex sheet placed on the surface of the airfoil as shown in Figure 3.4. A vortex sheet in two-dimensional flows is a curve along which infinitely-many point vortices are placed with the strength of the vortex at s being $\gamma(s)ds$. Thus, $\gamma(s)$ is a circulation per unit length. For a given airfoil geometry and angle of attack, the question is what is $\gamma(s)$ such that the flow is tangent to the airfoil and satisfies the Kutta condition. Then, once $\gamma(s)$ is determined, we can calculate the velocity field, the pressure distribution (using the Bernoulli equation), the lift coefficient (using the Kutta-Joukowsky Theorem), and so on.

The infinitesimal velocity contribution at $\mathbf{r}$ due to the point vortex at $\mathbf{r}'$ is,

$$d\mathbf{V}_\gamma(\mathbf{r}, \mathbf{r}') = -\frac{\gamma(s')ds'}{2\pi|\mathbf{r} - \mathbf{r}'|}\hat{\mathbf{e}}_{\theta'} \tag{3.6}$$

where $\hat{\mathbf{e}}_{\theta'}$ is the unit vector in the θ-direction from a coordinate system centers at $\mathbf{r}'$. This is equivalent to the velocity field of the point vortex given where

$\Gamma = \gamma(s')ds'$ and the vortex is located at $\mathbf{r}'$ instead of the origin. At $\mathbf{r}$, the direction of $\hat{\mathbf{e}}_{\theta'}$ is perpendicular to $\mathbf{r} - \mathbf{r}'$ and oriented counter-clockwise, thus,

$$\hat{\mathbf{e}}_{\theta'} = \frac{\mathbf{r} - \mathbf{r}'}{|\mathbf{r} - \mathbf{r}'|} \times \hat{\mathbf{j}} \tag{3.7}$$

Substituting this expression into Equation (9.6) produces,

$$d\mathbf{V}_\gamma(\mathbf{r}, \mathbf{r}') = \frac{\gamma(s')ds'}{2\pi} \frac{\hat{\mathbf{j}} \times (\mathbf{r} - \mathbf{r}')}{|\mathbf{r} - \mathbf{r}'|^2} \tag{3.8}$$

The velocity induced at $\mathbf{r}$ by the entire vortex sheet is then an integral around the sheet,

$$\mathbf{V}_\gamma(\mathbf{r}) = \frac{1}{2\pi} \oint \gamma(s') \frac{\hat{\mathbf{j}} \times (\mathbf{r} - \mathbf{r}')}{|\mathbf{r} - \mathbf{r}'|^2} ds' \tag{3.9}$$

Recall that the first step in our potential flow modeling approach (see Sections 1.8.3.1 and 1.8.3.6) is to construct a potential using linear superposition of basic building block flows that all satisfy conservation of mass (Laplaces equations). The vortex sheet velocity field in Equation (3.9) is a linear combination of (infinitesimal strength) point vortices, and point vortices satisfy conservation of mass. Thus, $\nabla \cdot \mathbf{V}_\gamma = 0$. Also, in using a vortex sheet, we have not expressed the potential of the vortex sheet, rather we have directly written the velocity induced by the sheet. This is just expedient since the analysis we will do focuses on the velocity field (in particular satisfying flow tangency and applying Bernoulli equation to find the pressures).

The entire velocity includes the freestream contribution so that the velocity at any point $\mathbf{r}$ is,

$$\mathbf{V}(\mathbf{r}) = \mathbf{V}_\infty + \mathbf{V}_\gamma(\mathbf{r}) = \mathbf{V}_\infty + \frac{1}{2\pi} \oint \gamma(s') \frac{\hat{\mathbf{j}} \times (\mathbf{r} - \mathbf{r}')}{|\mathbf{r} - \mathbf{r}'|^2} ds' \tag{3.10}$$

Flow tangency then requires that $\mathbf{V}(\mathbf{r}) \cdot \hat{\mathbf{n}}(\mathbf{r}) = 0$ for all $\mathbf{r}$ on the airfoil surface,

$$\frac{1}{2\pi} \oint \gamma(s') \frac{\hat{\mathbf{j}} \times (\mathbf{r} - \mathbf{r}') \cdot \hat{\mathbf{n}}(\mathbf{r})}{|\mathbf{r} - \mathbf{r}'|^2} ds' = -\mathbf{V}_\infty \cdot \hat{\mathbf{n}}(\mathbf{r}) \tag{3.11}$$

We must also satisfy the Kutta condition at the sharp trailing edge. To do this, we require that the strength of the point vortex at the trailing edge be zero. If this strength were non-zero, then the velocity induced by the point vortex would induce a flow around the trailing edge. The strength per (unit length) of the vortex at the trailing edge is a sum of $\gamma(0)$ and $\gamma(s_{te})$ where s_{te} is the length of the entire surface of the airfoil (in other words, the length starting at the trailing edge, wrapping around the airfoil, and reaching the trailing edge again). Thus, the Kutta condition requires,

$$\gamma(0) + \gamma(s_{te}) = 0 \tag{3.12}$$

Once the solution $\gamma(s)$ is determined that satisfies flow tangency (Equation 9.11) and the Kutta condition (Equation 9.12), the lift coefficient can be determined using the Kutta-Joukowsky The-orem result that $L' = \rho V_\infty \Gamma$. Since each portion ds of the vortex sheet has a vortex with strength $\gamma(s)ds$, then the total circulation is the integral,

$$\Gamma = \int_{s=0}^{s_{te}} \gamma(s')ds' \tag{3.13}$$

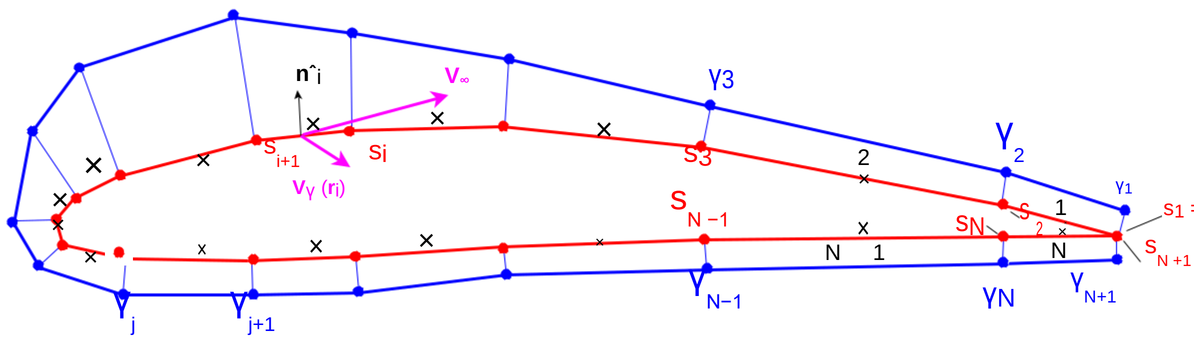

Figure 3.5: Panel representation of airfoil surface with linear-varying vortex sheet on each panel. Control points where flow tangency is enforced are marked by black × and labeled by the panel number.

3.3.3 Linear-varying vortex panel model

The vortex sheet model presented in Section 3.3.2 requires the solution of Equation (3.11) which is an integral equation for the $\gamma(s)$. This equation generally cannot be solved in closed-form analytically. Instead, we will solve it approximately.

The method we use will replace the geometry of the airfoil (and therefore the vortex sheet) with a set of panels as shown in Figure 3.5. The end points of the panels, which we will refer to as the **panel nodes**, are labeled with the surface distance s_i. Thus, panel i lies in the range $s_i \leq s \leq s_{i+1}$.

The $\gamma(s)$ distribution is assumed to vary linearly along each panel, such that for panel j,

$$\gamma(s) = \gamma_j + \frac{s - s_j}{s_{j+1} - s_j}(\gamma_{j+1} - \gamma_j) \tag{3.14}$$

It is this linear variation of $\gamma(s)$ on each panel that gives rise to the term **linear-varying vortex panel**. Note that at the trailing edge the upper and lower surface vortex strength γ_1 and γ_{N+1} have individual values. Thus, the total number of variables to describe $\gamma(s)$ over the entire paneled airfoil is N + 1. This means that we will need to have N + 1 equations to determine the N + 1 values of γ_i.

The N + 1 equations will be N flow tangency conditions and the Kutta condition. We will enforce flow tangency at the midpoints of each panel, which we will refer to as the **control points**. The control points are marked with × in Figure 3.5. The flow tangency condition in Equation (3.11) applied at the control point of panel i becomes,

$$\sum_{j=1}^{N} \frac{1}{2\pi} \int_{s_j}^{s_{j+1}} \gamma(s') \frac{\left(\hat{\mathbf{j}} \times (\mathbf{r}_i - \mathbf{r}')\right) \cdot \hat{\mathbf{n}}_i}{|\mathbf{r}_i - \mathbf{r}'|^2}\, ds' = -\mathbf{V}_\infty \cdot \hat{\mathbf{n}}_i \tag{3.15}$$

where $\gamma(s')$ is given in Equation (9.14), specifically,

$$\gamma(s') = \gamma_j + \frac{s' - s_j}{s_{j+1} - s_j}(\gamma_{j+1} - \gamma_j) \tag{3.16}$$

Also, $\mathbf{r}'$ is a function of s', specifically,

$$\mathbf{r}'(s') = \mathbf{r}_j + \frac{s' - s_j}{s_{j+1} - s_j}(\mathbf{r}_{j+1} - \mathbf{r}_j) \tag{3.17}$$

The integrals from s_j to s_{j+1}, while complicated, can be performed analytically. We will not cover the result here, but it can be done. The final result will depend linearly on the value of γ_j and γ_{j+1} and we will define the following notation,

$$\frac{1}{2\pi}\int_{s_j}^{s_{j+1}} \gamma(s') \frac{\hat{\mathbf{j}} \times (\mathbf{r}_i - \mathbf{r}') \cdot \hat{\mathbf{n}}_i}{|\mathbf{r}_i - \mathbf{r}'|^2} ds' = K_{i,j}^{(j)} \gamma_j + K_{i,j+1}^{(j)} \gamma_{j+1} \tag{3.18}$$

where $K_{i,j}^{(j)}$ and $K_{i,j+1}^{(j)}$ can be found by integration and will only be functions of the geometry of panel j and the location of control point i. Substituting Equation (9.18) into Equation (9.15) gives,

$$\sum_{j=1}^{N} K_{i,j}^{(j)}\gamma_j + K_{i,j+1}^{(j)}\gamma_{j+1} = -\mathbf{V}_\infty \cdot \hat{\mathbf{n}}_i \tag{3.19}$$

Since flow tangency is enforced at the control point of each panel, this produces N equations; that is, i = 1 through N .

In addition to flow tangency, the Kutta condition is also enforced using Equation (3.12), which for this vortex panel representation is,

$$\gamma_1 + \gamma_{N+1} = 0 \tag{3.20}$$

3.3.5 Influence coefficients and linear system

The N flow tangency equations (Equation 3.19) and the Kutta condition (Equation 3.20) can be written as a linear system of $N + 1$ equations of the form,

$$Kg = b \tag{3.22}$$

where g the length $N + 1$ vector of γ_i,

$$g = [\gamma_1, \gamma_2, \ldots, \gamma_N, \gamma_{N+1}] \tag{3.23}$$

K is an $N + 1 \times N + 1$ matrix, and b is a length $N + 1$ vector.

The flow tangency equations are placed in the first N rows of the K matrix, and the Kutta condition is placed in the last row. The system of equations has the following form,

$$\begin{bmatrix} K_{1,1} & K_{1,2} & \cdots & K_{1,N} & K_{1,N+1} \\ K_{2,1} & K_{2,2} & \cdots & K_{2,N} & K_{2,N+1} \\ \vdots & \vdots & & \vdots & \vdots \\ K_{N-1,1} & K_{N-1,2} & \cdots & K_{N-1,N} & K_{N-1,N+1} \\ K_{N,1} & K_{N,2} & \cdots & K_{N,N} & K_{N,N+1} \\ 1 & 0 & \cdots & 0 & 1 \end{bmatrix} \begin{bmatrix} \gamma_1 \\ \gamma_2 \\ \vdots \\ \gamma_{N-1} \\ \gamma_N \\ \gamma_{N+1} \end{bmatrix} = \begin{bmatrix} -V_\infty \cdot \hat{n}_1 \\ -V_\infty \cdot \hat{n}_2 \\ \vdots \\ -V_\infty \cdot \hat{n}_{N-1} \\ -V_\infty \cdot \hat{n}_N \\ 0 \end{bmatrix}$$

where the entries $K_{i,j}$ for $i \leq N$ are known as the influence coefficients and represent the entire influence of γ_j on the flow tangency condition at control point i. The values of $K_{i,j}$ are,

$$K_{i,j} = \begin{cases} K_{i,1}^{(1)} & \text{if } j = 1 \\ K_{i,j}^{(j-1)} + K_{i,j}^{(j)} & \text{if } 1 < j < N + 1 \\ K_{i,N+1}^{(N)} & \text{if } j = N + 1 \end{cases} \tag{3.25}$$

3.3.6 Sample vortex panel solutions on a NACA 4412

To demonstrate the behavior of the linear-varying vortex panel method described in this section, we consider the incompressible potential flow around a NACA 4412 airfoil. First, we consider the effect that the number of panels has on the solution. Figure 3.6 shows the geometry and C_p distributions for $N = 10$ to 320 panels. At $N = 10$ panels, the C_p distribution does not predict the low pressure at the leading edge, but for $N \geq 80$ panels, the minimum C_p is fairly constant at approximately -1.8. Figure 3.7 shows the c_l variation with N. We observe that the asymptotic answer (for large N) is approximately $c_l = 0.986$ and that already bu $N = 40$ panels, c_l is predicted within one percent of that value. The reality is that vortex panel methods require very little computation and so even for $N = 320$ panels run nearly instantaneously on laptops. Typically, the bigger issue is that the panel method by itself does not account for viscous effects and so the accuracy of the answer is limited by the inviscid assumption. Thus, linear-varying vortex panel methods for two-dimensional flows typically will only use 100-200 panels.

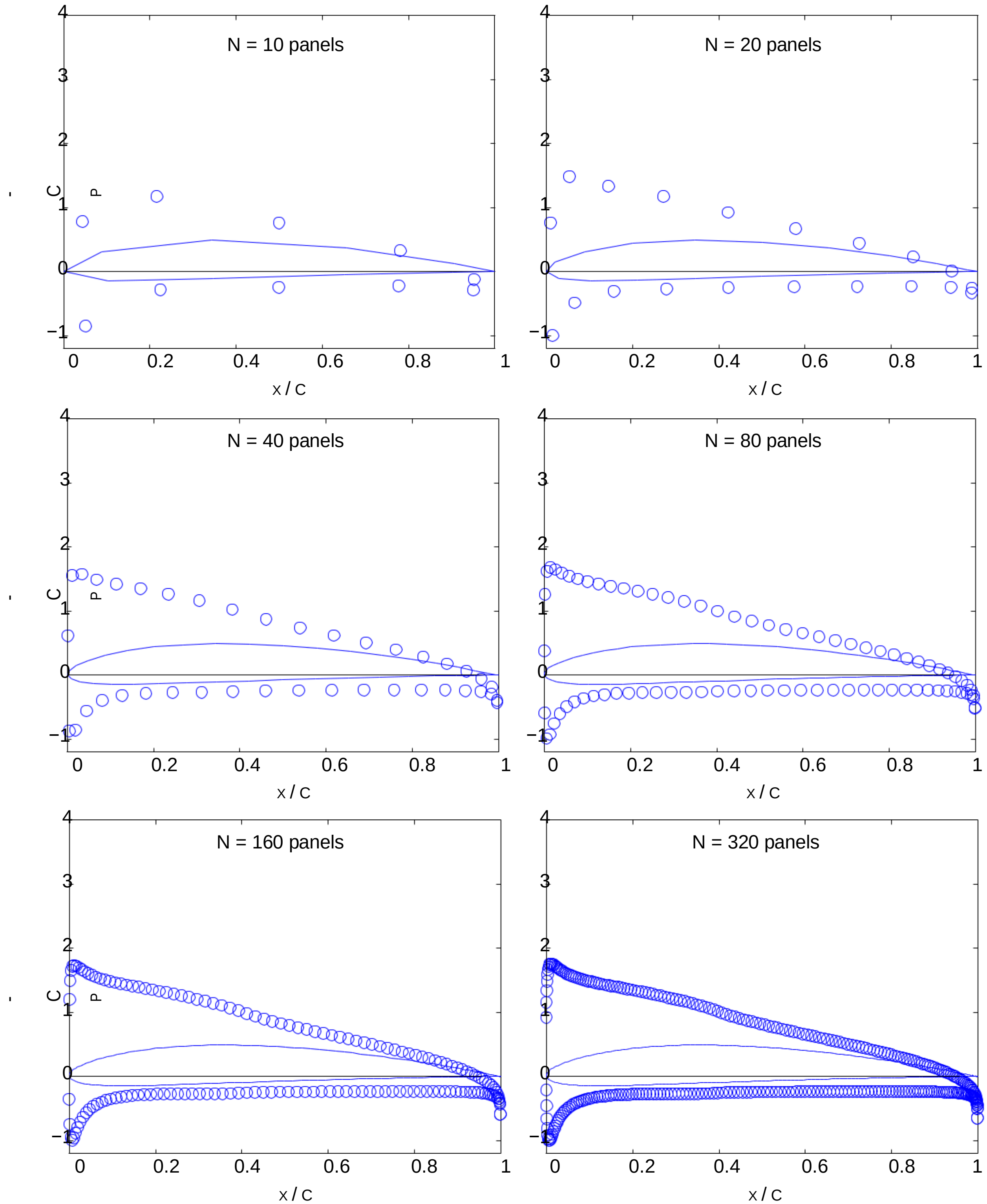

Figure 3.6: NACA 4412 incompressible flow, α = 5°. C_p distributions for different numbers of vortex panels.

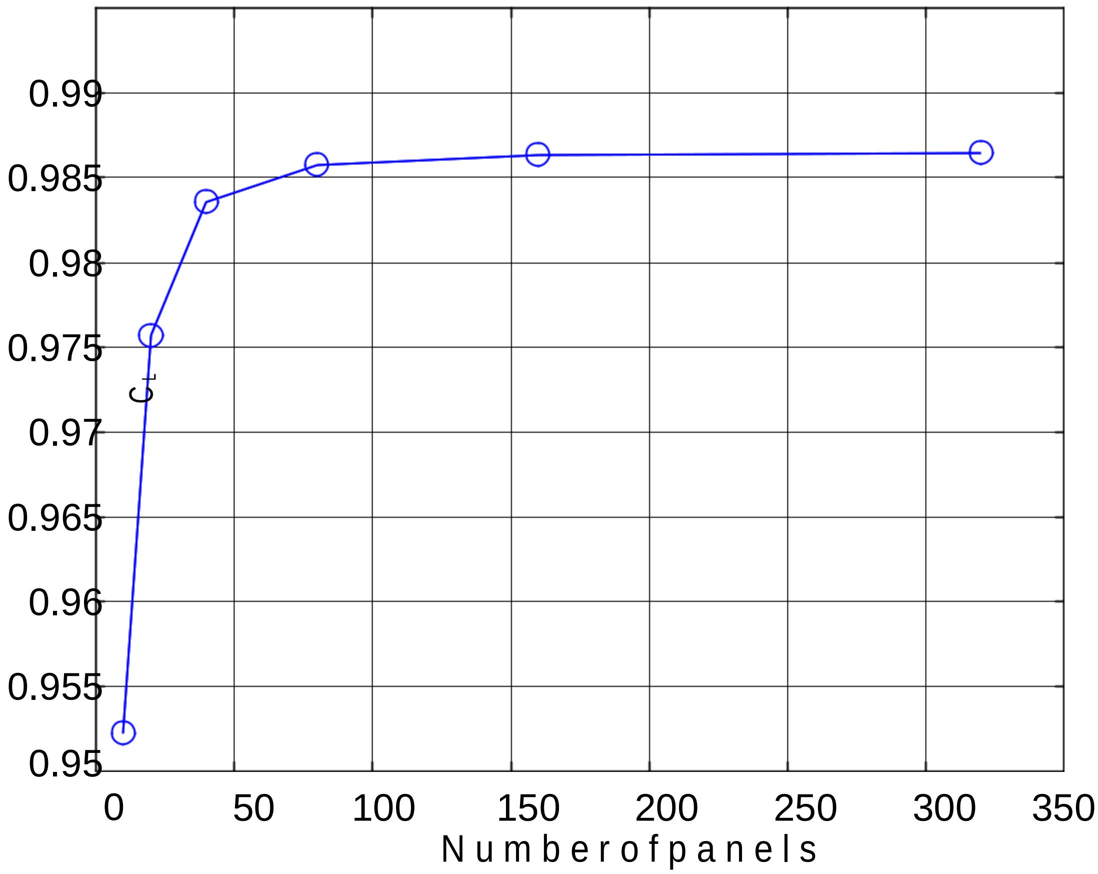

Figure 3.7: NACA 4412 incompressible flow, $\alpha = 5^{\circ}$. Convergence of c_l with number of vortex panels.

3.3.7 Lift coefficient behavior for a NACA 3510 using a vortex panel method: 1 Point

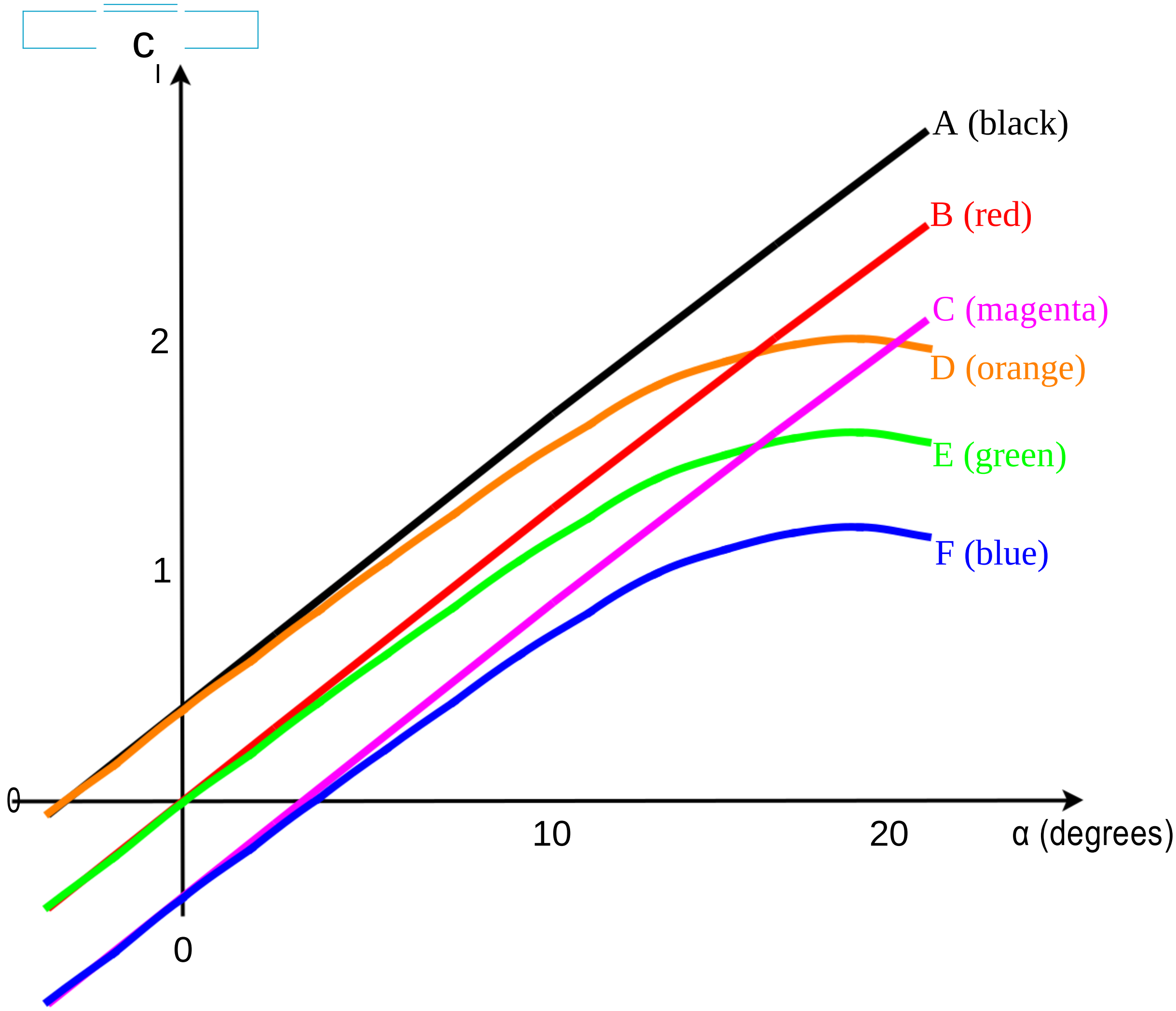

Which of the $c_l(\alpha)$ curves is the lift coefficient of a NACA 3510 airfoil modeled with the vortex panel method described in this module (assume that a large number of panels is used)?

3.4 Thin Airfoil Theory

3.4.1 Thin airfoil potential flow model

Panel methods are a critical tool in modern aerodynamic design. However, the dependence of the aerodynamic performance (C_p distribution, c_l, . . .) on geometry and angle of attack can only be determined by trial-and-error (running the panel method for variations in geometry and angle of attack). As a complement to a panel method, we therefore desire to have a theoretical understanding of how geometry and angle of attack influence the aerodynamic performance. In this section, we derive a simplied vortex sheet model which allows analytic solution. This model and the analytic results are known as **thin airfoil theory**.

The assumptions of thin airfoil theory are

- Two-dimensional, steady incompressible potential flow (see Section 1.8.3.1).
- Small angle of attack: $\alpha \ll 1$ (radians)
- Small thickness: $t_{max}/c \ll 1$
- Small camber and camber slope: $z_{c_{max}}/c \ll 1$ and $\frac{dz_c}{dx} \ll 1$
- Small velocity perturbations: $|\mathbf{V} - \mathbf{V}_\infty|/V_\infty \ll 1$.

Applying the small angle of attack assumption gives the freestream velocity in simplified form,

$$\mathbf{V}_\infty = V_\infty \cos\alpha \hat{\mathbf{i}} + V_\infty \sin\alpha \hat{\mathbf{k}} \approx V_\infty \hat{\mathbf{i}} + V_\infty \alpha \hat{\mathbf{k}} \tag{3.26}$$

Thin airfoil theory uses the vortex sheet model described in Section 3.3.2 applied to airfoils that have small thickness and camber. Applying the small thickness assumption, we collapse the vortex sheet on the upper and lower surfaces to the mean camber line. As shown in Figure 3.8, the resulting vortex sheet on the camber line has a strength $\gamma(x)$ which is effectively the sum of the upper and lower surface vortex sheet strengths in the original case with finite thickness. The flow tangency condition is applied on the camber line requiring on the upper surface,

$$\mathbf{V}_\gamma (x, z_c^+(x)) \cdot \hat{\mathbf{n}}_c(x) = -\mathbf{V}_\infty \cdot \hat{\mathbf{n}}_c(x) \tag{3.27}$$

and on the lower surface,

$$\mathbf{V}_\gamma (x, z_c^-(x)) \cdot \hat{\mathbf{n}}_c(x) = -\mathbf{V}_\infty \cdot \hat{\mathbf{n}}_c(x) \tag{3.28}$$

where $z_c^+(x)$ and $z_c^-(x)$ are defined as the value of z just above and below the camber line. However, while the velocity jumps across the vortex sheet, it can be shown that this jump is only in the velocity component tangential to the sheet. Specifically, defining the jump in the velocity across the sheet as,

$$\Delta\mathbf{V}_\gamma (x) \equiv \mathbf{V}_\gamma (x, z_c^+(x)) - \mathbf{V}_\gamma (x, z_c^-(x)) \tag{3.29}$$

Then,

$$\Delta\mathbf{V}_\gamma (x) \cdot \hat{\mathbf{n}}_c(x) = 0 \tag{3.30}$$

The tangential velocity jump is directly related to $\gamma(x)$,

$$\Delta\mathbf{V}_\gamma (x) \cdot \hat{\mathbf{t}}_c(x) = \gamma(x) \tag{3.31}$$

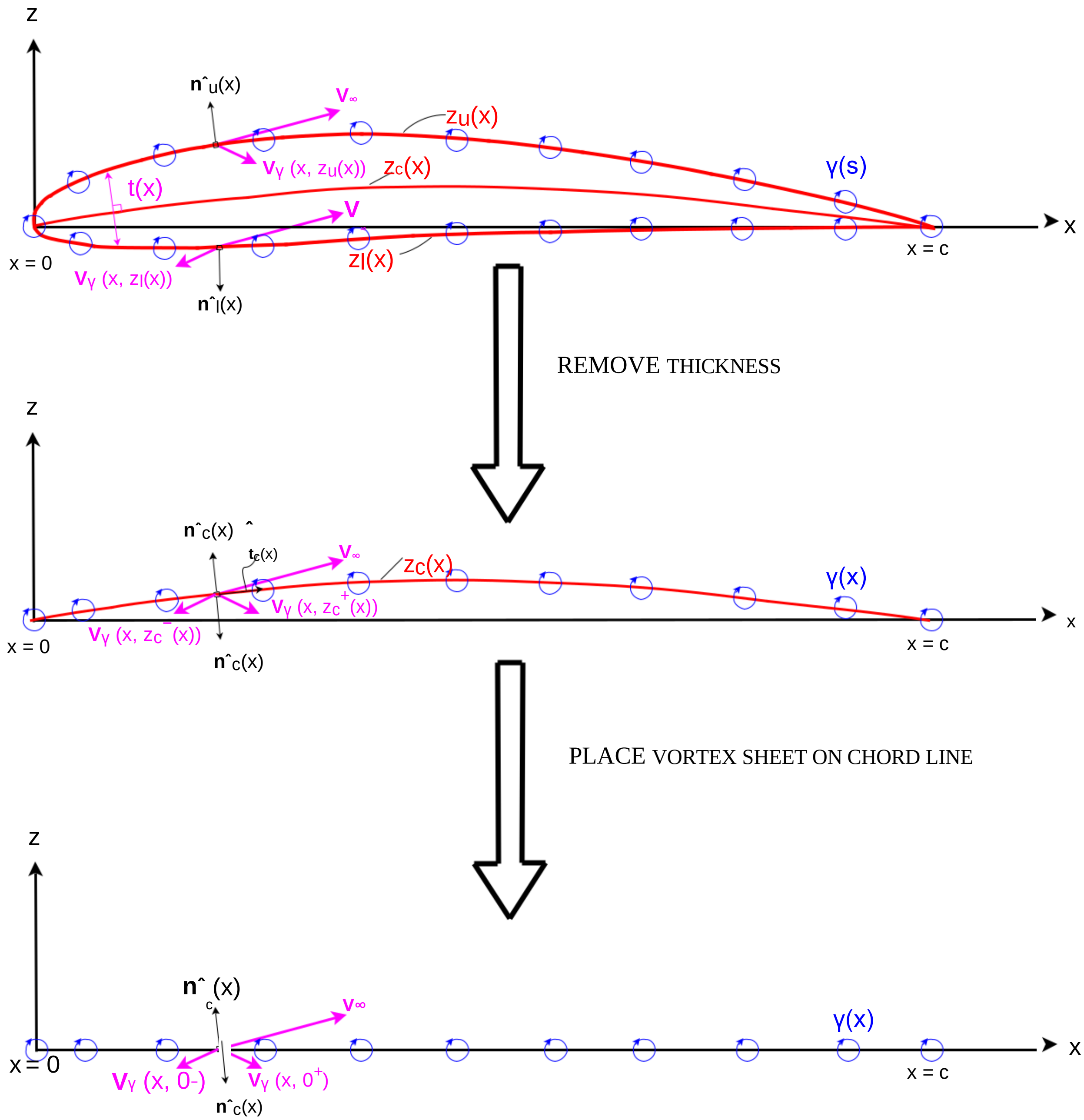

Figure 3.8: Transformation from vortex sheet on airfoil surface to thin airfoil representation with the vortex sheet on the chord line.

where $\hat{\mathbf{t}}_c(x)$ is the tangent unit vector defined as,

$$\hat{\mathbf{t}}_c(x) \equiv \hat{\mathbf{j}} \times \hat{\mathbf{n}}_c(x) \tag{3.32}$$

We note that Equations (9.30) and (9.31) are valid for any vortex sheet.

Since the normal velocity component is the same for both $z_c^{\pm}(x)$ then the flow tangency condition can just be written as,

$$\mathbf{V}_\gamma\,(x, z_c(x)) \cdot \hat{\mathbf{n}}_c(x) = -\mathbf{V}_\infty \cdot \hat{\mathbf{n}}_c(x) \tag{3.33}$$

Next, we apply the assumption that the camber is small. This allows the vortex sheet to be moved from the camber line to the chord line ($z = 0$). With this approximation, flow tangency is now,

$$\mathbf{V}_\gamma(x, 0) \cdot \hat{\mathbf{n}}_c(x) = -\mathbf{V}_\infty \cdot \hat{\mathbf{n}}_c(x) \tag{3.34}$$

Note that although the camber is small, we still use the slope of the camber line in applying flow tangency. If we had also set the slope to zero, then the normal $\hat{n}_c$ would be in the z direction. In other words, the thin airfoil theory would model every airfoil as if it had no camber.

3.4.2 Fundamental equation of thin airfoil theory

The flow tangency condition for the thin airfoil model in Equation (3.34) can be simplified. Recall that the expression for the velocity at a point induced by a general vortex sheet is given by Equation (3.9),

$$\mathbf{V}_\gamma(\mathbf{r}) = \frac{1}{2\pi}\int \gamma(s')\frac{\hat{\mathbf{j}} \times (\mathbf{r} - \mathbf{r}')}{|\mathbf{r} - \mathbf{r}'|^2}\, ds' \tag{3.35}$$

For the thin airfoil theory model, the sheet is along the x-axis so s = x (and similarly then the integration variable s' we will set to x'). To apply flow tangency, we need the velocity at (x, 0), thus,

$$\mathbf{r} = x\hat{\mathbf{i}} \quad \text{and} \quad \mathbf{r}' = x'\hat{\mathbf{i}} \tag{3.36}$$

Thus, $\mathbf{V}_\gamma$ at (x, 0) is,

$$\mathbf{V}_\gamma(x, 0) = -\hat{\mathbf{k}}\frac{1}{2\pi}\int_0^c \frac{\gamma(x')}{x - x'}\, dx' \tag{3.37}$$

Recall from Equation (3.10) that the angle of the camber line is $\tan\theta_c = dz_c/dx$. For small camber slope, this can be approximated as,

$$\tan\theta_c \approx \theta_c \approx \frac{dz_c}{dx} \tag{3.38}$$

The normal to the camber line is,

$$\hat{\mathbf{n}}_c = -\sin\theta_c\hat{\mathbf{i}} + \cos\theta_c\hat{\mathbf{k}} \approx -\frac{dz_c}{dx}\hat{\mathbf{i}} + \hat{\mathbf{k}} \tag{3.39}$$

Substituting Equations (3.37) and (3.39) into the flow tangency condition (Equation 9.34) gives,

$$\frac{1}{2\pi}\int_0^c \frac{\gamma(x')}{x - x'}\, dx' = V_\infty\left(\alpha - \frac{dz_c}{dx}\right) \tag{3.40}$$

which must be satisfied for all x from 0 < x < c. Equation (3.40) is known as the **fundamental equation of thin airfoil theory**. While it took some manipulations to get to this result, remember that it represents the flow tangency condition $\mathbf{V} \cdot \hat{n} = 0$ for a thin airfoil modeled with a vortex sheet along its chordline. The goal in performing thin airfoil theory analysis is to determine the $\gamma(x)$ that satisfies this equation for the desired camber and angle of attack.

Finally, in addition to satisfying Equation (3.40), the Kutta condition must also be satisfied. For the thin airfoil theory model, this requires,

$$\gamma(c) = 0 \tag{3.41}$$

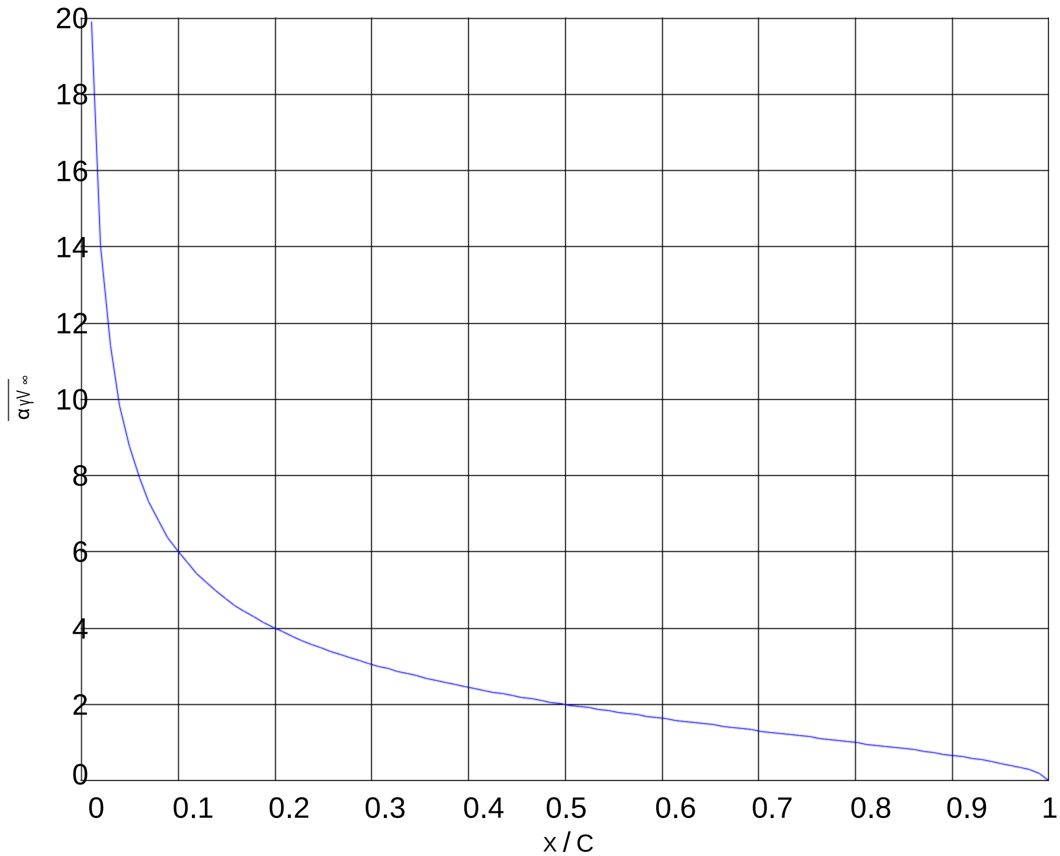

Figure 3.9: γ(x) distribution for a symmetric airfoil.

3.4.3 Symmetric airfoils

For a symmetric airfoil, $z_c = 0$. Thus, the fundamental equation of thin airfoil theory (Equation 9.40) reduces to,

$$\frac{1}{2\pi}\int_0^c \frac{\gamma(x')}{x - x'}\,dx' = V_\infty \alpha \tag{3.42}$$

The vortex strength distribution which satisfies this equation (and the Kutta condition) is,

$$\gamma(x) = 2\alpha V_\infty \sqrt{\frac{c - x}{x}} \tag{3.43}$$

A plot of this result is shown in Figure 3.9. We see that γ(x) is infinite at the leading edge. In the next section, we link the pressure differences to γ and discuss why γ(x) is infinite at the leading edge.

The lift can be determined from the Kutta-Joukowsky Theorem by calculating the circulation

$$\Gamma = \int_0^c \gamma(x')\,dx' \tag{3.44}$$

This integral of γ(x) can be performed through a transformation of variables from x to ξ where, ξ is defined as,

$$x \equiv \frac{c}{2}(1 - \cos \xi) \tag{3.45}$$

Note that $\xi = 0$ is the leading edge and $\xi = \pi$ is the trailing edge. Further, differentiation of this transformation gives,

$$dx \equiv \frac{c}{2} \sin \xi \, d\xi \qquad (3.46)$$

Substituting this transformation into Equation (3.43) gives,

$$\gamma(\xi) = 2\alpha V_\infty \frac{1 + \cos \xi}{\sin \xi} \qquad (3.47)$$

Finally, performing the integration,

$$\Gamma = \frac{c}{2} \int_0^\pi \gamma(\xi') \sin \xi' \, d\xi' \qquad (3.48)$$

$$= \alpha c V_\infty \int_0^\pi (1 + \cos \xi') d\xi' \qquad (3.49)$$

$$= \pi \alpha c V_\infty \qquad (3.50)$$

Thus,

$$L = \rho V_\infty \Gamma = \pi \alpha \rho V_\infty^2 c \qquad (3.51)$$

$$c_l = 2\pi\alpha \qquad (3.52)$$

The result that $c_l = 2\pi\alpha$ for symmetric airfoils is a classic result in aerodynamics. Figures 3.10 through 3.12 shows comparisons between this thin airfoil theory result, potential flow (using a vortex panel method) and predictions which include viscous effects. Three airfoils are considered: NACA 0006, 0012, and 0021. All results agree most closely for the thinnest airfoil (NACA 0006) with larger discrepancies for increasing thickness. Interesting, the potential flow model predicts larger lift than the thin airfoil theory result, and the thin airfoil theory result is in better agreement with the viscous results. This is a common behavior which is apparently due to the approximations made in thin airfoil theory having similar behavior as the viscous effects (however, there should not be anything more fundamental made of this point; just a coincidence that the two effects have similar behavior). In principle, thin airfoil theory has more approximations than the panel method in terms of solving potential flows.

3.4.4 Pressure differences

In this section, our goal is to relate $\gamma(x)$ from thin airfoil theory to the pressure distribution. We begin by defining the velocity field in terms of the freestream and perturbations. In thin airfoil theory, we have not aligned the freestream to the x-axis so the result is a little different, specifically,

$$u(x, z) = V_\infty \cos \alpha + \tilde{u}(x, z) \qquad (3.53)$$

$$w(x, z) = V_\infty \sin \alpha + \tilde{w}(x, z) \qquad (3.54)$$

The square of the velocity magnitude is then,

$$V^2 = u^2 + w^2 \qquad (3.55)$$

$$= (V_\infty \cos \alpha + \tilde{u})^2 + (V_\infty \sin \alpha + \tilde{w})^2 \qquad (3.56)$$

$$= V_\infty^2 + 2V_\infty (\tilde{u} \cos \alpha + \tilde{w} \sin \alpha) + \tilde{u}^2 + \tilde{w}^2 \qquad (3.57)$$

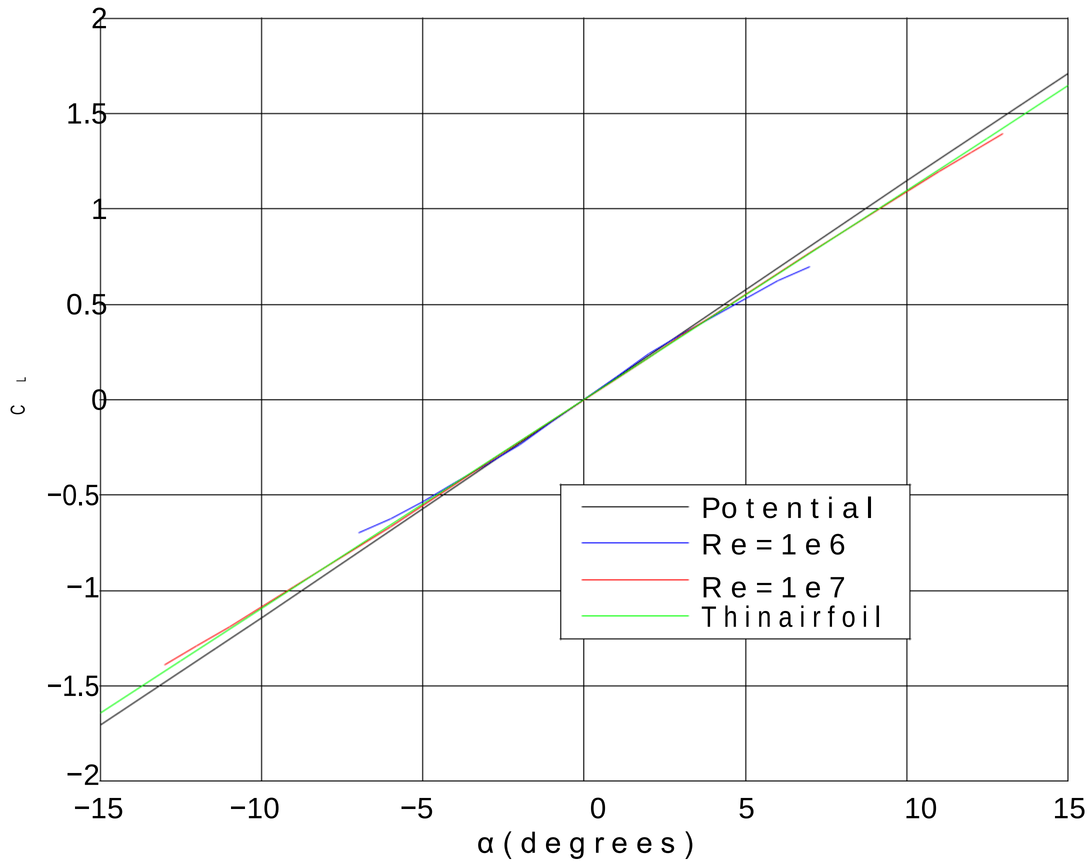

Figure 3.10: Comparison of $c_l(\alpha)$ for NACA 0006 for potential flow, thin airfoil theory, and Re = 1E6 and Re = 1E7 viscous calculations.

For small angles cos α ≈ 1 and sin α ≈ α, thus,

$$V^2 = V_\infty^2 + 2V_\infty(\tilde{u} + \tilde{w}\alpha) + \tilde{u}^2 + \tilde{w}^2 \tag{3.58}$$

Recall using Bernoulli's equation, C_p is,

$$C_p = 1 - \frac{V^2}{V_\infty^2} \tag{3.59}$$

$$\approx -2\frac{\tilde{u}}{V_\infty} - 2\frac{\tilde{w}}{V_\infty}\alpha - \frac{\tilde{u}^2}{V_\infty^2} - \frac{\tilde{w}^2}{V_\infty^2} \tag{3.60}$$

The first term is linear in small quantities (scaling with $\tilde{u}/V_\infty$) while the last three terms are quadratic (scaling with quadratic combinations of $\tilde{u}/V_\infty$, $\tilde{w}/V_\infty$, and α). Thus, under the assumptions of thin airfoil theory, these quadratic terms will be much smaller giving the following approximation for the C_p,

$$C_p \approx -2\frac{\tilde{u}}{V_\infty} \tag{3.61}$$

The jump in the pressure between the upper and lower surface (normalized by the dynamic

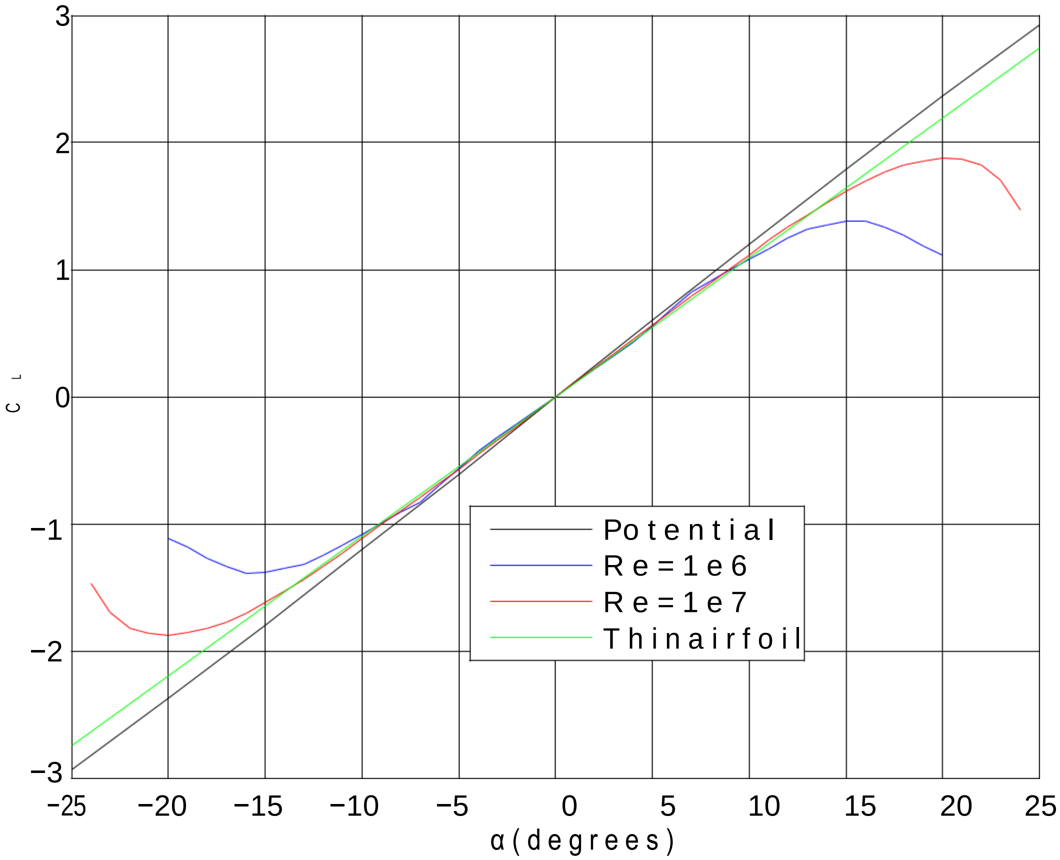

Figure 3.11: Comparison of $c_l(\alpha)$ for NACA 0012 for potential flow, thin airfoil theory, and Re = 1E6 and Re = 1E7 viscous calculations.

pressure) is,

$$\frac{p_l - p_u}{q_\infty} = \frac{p_l - p_\infty}{q_\infty} - \frac{p_u - p_\infty}{q_\infty} \tag{3.62}$$

$$= C_{p_l} - C_{p_u} \tag{3.63}$$

$$\approx 2\frac{\tilde{u}_u - \tilde{u}_l}{V_\infty} \tag{3.64}$$

For the vortex sheet in thin airfoil theory, Equation (3.31) gives,

$$\tilde{u}_u - \tilde{u}_l = \gamma \tag{3.65}$$

Thus, we arrive at the result that,

$$C_{p_l} - C_{p_u} \approx 2\frac{\gamma}{V_\infty} \tag{3.66}$$

In the following video, we discuss the results of the symmetric airfoil and in particular consider the leading-edge behavior of the pressure differences.

3.4.5 Cambered airfoils

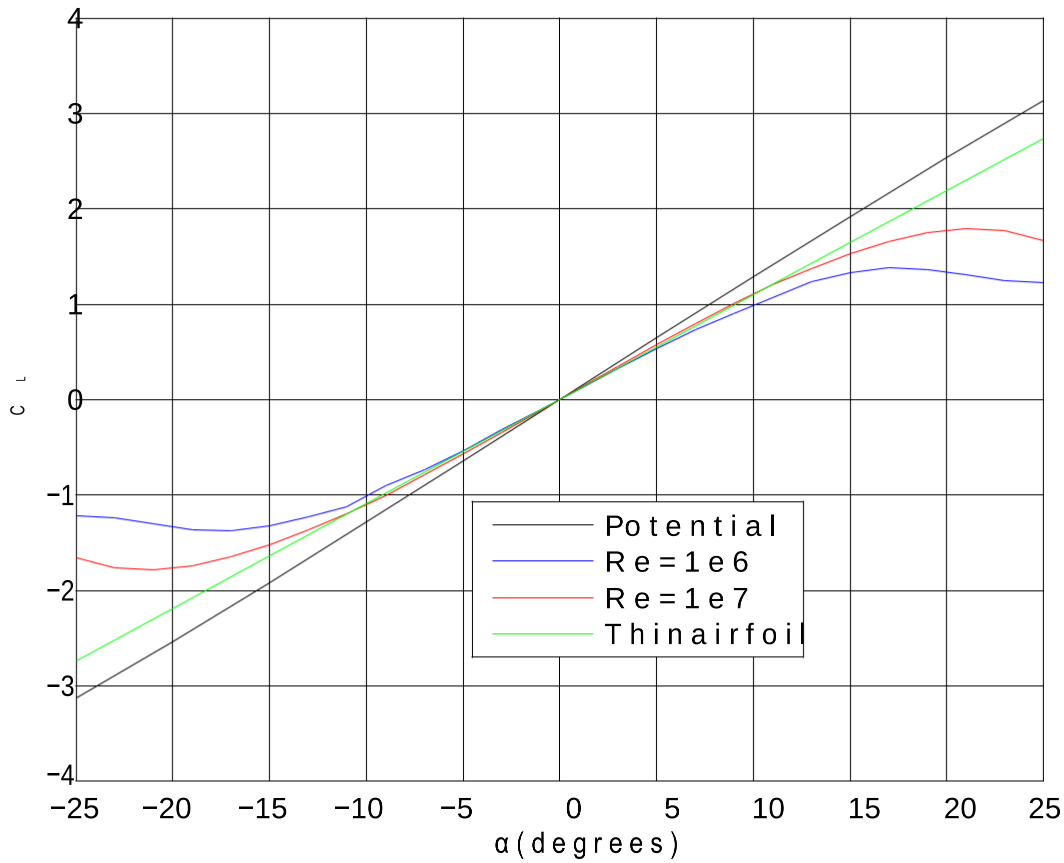

Figure 3.12: Comparison of $c_l(\alpha)$ for NACA 0021 for potential flow, thin airfoil theory, and Re = 1E6 and Re = 1E7 viscous calculations.

9.4

The analysis of cambered airfoils can be performed by expressing $\gamma(x)$ as a linear combination of the symmetric airfoil solution in Equation (3.43) and a series of additional modes. Specifically, using the ξ transformed coordinate, the general solution for $\gamma(x)$ is of the form,

$$\gamma(\xi) = 2V_\infty \left[A_0 \frac{1+\cos\xi}{\sin\xi} + \sum_{n=1}^{\infty} A_n \sin n\xi \right] \tag{3.67}$$

where all of the A_n are unknown values that determine the circulation distribution. With significant manipulations, the A_n can be related to the camber distribution and α,

$$A_0 = \alpha - \frac{1}{\pi}\int_0^\pi \frac{dz_c}{dx}\, d\xi \tag{3.68}$$

$$A_n = \frac{2}{\pi}\int_0^\pi \frac{dz_c}{dx} \cos n\xi \, d\xi \tag{3.69}$$

Thus, the solution process to determine $\gamma(x)$ is reduced to performing the integrals of the camber slope given in Equations (3.68) and (3.69).

The circulation can be determined for this general γ distribution (beginning with Equation 3.48),

$$\Gamma = \frac{c}{2}\int_0^{\pi} \gamma(\xi')\sin\xi'\,d\xi' \tag{3.70}$$

$$= cV_\infty\left[A_0\int_0^{\pi}(1+\cos\xi')d\xi' + \sum_{n=1}^{\infty}\int_0^{\pi}A_n\sin n\xi'\sin\xi'd\xi'\right] \tag{3.71}$$

The first integral is from the symmetric airfoil analysis done previously and has a value of π. The second integral is a result for Fourier integrals and is given by,

$$\int_0^{\pi}\sin n\xi\,\sin\xi\,d\xi = \begin{cases}\pi/2 & \text{for } n = 1\\ 0 & \text{for } n = 1\end{cases} \tag{3.72}$$

Thus, for this general distribution we have,

$$\Gamma = cV_\infty\left(\pi A_0 + \frac{\pi}{2}A_1\right) \tag{3.73}$$

Which leads to the lift coefficient being given by,

$$c_l = \pi(2A_0 + A_1) \tag{3.74}$$

Or, equivalently, using Equations (3.68) and (3.69),

$$c_l = 2\pi\left[\alpha + \frac{1}{\pi}\int_0^{\pi}\frac{dz_c}{dx}(\cos\xi' - 1)d\xi'\right] \tag{3.75}$$

This final form shows clearly that camber does not impact the lift slope which remains 2π, but camber does create an offset in the lift curve. A common way to write this result is,

$$c_l = 2\pi(\alpha - \alpha_{L=0}) \tag{3.76}$$

where the angle of zero lift is given by,

$$\alpha_{L=0} = \frac{1}{\pi}\int_0^{\pi}\frac{dz_c}{dx}(1 - \cos\xi')d\xi' \tag{3.77}$$

3.4.6 Pitching moment behavior

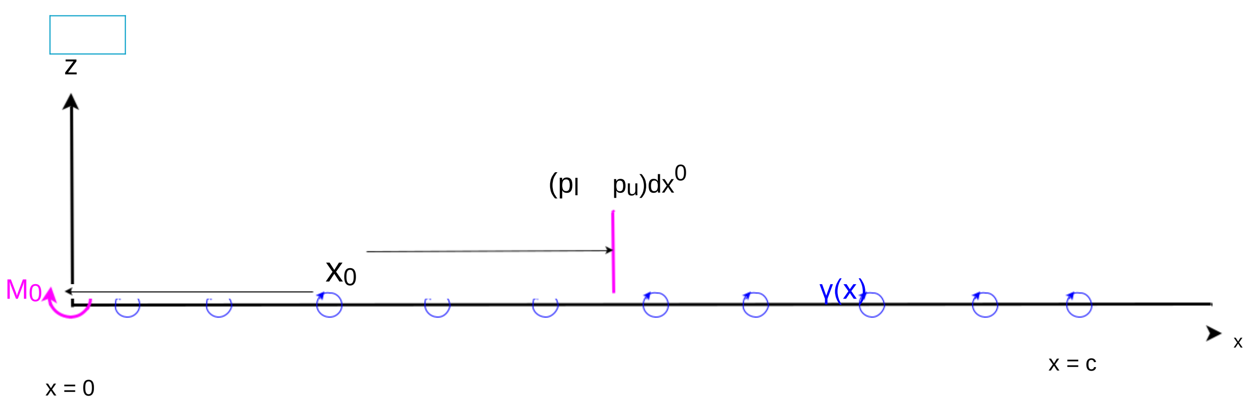

Figure 3.13: Calculation of the pitching moment about the leading edge from thin airfoil theory.

In addition to the lift, the moments created by aerodynamic forces are important and play a critical role in the stability of an aircraft. The pitching moment can be estimated in thin airfoil theory by integrating across the chord the moment created by the pressure differences as shown in Figure 3.13. The pitching moment is defined as positive when it raises the nose of the airfoil. Thus, the pitching moment about the leading edge is,

$$M_0 = -\int_0^c (p_l - p_u)x' dx' \tag{3.78}$$

$$= -\rho V_\infty \int_0^c \gamma(x')x' dx' \tag{3.79}$$

$$= -\frac{1}{2}\rho V_\infty^2 c^2 \int_0^\pi \left[A_0 \frac{1+\cos\xi'}{\sin\xi'} + \sum_{n=1}^{\infty} A_n \sin n\xi'\right](1-\cos\xi')\sin\xi' d\xi' \tag{3.80}$$

Performing the integration and normalizing by $q_\infty c^2$ produces the moment coefficient about the leading edge,

$$c_{m_{le}} = -\frac{\pi}{2}\left(A_0 + A_1 - \frac{A_2}{2}\right) \tag{3.81}$$

This can be written in terms of c_l as,

$$c_{m_{le}} + \frac{c_l}{4} = \frac{\pi}{4}(A_2 - A_1) \tag{3.82}$$

The left-hand side of this result is the moment coefficient taken about the quarter chord, i.e. $x = c/4$. Thus, another form of the thin airfoil theory moment result is,

$$c_{m_{c/4}} = \frac{\pi}{4}(A_2 - A_1) \tag{3.83}$$

Since A_1 and A_2 do not depend on α, then thin airfoil theory predicts that the moment about c/4 does not depend on the angle of attack. The location at which the aerodynamic moment is constant with respect to variations in α is called the **aerodynamic center**.

For symmetric airfoils, since $A_1 = A_2 = 0$, then $c_{m_{c/4}} = 0$. The **center of pressure** is the x-location at which the aerodynamic moments are zero. Thus, for symmetric airfoils, the center of pressure and the aerodynamic center are located at c/4. However, for cambered airfoils, the center of pressure will vary with α. Specifically, we can solve for x_{cp} be determing the location at which the moment is zero:

$$c_m(x_{cp}) = 0 \tag{3.84}$$

$$= c_{m_{c/4}} + \left(\frac{x_{cp}}{c} - \frac{1}{4}\right)c_l \tag{3.85}$$

$$\Rightarrow \frac{x_{cp}}{c} = \frac{1}{4} - \frac{c_{m_{c/4}}}{c_l} \tag{3.86}$$

SATHYABAMA
INSTITUTE OF SCIENCE AND TECHNOLOGY
(DEEMED TO BE UNIVERSITY)
Accredited "A" Grade by NAAC | 12B Status by UGC | Approved by AICTE
www.sathyabama.ac.in

SCHOOL OF MECHANICAL ENGINEERING
DEPARTMENT OF AERONAUTICAL ENGINEERING

UNIT – IV –LOW SPEED AERODYNAMICS – SAEA1403

UNIT 4

WING THEORY

4.1 Overview

4.1.1 Measurable outcomes

In this module, we develop potential flow models for estimating the aerodynamic performance of three-dimensional bodies, in particular wings. Along the way, we will discover that three-dimensional potential flow around bodies that generate lift have non-zero drag. This lift-related drag is often refered to as **induced drag**.

Specifically, students successfully completing this module will be able to:

4.1. Define the velocity field for a source and doublet in three dimensions. Derive the relationship between the strength of a source, mass flow, and the conservation of mass.

4.2. Combine a freestream and doublet to model the potential flow around a sphere. Determine the pressure coefficient distribution on the sphere surface.

4.3. Utilize the Biot-Savart law to determine the velocity field induced by vortex filament. Show that the flow induced by vortex filament satisfies conservation of mass and is irrotational (except on the filament).

4.4. Describe how the generation of lift on a wing results in a vortical motion behind the wing due to the general motion of the flow from the high pressure lower surface around to the lower pressure upper surface.

4.5. Describe how the sectional lift distribution is a related to the bending moment at the root of a wing. Describe how the sectional lift coefficient behavior is related to the potential for stall.

4.6. Describe how the presence of a vortical wake gives rise to finite velocity perturbations in the Trefftz plane and that these perturbations, which increase the kinetic energy of the flow, must result from work being done on the air by a force acting in the direction of motion of the body (i.e. equal-and-opposite of the drag force which acts on the body). Further, interpret the induced drag in terms of the downwash created by the trailing vortical wake which tilts the effective sectional lift into the freestream direction.

4.7. Explain the lifting line model for a high aspect ratio wing including the assumptions. Describe the key results for the lift and induced drag including the dependence on aspect ratio, the relationship to two-dimensional potential flow, and the optimality of the elliptic lift distri-bution. Describe how the variation in the lift distribution is related to the vorticity in the trailing wake.

4.8. Apply the lifting line model to estimate the behavior of the flow and the aerodynamic perfor-mance of a wing. Apply the lifting line model to design a wing that meets desired aerodynamic performance.

4.2 Three-dimensional Nonlifting Flows

4.2.1 Spherical coordinate system

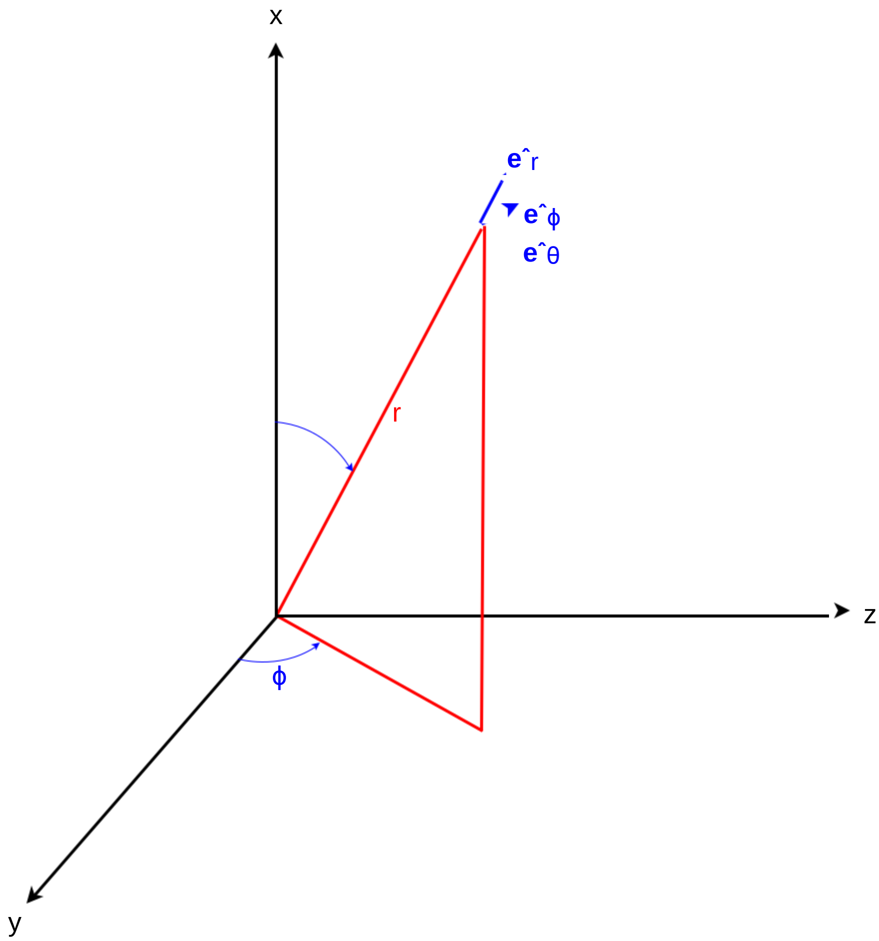

Figure 4.1: Three-dimensional spherical coordinate system

Spherical coordinates can be useful in describing three-dimensional potential flows. Figure 4.1 shows the spherical coordinate system we will use in this course. Specifically, the relationship between (x, y, z) and (r, θ, ϕ) is,

$$x = r\cos\theta \tag{4.1}$$

$$y = r\sin\theta\cos\phi \tag{4.2}$$

$$z = r\sin\theta\sin\phi \tag{4.3}$$

The unit vectors in the r, θ, and ϕ directions are,

$$\hat{e}_r = \cos\theta\,\hat{\mathbf{i}} + \sin\theta\cos\phi\,\hat{\mathbf{j}} + \sin\theta\sin\phi\,\hat{\mathbf{k}} \tag{4.4}$$

$$\hat{e}_\theta = -\sin\theta\,\hat{\mathbf{i}} + \cos\theta\cos\phi\,\hat{\mathbf{j}} + \cos\theta\sin\phi\,\hat{\mathbf{k}} \tag{4.5}$$

$$\hat{e}_\phi = -\sin\phi\,\hat{\mathbf{j}} + \cos\phi\,\hat{\mathbf{k}} \tag{4.6}$$

The radial, ϕ, and θ velocity components are related to u, v and w by,

$$u_r = u\cos\theta + v\sin\theta\cos\phi + w\sin\theta\sin\phi \tag{4.7}$$

$$u_\theta = -u\sin\theta + v\cos\theta\cos\phi + w\cos\theta\sin\phi \tag{4.8}$$

$$u_\phi = -v\sin\phi + w\cos\phi \tag{4.9}$$

The gradient operator in spherical coordinates can be applied to φ to find u_r, u_θ, and u_ϕ

$$u_r = \frac{\partial\varphi}{\partial r} \tag{4.10}$$

$$u_\theta = \frac{1}{r}\frac{\partial\varphi}{\partial\theta} \tag{4.11}$$

$$u_\phi = \frac{1}{r\sin\theta}\frac{\partial\varphi}{\partial\phi} \tag{4.12}$$

The divergence and curl of the velocity vector in spherical coordinates are,

$$\nabla\cdot\mathbf{V} = \frac{1}{r^2}\frac{\partial}{\partial r}\left(r^2 u_r\right) + \frac{1}{r\sin\theta}\frac{\partial}{\partial\theta}\left(u_\theta\sin\theta\right) + \frac{1}{r\sin\theta}\frac{\partial u_\phi}{\partial\phi} \tag{4.13}$$

$$\nabla\times\mathbf{V} = \frac{1}{r^2\sin\theta}\begin{vmatrix} \hat{\mathbf{e}}_r & r\hat{\mathbf{e}}_\theta & (r\sin\theta)\hat{\mathbf{e}}_\phi \\ \frac{\partial}{\partial r} & \frac{\partial}{\partial\theta} & \frac{\partial}{\partial\phi} \\ u_r & r u_\theta & (r\sin\theta)u_\phi \end{vmatrix} \tag{4.14}$$

Finally, we note that Laplace's equation for φ in spherical coordinates is,

$$\nabla^2\varphi = \frac{1}{r^2}\frac{\partial}{\partial r}\left(r^2\frac{\partial\varphi}{\partial r}\right) + \frac{1}{r^2\sin\theta}\frac{\partial}{\partial\theta}\left(\sin\theta\frac{\partial\varphi}{\partial\theta}\right) + \frac{1}{r^2\sin^2\theta}\frac{\partial^2\varphi}{\partial\phi^2} = 0 \tag{4.15}$$

4.2.2 Source in 3D flow

Similar to the source in two-dimensional flow discussed in Section 4.4.3, a three-dimensional source has only radial velocity. In three dimensions, the potential and velocity components of a source are,

$$\varphi = -\frac{\lambda}{4\pi r} \tag{4.16}$$

$$u_r = \frac{\lambda}{4\pi r^2} \tag{4.17}$$

$$u_\theta = 0 \tag{4.18}$$

$$u_\phi = 0 \tag{4.19}$$

where λ is source strength. Similar to the two-dimensional case, the following results can be proven,

- A 3D source emits mass at a rate of $\rho\lambda$.
- A source satisfies the conservation of mass except at its origin. That is $\nabla\cdot\mathbf{V} = 0$ everywhere in the flow expect at its origin. And, at the origin, $\nabla\cdot\mathbf{V}$ is infinite.

4.2.3 Doublet in 3D flow

Analogous to the two-dimensional doublet flow described in Section 4.4.7, a doublet in three-dimensional flow can be defined by combining two sources at (x, y, z) = (±l, 0, 0) with strength ∓λ and taking the limit l ! 0 while holding $\mu \equiv 2\lambda l$ = constant. μ is the strength of the 3D doublet. The potential and velocity components for this flow are,

$$\varphi = \frac{\mu}{4\pi}\frac{\cos\theta}{r^2} \tag{4.20}$$

$$u_r = -\frac{\mu}{2\pi}\frac{\cos\theta}{r^3} \tag{4.21}$$

$$u_\theta = -\frac{\mu}{4\pi}\frac{\sin\theta}{r^3} \tag{4.22}$$

$$u_\phi = 0 \tag{4.23}$$

4.2.4 Nonlifting flow over a sphere

By combining a freestream (in the x-direction) with a doublet, the potential flow over a sphere can be determined. First, we begin by determining the relationship between the doublet strength (μ), the freestream velocity (V_∞), and the radius of the sphere (R). The velocity components for this flow are,

$$u_r = V_\infty\cos\theta - \frac{\mu}{2\pi}\frac{\cos\theta}{r^3} \tag{4.24}$$

$$u_\theta = -V_\infty\sin\theta - \frac{\mu}{4\pi}\frac{\sin\theta}{r^3} \tag{4.25}$$

$$u_\phi = 0 \tag{4.26}$$

On the surface of the sphere, flow tangency requires $u_r(R, \theta) = 0$. Evaluating u_r at r = R and enforcing $u_r = 0$ gives the doublet strength in terms of V_∞ and R,

$$u_r(R,\theta) = V_\infty\cos\theta - \frac{\mu\cos\theta}{2\pi R^3} = 0 \Rightarrow \mu = 2\pi R^3 V_\infty \tag{4.27}$$

Thus, the velocity components for the flow around a sphere of radius R in a freestream of velocity V_∞ are,

$$u_r = V_\infty\cos\theta\left(1 - \frac{R^3}{r^3}\right) \tag{4.28}$$

$$u_\theta = -V_\infty\sin\theta\left(1 + \frac{1}{2}\frac{R^3}{r^3}\right) \tag{4.29}$$

$$u_\phi = 0 \tag{4.30}$$

On the surface of the sphere where r = R, the velocity components and velocity magnitude are,

$$u_r = 0 \tag{4.31}$$

$$u_\theta = -\frac{3}{2}V_\infty\sin\theta \tag{4.32}$$

$$u_\phi = 0 \tag{4.33}$$

$$V = \frac{3}{2}V_\infty|\sin\theta| \tag{4.34}$$

The pressure on the surface can then be determined using Bernoulli's equation,

$$p(R,\theta) = p_\infty + \frac{1}{2}\rho V_\infty^2 - \frac{1}{2}\rho V^2 \tag{4.35}$$

$$= p_\infty + \frac{1}{2}\rho V_\infty^2 \left(1 - \frac{9}{4}\sin^2\theta\right) \tag{4.36}$$

The corresponding pressure coefficient on the surface is,

$$C_p(R,\theta) = \frac{p(R,\theta) - p_\infty}{\frac{1}{2}\rho V_\infty^2} = 1 - \frac{9}{4}\sin^2\theta \tag{4.37}$$

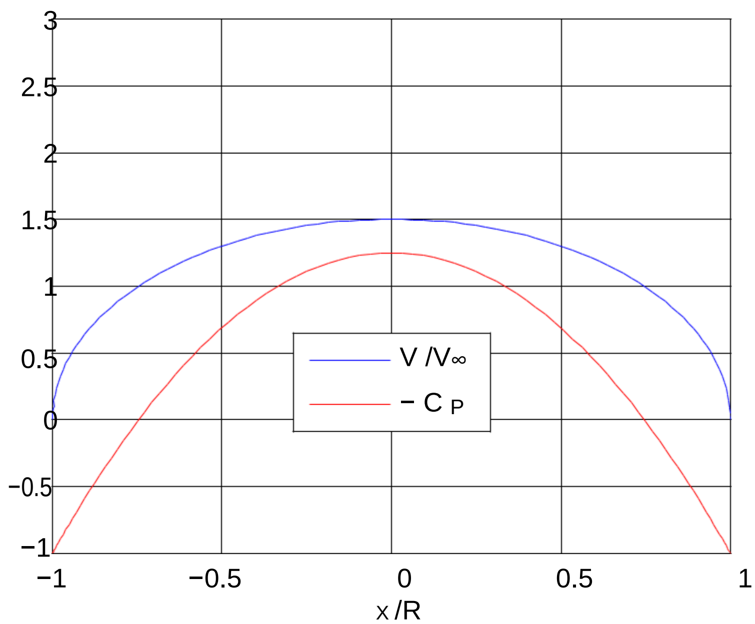

Figure 4.2: Surface V/V_∞ and C_p on a nonlifting sphere.

A plot of the surface velocity and pressure are shown in Figure 4.2. The velocity begins and ends at stagnation points and reaches a maximum speed which is $\frac{3}{2}V_\infty$ at the apex of the sphere. The C_p has the corresponding behavior with $C_p = 1$ at the high pressure stagnation points and $C_p = -\frac{5}{4}$ at the low pressure apex. Recall that the flow around the cylinder achieves a faster velocity of $2V_\infty$ at its apex. This behavior in which the perturbations from the freestream are larger in two-dimensional flows than in three-dimensional flows is common and is often referred to as **three-dimensional relief**. One way to understand this is to consider that the two-dimensional cylinder flow is equivalent to a cylinder with infinite span in the three-dimensional flow. Thus, it is not surprising that the cylinder will perturb the flow more significantly than the sphere which has a finite span.

Finally, analogous to the cylinder flow, the symmetry of the flow field from front-to-back implies that the drag will zero due to equal and opposite pressure force contributions. As well, symmetric from top-to-bottom implies the lift will be zero.

4.3 Introduction to Flow over Wings

4.3.1 Rectangular wings

The purpose of this entire section is to provide an introduction to the flow over wings. While we will not develop a model to estimate the aerodynamic performance of wings, we will introduce some key concepts in the behavior of the flow over wings and as well define the generic wing geometry.

To begin this section, we will start relatively simply with a rectangular wing having the same airfoil along the entire span. In this video, we introduce the key idea that the lift is distributed along the span of the wing such that even though the airfoil is identical at all spanwise locations (recall that the spanwise direction is along the y-axis), the lift (per unit span) and lift coefficient will generally vary with y.

- For a wing generating lift, the (generally) lower pressures on the upper surface and (generally) higher pressures on the lower surface cause an outward motion of the air towards the wing tips on the lower surface and inward motion towards the wing root on the upper surface. The result is a swirling, vortical motion which will remain downstream of the wing in the form of a vortical wake.
- At the wing tips, the upper and lower surface pressures equalize such that the lift generated by the airfoil at the wing tip is approximately zero, thus $L'(y = \pm b/2) = 0$. Over the rest of the wing, the lift will vary with the spanwise location $L' = L'(y)$.
- As the aspect ratio of the wing increases, the relieving effect of the pressure equalization at the wing tips will have less influence on the flow over the central portion of the wing. Thus, as AR increases, we expect the performance of the wing to approach two-dimensional behavior.
- The total lift generated by the wing is,

$$L = \int_{-b/2}^{b/2} L'(y)\,dy \tag{4.39}$$

- Since the lift generated by the airfoil sections varies with spanwise location, the sectional lift coefficient c_l is also a function of y,

$$c_l(y) = \frac{L'(y)}{q_\infty c} \tag{4.40}$$

- If we choose the reference area as the planform area, $S_{ref} = bc$ then the lift coefficient of the wing is equal to the average sectional lift coefficient, $C_L = \overline{c_l}$ where

$$\overline{c_l} \equiv \frac{1}{b}\int_{-b/2}^{b/2} c_l(y)\,dy \tag{4.41}$$

4.3.2 Trailing vortex images

The following is a small collection of images depicting wing tip vortices.

Figure 4.3: Wing tip vortex of an agricultural plane highlighted by a colored smoke rising from the ground. (NASA Langley Research Center. Photo ID: EL-1996-00130. Public domain image).

4.3.3 General unswept wings

Now we move away from rectangular wings with constant airfoil sections, to allow more general wing shapes. Specifically, we will consider wings with the following properties:

- The chord distribution can vary with y: $\Rightarrow c = c(y)$
- The quarter-chord location of the airfoils is unswept and level (no dihedral or anhedral). These assumptions can be removed, but in this first look at the flow over wings, we will not consider these effects.
- The wing can have **geometric twist** such that the angle of the local chordline can vary with y: $\Rightarrow \alpha_g = \alpha_g(y)$
- The airfoil sections can vary with span. This is often referred to as **aerodynamic twist**.

The constraint that the quarter-chord line is unswept requires the line to be perpendicular to the freestream direction (the x-axis). The constraint that the quarter-chord line is level requires

Figure 4.4: Wingtip vortices on a C-17 Globemaster III highlighted by smoke from flares. (U.S. Air Force. Author: Tech. Sergeant Russell E. Cooley IV. May 16, 2006. Public domain image).

that it has constant z. We will define our unswept, level wing geometry such that the quarter-chord line lies along the y-axis ($x = z = 0$). The planform view of one such unswept wing with varying chord is shown in Figure 4.6.

The geometric twist angle $\alpha_g(y)$ is defined relative to an arbitrarily chosen reference line. Com-monly, this reference line is chosen to be the axis of the fuselage. Thus, the overall angle of attack of an airfoil section is the sum of $\alpha + \alpha_g(y)$, where α is the angle from the freestream direction to the reference line, and $\alpha_g(y)$ is the angle from the reference line to the local chord line. In our analysis, we align the freestream with the x-axis. This is shown in Figure 4.7.

As described in the discussion of rectangular wings (see Section 4.3.1), the sectional lift $L'(y)$ and the sectional lift coefficient $c_l(y)$ are all functions of the spanwise location y. For rectangular wings, since the chord is constant, then $c_l(y)$ and $L'(y)$ have the same variation with y except for the constant scale factor of $q_\infty c$. For a wing with varying chord, this is no longer true and $c_l(y)$ will have a different dependence on y than $L'(y)$. Both the behavior of $L'(y)$ and $c_l(y)$ play an important role in the design of wings. $L'(y)$ is important in determining the bending moments which the wing structure must be designed for. $c_l(y)$ is important in determining the stall behavior of the wing. In the following video, we discuss both of these points.

Figure 4.5: Vortex caused by flap illustrating the creation of vortices in locations where lift distribution changes rapidly. (November 28, 2006. Author: Miguel Andrade. Public domain image).

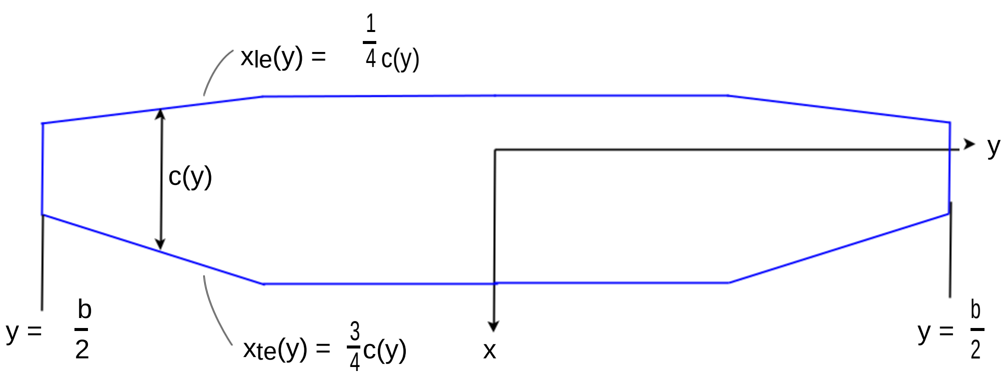

Figure 4.6: Planform view of wing with varying chord and unswept quarter-chord along y-axis

- The bending moment at the root ($y = 0$) of a wing is given by

$$M_{bend} = \int_0^{b/2} yL'(y)dy \tag{4.42}$$

- A common non-dimensional measure used to report the lift distribution $L'(y)$ is

$$\frac{L'(y)}{q_\infty c_{ref}} = \frac{c_l(y)c(y)}{c_{ref}} \tag{11.43}$$

where c_{ref} is a reference length (for example, the root chord, the average chord, and so on).

- Since we are using a potential flow model, the model cannot predict stall which is a viscous phenomenon. However, we can use the sectional lift coefficient as an indication of where on the wing stall is more likely. Specifically, regions on a wing where the sectional lift coefficient $c_l(y)$ is high are more likely to stall (assuming the airfoil sections have similar maximum c_l).

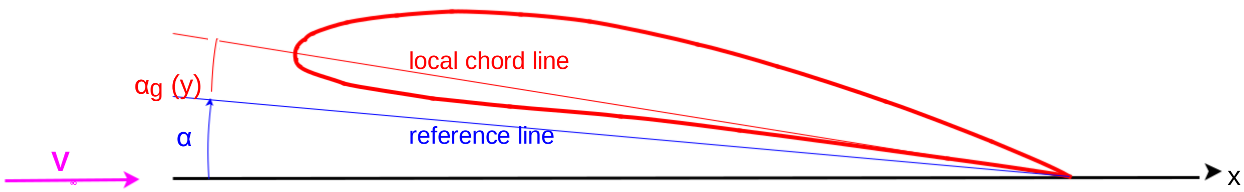

Figure 4.7: Definition of geometric angle of attack $\alpha_g(y)$ for an airfoil section of a wing and the freestream angle of attack α. Both angles are defined relative to a chosen reference line orientation.

If we have estimates for the $c_{l_{max}}(y)$, then we can compare the $c_l(y)$ to $c_{l_{max}}(y)$ to determine where stall is likely.

- When the reference area used in the calculation of C_L is chosen as the planform area of the wing, C_L is equal to the planform-area-weighted average of the sectional lift coefficients $c_l(y)$. As a result, C_L must lie in the range of the $c_l(y)$ on the wing (but will generally not be equal to $\bar{c_l}$ defined in Equation 4.41).

4.3.4 Impact of geometric twist on sectional lift coefficient

In this problem, we will consider the impact of geometric twist on the $c_l(y)$ distribution. A wing with **geometric washin** has a geometric angle of attack that is larger at the wing tip ($y = \pm b/2$) than at the wing root ($y = 0$). A wing with **geometric washout** has a geometric angle of attack that is larger at the wing root ($y = 0$) than at the wing tip ($y = \pm b/2$).

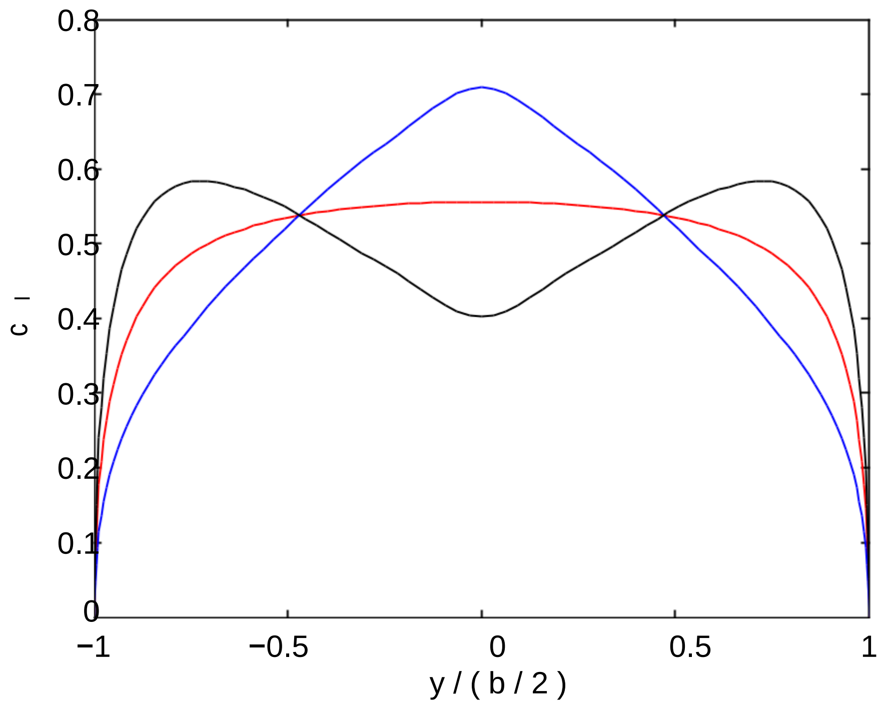

The sectional lift coefficient distribution, $c_l(y)$ is shown in the figure for three AR = 10 wings producing $C_L = 0.5$. The wings are identical except for the geometric twist. In particular, the wings have a rectangular planform ($c(y)$ = constant), and the airfoil shape does not vary with y (no aerodynamic twist). The three twist distributions are:

- No geometric twist ($\alpha_g(y) = 0$)
- Geometric washout varying linearly with y from $\alpha_g(0) = 5^\circ$ to $\alpha_g(\pm b/2) = 0^\circ$.
- Geometric washin varying linearly with y from $\alpha_g(0) = 0^\circ$ to $\alpha_g(\pm b/2) = 5^\circ$.

4.4 Lifting Line Models of Unswept Wings

4.4.1 Vortex filaments

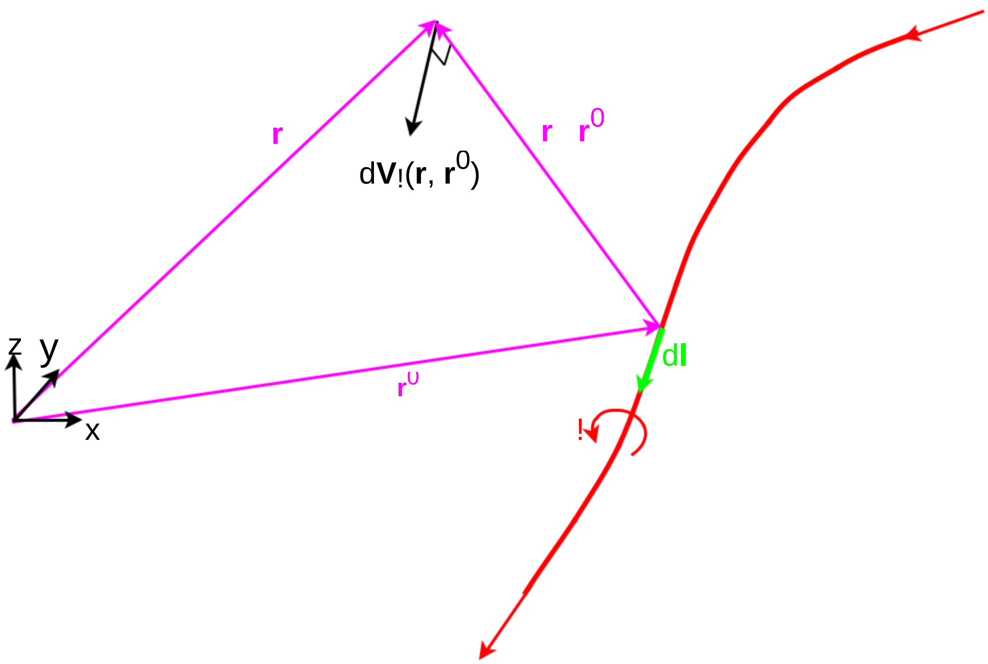

Figure 4.8: Vortex filament with strength Γ inducing a velocity d**V** (**r**, **r**ʹ).

The three-dimensional version of a point vortex is a vortex filament. As shown in Figure 4.8, a vortex filament has a strength Γ and the infinitesimal velocity induced by a length d**l** of the filament is given by,

$$d\mathbf{V}(\mathbf{r}, \mathbf{r}') = \frac{\Gamma}{4\pi} \frac{d\mathbf{l} \times (\mathbf{r} - \mathbf{r}')}{|\mathbf{r} - \mathbf{r}'|^3} \tag{4.44}$$

By applying Stokes theorem on a surface surrounding a filament, it can be shown that the strength of the filament can never change. In other words, Γ is a constant along the entire filament. Further, this implies that a filament cannot simply end in the fluid, since this is equivalent to the strength Γ changing to zero. Thus, a vortex filament must be infinitely long, or it must form a closed circuit. These results are known as Helmholtz vortex theorems.

The velocity induced by the entire filament can be found by integrating along the length of the filament,

$$\mathbf{V}(\mathbf{r}) = \frac{\Gamma}{4\pi} \int_{\text{filament}} \frac{d\mathbf{l} \times (\mathbf{r} - \mathbf{r}')}{|\mathbf{r} - \mathbf{r}'|^3} \tag{4.45}$$

This integral is equivalent to the calculation of a magnetic field induced by an electric current using the Biot-Savart Law. In our aerodynamic case, a velocity field is induced by the circulation.

As a simple example, in the following video we consider a straight (infinitely long) vortex filament lying along the y-axis. We show that the velocity induced by this vortex filament is equivalent to the point vortex in two-dimensional flow. Thus, we can interpret the two-dimensional point vortex in the (x, z) plane as the flow induced by an infinitely long, straight vortex filament along the y-direction.

4.4.2 Lifting line model

In principle, the potential flow around a three-dimensional lifting body can be modeled by placing vortex filaments (on panels) over the entire body surface similar to the vortex panel method developed for airfoils. We will simplify this approach considerably to arrive at a model that demonstrates the fundamental issues that arise in three-dimensional lifting flows while being significantly easier to analyze theoretically (without the aid of a computer). This simpler model is known as lifting line and was originally developed by Ludwig Prandtl around the time of World War I.

An assumption inherent in the lifting line model is that the wing is high aspect ratio. Lifting line takes this assumption to its extreme and views the wing simply as a line (imagine looking at a high aspect ratio wing from far overhead such that it effectively looks like a line). Then, the flow due to the airfoil sections is represented by a vortex placed along this line. This vortex is often referred to as the **bound vortex**. However, the circulation of the bound vortex must vary with y since the sectional lift varies $L'(y)$. This implies that a single vortex filament cannot be used to represent the bound vortex since a vortex filament must have a constant circulation.

To model the varying circulation $\Gamma(y)$ of the bound vortex, the lifting line approach combines many vortex filaments with a shape known as a horseshoe vortex as shown in Figure 4.9. While the figure only shows four horseshoe vortices for clarity, we will in fact use infinitely many vortices. The horseshoe vortex starts far downstream (at x ! ∞) and runs parallel to the x-axis until it reaches the y axis. Then, it turns to the right along the y-axis and, after an infinitesimal distance dy, turns back into the x direction returning infinitely far downstream. The strength of the horeshoe vortex centered at y is $\Gamma(y)$. By combining (infinitely) many of these horseshoe vortices, an arbitrary circulation (and therefore an arbitrary section lift) distribution can be represented.

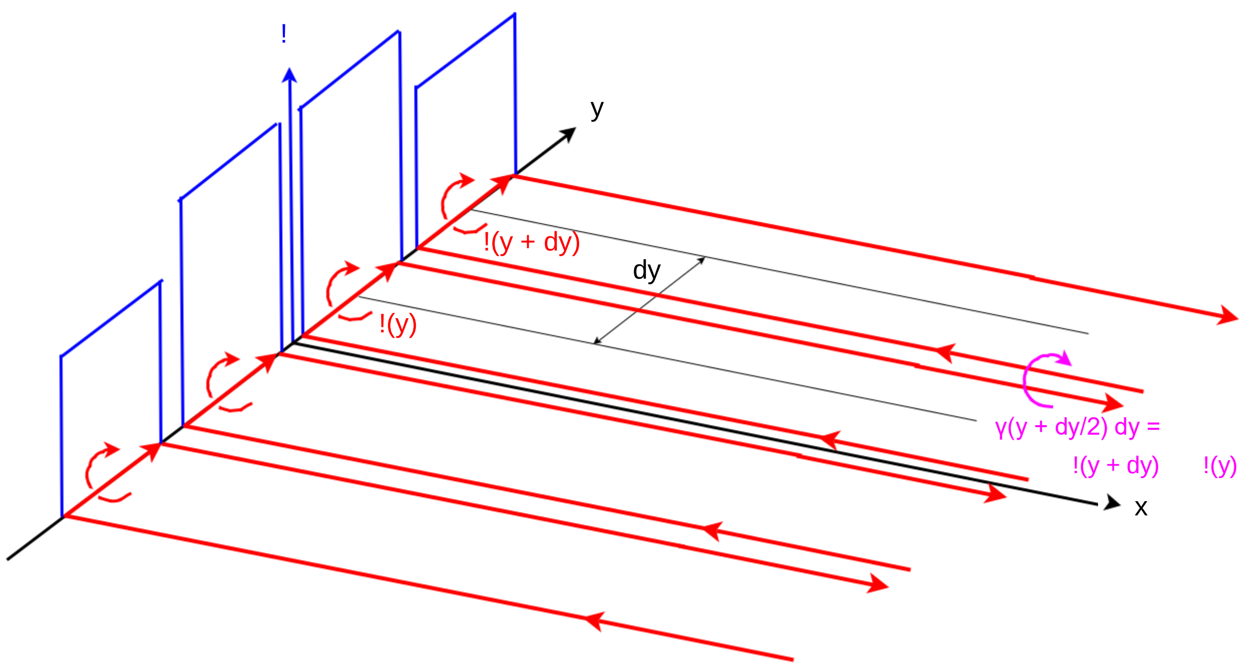

Figure 4.9: Construction of a lifting line from horseshoe vortices

The two neighboring horseshoe vortices at y and $y + dy$ combine so that the net strength of the filament at $y + dy/2$, which we label $\gamma(y + dy/2)\,dy$, is,

$$\gamma(y + dy/2)\,dy = \Gamma(y + dy) - \Gamma(y) \tag{4.46}$$

Then, taking the limit as dy ! 0,

$$\lim_{dy\to 0} \gamma(y + dy/2)dy = \lim_{dy\to 0} \Gamma(y + dy) - \Gamma(y) \tag{4.47}$$

$$\gamma(y)dy = \frac{d\Gamma}{dy}dy \tag{4.48}$$

In the limit of dy ! 0, the lifting line model as shown in Figure 4.10 is a vortex sheet with a bound vortex of strength Γ(y) and the trailing sheet composed of semi-infinite vortex filaments (from x = 0 to x ! ∞) with strength per length γ(y) = dΓ/dy.

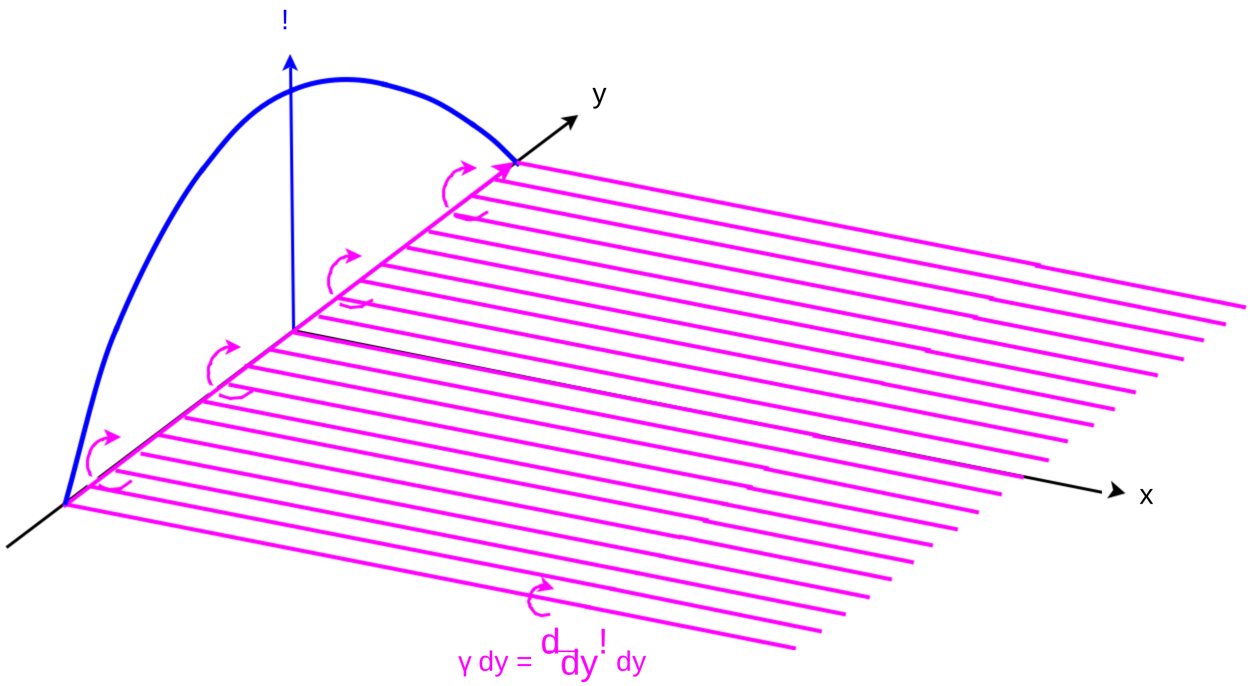

Figure 4.10: Lifting line with trailing vortices of strength $\gamma\, dy = \frac{d}{dy} dy$

The following video is another of the classic videos in the NSF Fluid Mechanics Series. While the entire video is interesting, in particular please watch the following portions of the video:

- From 2:59 through 6:42: the discussion of the generation of circulation as an airfoil accelerates from rest.
- From 7:50 though 11:20: the discussion of the vortex system of a wing

4.4.3 Trefftz plane flow of lifting line model

Although this lifting line model appears somewhat contrived, in fact the actual flow over a high aspect ratio wing is quite similar to this model. In particular, a wing does have a wake in which the vorticity is concentrated. However, the actual wake is not planar, but instead rolls up into concentrated trailing vortices (see the images in Section 4.3.2). That is, the vorticity in the actual flow convects into concentrated trailing vortices while the vorticity in the lifting line model is in the planar sheet. This difference in the wake structure leads to an error between the lifting line and the actual flow, however, this error has a relatively small impact on the estimation of the lift-related forces on a high-aspect ratio wing.

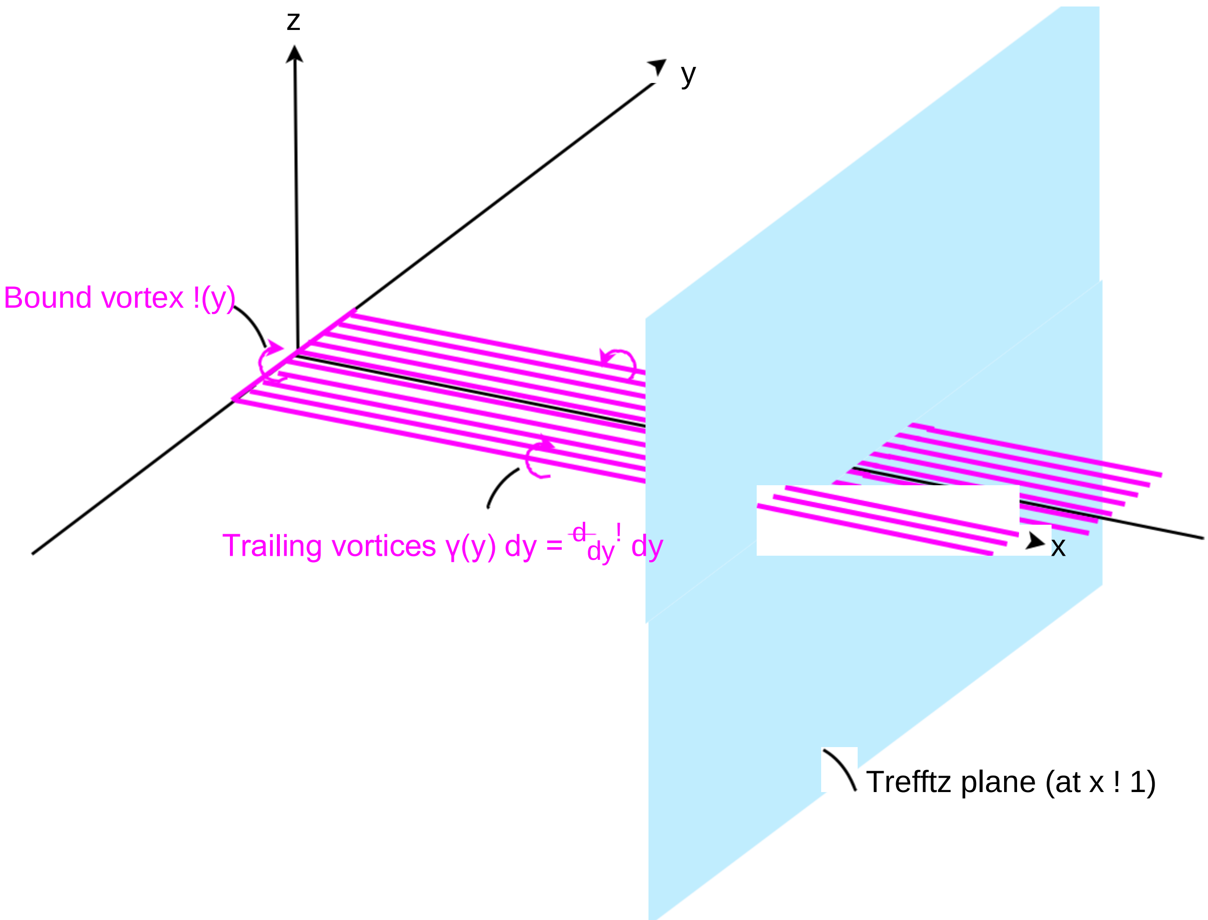

Figure 4.11: Trefftz plane with lifting line model

Some additional insight can be gained by considering the velocity distribution in the plane far downstream of the wing as shown in Figure 4.11. This plane is known as the Trefftz plane. Recall that we have already seen how the lift and drag can be related to the flow in the Trefftz. We will return to calculating the lift and drag for the lifting line model shortly, for now, we look at the velocity in the Trefftz plane.

Since the Trefftz plane is infinitely far from the y axis, the lifting line's bound vortex has no contribution to the velocity. Further, since the vortex filaments in the trailing sheet are all parallel to the x-axis, the x-velocity in the Trefftz plane is not perturbed at this location. Thus, in the Trefftz's plane, $u = V_\infty$.

To calculate the y and z components of the velocity, we can apply the Biot-Savart law over the entire wake. In the Trefftz plane, the vortex filaments extend infinitely far upstream and downstream, so the velocity induced by each vortex filament is equivalent to the two-dimensional velocity induced by a point vortex with strength $\gamma(y)\,dy$ (see Figure 4.12). Thus, the velocity induced by the lifting line in the Trefftz plane can be found by integrating the contributions from the entire sheet of filaments,

$$\mathbf{V}_{w,\text{line}}(y, z) = -\int_{-b/2}^{b/2} \frac{\gamma(y')\,dy'}{2\pi r'}\,\hat{\mathbf{e}}_{\theta'} \tag{4.49}$$

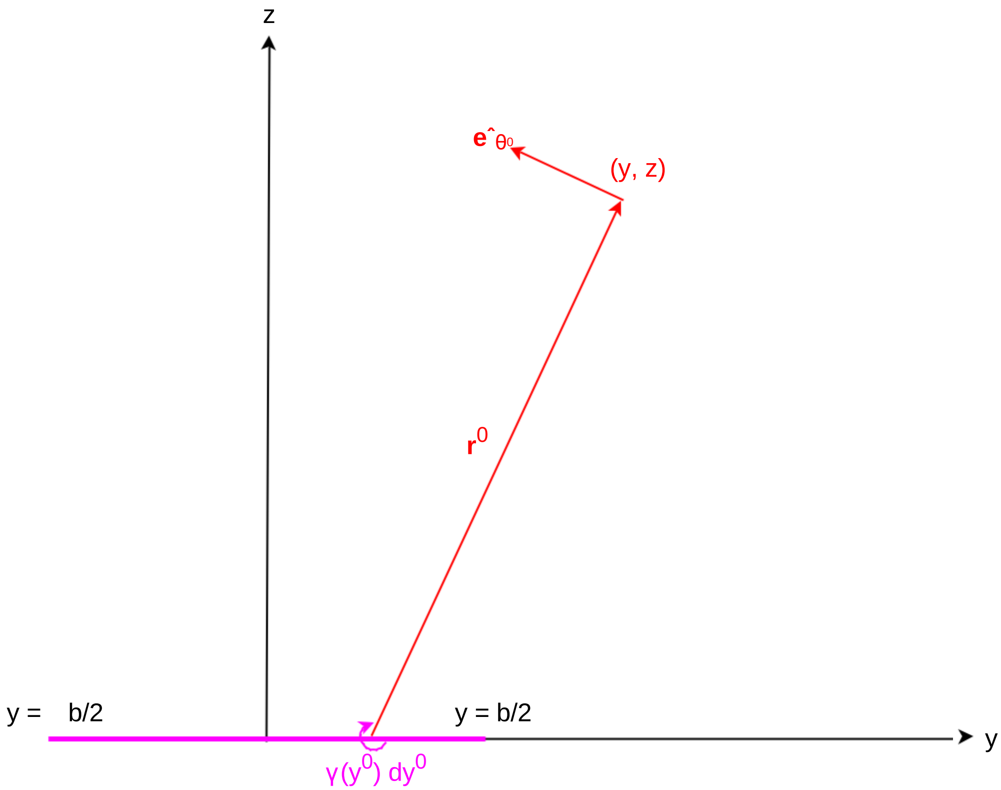

Figure 4.12: Trefftz plane showing trailing vortex sheet from lifting line model and geometry for velocity calculation

We will now consider the Trefftz plane velocity distribution for a couple of representive circula-tion distributions. We begin with perhaps the most important circulation distribution,

$$\Gamma = \Gamma_0 \sqrt{1 - \left(\frac{y}{b/2}\right)^2} \tag{4.50}$$

where Γ_0 is a parameter that is equal to the circulation at the root ($y = 0$). This is known as the **elliptic distribution** (because the formula is that of an ellipse) and is shown Figure 4.13.

Recall that the strength of the vortex filaments is given by $\gamma(y)\, dy = d\Gamma/dy\, dy$ and thus the strongest filaments will be where the most rapid variation of Γ is. This occurs at the wing tips for the elliptic lift distribution, and therefore we expect the vortical flow to be most evident at the tips. The velocity vectors in the Trefftz plane for the elliptic distribution are shown in Figure 4.14. The presence of the wing tip vortices can be clearly seen in the velocity vectors.

Next, we consider what the circulation and Trefftz plane flow might look like with a trailing-edge flap deflected. Since the trailing edge flap will increase the local lift, we will increase Γ in the region of the flap. Specifically, as shown in Figure 4.15, we add a rapid increase in the circulation from $0.25 < |y|/(b/2) < 0.5$ to represent what the circulation might be with a trailing edge flap deflected in this region (note: we will discuss how to specifically calculate the impact of geometry including flaps on Γ. So, for now, this is just representative of what Γ might be).

The velocity vectors in the Trefftz plane are shown in Figure 4.16 and zoomed in to the region of the flap in Figure 4.17. At the larger view in Figures 4.14 and 4.16, it is difficult to see much difference. However, the zoomed figure clearly shows the presence of two smaller vortices at approximately $y/(b/2) = 0.25$ and $y/(b/2) = 0.5$. Thus we again observe vortical flow where the sectional lift, and therefore the circulation, vary rapidly with y. You might also refer back to

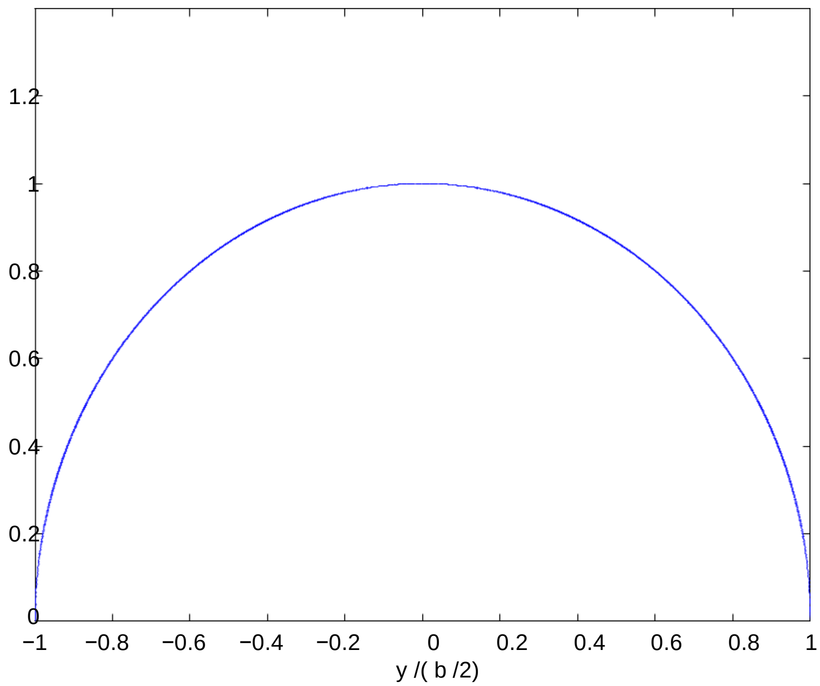

Figure 4.13: Elliptic circulation distribution

the photograph of a flap vortex in Figure 4.5, which shows physical evidence of the existence of a vortex generated at the edges of the flap.

4.4.4 Trefftz plane results for lift and drag

In this section, we will relate the lift and drag to the circulation distribution using the Trefftz plane. Specifically, recall the derivation from the problem in Section 3.6.1 relating the farfield flow behavior to the lift. Note that this result was derived with the y-axis being the lift direction. However, the coordinate system we have been using in our discussion of 3D flows uses the z-axis as the lift direction. Thus, switching to the z-axis being the lift direction, the result for the lift is,

$$L = -\iint_{S_W} \rho_W w_W u_W \, dS. \tag{4.51}$$

As we are considering incompressible flow, $\rho_W = \rho$. Also, for the lifting line model, $u_W = V_\infty$ giving,

$$L = -\rho V_\infty \iint_{S_W} w_W \, dS. \tag{4.52}$$

From this point, the derivation gets a little mathematically intense, but we can eventually find the unsurprising result that for the lifting line model,

$$L=\rho V_\infty \int_{-b/2}^{b/2} \Gamma(y) dy \tag{4.53}$$

For the drag, which showed that for an inviscid,

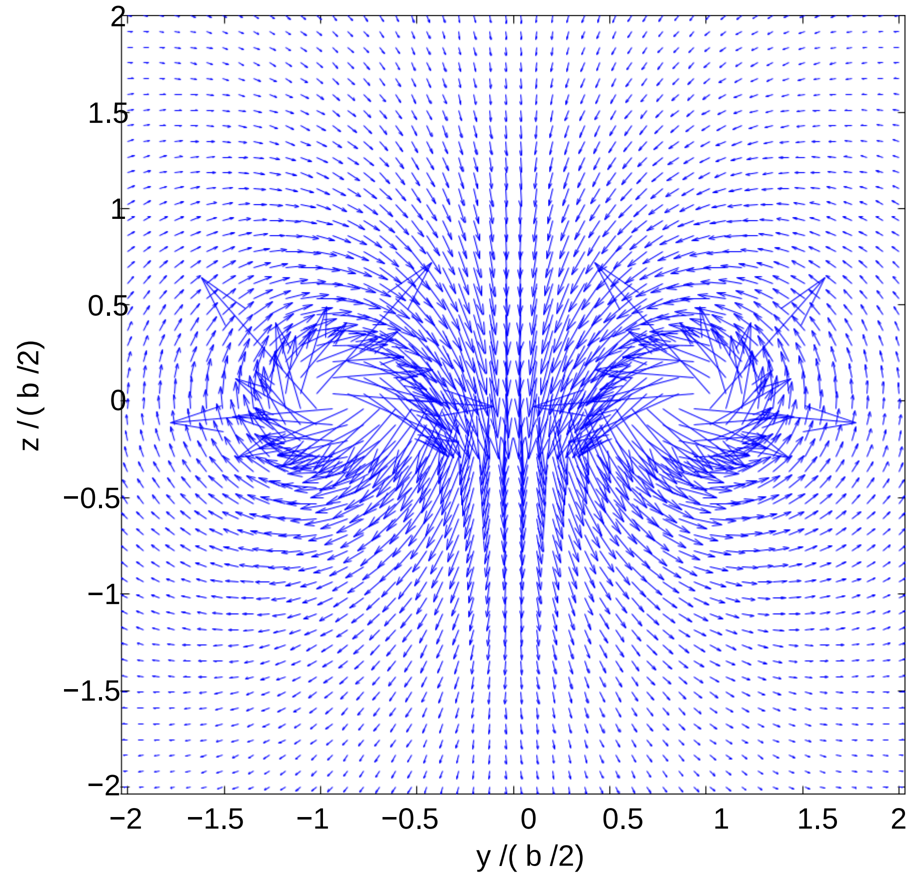

Figure 4.14: Velocity vectors in the Trefftz plane for the elliptic circulation distribution

incompressible flow, the drag is related to the Trefftz plane flow by,

$$D_i = \frac{1}{2}\rho \int_{S_w} \left(\tilde{v}_w^2 + \tilde{w}_w^2 - \tilde{u}_w^2\right) dS \tag{4.54}$$

where D_i is used to indicate that this is the induced drag (the only drag present in an incompressible potential flow). Recall that for the lifting line model $u_w = V_\infty$ thus $\tilde{u}_w = u_w - V_\infty = 0$ in the wake. Further, since the freestream is in the x direction, $\tilde{v} = v$ and $\tilde{w} = w$ giving,

$$D_i = \frac{1}{2}\rho \int_{S_w} \left(v_w^2 + w_w^2\right) dS \tag{4.55}$$

Again, the mathematical derivation gets a bit challenging, but it is possible to then express this result in terms of the lifting line circulation,

$$D_i = -\frac{1}{2}\rho \int_{-b/2}^{b/2} w_w(y, 0)\Gamma(y)dy \tag{4.56}$$

Applying Equation (11.49) gives,

$$w_w(y, 0) = \int_{-b/2}^{b/2} \frac{\gamma(y')dy'}{2\pi(y' - y)} \tag{4.57}$$

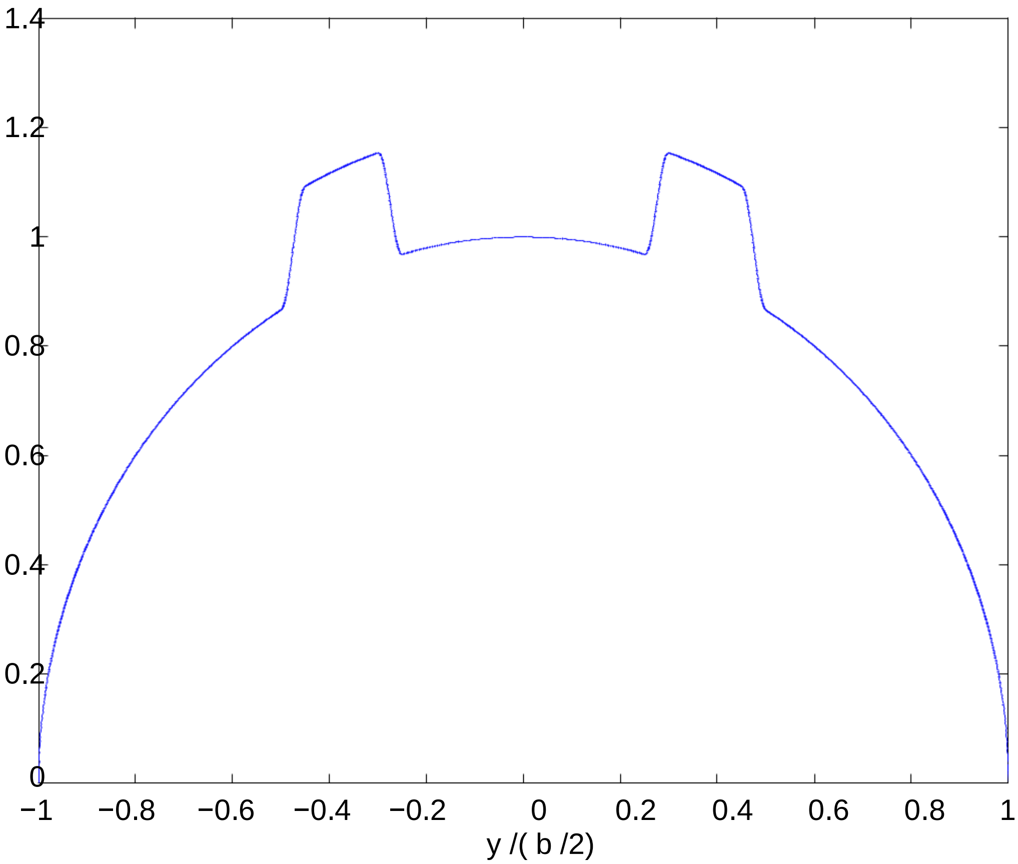

Figure 4.15: Elliptic circulation distribution with a flap deflection from 0.25 < **|y|**/(b/2) < 0.5

Before we move on, let’s take a short break to notice that the induced drag result in Equa-tion (4.55) is the integral of the kinetic energy due to the velocity components that are perpen-dicular to the freestream (often referred to as the **crossflow**). Upstream of the wing, the freestream is uniform. However, downstream of the wing the vortical wake induces velocity in the crossflow direction. The result is a change in the kinetic energy of the flow. This change in kinetic energy of the flow as the airplane moves must be a result of work being done on the flow. And, this work is provided by the induced drag. In other words, while the air is acting on the wing with a force to oppose its motion, the wing acts on the air with an equal and opposite force. Since it is opposite the drag, this means the force on the air is in the direction of motion of the wing. Thus, the reaction force to the drag does work on the air. We can state this as a rate, which is to say the rate of work

done on the air is $D_i V_\infty$ and the rate of increase of kinetic energy in the air is $V_\infty \int \frac{1}{2}\rho(\tilde{v}^2 + \tilde{w}^2)dS$.

Equating these two expressions gives our earlier result,

$$D_i = \int_{S_W} \frac{1}{2}\rho(\tilde{v}^2 + \tilde{w}^2)dS \tag{4.58}$$

4.4.5 Downwash and induced angle of attack

The Trefftz plane results for lift and induced drag in Equations (4.53) and (4.56) can be intrepreted in terms of the behavior of the sectional flow on the wing.

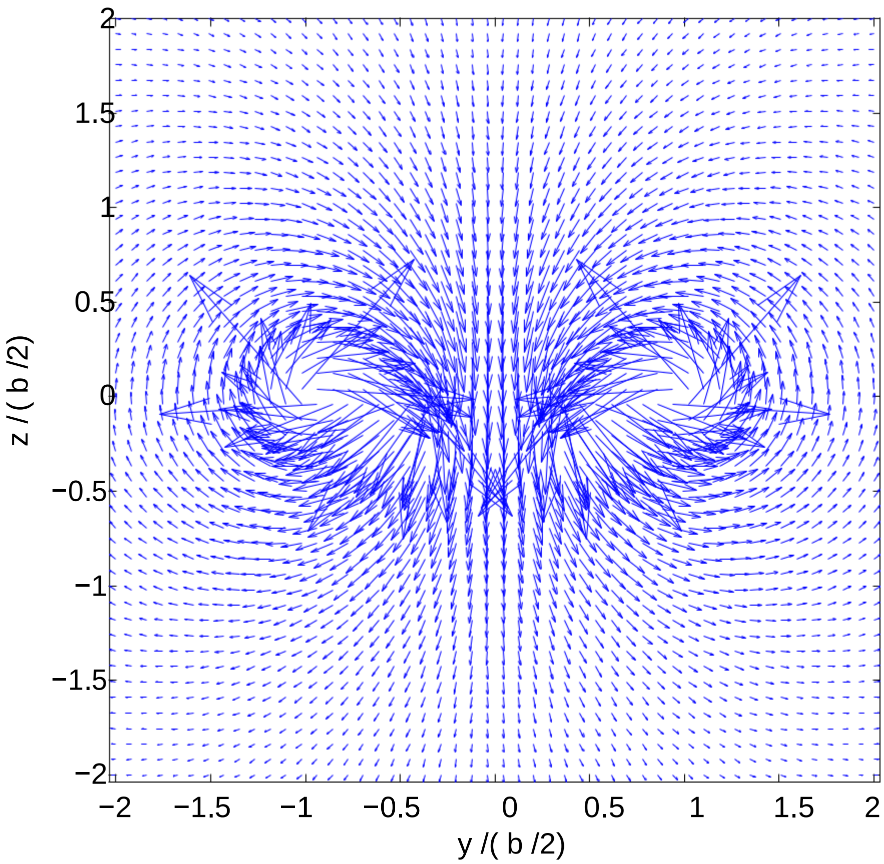

Figure 4.16: Velocity vectors in the Trefftz plane for an elliptic circulation distribution with a trailing edge flap deflection from $0.25 < |y|/(b/2) < 0.5$.

We begin this intrepretation by comparing the velocity induced by the trailing wake at the bound vortex at $(x, y, z) = (0, y, 0)$ and at the corresponding location in the Trefftz plane at $(\infty, y, 0)$. At the bound vortex, the vortex filaments are semi-infinite (extending only downstream to $x \to \infty$). From a position on the Trefftz plane, the filaments extend infinitely in both directions (upstream to the bound vortex which is infinitely far away, and downstream they never end). Thus, the velocity induced by the wake at the bound vortex is exactly half the velocity induced at the cor-responding location in the Trefftz plane. In particular, for the z-velocity component which enters Equation (4.56), this implies

$$w(0, y, 0) = \frac{1}{2} w(\infty, y, 0) \tag{4.59}$$

Thus, the induced drag for the lifting-line model can be equivalently written as,

$$D_i = -\rho \int_{-b/2}^{b/2} w_i(y)\Gamma(y)dy \tag{4.60}$$

where $w_i(y)$ is the velocity induced by the wake along the bound vortex,

$$w_i(y) \equiv w(0, y, 0) \tag{4.61}$$

Over most of the bound vortex, $w_i(y)$ is negative and as a result $-w_i(y)$ is frequently is referred to as the **downwash**. However, $w_i(y)$ can be positive in particular in regions of the wing where the

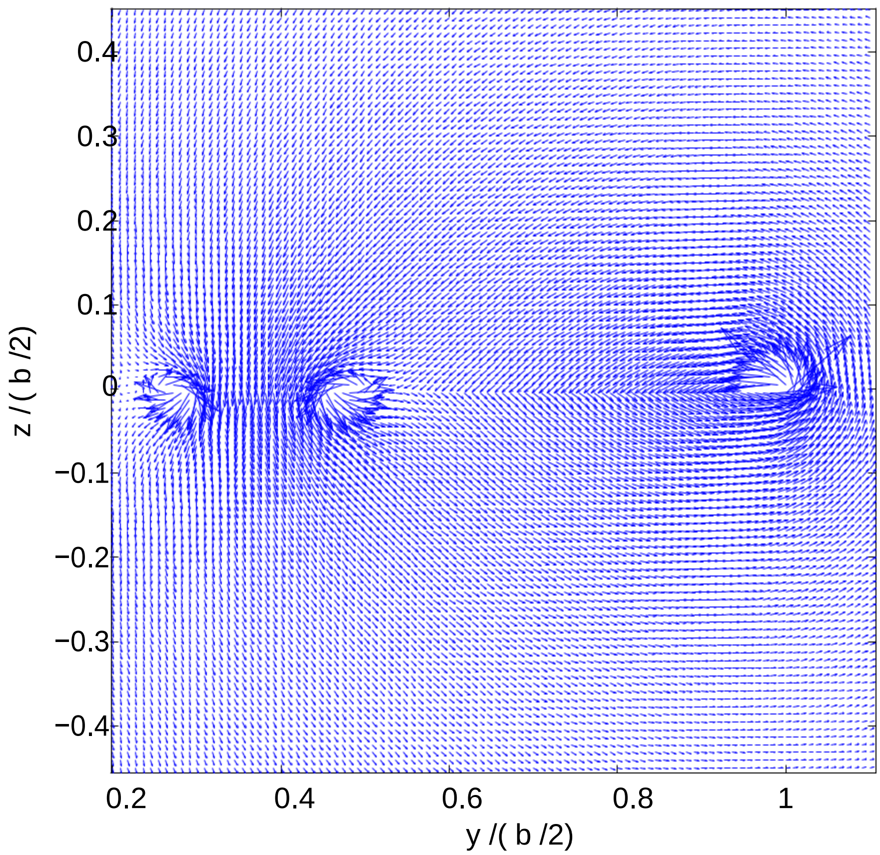

Figure 4.17: Velocity vectors in the Trefftz plane for an elliptic circulation distribution with a trailing edge flap deflection from $0.25 < |y|/(b/2) < 0.5$. This image is zoomed in to highlight the effect of the flap deflection on the Trefftz plane flow.

circulation is increasing rapidly (for example, at the edges of a flap $w_i(y)$ can be upward as can be seen in the Trefftz plane velocity shown in Figure 4.17).

The downwash can be thought of as changing the angle of attack at the bound vortex. As shown in Figure 4.18, the angle of attack of the local section relative to the freestream velocity is $\alpha + \alpha_g(y)$. However, the presence of the downwash creates an effective velocity $\mathbf{V}_{eff}$ which is at a smaller **effective angle of attack**, α_{eff} , where

$$\alpha_{eff}(y) = \alpha + \alpha_g(y) - \alpha_i(y) \tag{4.62}$$

and the **induced angle of attack** is,

$$\alpha_i = \tan^{-1}\left(-\frac{w_i}{V_\infty}\right) \approx -\frac{w_i}{V_\infty} \tag{4.63}$$

where the final result assumes $|w_i|/V_\infty \ll 1$.

Next, substituting for w_i into Equation (11.60),

$$D_i = \rho V_\infty \int_{-b/2}^{b/2} \alpha_i(y)\Gamma(y)dy \tag{4.64}$$

From the Kutta-Joukowski Theorem, we can intrepret $\rho V_\infty \Gamma(y)$ as the sectional lift produced at y. But, since the effective freestream direction is $\mathbf{V}_{eff}(y)$, then the lift produced by the potential flow

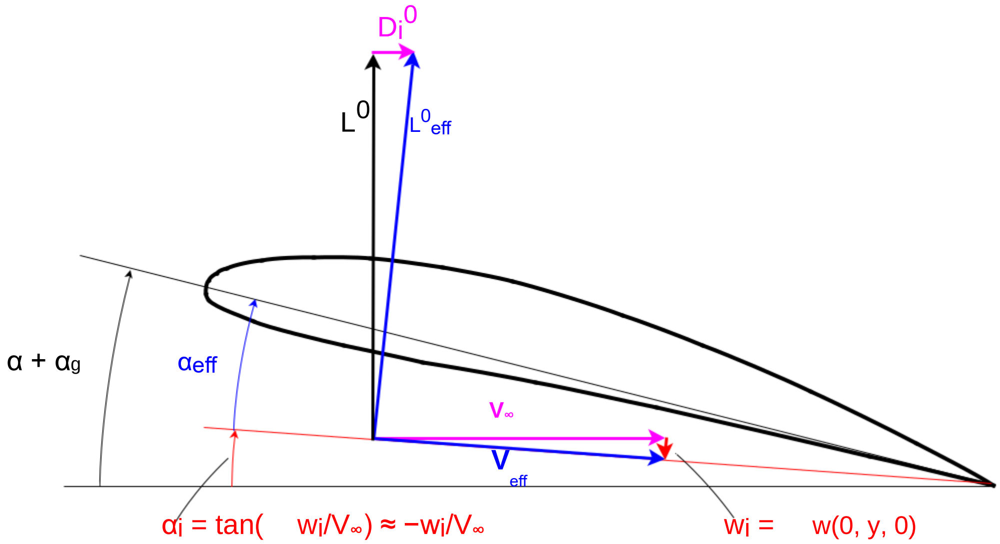

Figure 4.18: Downwash caused by the vortex wake creates an effective velocity $\mathbf{V}_{eff}$ which is different than the freestream $\mathbf{V}_\infty$. The lift L'_{eff} generated by the airfoil is perpendicular to $\mathbf{V}_{eff}$ which tilts it slightly into the drag direction producing a sectional contribution to the induced drag D'_i.

around this section would act perpendicular to this effective direction. So, we define this as the effective lift,

$$L'_{eff}(y) = \rho V_\infty \Gamma(y) \tag{4.65}$$

The final step is to resolve this effective lift into the lift and drag directions relative to the actual freestream velocity $\mathbf{V}_\infty$. The contribution to the sectional lift (defined relative to the actual freestream) is,

$$L' = L'_{eff} \cos \alpha_i \approx L'_{eff} \tag{4.66}$$

and the contribution to the sectional induced drag (in the actual freestream direction) is,

$$D'_i = L'_{eff} \sin \alpha_i \approx L'_{eff} \alpha_i \tag{4.67}$$

Comparing this result to the integrand in Equation (4.60) shows they are completely consistent. In otherwords, we may interpret the production of induced drag to be the result of downwash at the bound vortex, created by the trailing vortical wake, that tilts the sectional lift into the streamwise direction.

4.4.6 Elliptic lift distribution results

In this section, we consider the specific case of the elliptic lift distribution as given in Equation (11.50). First, we calculate the total lift by integrating the sectional lift for an elliptic lift distribution,

$$L = \rho V_\infty \Gamma_0 \int_{-b/2}^{b/2} \sqrt{1 - \left(\frac{y}{b/2}\right)^2}\, dy \tag{4.68}$$

Then, we use the following variable transformation to bring this integral into a well-known form,

$$y = -\frac{b}{2} \cos \beta \tag{4.69}$$

where the spanwise direction varies between $0 \leq \beta \leq \pi$. Thus, the elliptic lift distribution in terms of β is,

$$\Gamma = \Gamma_0 \sqrt{1 - \left(\frac{y}{b/2}\right)^2} \tag{4.70}$$

$$= \Gamma_0 \sqrt{1 - \cos^2 \beta} \tag{4.71}$$

$$= \Gamma_0 \sin \beta \tag{4.72}$$

In other words, we are expressing the lift distribution as a function of the new variable β instead of y.

Then, differential changes in y are related to changes in β by,

$$dy = \frac{b}{2} \sin \beta \, d\beta \tag{4.73}$$

Substituting Equations (11.69) and (11.73) into the lift integral gives,

$$L = \frac{1}{2} \rho V_\infty b \Gamma_0 \int_0^\pi \sin^2 \beta \, d\beta \tag{4.74}$$

$$\Rightarrow L = \frac{\pi}{4} \rho V_\infty b \Gamma_0 \tag{4.75}$$

where the last step of this derivation uses $\int_0^\pi \sin^2 \beta \, d\beta = \pi/2$. The lift coefficient then is,

$$C_L = \frac{L}{q_\infty S_{ref}} = \frac{\pi}{2} \frac{\Gamma_0 b}{V_\infty S_{ref}} \tag{4.76}$$

The induced drag requires calculation of $w_i(y)$,

$$w_i(y) = \frac{1}{4\pi} \int_{-b/2}^{b/2} \frac{\gamma(y')dy'}{y' - y} \tag{4.77}$$

First determining $\gamma(y')dy'$,

$$\gamma \, dy' = \frac{d\Gamma}{dy'} dy' = \frac{d\Gamma}{d\beta'} d\beta' = \Gamma_0 \cos \beta' \, d\beta' \tag{4.78}$$

This gives,

$$w_i(\beta) = \frac{\Gamma_0}{2\pi b} \int_0^\pi \frac{\cos \beta' \, d\beta'}{\cos \beta - \cos \beta'} \tag{4.79}$$

The value of the integral can be shown to be,

$$\int_0^\pi \frac{\cos \beta' \, d\beta'}{\cos \beta' - \cos \beta} = \pi \tag{4.80}$$

$$\Rightarrow w_i(\beta) = -\frac{\Gamma_0}{2b} \tag{4.81}$$

In others words, the downwash for elliptic lift is constant (i.e. it does not depend on y).

The induced drag can now be determined using Equation (4.60),

$$D_i = -\rho \int_{-b/2}^{b/2} w_i(y)\Gamma(y)dy \tag{4.82}$$

$$\Rightarrow D_i = \frac{\pi}{8} \rho \Gamma_0^2 \tag{4.83}$$

The induced drag coefficient is,

$$C_{D_i} \equiv \frac{D_i}{q_\infty S_{ref}} = \frac{\pi \rho \Gamma_0^2}{8 q_\infty S_{ref}} \qquad (4.84)$$

This can be written in a convenient form in terms of the lift coefficient using Equation (4.76),

$$C_{D_i} = \frac{C_L^2}{\pi AR} \qquad (4.85)$$

Comparing this to the more general result given in Equation (4.53), we can see that the span efficiency for an elliptic lift distribution is $e = 1$. Though we have not yet derived the following result, it can be shown that the span efficiency for the lifting line model is at most one, i.e. $e \leq 1$. Thus, the elliptic lift distribution produces the lowest amount of induced drag for a given lift and aspect ratio. A very important corollary to this result is that by including three-dimensional effects, even potential flow models will have non-zero drag for bodies which generate lift. That is, drag is an unavoidable consequence of producing lift (even without including viscous effects or shock waves, both of which will further increase the drag).

4.4.9 General distribution of lift

In general, the lift on a wing will not have an elliptic distribution. Thus, we need a method for analyzing wings for a general lift distribution. To do this, we will utilize a Fourier series decomposition of the lift distribution. Specifically, in terms of β, we will now utilize a Fourier series representation of the circulation distribution,

$$\Gamma(\beta) = 2bV_\infty \sum_{n=1}^{\infty} B_n \sin n\beta \tag{4.86}$$

A few important points on this Fourier series choice are:

- As described in Section 4.3.1, the lift at the wing tips goes to zero, $L'(\pm b/2) = 0$. Since $L' = \rho V_\infty \Gamma$, then $\Gamma(\pm b/2) = 0$. In terms of β, this means $\Gamma(\beta = 0) = \Gamma(\beta = \pi) = 0$. The choice of a Fourier series using $\sin n\beta$ terms satisfies this requirement.
- The odd terms, B_1, B_3, B_5, . . ., are symmetric with respect to the wing root. The even terms, B_2, B_4, B_6, . . ., are asymmetric. Plots of $\sin n\beta$ are shown in Figure 4.19.

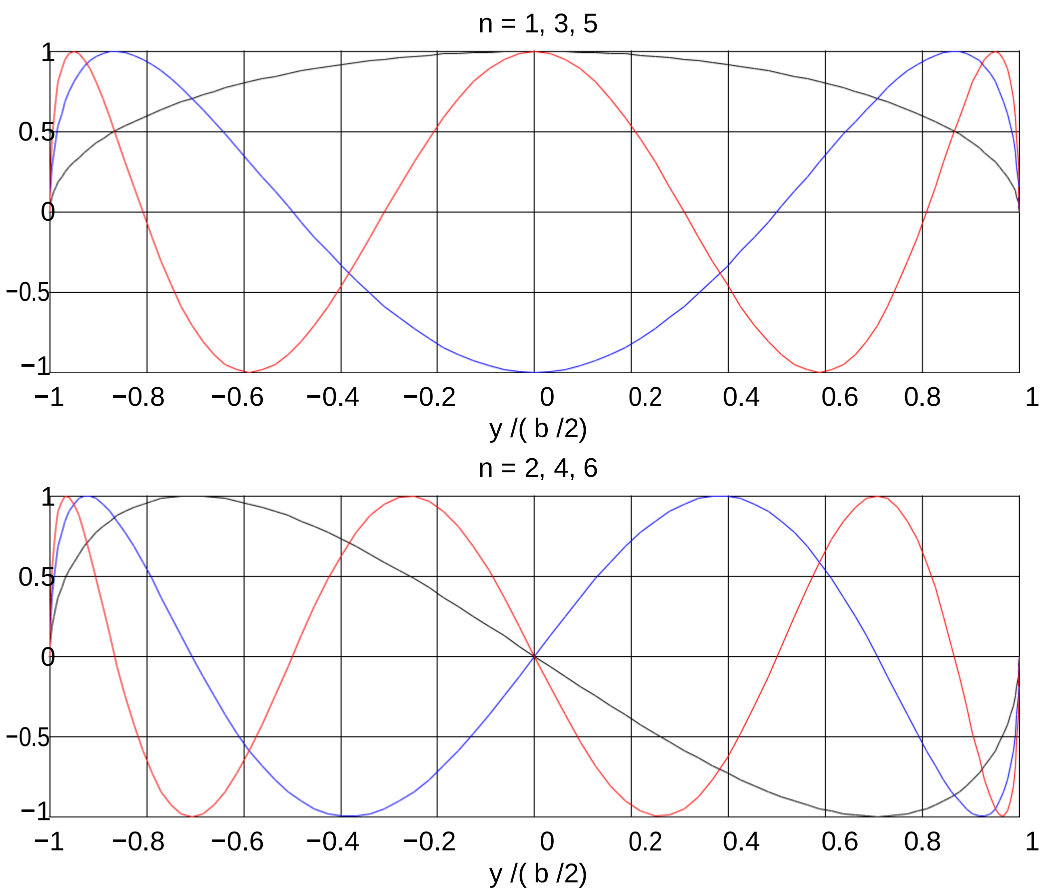

Figure 4.19: Plots of $\sin n\beta$ versus $y/(b/2) = -\cos\beta$.

- The $n = 1$ term ($\sin\beta$) corresponds to the elliptic lift distribution in Equation (4.50). Specifically,

$$\Gamma = \Gamma_0 \sqrt{1 - \left(\frac{y}{b/2}\right)^2} \tag{4.87}$$

$$= \Gamma_0 \sqrt{1 - \cos^2\beta} \tag{4.88}$$

$$= \Gamma_0 \sin\beta \tag{4.89}$$

- A Fourier series can be used to represent any (smooth) function. Thus, the use of a Fourier series to represent the circulation is not an assumption. Rather, it is just a re-statement of the problem where the unknowns are now the coefficients B_n.

4.4.10 Calculation of lift, induced drag, and span efficiency

Substituting the Fourier series into Equation (4.53),

$$L = \rho V_\infty \int_{-b/2}^{b/2} \Gamma(y)dy \tag{4.90}$$

$$= \rho V_\infty^2 b^2 \sum_{n=1}^{\infty} \int_0^{\pi} B_n \sin n\beta \sin\beta \, d\beta \tag{4.91}$$

$$\Rightarrow L = \frac{\pi}{2} \rho V_\infty^2 b^2 B_1 \tag{4.92}$$

where the last step of this derivation uses $\int_0^\pi \sin n\beta \sin\beta \, d\beta = 0$ for $n > 1$ and equals $\pi/2$ for $n = 1$. Thus, the only term in the Fourier series that contributes to the lift is for $n = 1$. The lift coefficient then is,

$$C_L = \frac{L}{q_\infty S_{ref}} = \pi AR B_1 \tag{4.93}$$

The induced drag requires calculation of $w_i(y)$,

$$w_i(y) = \frac{1}{4\pi} \int_{-b/2}^{b/2} \frac{\gamma(y')dy'}{y' - y} \tag{4.94}$$

First determining $\gamma(y')dy'$,

$$\gamma \, dy' = \frac{d\Gamma}{dy'} dy' = \frac{d\Gamma}{d\beta'} d\beta' = 2bV_\infty \left[\sum_{n=1}^{\infty} nB_n \cos n\beta'\right] d\beta' \tag{4.95}$$

This gives,

$$w_i(\beta) = \frac{V_\infty}{\pi} \sum_{n=1}^{\infty} nB_n \int_0^{\pi} \frac{\cos n\beta' \, d\beta'}{\cos\beta - \cos\beta'} \tag{4.96}$$

The value of the integral can be shown to be,

$$\int_0^{\pi} \frac{\cos n\beta' \, d\beta'}{\cos\beta' - \cos\beta} = \pi \frac{\sin n\beta}{\sin\beta} \tag{4.97}$$

$$\Rightarrow w_i(\beta) = -V_\infty \sum_{n=1}^{\infty} nB_n \frac{\sin n\beta}{\sin\beta} \tag{4.98}$$

The induced drag can now be determined using Equation (4.60),

$$\begin{aligned} D_i &= -\rho \int_{-b/2}^{b/2} w_i(y)\Gamma(y)dy & (4.99) \\ &= \rho V_\infty^2 b^2 \int_0^\pi \left[\sum_{m=1}^{\infty} mB_m \sin m\beta\right]\left[\sum_{n=1}^{\infty} B_n \sin n\beta\right] d\beta & (4.100) \\ \Rightarrow D_i &= \frac{\pi}{2}\rho V_\infty^2 b^2 \sum_{n=1}^{\infty} nB_n^2 & (4.101) \end{aligned}$$

We note that all of the terms in the induced drag are positive. Thus, $D_i > 0$ (technically, the induced drag could be zero but this is only for the trivial solution in which the circulation is zero everywhere on the wing).

A key result in the aerodynamic performance of wings can be now observed using the results for the lift in Equation (4.92) and induced drag in Equation (4.101). Specifically, while the lift only depends on B_1, all B_n produce positive contributions to the induced drag. Thus, for a specified amount of lift for a given wing (which sets B_1), the minimum induced drag occurs when $B_n = 0$ for $n > 1$. Therefore, as we previously stated in Section 4.4.6, the elliptic lift distribution produces the lowest amount of induced drag for a given wing and lift.

The induced drag coefficient is,

$$C_{D_i} \equiv \frac{D_i}{q_\infty S_{ref}} = \pi AR \sum_{n=1}^{\infty} nB_n^2 \tag{4.102}$$

This can be written in a convenient form in terms of the lift coefficient using Equation (4.93),

$$C_{D_i} = \frac{C_L^2}{\pi ARe} \tag{4.103}$$

where e is called the **Oswald span efficiency factor** and using this lifting line model is given by,

$$e^{-1} = 1 + \sum_{n=2}^{\infty} n\left(\frac{B_n}{B_1}\right)^2 \tag{4.104}$$

This result shows that $e \leq 1$ and $e = 1$ only when $B_n = 0$ for $n > 1$ (i.e. when the lift distribution is elliptic).

4.4.11 Connecting circulation to wing geometry

We have used the lifting line model to derive many important results about the relationship between the lift distribution and induced drag. But, thus far, the properties of the airfoil sections have not entered the analysis. Thus, while we know that an elliptic lift distribution produces the lowest C_{D_i} for a given C_L and AR, we have no idea what the shape of the wing needs to be to achieve the elliptic lift distribution. Similarly, if we were given a particular wing shape (geometric twist and airfoil shapes), we would not know how to apply lifting line to estimate C_L and C_{D_i}. In this part of our lifting line presentation, we finally connect the wing shape to aerodynamic performance.

The classic approach utilized by Prandtl to connect the airfoil shape and geometric twist applies thin airfoil theory results to each section. In doing this, the angle of attack of each section is taken to be the effective angle of attack. Thus, each section's lift coefficient is given by,

$$c_l(y) = 2\pi\left[\alpha_{eff}(y) - \alpha_{L=0}(y)\right] \tag{4.105}$$

Substituting in Equation (4.62) for α_{eff} gives,

$$c_l(y) = 2\pi \left[\alpha + \alpha_g(y) - \alpha_i(y) - \alpha_{L=0}(y)\right] \tag{4.106}$$

The sectional lift coefficient can also be related to the circulation distribution as follows,

$$c_l(y) = \frac{L'_{eff}(y)}{q_\infty c(y)} \tag{4.107}$$

$$= \frac{\rho V_\infty \Gamma(y)}{q_\infty c(y)} \tag{4.108}$$

$$= 4\frac{b}{c(\beta)} \sum_{n=1}^{\infty} B_n \sin n\beta \tag{4.109}$$

We note that when we write $c(\beta)$ we really should write $c(y(\beta))$ since c was described as a function of y. However, to keep the notation somewhat cleaner, we will use just $c(\beta)$ and similarly, $\alpha_g(\beta)$, $\alpha_{L=0}(\beta)$, and so on.

Substituting Equations (4.109), (4.63), and (4.98 into Equation (4.106) gives,

$$\frac{2}{\pi}\frac{b}{c(\beta)} \sum_{n=1}^{\infty} B_n \sin n\beta + \sum_{n=1}^{\infty} nB_n \frac{\sin n\beta}{\sin\beta} = \alpha + \alpha_g(\beta) - \alpha_{L=0}(\beta) \tag{4.110}$$

This equation has been written so that the Fourier coefficients B_n for the circulation distribution are all on the left-hand side. Suppose we wish to analyze a particular wing. In that case, b, $c(\beta)$, $\alpha_g(\beta)$, and $\alpha_{L=0}(\beta)$ will be given. The freestream angle of attack α will likely also be given though perhaps over a range of relevant values. Then, for a specific α, we would need to solve Equation (4.110) for all of the B_n. However, in practice, we do not solve for the infinitely many values of B_n. Instead, the approach taken is to approximate the solution with a chosen number of modes, and satisfy Equation (4.110) in some approximate manner.

4.4.12 Assumptions of the lifting line model

The assumptions of the lifting line model have occurred throughout this entire section. The following is an explicit list of the assumptions we have utilized to derive the lifting line model:

- Incompressible, steady, inviscid, potential flow
- High aspect ratio, unswept wing without dihedral
- All of the assumptions required for thin airfoil theory
- Planar trailing vortex wake

SATHYABAMA
INSTITUTE OF SCIENCE AND TECHNOLOGY
(DEEMED TO BE UNIVERSITY)
Accredited "A" Grade by NAAC | 12B Status by UGC | Approved by AICTE
www.sathyabama.ac.in

SCHOOL OF MECHANICAL ENGINEERING
DEPARTMENT OF AERONAUTICAL ENGINEERING

UNIT – V –LOW SPEED AERODYNAMICS – SAEA1403

UNIT 5

VISCOUS FLOW

5.1 Overview

5.1.1 Measurable outcomes

While we have discussed the importance of viscous effects in early modules, thus far we have not developed methods to analyze these effects either qualitatively or quantitatively. In this module, we now rectify that problem and consider viscous effects. Initially, we will focus on classical solutions to the Navier-Stokes equations which will form a foundation for the main event: boundary layers. In this module, we consider laminar boundary layers, and in the next module, we will extend these ideas to turbulent boundary layers.

Specifically, students successfully completing this module will be able to:

5.1. State the linear stress-strain rate relationship for a general compressible flow and its simplifi-cation for incompressible flow.

5.2. State the incompressible, constant viscosity form of the Navier-Stokes equations (including conservation of mass) and the no slip boundary condition at solid surfaces. Solve the incompressible Navier-Stokes equations for various classical (usually parallel) flows.

5.3. Explain the concept of a laminar boundary layer including the definition of the displacement thickness and the skin friction coefficient and the importance of the Reynolds number in determining the presence and behavior of a boundary layer.

5.4. Derive the laminar boundary layer equations by performing an order-of-magnitude scaling analysis on the incompressible Navier-Stokes equations.

5.5. Describe the balance of pressure force, viscous force, and momentum change that occurs in a laminar boundary layer. Apply the boundary layer equations to estimate the flow behavior in laminar boundary layers.

5.6. Apply the results of Blasius flat plate boundary layer theory to estimate the behavior of laminar boundary layers including the variation of the skin friction and boundary layer thickness with streamwise distance.

5.7. Explain how the boundary layer alters the streamlines of the outer inviscid flow and, using streamline curvature, describe the impact on the pressure distribution and drag (relative to purely inviscid flow).

5.8. Describe laminar boundary layer separation and the factors which contribute to it.

.

5.2 The Navier-Stokes Equations

5.2.1 Stress tensor

In this section, we define the viscous stress tensor which is used to calculate the viscous stresses. Recall from Equation (4.59) that conservation of j-momentum is,

$$\rho \frac{Du_j}{Dt} = -\frac{\partial p}{\partial x_j} + f_j^T \tag{5.1}$$

where f_j^T is the net viscous force (in the j-direction) per unit volume acting on a fluid element and was defined in Equation (4.43) as,

$${}_V f_j^T \, dV = {}_S \tau_j \, dS \tag{5.2}$$

where V and S are the volume and surface of a fluid element.

Common practice in calculating f_j^T is to use the viscous stress tensor, τ_{ij} . Figure 5.1 shows the convention used to define τ_{ij} . (Note that we will largely use only two dimensions in the figures and derivations for viscous flows. This is for simplicity, as the results all directly extend to three-dimensional flows.) Specifically, the definition of τ_{ij} is:

τ_{ij} **is the viscous stress in the** $\hat{e}_j$ **-direction acting on a surface with normal in the** $\hat{e}_i$**-direction.**

Mathematically, we can write this definition of τ_{ij} as

$$\tau_{ij} \equiv \tau_j (\hat{e}_i) \tag{5.3}$$

As shown in the Figure 13.1, when the surface normal is in the positive i-direction, the stresses are defined by convention to be oriented in the positive j-directions. And, when the normal is in the negative i-direction, the stresses are in the negative j-directions. This switching of directions of τ_{ij} is required because the stress exerted on one face of a fluid element must be equal and opposite of the stress exerted on the fluid element sharing that face (applying Newton's Third Law).

Next, let's calculate the net viscous stress in the j-direction acting on the fluid element (again, only consider two-dimensional flows),

$$
\begin{aligned}
{}_S \tau_j \, dS &= dy\,[\tau_{1j}(x + dx/2, y) - \tau_{1j}(x - dx/2, y)] && (5.4)\\
&+ dx\,[\tau_{2j}(x, y + dy/2) - \tau_{2j}(x, y - dy/2)] && (5.5)\\
&= \left(\frac{\partial \tau_{1j}}{\partial x} + \frac{\partial \tau_{2j}}{\partial y}\right) dx\,dy && (5.6)
\end{aligned}
$$

$$\lim \frac{1}{\;} \qquad \frac{\partial \tau_{ij}}{\;} \tag{5.7}$$

where the derivation utilizes a Taylor series of τ_{ij} about (x, y). Then, substituting the result into Equation (5.2) gives,

$$f_j^T = \frac{\partial \tau_{ij}}{\partial x_i} \tag{5.8}$$

Finally, substitution into Equation (4.59) gives the conservation of j-momentum,

$$\rho \frac{Du_j}{Dt} = -\frac{\partial p}{\partial x_j} + \frac{\partial \tau_{ij}}{\partial x_i} \tag{5.9}$$

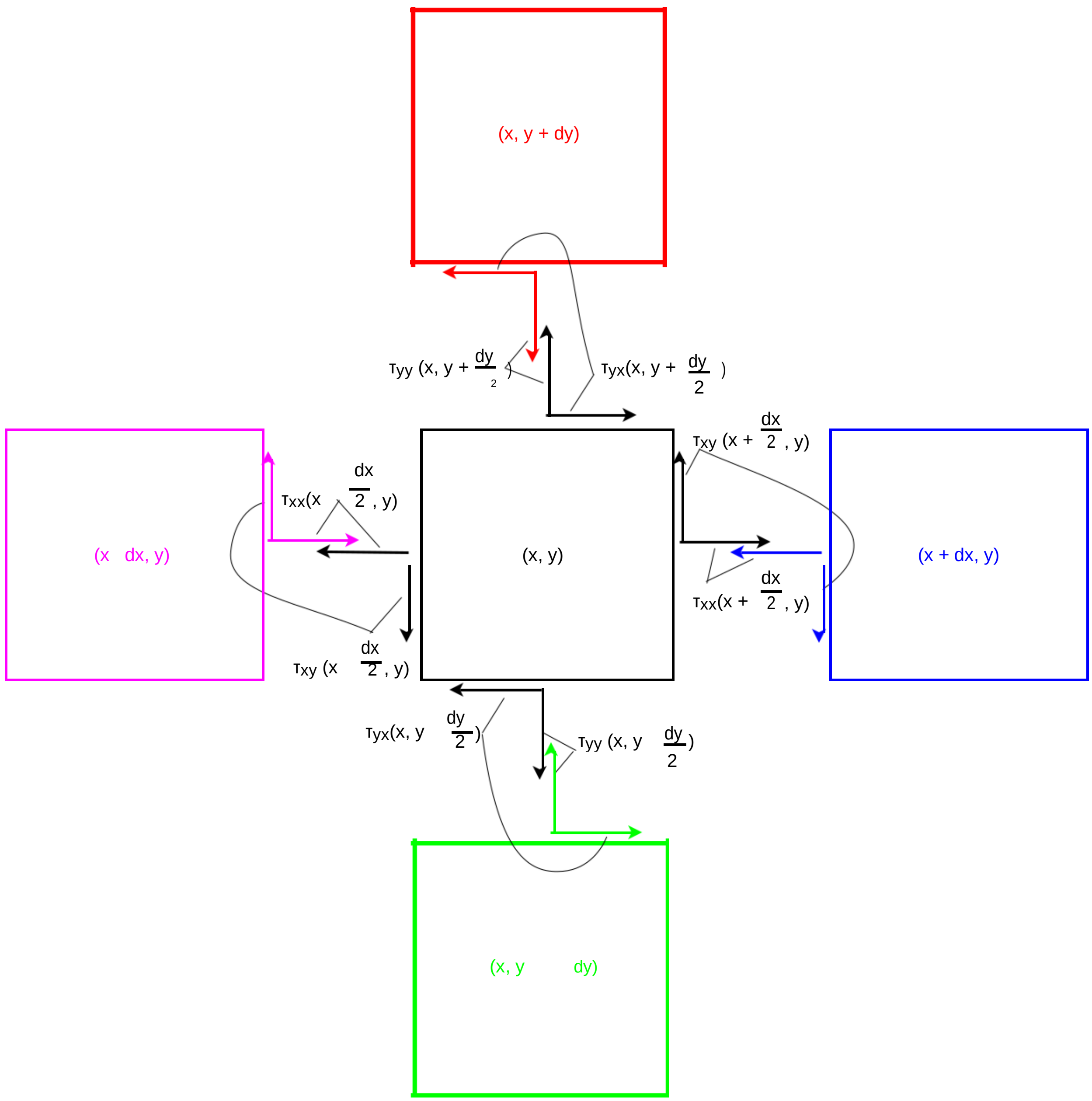

Figure 5.1: Viscous stress tensor τ_{ij} conventions

As we close our introduction to the viscous stress tensor, we note that often the viscous stress must be calculated on a surface that does not align with the coordinate directions. Suppose the surface at a point had an outward pointing normal $\hat{n}$. Then, the viscous stress acting at that point is given by,

$$\tau_j(\hat{n}) = \tau_{ij}\,\hat{n}_i \tag{5.10}$$

5.2.3 Stress-strain rate relationship

The next step we take is to relate the stress tensor τ_{ij} to the strain rate tensor ϱ_{ij} for an incom-pressible flow. We begin by asking you to watch the following video in the NSF Fluid Mechanics Series. In this video, Professor Ascher Shapiro introduces the basic principles of viscosity and the relationship between stress and strain rate.

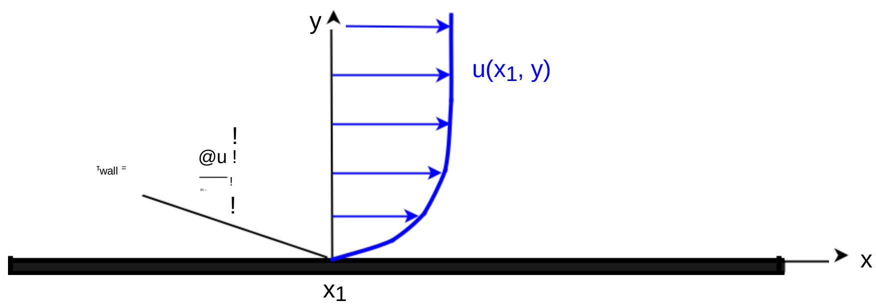

Figure 5.2: τ_{wall} for a straight wall

Now, let's start to get a little more specific. Consider the flow over a straight wall as shown in Figure 5.2. The stress acting on the wall due to the viscous stress in the flow is,

$$\tau_{wall} = \mu \left.\frac{\partial u}{\partial y}\right|_{y=0} \tag{5.12}$$

As derived in Equation (4.5), $\partial u/\partial y$ is the time rate of change of the shearing angle. Thus, as described by Professor Shapiro, the dynamic viscosity μ is the ratio of shear stress to the strain rate.

This result can be generalized to relate τ_{ij} to ϱ_{ij} . The key assumptions made in this generaliza-tion are that the fluid is isotropic. Isotropic behavior requires that the stress-strain rate relationship is unchanged by a rotation of the coordinate system. With this assumption (in addition to requiring the stress tensor to be dependent on linear combinations of the strain rate tensor), the following general form of the stress-strain rate relationship may be derived,

$$\tau_{ij} = 2\mu\varrho_{ij} + \delta_{ij}\,\lambda\varrho_{kk} \tag{5.13}$$

where δ_{ij} is the Kronecker delta which is equal to one when $i = j$ and equal to zero otherwise. λ is refered to as the bulk viscosity coefficient or the second coefficient of viscosity. This stress-strain rate model is known as a Newtonian fluid model and is a very accurate for air and gases in most conditions. Also, for liquids with simple molecular structures (like water), a Newtonian fluid model is very appropriate.

Noting that $\varrho_{kk} = \partial u_k/\partial x_k = \nabla \cdot \mathbf{V}$, then we see that for an incompressible flow, the bulk viscosity term is zero (because of conservation of mass). Thus, for incompressible flow, the stress-strain rate relationship is,

$$\tau_{ij} = 2\mu\varrho_{ij} \tag{5.14}$$

5.2.5 Navier-Stokes equations for incompressible flow

For incompressible flows, we will also assume that the viscosity does not vary significantly. For gases and liquids, μ is largely a function of temperature, with little dependence on the pressure. Thus $\mu = \mu(T)$. We will assume that the variations in temperature result in small variations in μ. Including the temperature dependence of $\mu(T)$ does not change the qualitative behavior, but does significantly complicate the analysis. So, in this course, we will assume that μ is constant when analyzing viscous incompressible flows.

For the case of constant viscosity, the net viscous stress terms reduce significantly,

$$f_j^T = \frac{\partial \tau_{ij}}{\partial x_i} \tag{5.19}$$

$$= \mu \frac{\partial}{\partial x_i}\left(\frac{\partial u_j}{\partial x_i} + \frac{\partial u_i}{\partial x_j}\right) \tag{5.20}$$

$$= \mu \frac{\partial^2 u_j}{\partial x_i \partial x_i} + \mu \frac{\partial}{\partial x_i}\frac{\partial u_i}{\partial x_j} \tag{5.21}$$

$$= \mu \frac{\partial^2 u_j}{\partial x_i \partial x_i} + \mu \frac{\partial}{\partial x_j}\frac{\partial u_i}{\partial x_i} \tag{5.22}$$

$$= \mu \frac{\partial^2 u_j}{\partial x_i \partial x_i} \tag{5.23}$$

In the last step of this derivation, we use the fact that $\partial u_i/\partial x_i = 0$ for an incompressible flow. Thus, the momentum equation for incompressible, constant viscosity flow then becomes,

$$\rho \frac{Du_j}{Dt} = -\frac{\partial p}{\partial x_j} + \mu \frac{\partial^2 u_j}{\partial x_i \partial x_i} \tag{5.24}$$

This is the incompressible form of the celebrated Navier-Stokes equation, named for Claude-Louis Navier and George Stokes. In addition, the incompressible form of the conservation of mass is also needed and, as we have seen many times now, is given by,

$$\frac{\partial u_i}{\partial x_i} = 0 \tag{5.25}$$

We could derive an energy equation for this incompressible, constant viscosity flow, however, it is not needed to solve for the velocity and pressure since the conservation of mass and momentum for this situation completely decouple from the internal energy. In other words, Equations (5.25) and (5.24) do not contain the internal energy (or related quantities such as the temperature). Said another way, for a d dimensional problem, we have d + 1 unknown variables: the pressure and d velocity components. And, we have d + 1 equations: the conservation of mass and d conservation of momentum components.

For viscous flows, we also modify the boundary condition at solid surfaces to require that the flow and the surface have the same velocity. This is known as the **no slip** condition. In other words, the flow velocity cannot **slip** relative to the surface. For a stationary surface, which is largely what we will focus on, the no slip condition reduces to all velocity components being zero. Thus, **V** = 0 on stationary surfaces.

5.3 Laminar Boundary Layers

5.3.1 Introduction to boundary layers

We will again return to the NSF Fluid Mechanics Series for an introduction to boundary layers. You'll find some nice flow visualization and a lot of useful terms (adverse and favorable pressure gradients, separation, laminar and turbulent boundary layers). The material on turbulent boundary layers we will not use until the next module.

5.3.2 Order-of-magnitude scaling analysis: Introduction

We have seen in our study of potential flows that pressure distributions on airfoils and wings can often be reasonably predicted, even though viscous effects have been neglected. However, even when the pressure distributions are reasonably predicted from inviscid models, the viscous effects must be accounted for in estimating the drag. Further, viscous effects can, in fact, significantly modify pressure distributions from inviscid flow theory predictions. In particular, as boundary layers thicken and, in the extreme situation, when separation occurs, the pressure distributions observed on airfoils can deviate significantly from inviscid models.

In this section, we will begin our consideration of viscous effects in high Reynolds number flows. As previously described in Section 4.4.6, at high Reynolds numbers, boundary layers form near the surface of a body. In the boundary layer, the flow rapidly varies from near freestream velocities at the edge of the boundary layer to zero velocity at the wall. Fluid acceleration, pressure forces, and viscous forces play an equally important role in the evolution of the flow. To better understand how these three terms balance in the boundary layer, we will use a scaling analysis of the incompressible Navier-Stokes equations.

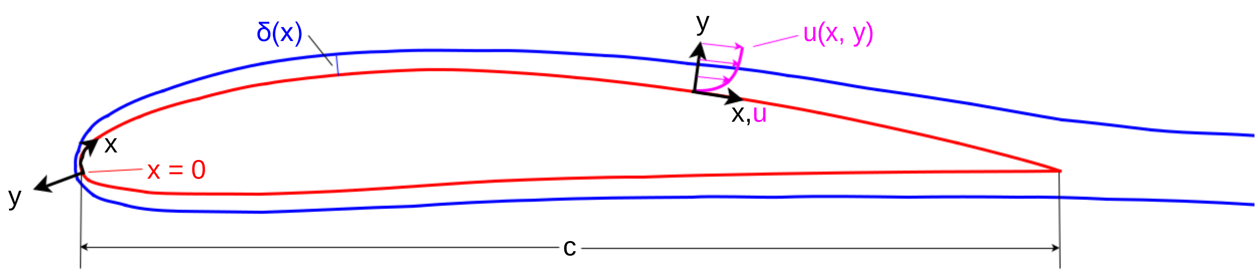

Figure 5.3: Boundary layer coordinate system

As shown in Figure 5.3, the (x, y) coordinate system for boundary layer analysis is wrapped around the surface with x being tangential to the surface and y being normal to the surface. Thus, the boundary layer coordinate system is curved. We place $x = 0$ at the location of the stagnation point at the leading edge. Further, we will assume that,

- $\delta/c \ll 1$ as Re ! ∞
- $\delta/R \ll 1$ as Re ! ∞

Though we do not prove this, the second assumption allows the governing equations in this curved coordinate system to be written unchanged from the usual equations for an (x, y) coordinate system without curvature. Specifically, the governing equations for incompressible, steady, two-dimensional flow in this curved coordinate system are,

$$\frac{\partial u}{\partial x} + \frac{\partial v}{\partial y} = 0 \tag{5.26}$$

$$\rho u \frac{\partial u}{\partial x} + \rho v \frac{\partial u}{\partial y} = -\frac{\partial p}{\partial x} + \mu \frac{\partial^2 u}{\partial x^2} + \mu \frac{\partial^2 u}{\partial y^2} \tag{5.27}$$

$$\rho u \frac{\partial v}{\partial x} + \rho v \frac{\partial v}{\partial y} = -\frac{\partial p}{\partial y} + \mu \frac{\partial^2 v}{\partial x^2} + \mu \frac{\partial^2 v}{\partial y^2} \tag{5.28}$$

Note that if δ/R is not small, then the y-momentum equation must be modified to include the streamline curvature term $\rho V^2/R$.

Next, we non-dimensionalize these equations using the following non-dimensional variables,

$$x^* \equiv \frac{x}{c} \qquad y^* \equiv \frac{y}{c} \qquad u^* \equiv \frac{u}{V_\infty} \qquad v^* \equiv \frac{v}{V_\infty} \tag{5.29}$$

Substitution of these definitions into Equations (5.26)-(5.28) produces,

$$\frac{\partial u^*}{\partial x^*} + \frac{\partial v^*}{\partial y^*} = 0 \tag{5.30}$$

$$u^* \frac{\partial u^*}{\partial x^*} + v^* \frac{\partial u^*}{\partial y^*} = -\frac{1}{\rho V_\infty^2}\frac{\partial p}{\partial x^*} + \frac{1}{Re}\frac{\partial^2 u^*}{\partial x^{*2}} + \frac{1}{Re}\frac{\partial^2 u^*}{\partial y^{*2}} \tag{5.31}$$

$$u^* \frac{\partial v^*}{\partial x^*} + v^* \frac{\partial v^*}{\partial y^*} = -\frac{1}{\rho V_\infty^2}\frac{\partial p}{\partial y^*} + \frac{1}{Re}\frac{\partial^2 v^*}{\partial x^{*2}} + \frac{1}{Re}\frac{\partial^2 v^*}{\partial y^{*2}} \tag{5.32}$$

We see from these non-dimensional equations that by defining,

$$p^* \equiv \frac{p}{\rho V_\infty^2} \tag{5.33}$$

then the non-dimensional incompressible two-dimensional governing equations are,

$$\frac{\partial u^*}{\partial x^*} + \frac{\partial v^*}{\partial y^*} = 0 \tag{5.34}$$

$$u^* \frac{\partial u^*}{\partial x^*} + v^* \frac{\partial u^*}{\partial y^*} = -\frac{\partial p^*}{\partial x^*} + \frac{1}{Re}\frac{\partial^2 u^*}{\partial x^{*2}} + \frac{1}{Re}\frac{\partial^2 u^*}{\partial y^{*2}} \tag{5.35}$$

$$u^* \frac{\partial v^*}{\partial x^*} + v^* \frac{\partial v^*}{\partial y^*} = -\frac{\partial p^*}{\partial y^*} + \frac{1}{Re}\frac{\partial^2 v^*}{\partial x^{*2}} + \frac{1}{Re}\frac{\partial^2 v^*}{\partial y^{*2}} \tag{5.36}$$

A simplistic analysis of these equations would suggest that as $Re \to \infty$ then the viscous effects could be neglected. This leads to the inviscid equations and the potential flow models we have been studying. However, this conclusion neglects that fact that as Re increases, so does the magnitude of $\partial^2 u^*/\partial y^{*2}$ near the wall. As a result, the viscous terms cannot be entirely neglected in the high Reynolds number limit.

We now perform an order-of-magnitude scaling analysis on the incompressible Navier-Stokes equations. Our goal is to develop a model for the flow in the boundary layer which is less complex than the two-dimensional incompressible Navier-Stokes equations. And, by applying this model, we hope to gain insight into the fundamental physics at work in boundary layer flows.

We begin by considering the spatial length scales in the boundary layer flow shown in Figure 5.3. Two length scales are apparent:

- c, the chord of the airfoil

- $\delta(x)$, the thickness of the boundary layer

We expect that the airfoil chord will control the spatial variations in the x direction. In particular, we expect that the x-derivatives of the flow variables will scale with 1/c. Mathematically, we write this as,

$$\frac{\partial}{\partial x} \sim \frac{1}{c} \tag{5.37}$$

Here is another way to think about this scaling idea. Consider the boundary layer problem with dimensional inputs, if we increase c by say a factor of two but keep everything else constant (ρ, μ, V_∞, airfoil shape), then our scaling assumption says that the x-derivatives in the flow will decrease by a factor of two.

In the y-direction, we expect the flow will vary over a distance of the boundary layer thickness, δ. For example, we know that at the wall that **V**(x, y = 0) = 0 (no slip condition) but just outside of the boundary layer the velocity will be (approximately) **V**(x, δ) ≈ $\mathbf{V}_\infty$. Thus,

$$\frac{\partial}{\partial y} \sim \frac{1}{\delta} \tag{5.38}$$

Similar to the length scales, we can set scales for other quantities. In particular, for the x-velocity, we will assume that the freestream velocity is an appropriate scale. Thus,

$$u \sim V_\infty \tag{5.39}$$

To make our scaling assumptions a bit more precise, we will introduce the following order-of-magnitude notation in the limit as Re ! ∞. Specifically, consider two functions, f (Re) and g(Re). These functions have the same order of magnitude,

$$f(Re) = O(g(Re)) \text{ as } Re \,!\, \infty \tag{5.40}$$

if finite constants C and Re_0 exist such that,

$$|f(Re)| \le C\,|g(Re)| \text{ for all } Re \ge Re_0 \tag{5.41}$$

Based on our previous scaling assumptions for x and u, we make the following order of magnitude assumption,

$$\frac{\partial(u/V_\infty)}{\partial(x/c)} = \frac{\partial u^*}{\partial x^*} = O(1) \tag{5.42}$$

Similarly, based on our previous scaling assumptions for y and u, we make the following order of magnitude assumption,

$$\frac{\partial(u/V_\infty)}{\partial(y/\delta)} = \frac{\delta}{c}\frac{\partial u^*}{\partial y^*} = O(1) \tag{5.43}$$

This last result can be re-arranged to show that,

$$\frac{\partial u^*}{\partial y^*} = O\left(\frac{c}{\delta}\right) \tag{5.44}$$

Thus, based on our assumptions, we see that as the boundary layer thickness decreases (relative to the chord), the magnitude of $\partial u^*/\partial y^*$ increases.

5.3.3 Order-of-magnitude scaling analysis: Conservation of mass

Next, we consider the order of magnitude of the terms in the conservation of mass. Clearly, the two terms in Equation (13.34) are the same order-of-magnitude since they sum to zero,

$$\Rightarrow \frac{\partial v^*}{\partial y^*} = O\left(\frac{\partial u^*}{\partial x^*}\right) = O(1) \tag{5.45}$$

We can then manipulate this result to determine the order-of-magnitude scaling for v^*:

$$\frac{\partial v^*}{\partial y^*} = \frac{c}{\delta}\frac{\partial v^*}{\partial(y/\delta)} \tag{5.46}$$

$$\frac{\partial v^*}{\partial(y/\delta)} = O\left(\frac{\delta}{c}\right) \tag{5.47}$$

$$\underline{v} \qquad \underline{\delta} \tag{5.48}$$

The final result is true since at the wall, $v = 0$ and therefore a Taylor series analysis at the wall produces,

$$\underline{v} \quad \underline{y} \qquad \underline{y}\,\underline{\delta} \qquad \underline{\delta}$$

where the last step is true because in the boundary layer, $y/\delta = O(1)$. Thus, we see that the normal velocity is the same order as the boundary layer thickness (and therefore $v/V_\infty \ll 1$).

5.3.4 Order-of-magnitude scaling analysis: Conservation of x-momentum

Now we turn our attention to the x-momentum given by Equation (5.35). From our previous order-of-magnitude results, we see that,

$$u^*\frac{\partial u^*}{\partial x^*} = O(1) \text{ and } v^*\frac{\partial u^*}{\partial y^*} = O(1) \tag{5.50}$$

The pressure term, $\partial p^*/\partial x$, can also be assumed to be $O(1)$ since at the outer edge of the boundary layer, where viscous effects will be neglible, the pressure and acceleration terms must balance. This leaves the second-derivative terms arising from the viscous stress contributions. We will assume (x/c)-derivatives and (y/δ)-derivatives do not have any Reynolds number dependence, thus,

$$\frac{\partial^2 u^*}{\partial x^{*2}} = O(1) \text{ and } \frac{\partial^2 u^*}{\partial(y/\delta)^2} = O(1) \tag{5.51}$$

The (y/δ) derivative order-of-magnitude scaling can be re-arranged to give,

$$\frac{\partial^2 u^*}{\partial(y/\delta)^2} = \left(\frac{\delta}{c}\right)^2\frac{\partial^2 u^*}{\partial y^{*2}} \tag{5.52}$$

$$\Rightarrow \frac{\partial^2 u^*}{\partial y^{*2}} = O\left((c/\delta)^2\right) \tag{5.53}$$

Thus, the two viscous terms have the following scaling,

$$\frac{1}{Re}\frac{\partial^2 u^*}{\partial x^{*2}} = O\left(Re^{-1}\right) \text{ and } \frac{1}{Re}\frac{\partial^2 u^*}{\partial y^{*2}} = O\left(Re^{-1}(c/\delta)^2\right) \tag{5.54}$$

This shows that, as Re ! ∞, the x-derivative term in the viscous stress is negligible compared to all of the other terms in the x-momentum equation. Further, since in the boundary layer we must have some viscous effect that is not negligible, we will require that y-derivative viscous stress term must have the same order as the other terms in the momentum equation. Since these other terms are O(1), this means that,

$$Re^{-1} (c/\delta)^2 = O(1) \tag{5.55}$$

$$\Rightarrow \frac{\delta}{c} = O\left(\frac{1}{\sqrt{Re}}\right) \tag{5.56}$$

This is a classic result in laminar boundary layer theory. It is quite general and says that the thickness of a boundary layer relative to the chord is expected to scale with $Re^{-1/2}$ for increasing Reynolds number.

5.3.6 Order-of-magnitude scaling analysis: Conservation of y-momentum

Now we turn our attention to the y-momentum given by Equation (5.36). Recall from Equation (13.48) that $v^* = O(\delta/c)$. Then, using the result that $\delta/c = O(Re^{-1/2})$, gives

$$v^* = O\left(Re^{-\frac{1}{2}}\right) \quad (13.57)$$

Except for the pressure gradient, the terms of the y-momentum equation have the following order-of-magnitude,

$$u^* \frac{\partial v^*}{\partial x^*} = O\left(Re^{-\frac{1}{2}}\right) \qquad v^* \frac{\partial v^*}{\partial y^*} = O\left(Re^{-\frac{1}{2}}\right) \quad (5.58)$$

$$\frac{1}{Re}\frac{\partial^2 v^*}{\partial x^{*2}} = O\left(Re^{-\frac{3}{2}}\right) \qquad \frac{1}{Re}\frac{\partial^2 v^*}{\partial y^{*2}} = O\left(Re^{-\frac{1}{2}}\right) \quad (5.59)$$

Since all of these terms are negligible at $Re \to \infty$, this implies that the pressure gradient in y must also be negligible in the boundary layer.

$$\frac{\partial p^*}{\partial y^*} \approx 0 \quad (5.60)$$

As a result, the pressure in the boundary layer is only a function of x. Therefore, the pressure in boundary layer analysis is often refered to as the edge pressure and given the notation $p_e(x)$.

5.3.7 Boundary layer equations

In this section, we summarize the two-dimensional, incompressible laminar boundary layer equa-tions. Specifically, the boundary layer equations are,

$$\frac{\partial u}{\partial x} + \frac{\partial v}{\partial y} = 0 \quad (5.61)$$

$$\rho u \frac{\partial u}{\partial x} + \rho v \frac{\partial u}{\partial y} = -\frac{dp_e}{dx} + \mu \frac{\partial^2 u}{\partial y^2} \quad (5.62)$$

$$p(x, y) = p_e(x) \quad (5.63)$$

Another manipulation that is frequently applied is to relate the edge pressure to the velocity at the edge of the boundary layer using Bernoulli equation. This is permissible because outside of the boundary layer, the flow is assumed to be inviscid. Thus, Bernoulli equation gives,

$$p_e + \frac{1}{2}\rho V_e^2 = \text{constant} \quad (5.64)$$

This can be simplified a bit further since the normal velocity $v/V_\infty = O(1/\sqrt{Re})$ is much smaller than the tangential velocity $u/V_\infty = O(1)$. Thus,

$$\lim_{Re\to\infty} V_e^2 = \lim_{Re\to\infty} u_e^2 + v_e^2 = u_e^2 \quad (5.65)$$

Thus, Bernoulli's equation applied at the edge of the boundary layer is,

$$p_e + \frac{1}{2}\rho u_e^2 = \text{constant} \quad (5.66)$$

Differentiating with respect to x gives,

$$\frac{dp_e}{dx} = -\rho u_e \frac{du_e}{dx} \tag{5.67}$$

Thus, an equivalent form of the boundary layer x-momentum equation is,

$$u\frac{\partial u}{\partial x} + v\frac{\partial u}{\partial y} = u_e \frac{du_e}{dx} + v\frac{\partial^2 u}{\partial y^2} \tag{5.68}$$

5.3.9 Blasius flat plate boundary layer solution

The boundary flow over a flat plate (at zero angle of attack) was theoretically studied by Blasius, a doctoral student of Prandtl, in 1908. For the flat plate analysis, we assume that the boundary layer is thin enough so that the edge pressure can be well-approximated as a constant. That is,

$$p_e(x) = p_\infty \tag{5.69}$$

The boundary layer equations for the flat plate case therefore have the following form,

$$\frac{\partial u}{\partial x} + \frac{\partial v}{\partial y} = 0 \tag{5.70}$$

$$u\frac{\partial u}{\partial x} + v\frac{\partial u}{\partial y} = \nu\frac{\partial^2 u}{\partial y^2} \tag{5.71}$$

where ν is the kinematic viscosity, $\nu = \mu/\rho$. These two equations can be reduced to a single equation by defining the velocity components as derivatives of a streamfunction ψ,

$$u = \frac{\partial \psi}{\partial y} \qquad v = -\frac{\partial \psi}{\partial x} \tag{5.72}$$

Substitution of Equation (13.72) into the conservation of mass shows that it is identically satisfied,

$$\frac{\partial u}{\partial x} + \frac{\partial v}{\partial y} = \frac{\partial}{\partial x}\frac{\partial \psi}{\partial y} + \frac{\partial}{\partial y}\left(-\frac{\partial \psi}{\partial x}\right) = 0 \tag{5.73}$$

And, the x-momentum equation is then given by,

$$\frac{\partial \psi}{\partial y}\frac{\partial^2 \psi}{\partial x \partial y} - \frac{\partial \psi}{\partial x}\frac{\partial^2 \psi}{\partial y^2} = \nu\frac{\partial^3 \psi}{\partial y^3} \tag{5.74}$$

Thus, we have reduced the boundary layer equations down to a single partial differential equation for ψ.

This equation can even be further reduced by transforming from (x, y) to (x, η) where,

$$\eta \equiv y\sqrt{\frac{V_\infty}{\nu x}} \tag{5.75}$$

and making the following substitution for ψ,

$$\psi = \sqrt{\nu x V_\infty}\, f(\eta) \tag{5.76}$$

where $f(\eta)$ is the unknown function, and is only a function of η. The velocity components are given by,

$$\frac{u}{V_\infty} = f' \tag{5.77}$$

$$\frac{v}{V_\infty} = \frac{1}{2}\sqrt{\frac{\nu}{V_\infty x}}\left(\eta f' - f\right)$$

where $()'$ denotes differentiation with respect to η. After a lot of algebra, Equation (13.74) can be reduced to,

$$2f''' + ff'' = 0 \tag{5.79}$$

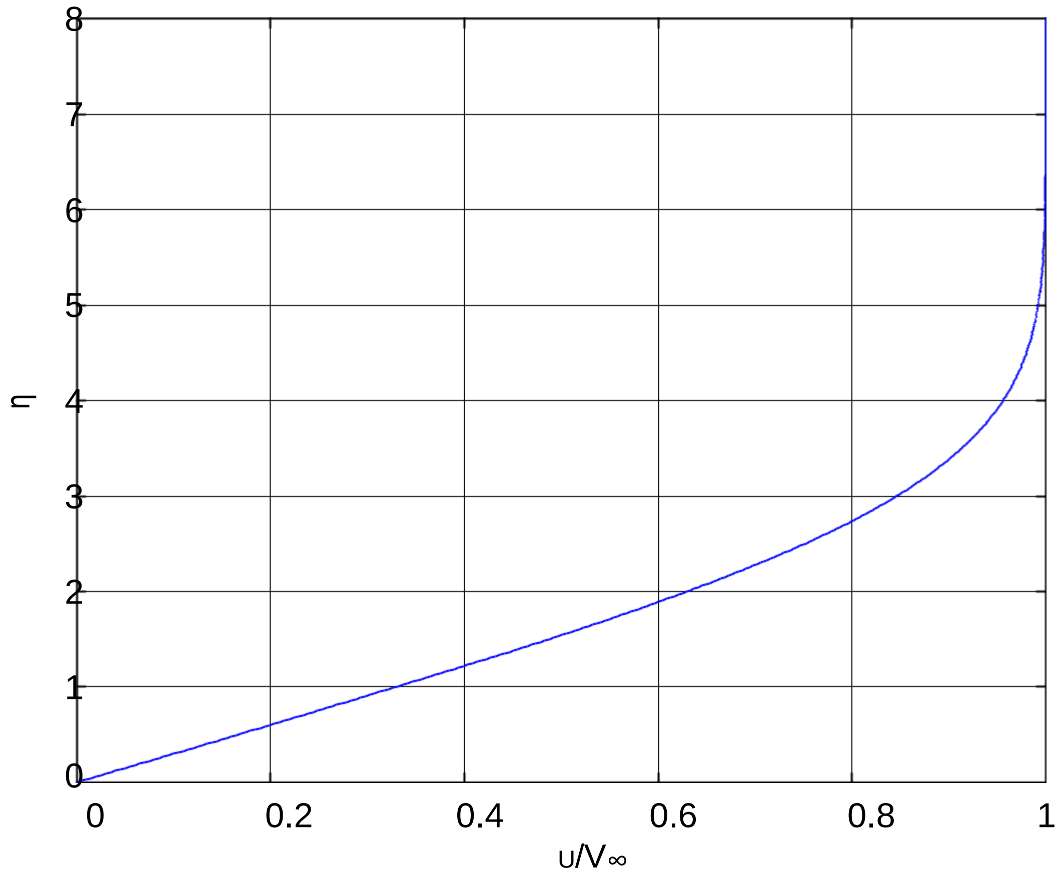

Figure 5.4: u/V_∞ distribution for Blasius flat plate laminar boundary solution .

which is an ordinary though still nonlinear differential equation. Because of nonlinearity, the Blasius equation does not have a closed-form analytic solution and must be solved numerical. More importantly, we see that the u velocity profile will be solely a function of η. The profile is plotted in Figure 5.4.

A common measure of the thickness of the boundary layer is the y location at which the velocity in the boundary layer reach 99% of the freestream value. We will simply use the symbol δ for this 99% thickness. For the flat plate boundary layer, we can first find the value of η at which $u/V_\infty = 0.99$. This occurs at $\eta \approx 4.91$. Thus,

$$\delta\sqrt{\frac{V_\infty}{\nu x}} = 4.91 \tag{5.80}$$

$$\delta = 4.91\sqrt{\frac{\nu x}{V_\infty}} \tag{5.81}$$

A very common parameter used throughout boundary layer theory is the Reynolds number based on distance from the leading edge which is defined as,

$$Re_x \equiv \frac{V_\infty x}{\nu} \tag{5.82}$$

Using Re_x, the Blasius result for δ can be written,

$$\delta = 4.91\frac{x}{\sqrt{Re_x}} \tag{5.83}$$

Recall from Equation (4.32) that the wall stress τ_{wall} is typically reported in a non-dimensional form as the skin friction coefficient, C_f defined as,

$$C_f \equiv \frac{\tau_{wall}}{\frac{1}{2}\rho_\infty V_\infty^2} \tag{5.84}$$

For the specific case of the Blasius flat plate boundary layer, C_f is,

$$C_f = \frac{0.664}{\sqrt{Re_x}} \tag{5.85}$$

Finally, we consider the drag coefficient on a flat plate (at zero angle of attack) in an incompressible flow. The drag for the flat plate is can be found by integrating the wall stress,

$$D' = 2\int_0^c \tau_{wall}\, dx \tag{5.86}$$

where the factor of 2 is to account for both the upper and lower surfaces of the plate. The drag coefficient is then,

$$c_d = \frac{D'}{q_\infty c} \tag{5.87}$$

$$= 2\int_0^1 C_f \, d(x/c) \tag{5.88}$$

$$= 1.328\int_0^1 \sqrt{\frac{\nu}{V_\infty x}}\, d(x/c) \tag{5.89}$$

$$= 1.328\int_0^1 \sqrt{\frac{\nu}{V_\infty c}}\sqrt{\frac{c}{x}}\, d(x/c) \tag{5.90}$$

$$= \frac{1.328}{\sqrt{Re}}\int_0^1 \sqrt{\frac{c}{x}}\, d(x/c) \tag{5.91}$$

$$\Rightarrow c_d = \frac{2.656}{\sqrt{Re}} \tag{5.92}$$

5.4 Form Drag and Separation

5.4.1 Displacement thickness and effective body

In our previous study of potential flows, we developed methods (panel methods and thin airfoil theory in particular) to estimate the pressure distributions around airfoils. Since these models are purely inviscid, they completely ignored the presence of the boundary layer. Although we can often model the flow outside of the boundary layer as being inviscid, this outer inviscid flow is in fact modified by the presence of the boundary layer. In particular, the boundary layer causes the streamlines to be displaced away from the body relative to a purely inviscid flow model.

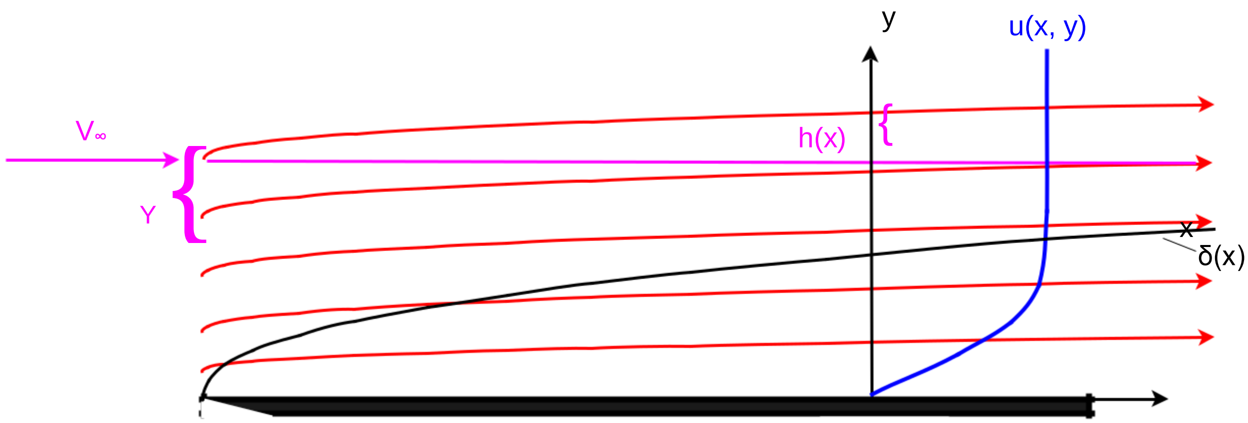

Figure 5.5: Streamlines for flat plate boundary flow showing the displacement h(x) of a streamline that is a height Y above the plate at the leading edge.

Consider the boundary flow over a flat plate. The streamlines for this flow are sketched in Figure 5.5. As shown in the sketch, a streamline that is a height Y above the plate at the leading edge is displaced a distance h(x) due to the growth of the boundary layer. A purely inviscid flow

$\mathbf{V}(x,y) = V_\infty \mathbf{i}$ everywhere.

The displacement of the streamlines due to the boundary layer could be modeled in an inviscid flow by determining an effective body shape that would produce the same streamlines as the viscous flow. This concept is illustrated in Figure 5.6. $\delta^*(x)$ is known as the **displacement thickness** and is the distance the actual body surface needs to be displaced so that the streamlines of the inviscid flow around this **effective body** are the same as the viscous flow around the actual body. To determine this displacement thickness, we apply conservation of mass so that the inviscid flow has the same amount of mass as the boundary layer flow. Specifically,

$$\rho u_e (Y - \delta^*) = \rho \int_0^Y u \, dy \tag{5.93}$$

$$u_e \delta^* = \int_0^Y (u_e - u) \, dy \tag{5.94}$$

$$\Rightarrow \delta^* = \int_0^Y \left(1 - \frac{u}{u_e}\right) dy \tag{5.95}$$

The specific distance Y used in this definition does not need to be precisely defined as long as it is at least δ. Since for $y > \delta$, the velocity $u(x, y) \approx u_e(x)$ and therefore the contribution to the integral will negligible.

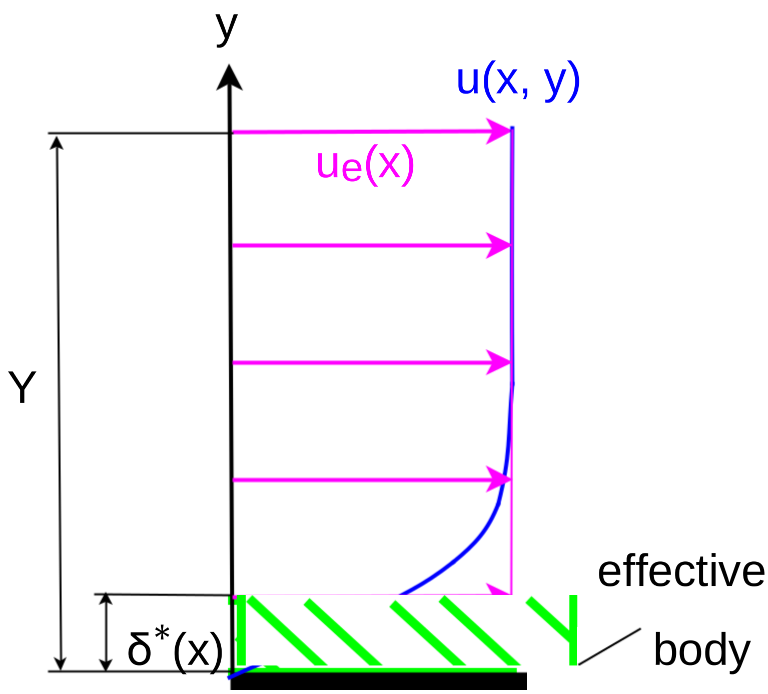

Figure 5.6: Displacement thickness and effective body

For the Blasius laminar flat plate, the displacement thickness is,

$$\delta^* = 1.72 \frac{x}{\sqrt{Re_x}} \qquad (5.96)$$

5.4.2 Form drag

The displacement effect of the boundary layer modifies the pressure from a purely inviscid flow around the (actual) body. As a result, the pressure forces acting on an airfoil will produce a finite drag. This source of drag is commonly refered to as **form drag**.

The form drag will generally be larger when δ^* is larger. Thus, from the Blasius result, we expect δ^* to be larger for lower Reynolds numbers since $\delta^* \propto 1/\sqrt{Re_x}$. The Table shows the drag coefficient data for NACA 0006 and NACA 0012 airfoils at $\alpha = 0$ and $Re = 10^3$ and 10^4. The Reynolds number trends clearly show that the form drag decreases with increasing Reynolds number. The friction drag data also shows the expected decrease with Reynolds number. In particular, the flat plate c_{df} values (taken from Equation 5.92) are shown to be good approximations to the c_{df} for the NACA airfoils. Note that there is no form drag for a flat plate since the surface of the flat plate only has normals in the y-direction and thus the pressure stresses only act in the y-direction.

Figure 5.7 shows the c_p distributions and the effective shape of the body. The effective shape (which is drawn as the airfoil shape with the displacement thickness δ^* added normal to the shape) is clearly seen to be closer to the actual shape for the higher Reynolds number. As a result, the c_p distributions for the viscous flow more closely approximates the inviscid flow c_p (shown in the dashed line of the plots) and, therefore, the form drag also decreases.

Though somewhat difficult to discern from Figure 5.7, note that the displacement thickness for the NACA 0012 airfoil is larger than that of the NACA 0006 airfoil on the downstream half (0.5 < x/c < 1) of the airfoils. This can be explained as follows. The NACA 0012 airfoil generates a lower

Airfoil	Re_∞	c_{df}	c_{dform}	c_d
flat plate	1×10^3	0.0840	0	0.0840
flat plate	1×10^4	0.0266	0	0.0266
NACA 0006	1×10^3	0.0892	0.0166	0.1058
NACA 0006	1×10^4	0.0257	0.0059	0.0316
NACA 0012	1×10^3	0.0833	0.0346	0.1179
NACA 0012	1×10^4	0.0232	0.0162	0.0395

Table 1: Drag coefficient due to friction (c_{df}), form drag (c_{dform}) and total drag (c_d) for flat plate (Blasius solution), NACA 0006, and NACA 0012 at α = 0

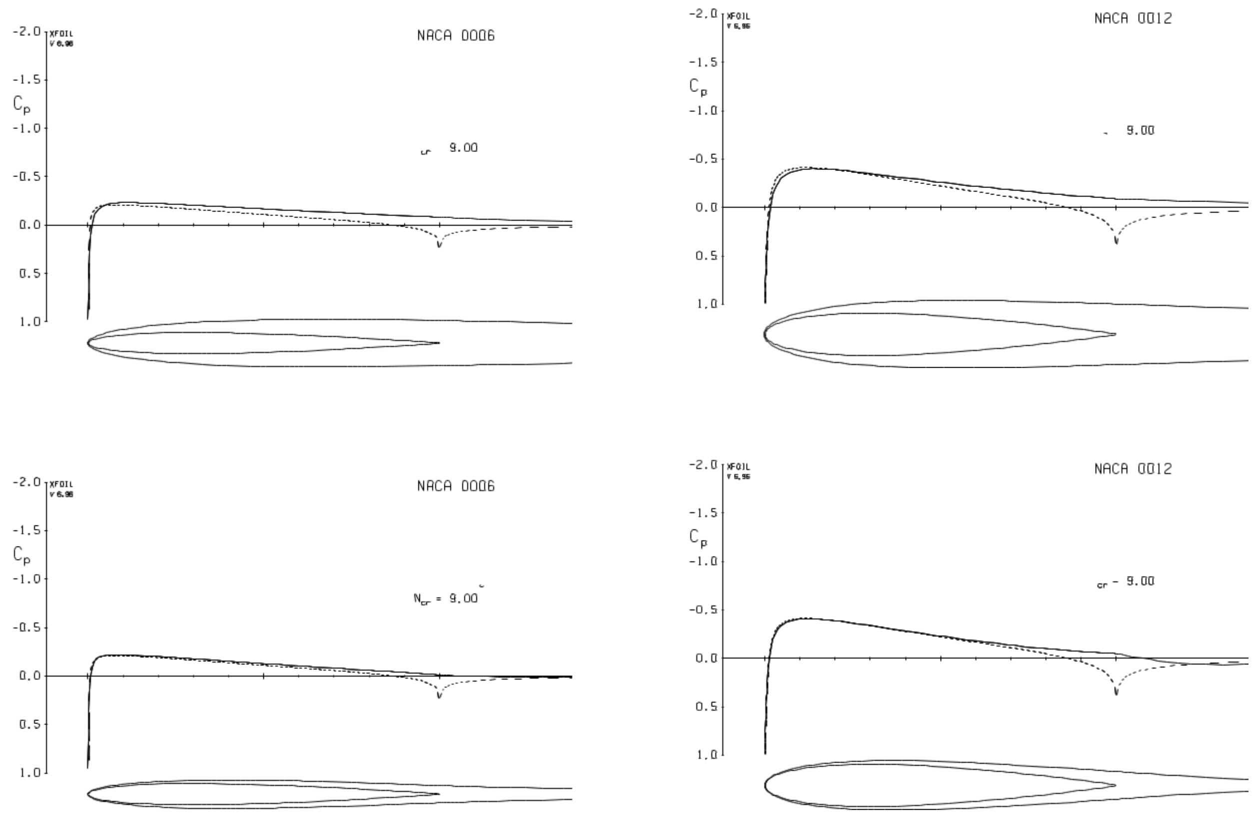

Figure 5.7: c_p and effective shape for NACA 0006 and NACA 0012 incompressible laminar flows at α = 0 and Re = 1, 000 and 10, 000. Note: c_p for purely inviscid flow is shown as dashed line in c_p plot.

minimum pressure (roughly at the location of maximum thickness) than the NACA 0006 because of the decreased radius of curvature for the thicker airfoils (see Section 5.3.3 for the streamline curvature discussion of the impact of thickness on c_p). As a result, the edge pressure gradient, dp_e/dx will tend to be larger (more adverse) on the downstream half of the NACA 0012 than on the NACA 0006. Note that if the flow were inviscid, the velocity at the trailing edge for both of these airfoils would stagnate and the pressure at the trailing edge would therefore be the freestream stagnation pressure. Thus, a lower minimum pressure on the airfoil implies generally larger adverse pressure gradients would be observed downstream. The connection between the pressure gradient and the boundary layer thickness can be explained by considering the momentum equation along the streamwise direction in a boundary layer. This equation can be shown to be,

$$\rho u \frac{\partial u}{\partial s} = -\frac{dp_e}{ds} + \mu \frac{\partial^2 u}{\partial n^2} \tag{5.97}$$

Note, the essential differences between this equation and the boundary layer x-momentum equation (Equation 5.62) are that

- the derivatives are taken along a streamline direction (s) and normal to the streamline (n) as opposed to in x and y.
- the normal velocity term in the substantial derivative, $u_n \partial u/\partial n$ is zero since the velocity normal to a streamline is, by definition, zero (i.e. a streamline is tangent to the velocity).
- While the velocity in the substantial derivative terms of this equation should be V (the velocity magnitude), since v is neglible compared to u, then $V \approx u$ in the limit of high Re.

Dividing Equation (5.97) by ρu gives,

$$\frac{\partial u}{\partial s} = -\frac{1}{\rho u}\frac{dp_e}{ds} + \frac{\mu}{\rho u}\frac{\partial^2 u}{\partial n^2} \tag{5.98}$$

This equation shows that for regions of lower velocity, the pressure gradient will create a larger change in the velocity. In particular, for adverse pressure gradients, this leads to a feedback in which the adverse pressure gradient ($dp_e/ds > 0$) decelerates the velocity ($\partial u/\partial s < 0$) which then further amplifies the impact of an adverse pressure gradient. For favorable pressure gradients, the opposite happens in which the favorable pressure gradient accelerates the flow and lessens the impact of further favorable pressure gradients. As a result, while the decreased pressure due to increased thickness of an airfoil will tend to decrease δ^* on the upstream portion of the airfoil, the negative feedback will generally lead to larger δ^* on the downstream portion of the airfoil. This behavior of δ^* can be observed in Figure 5.8 which shows a plot of $\delta^*(x)$ for the two airfoils and the flat plate result (Equation 5.96) at Re = 1, 000. In summary, increased airfoil thickness overall will tend to increase δ^* and lead to larger form drags.

Beyond increased airfoil thickness, any effect that results in larger adverse pressure gradients on the airfoil also increases the likelihood of larger δ^* and therefore increased form drag. In particular,

- Increasing c_l will require lower pressures on the upper surface which will lead to increased adverse pressure gradients as the pressure increases towards the rear of the airfoil.
- Suction peaks create very low pressures which will result in large adverse pressure gradients immediately downstream of the peak.

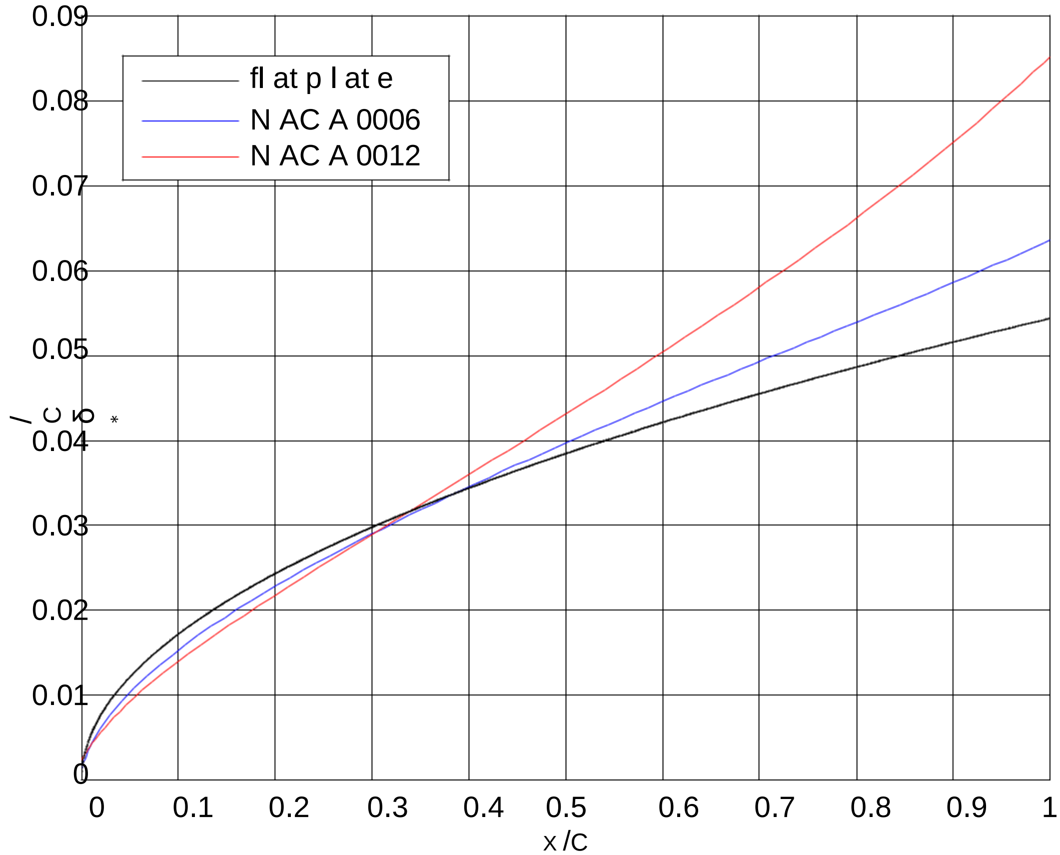

Figure 5.8: δ^*/c versus x/c for incompressible laminar flows at $\alpha = 0$ over a flat plate and NACA 0006 and NACA 0012 airfoils at Re = 1, 000.

5.4.4 Separation

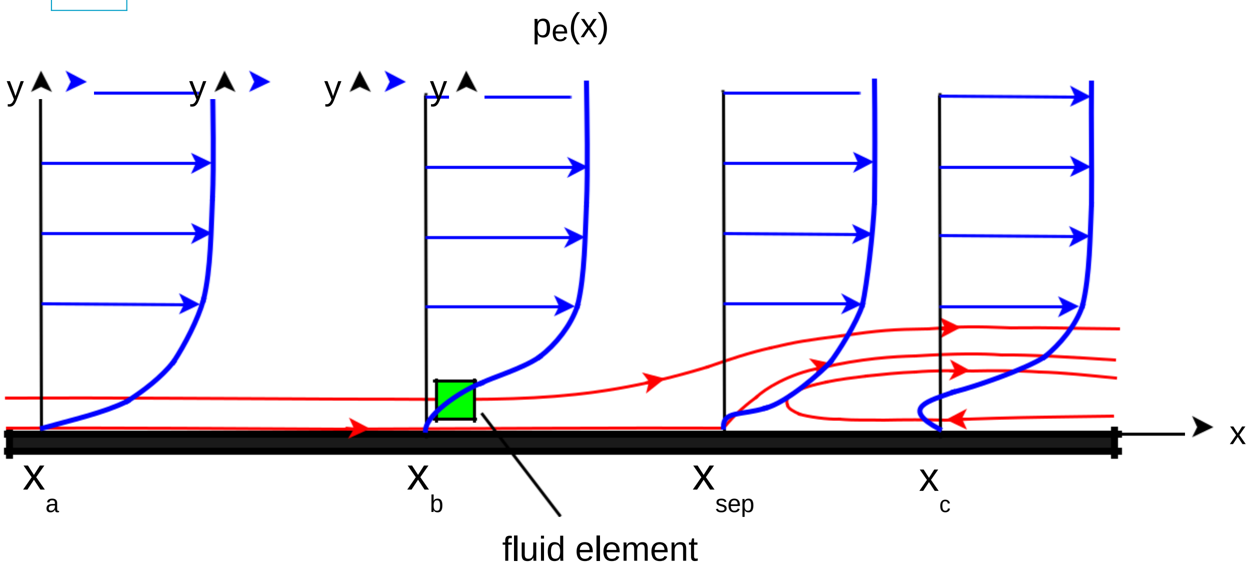

Figure 5.9: Velocity profiles and streamlines in the vicinity of flow separation.

As shown in Figure 5.9, the separation location x_{sep} is where the streamline infinitesimally above the surface no longer remains tangent to the surface (on the surface, the flow always has zero velocity and is always tangent). the skin friction $\tau_{wall} = 0$ at this location. Thus, $C_f = \tau_{wall}/q_\infty = 0$ at separation.

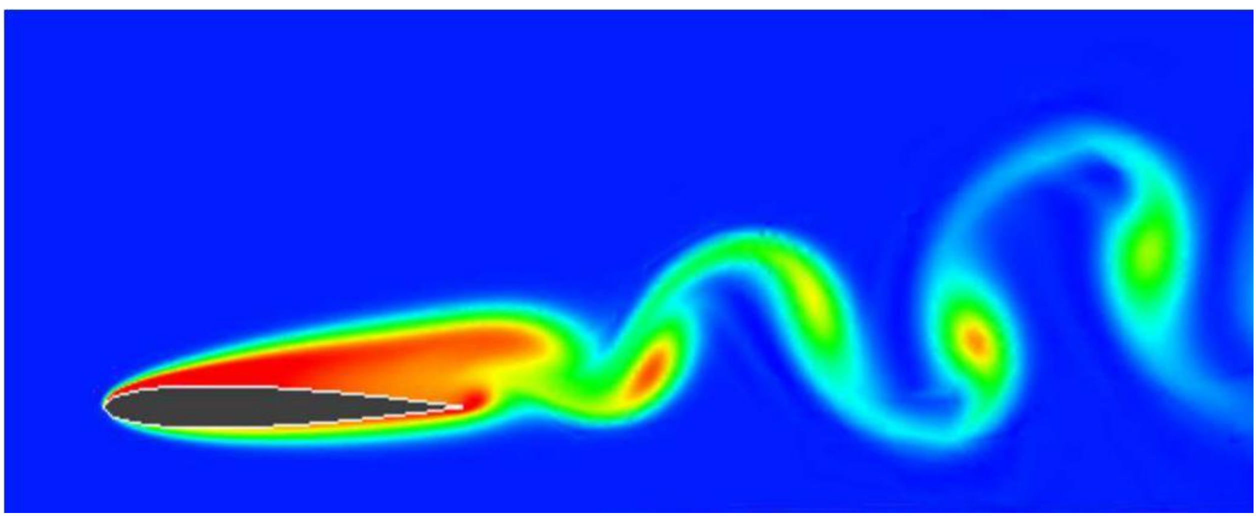

Figure 5.10: Instantaneous distribution of the entropy for large-scale separation of a NACA 0012 airfoil at Re = 1, 500, $M_\infty = 0.5$, and $\alpha = 10^\circ$ (Results from Joshua Krakos, MIT PhD Thesis, 2012)

Depending on the specific situation, separation can range from a relatively small bubble near the leading-edge of an airfoil, to a larger separation region on the downstream portions of the airfoil, or even to massive separation occurring over essentially the entire airfoil (such as shown for laminar flow in Figure 5.10). An example of separation near the trailing edge is actually the NACA 0012 $\alpha = 0$, Re = 10, 000 we discussed in Section 5.4.2. Viewing only the displacement thickness distribution for this flow in Figure 5.7, it is impossible (at least I think so) to tell separation has occurred. The velocity profiles, shown in Figure 5.11, do not help significantly either. However, if you look closely enough, you might convince yourself that there is a region of reversed flow (only very near the surface) as the trailing edge is approached. More effective for identification of separation is the skin friction coefficient shown in Figure 5.12. The presence of $C_f < 0$, and therefore separation, is clearly evident for approximately $x/c > 0.8$.

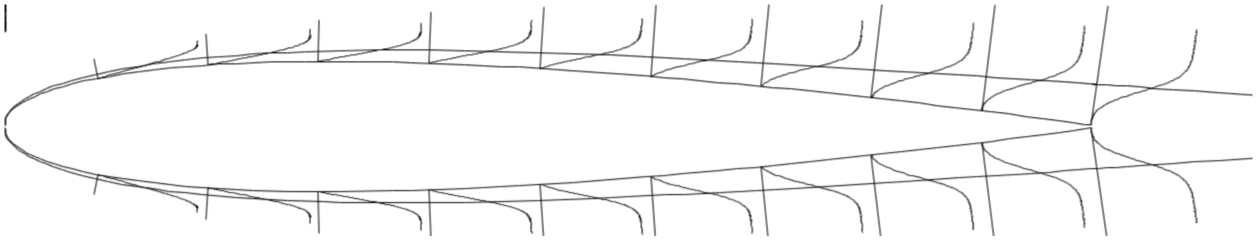

Figure 5.11: Boundary layer velocity profiles with the displacement thickness superimposed for incompressible laminar flows at α = 0 over a NACA 0012 airfoil at Re = 10, 000.

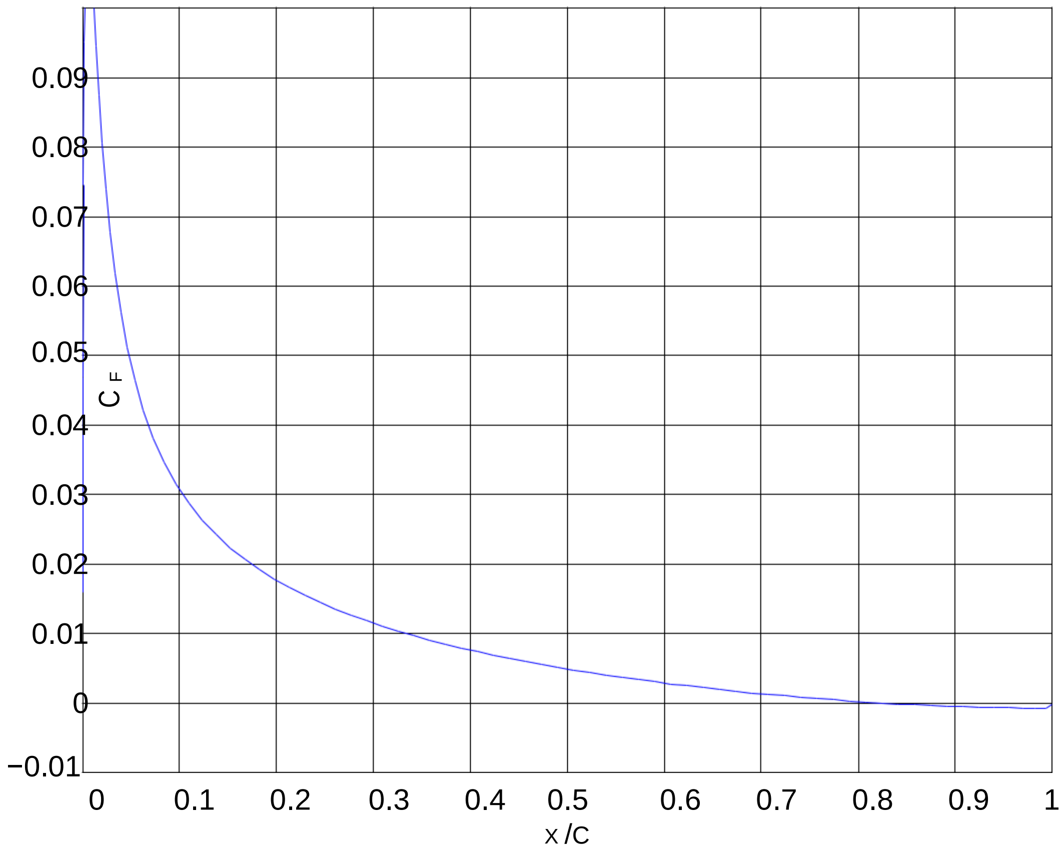

Figure 5.12: C_f distribution for incompressible laminar flows at α = 0 over a NACA 0012 airfoil at Re = 10, 000.

Exactly if separation occurs and the form it takes (leading bubble, moderate trailing edge separation, large-scale separation, etc) is dependent on many factors including the airfoil geometry, the angle of attack, the Reynolds number, the surface roughness, the level of turbulence in the freestream, and many other parameters. As a result, separation remains among the most significant challenges to predict using theoretical methods including computational simulation. Further, experiments are equally challenged because of the difficulty in achieving dynamic similarity for many aeronautical applications. We will revisit separation in more detail in the following module on turbulent boundary layers.

However, one certain thing which can be said is that adverse pressure gradients play a critical role. As we discussed in Section 5.4.2, adverse pressure gradients cause the flow near the wall to decelerate more rapidly than the flow at the edge of the boundary layer. As a result, flow near the wall can reverse directions while the flow outside the boundary layer is still directed downstream.

Further, for the flow upstream of separation as shown in Figure 5.9, adverse pressure gradients must be present as viscous effects cannot, by themselves, cause flow reversal. To see this, consider the velocity profile at $x = x_b$ in the figure, which is the typical profile just before separation. For fluid elements near the wall, $d^2u/dy^2 > 0$. Thus, the viscous effects for fluid elements in this region will cause a positive net force in the x-direction. That is, the low speed flow near the wall is being **pulled** along by the fast flow above it. Without an adverse pressure gradient, the flow would not separate.

SATHYABAMA
INSTITUTE OF SCIENCE AND TECHNOLOGY
(DEEMED TO BE UNIVERSITY)
Accredited "A" Grade by NAAC | 12B Status by UGC | Approved by AICTE
www.sathyabama.ac.in

SCHOOL OF MECHANICAL ENGINEERING
DEPARTMENT OF AERONAUTICAL ENGINEERING

UNITS I -V APPENDIX –LOW SPEED AERODYNAMICS/ SAEA1403

APPENDIX

Boundary Layer Transition and Turbulence

14.1 Overview

14.1.1 Measurable outcomes

We have now made it to the final module! Congratulations! In this module, we discuss the onset and impact of turbulence in boundary layers. The boundary layers discussed in Module 13 were assumed to be steady flows and refered to as a **laminar boundary layer**. However, for many aeronautics applications, the flow inside the boundary layers is in fact not steady. The technical term for this unsteadiness is turbulence, and the boundary layer is refered to as a **turbulent boundary layer**. Turbulence makes dramatic changes in the boundary layer behavior and therefore is critical to account for in the design of most aeronautical vehicles.

Specifically, students successfully completing this module will be able to:

14.1. Explain transition, i.e. the onset of turbulence in a boundary layer and the use of linear stability analysis to predict transition, and describe the dependence of transition on Reynolds number and pressure gradient.

14.2. Explain the qualitative effects of turbulence on boundary layer evolution including the impact on velocity profile, skin friction coefficient, boundary layer thickness, and separation.

14.3. Estimate friction drag on 2-D and 3-D configurations by decomposing the geometry into patches and assuming appropriate skin friction behavior including the possibility of laminar or turbulent boundary layer conditions.

14.2 Boundary Layer Transition

14.2.1 Introduction to flow instability

We return to the excellent NSF Fluid Mechanics Series to introduce the basic ideas of flow instability. While the video does not address instability in boundary layers (which is our application of interest), the basic concepts of flow instability are the same.

The key concepts in this video which we will use in describing boundary layer transition are:

- From approximately 1:29 to 1:50 of the video, a smoke plume is shown rising. The plume starts out steady and laminar at its source and as it rises becomes unstable and, eventually, turbulent. Boundary layer behavior is very similar. Near the leading edge of a body, boundary layers can be stable. Due to a variety of effects (which we will consider shortly), the boundary layer can become unstable further downstream along the surface of the body, eventually leading to a transition to a turbulent boundary layer flow at some downstream location.

- From approximately 5:15 to 13:35, Prof. Erik Mollo-Christensen discusses instability of surface waves and shows several key concepts in flow instability. Specifically:

  – There are ranges of parameters in a flow problem under which small disturbances are amplified. For this surface wave demonstration, the wind speed is the parameter varied. More generally, this wind speed would be non-dimensionalized with combinations of other inputs in the problem to produce a non-dimensional parameter.

  – Even in parameter ranges where the flow is unstable, not all disturbances are amplified. That is, the flow acts as a selective amplifier. Specifically, only disturbances in a specific range of frequencies are amplified. Curves of constant amplication rate can be drawn as functions of the wind speed and frequency. Along the **neutral curve**, disturbances do not decay or amplify. Just to one side of the neutral curve, the combination of parameter value and frequency will be stable (i.e. the disturbance at the given wind speed and frequency will decay); while just to the other side of this neutral curve, the combination of parameter value and frequency will be unstable (i.e. the disturbance will amplify).

  – The critical parameter value is the lowest value of a parameter for which some frequency is amplified. Below this critical parameter value, small disturbances decay and the flow is stable (to small disturbances). Above this parameter value, a range of frequencies will be amplified.

- From approximately 23:50 to 25:10, the flow around a cylinder is shown to have a critical Reynolds number above which the wake is unsteady and forms a vortex sheet (known as a Karman vortex sheet). However, in an important demonstration, Prof. Mollo-Christensen shows that by introduction of a larger disturbance, it is possible to cause a vortex sheet even below the critical Reynolds number. This phenomenon of subcritical, or bypass, transition, occurs in many flows and in particular in boundary layers. This implies that transition will be a function of the amplitude of disturbances present in the flow field. That is, for infinitesimal disturbances, a flow may be stable, but with a sufficiently large disturbances, the flow may still transition to a different (frequently turbulent) state.

14.2.2 Types of boundary layer transition

Next in our consideration of boundary layer transition to turbulence, we recommend revisiting NSF Fluid Mechanics Series video on boundary layers.

The transition process described in the video is commonly referred to as **natural transition** and is representative of boundary layer transition when the disturbances in the flow are very small.

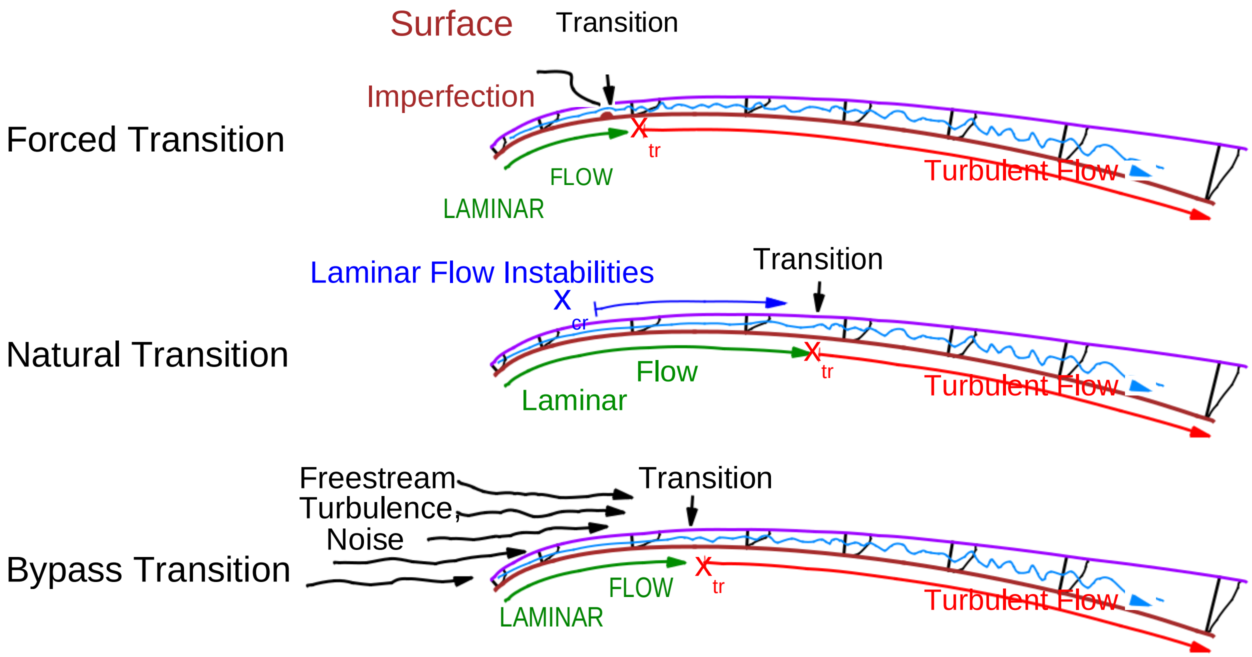

Figure 14.1: Types of boundary layer transition. (Adapted from Drela, **Flight Vehicle Aerodynamics**)

Figure 14.1 shows three types of boundary layer transition: forced transition, natural transition, and bypass transition. Note that the location at which the flow becomes turbulent is labeled x_{tr}. While this figure may imply that the location at which the flow is turbulent is precisely defined, in fact that is not true. This is really because the definition of turbulent flow is not precise.

- Forced transition occurs when a geometric perturbation causes the boundary layer to become turbulent. This geometric perturbation may be unintentional (e.g. due to surface roughness or icing) or may be intentional (e.g. trips strips placed with the intention of causing transition).
- Natural transition occurs when small disturbances are amplified in the boundary layer due to the instability of the laminar boundary layer flow. The point at which the boundary layer is unstable and some disturbances are amplified is called the critical location, x_{cr}. This initial growth of disturbances in natural transition is well described by linearized boundary layer theory. As the disturbances amplify, at some point they will become sufficiently large for nonlinear effects to be important and, eventually, the flow becomes turbulent at x_{tr}.
- Bypass transition occurs when the flow disturbances outside the boundary layer (due to freestream turbulence or noise sources) are sufficiently large that the linear behavior is never observed and the boundary layer immediately becomes turbulent.

14.2.3 Spatial stability of the Blasius flat plate boundary layer

The natural transition process begins with the amplification of infinitesimal waves once the boundary layer flow becomes unstable at x_{cr}. As described in Section 14.2.1, the boundary layer flow acts as a selective amplifier above a critical Reynolds number. The amplification of infinitesimal waves can be analyzed using linear stability theory. Linear stability theory consists of linearizing the Navier-Stokes equations about a steady laminar flow solution and determining if infinitesimal disturbances will be amplified (i.e. the flow is unstable) or will be damped (i.e. the flow is stable).

In particular, we will consider **spatial stability** of boundary layer flows. Spatial stability deter-mines if infinitesimal disturbances with a temporal frequency f grow as they move downstream (that is as x increases). Specifically, we will consider infinitesimal perturbations (about a steady laminar flow) of the form,

$$\tilde{u}(t, x, y, z) = \exp(i2\pi f t)\, \hat{u}(x, y, z) \tag{14.1}$$

$$\tilde{v}(t, x, y, z) = \exp(i2\pi f t)\, \hat{v}(x, y, z) \tag{14.2}$$

$$\tilde{w}(t, x, y, z) = \exp(i2\pi f t)\, \hat{w}(x, y, z) \tag{14.3}$$

$$\tilde{p}(t, x, y, z) = \exp(i2\pi f t)\, \hat{p}(x, y, z) \tag{14.4}$$

So, a spatially stable boundary layer flow is one in which $\hat{u}$, $\hat{v}$, $\hat{w}$, and $\hat{p}$ all decrease in magnitude as $x \to \infty$. Applying spatial stability theory to Blasius flat plate boundary layer flow gives the neutral curve shown in Figure 14.2 plotted as a function of Re_{δ_*},

$$Re_{\delta_*} \equiv \frac{V_\infty \delta^*}{\nu_\infty} \tag{14.5}$$

The critical Reynolds number is,

$$Re_{\delta_*,cr} \approx 400 \tag{14.6}$$

Using Equation (13.96), the critical Reynolds number based on x can be determined,

$$Re_{x,cr} = Re_{\delta_*,cr} \left(\frac{x}{\delta_*}\right)_{cr} \tag{14.7}$$

$$= Re_{\delta_*,cr} \frac{Re_{x,cr}}{1.72} \tag{14.8}$$

$$\Rightarrow Re_{x,cr} = \left(\frac{Re_{\delta_*,cr}}{1.72}\right)^2 \tag{14.9}$$

$$\Rightarrow Re_{x,cr} = 54,000 \tag{14.10}$$

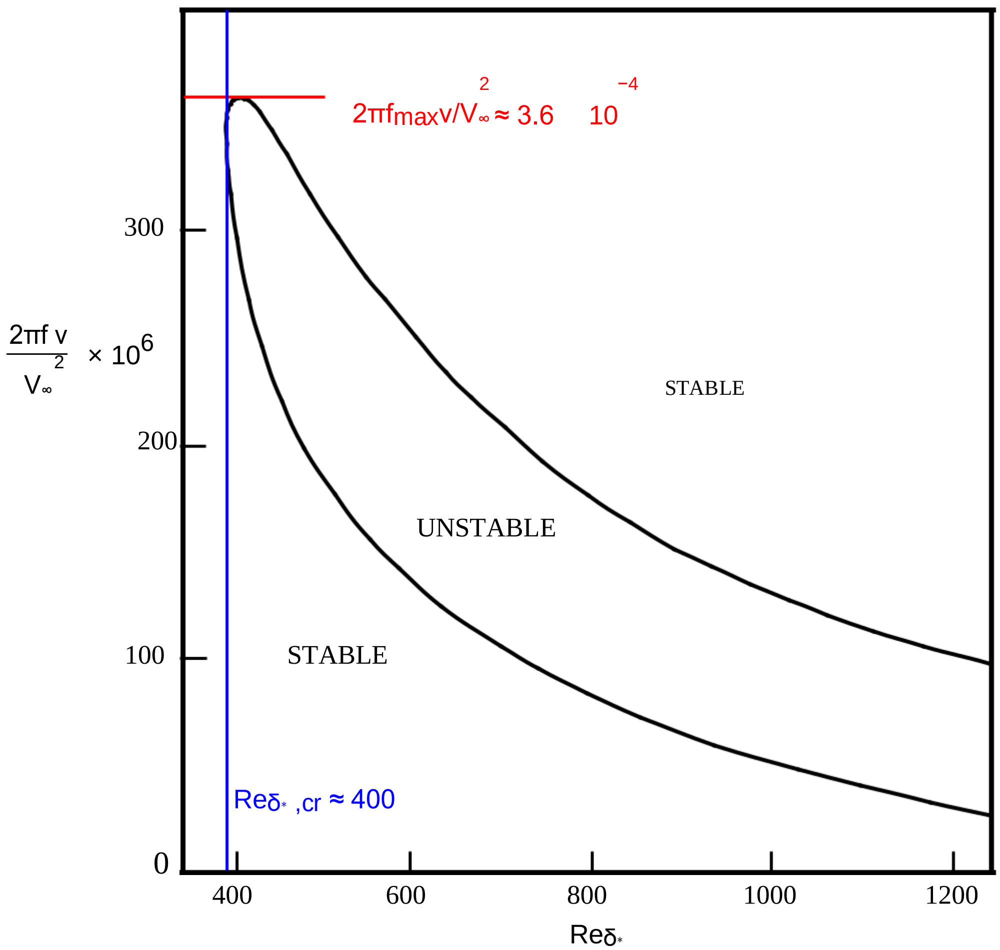

Figure 14.2: Neutral curve for Blasius boundary layer flow

14.2.5 Transition prediction

Although small disturbances are amplified once the boundary layer is unstable, the flow does not immediately transition at x_{cr} as the disturbances must grow to sufficient amplitude for turbulence to occur. A common engineering approach for the prediction of transition is known as the e^N method and is based on the spatial stability theory discussed in Section 14.2.3. The idea is to estimate the amplification of disturbances as a function of downstream distance. Let the amplitude of a disturbance of frequency f be $a_f(x)$. The amplification (or growth) rate of this disturbance is defined as $\alpha_f(x)$ where,

$$\frac{da_f}{dx} = \alpha_f a_f \qquad (14.11)$$

Or, alternatively, this can be written as,

$$\frac{d}{dx}(\ln a_f) = \alpha_f \qquad (14.12)$$

Note that the dependence of the growth rate on f and x can be observed in the flat plate boundary layer results in Figure 14.2. For low x values (i.e low Re_{δ^*} values), disturbances are damped and therefore $\alpha_f < 0$. Then, as x increases, for certain values of f , the flow is unstable and therefore $\alpha_f > 0$.

The e^N method considers the greatest amplification for all f by defining the overall amplitude A,

$$\frac{d}{dx}(\ln A) \equiv \max_f(\alpha_f, 0) \qquad (14.13)$$

Let the initial amplitude of a disturbance as it enters the boundary layer be A_0. The e^N method claims that transition to turbulence occurs when A/A_0 reaches a critical value of $e^{N_{cr}}$. Or, taking the natural log, transition occurs when $\ln A/A_0 = N_{cr}$. We note that Equation (14.13) can be written equivalently as,

$$\frac{dN}{dx} = \max_f(\alpha_f, 0) \qquad \text{where } N \equiv \ln(A/A_0) \qquad (14.14)$$

And then transition occurs when $N = N_{cr}$.

The value of N_{cr} is dependent on the disturbances which are present in the flow, including geometry perturbations or any other effect which can create flow disturbances. Some typical values of N_{cr} are:

- For very clean flow such as a sailplane in flight or a very clean wind tunnel $N_{cr} = 12$.
- For an average wind tunnel, $N_{cr} = 9$.
- For a fairly turbulent wind tunnel, $N_{cr} = 4$.

An example of the evolution of N for a NACA 0004 airfoil at $\alpha = 0^\circ$ at $Re = 10^5$ and 2×10^6 is shown in Figure 14.3 (these results were generated using Xfoil). For the $Re = 1 \times 10^5$ flow, the value of $N = 0$ until approximately $x/c = 0.5$, at which point N increases indicating the boundary layer has become unstable. Since the airfoil is quite thin, we expect the behavior to be similar to a flat plate flow. Recalling that for flat plate flow $Re_{x,cr} = 54,000$, then we expect,

$$\frac{x_{cr}}{c} = \frac{Re_{x,cr}}{Re} = \frac{54,000}{Re} \qquad (14.15)$$

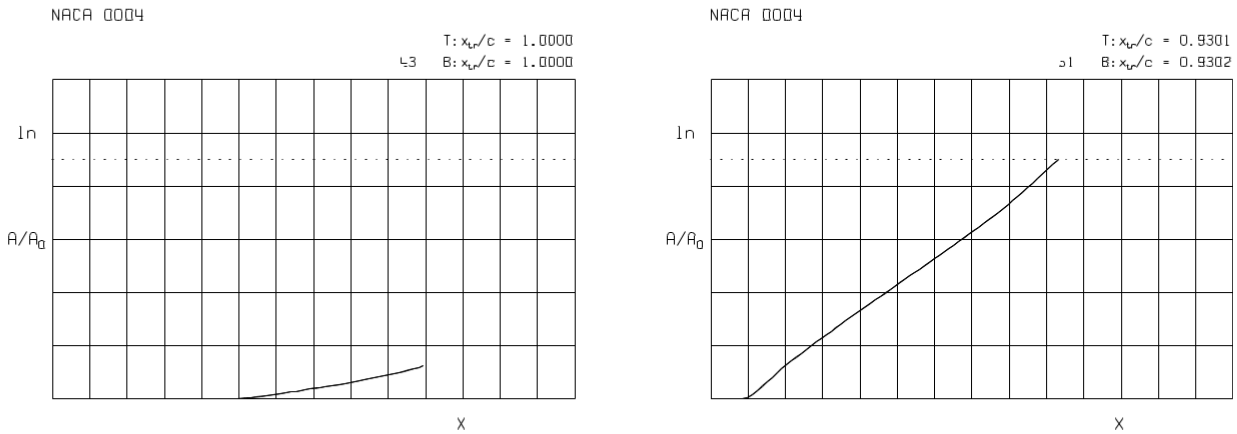

Figure 14.3: N (x) variation for NACA 0004 incompressible flow at $\alpha = 0^{\circ}$, and $Re = 1 \times 10^{5}$ and $Re = 2 \times 10^{6}$

Thus, for $Re = 10^{5}$, flat plate theory would predict $x_{cr}/c = 0.54$, which is in good agreement with the results of the figure. For $x/c > 0.5$, the results show that N increases to approximately a value of 1.5 at the trailing edge. Thus, transition does not occur at this condition (unless $N_{cr} \leq 1.5$ which is highlighly unlikely).

For the higher Reynolds number $Re = 2 \times 10^{6}$ flow, instability is observed in the Xfoil results at approximately $x/c = 0.1$. This is in reasonable agreement with the flat plate result which gives $x_{cr}/c = 0.03$. At this higher Reynolds number, N (x) grows and reaches the critical value, which was chosen as $N_{cr} = 9$. Specifically, transition is predicted at $x_{tr}/c = 0.93$.

In general, boundary layers in regions with adverse pressure gradients are unstable and will amplify disturbances, and the greater the magnitude of the adverse pressure gradient the larger the amplification will tend to be. While favorable pressure gradients generally improve the stability of a boundary layer, the impact is not as significant as the destabilizing influence of an adverse pressure gradient. As a result, any effect that lowers the minimum surface pressure on the airfoil almost always will increase the likelihood of transition. This behavior is demonstrated in Figure 14.4 which shows N (x) for a set of symmetric NACA airfoils at $Re = 10^{5}$ and $\alpha = 0^{\circ}$. As the thickness increases, and therefore the minimum pressure drops, the boundary layer has large values of N (x). Thus, the boundary layers transition sooner on the thicker airfoils.

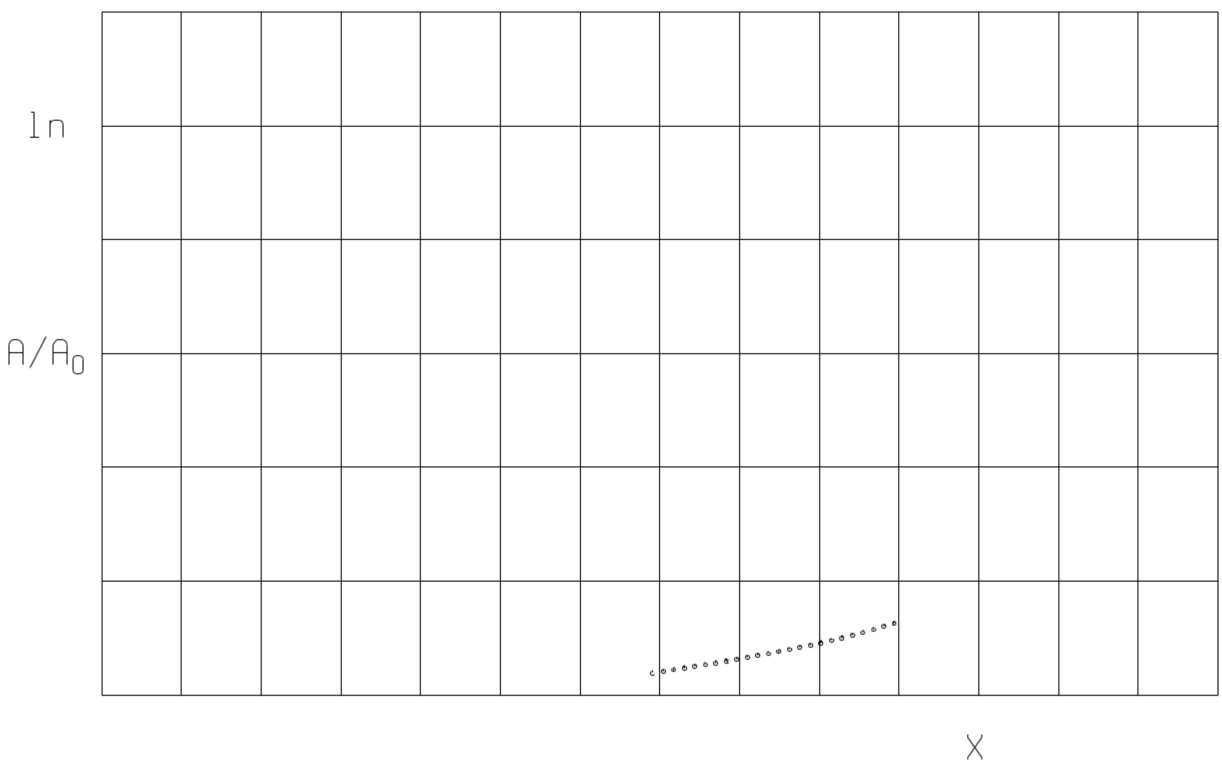

Figure 14.4: N (x) variation for incompressible flow over NACA 00XX airfoils at $\alpha = 0^\circ$ and $Re = 10^5$

14.3 Turbulent boundary layers

14.3.1 Introduction to turbulence

We once again return to the NSF Fluid Mechanics Series to introduce the basic ideas of turbu-lence.

The key concepts in this video with respect to turbulent boundary layers are:

- The unsteadiness in a turbulent flow causes mixing that significantly changes the distribution of the mean velocity in a turbulent boundary layer from the steady flow in a laminar boundary layer. Specifically, the turbulent motion causes higher velocity fluid away from the wall to be mixed into the flow near the wall causing an increase in the mean velocity near the wall. Similarly, the low velocity fluid near the wall is mixed into the flow away from the wall causing the mean velocity away from the wall to decrease. As a result, the skin friction will generally be larger for a turbulent boundary layer compared to a laminar boundary layer (at similar Reynolds number) since the near-wall velocity and, therefore, the velocity gradient ($\partial u/\partial y$) will be larger in a turbulent flow. Further, because of these slower mean velocity away from the wall, a turbulent boundary layer will tend to be thicker than a laminar boundary layer (assuming the flow has not separated). This discussion of the impact of turbulent mixing on the velocity field is demonstrated in the discussion of the velocity distribution in pipe flow from 10:05 to 14:05. In particular, carefully study the motion of the colored dye flow to see how the fluid in the center of the pipe moves toward the wall, and similarly the fluid near the wall moves toward the center of the pipe.

- The large scale motion of a turbulent flow is not significantly affected by the Reynolds number. However, the Reynolds number does impact the fine scale motion. For turbulent flows, the length scales of the smallest eddies (relative to the largest length scales in the flow) will decrease as the Reynolds number increases.

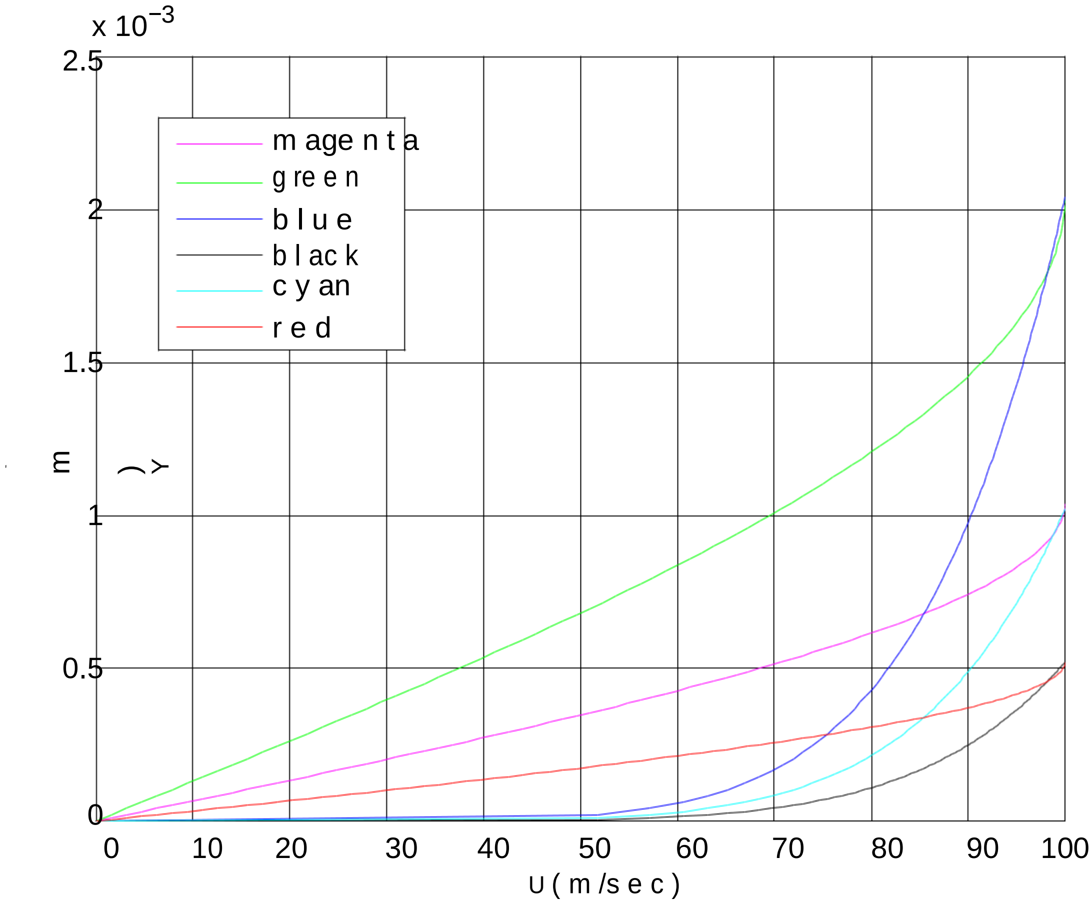

14.3.3 Turbulent flat plate flow

As described in the previous section, the skin friction in a turbulent boundary layer is generally higher than a laminar boundary layer at similar Reynolds numbers because of the fuller velocity profile. Figure 14.5 shows a comparison of laminar and turbulent skin friction coefficients C_f as a function of Re_x. The laminar result is taken from the Blasius flat plate boundary layer theory. The two turbulent results are based on experimental data and are frequently used when estimate skin friction drag of turbulent flows. The most accurate skin friction result is

$$C_f = 0.370 (\log_{10} Re_x)^{-2.58} \tag{14.20}$$

which accurately represents the experimental behavior of turbulent flows over the entire range of Reynolds numbers shown. The other result is

$$C_f = 0.0576 Re_x^{-0.2} \tag{14.21}$$

While this approximation is frequently used because of its simplicity, it is only quantitatively accurate from approximately $10^5 \le Re \le 10^6$ (though clearly the qualitative trends of C_f (Re_x) are still well represented outside of this range).

Depending on the specific Reynolds number, we note that the skin friction in the turbulent regime can be 3-6 times larger than the skin friction in the laminar regime (at the same Reynolds number). Thus, this large difference in skin friction combined with the general uncertainty of where

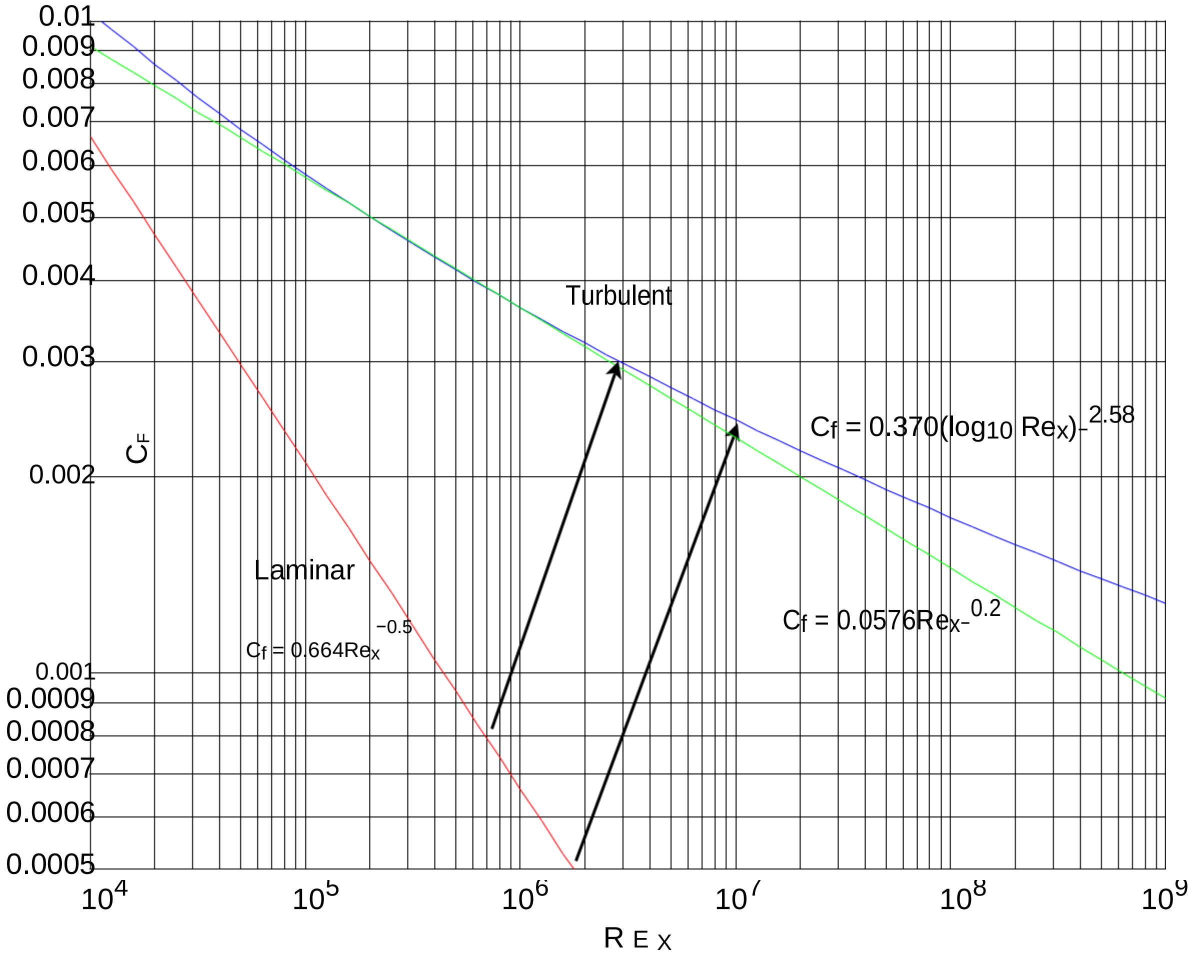

Figure 14.5: Comparison of skin friction on a flat plate for laminar and turbulent flow. Note that the $C_f = 0.370(\log_{10} Re_x)^{-2.58}$ turbulent flow formula is accurate of the entire range of Reynolds numbers while the $C_f = 0.0576 Re_x^{-0.2}$ is only accurate from approximately $10^5 < Re_x < 10^6$

transition will occur on an airfoil makes the estimation of friction drag difficult for problems in which the chord Reynolds number is between approximately $10^4 < Re < 10^7$. For $Re < 10^4$, the flow generally does not transition unless separation is involved. And, for $Re > 10^7$, the flow transition typically occurs so close to the leading edge that we can effectively model the entire boundary layer as being turbulent with minimal errors.

Figure 14.6 demonstrates how the C_f behavior is impacted by changes in Re, and in particular shows that when transition occurs the C_f increases rapidly. We note that for $Re = 10^6$, transition does not occur (using $N_{cr} = 9$), while for $Re = 10^7$ the transition occurs at approximately 33% of the chord. And, for $Re = 10^8$, transition occurs within the first few percent of the chord. In both cases, note the rapid increase in C_f as a result of transition to turbulence.

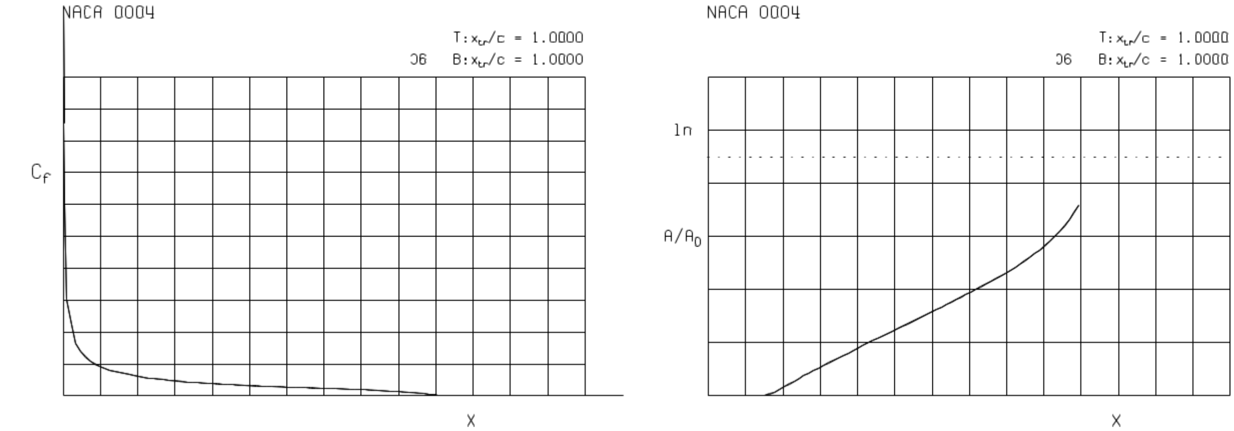

(a) Re = 10^6

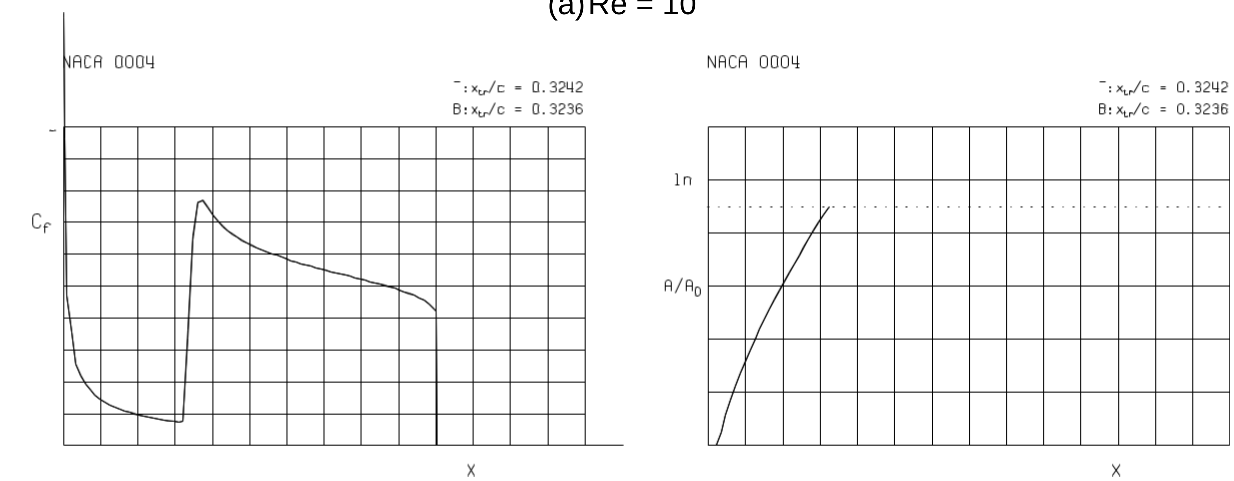

(b) Re = 10^7

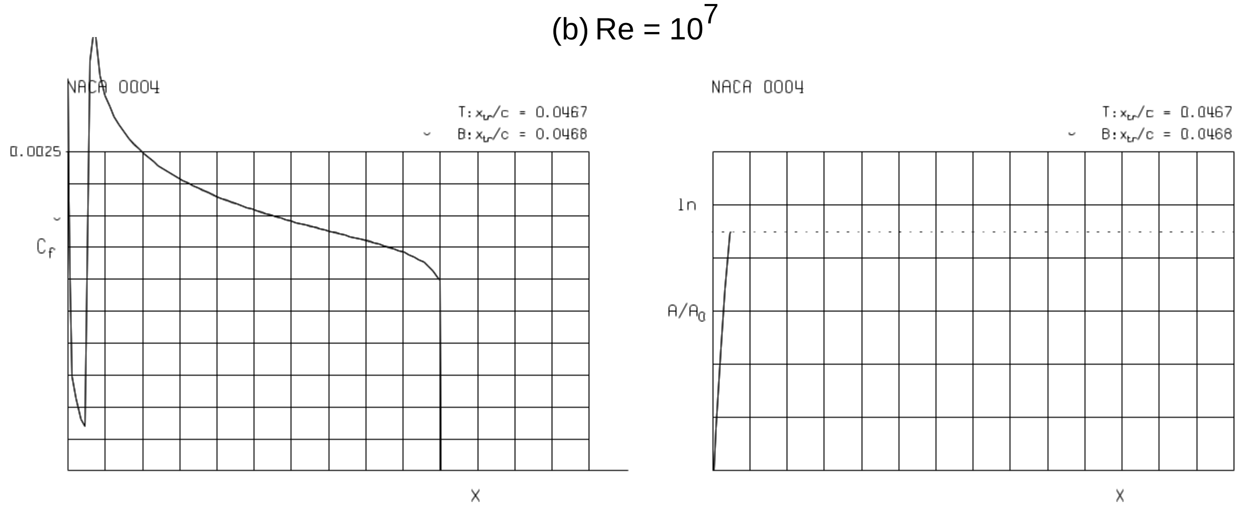

(c) Re = 10^8

Figure 14.6: Impact of Re on C_f (x/c) and N (x/c) for NACA 0004 airfoil at α = 0

14.3.5 Turbulence and separation

While mixing in a turbulent boundary layer leads to an increase in skin friction, the mixing is actually beneficial in terms of separation. As we discussed in Section 13.4.4, separation is a result of adverse pressure gradients which decelerate the flow near the wall eventually leading to a reversal of the flow direction (relative to the flow outside of the boundary layer). However, since turbulent mixing continually brings higher velocity fluid towards the wall, then a turbulent boundary layer will be able to sustain larger increases in pressure before separation occurs (relative to laminar flow).

To demonstrate this behavior, we consider the flow over a NACA 5512 airfoil at $\alpha = 0.5^\circ$. For Re $= 10^5$ with natural transition (see Figure 14.7), the flow separates from the upper surface at approximately $x/c = 0.53$ (this can be determined from where $c_f < 0$). The flow in this separation does transition to turbulence at $x/c = 0.83$, however, it remains separated. The associated table shows the drag and lift coefficient for this flow. The total drag $c_d = 0.02737$ is quite high with most of this drag due to the form drag $c_{dform} = 0.02030$. The lift is also low with $c_l = 0.4904$ compared to the inviscid (potential flow) value of $c_l = 0.7150$.

A common approach for flows in this Reynolds number regime is to cause turbulent mixing by tripping the flow prior to where separation would otherwise occur. This is shown in Figure 14.8 where the flow on the upper surface has been tripped at $x/c = 0.5$. As the results show, the flow no longer separates and the overall drag is significantly reduced to $c_d = 0.01507$. This reduction is due solely to the decreased form drag which is now $c_{dform} = 0.00545$; in fact, the skin friction drag has increased because the boundary layer remains attached. The lift, $c_l = 0.5804$, is also higher because of the flow remaining attached.

Finally, we consider natural transition again, but this time at a higher Reynolds number of $Re = 5 \times 10^6$. As shown in Figure 14.9, transition occurs at $x/c = 0.58$ on the upper surface and the flow remains attached without the need for forcing transition. Thus, higher Reynolds number flows will generally be more resistant to separation because of the greater likelihood of turbulence in the boundary layers. We also note for this high Reynolds number case that the lift $c_l = 0.7150$ is nearly the inviscid value.

Re	Transition	c_d	c_{df}	c_{dform}	c_l
10^5	natural	0.02737	0.00707	0.02030	0.4904
10^5	tripped	0.01507	0.00962	0.00545	0.5804
5×10^6	natural	0.00514	0.00429	0.00085	0.7150
Inviscid					0.7575

Table 1: Aerodynamic performance of NACA 5512 at $\alpha = 0.5^\circ$

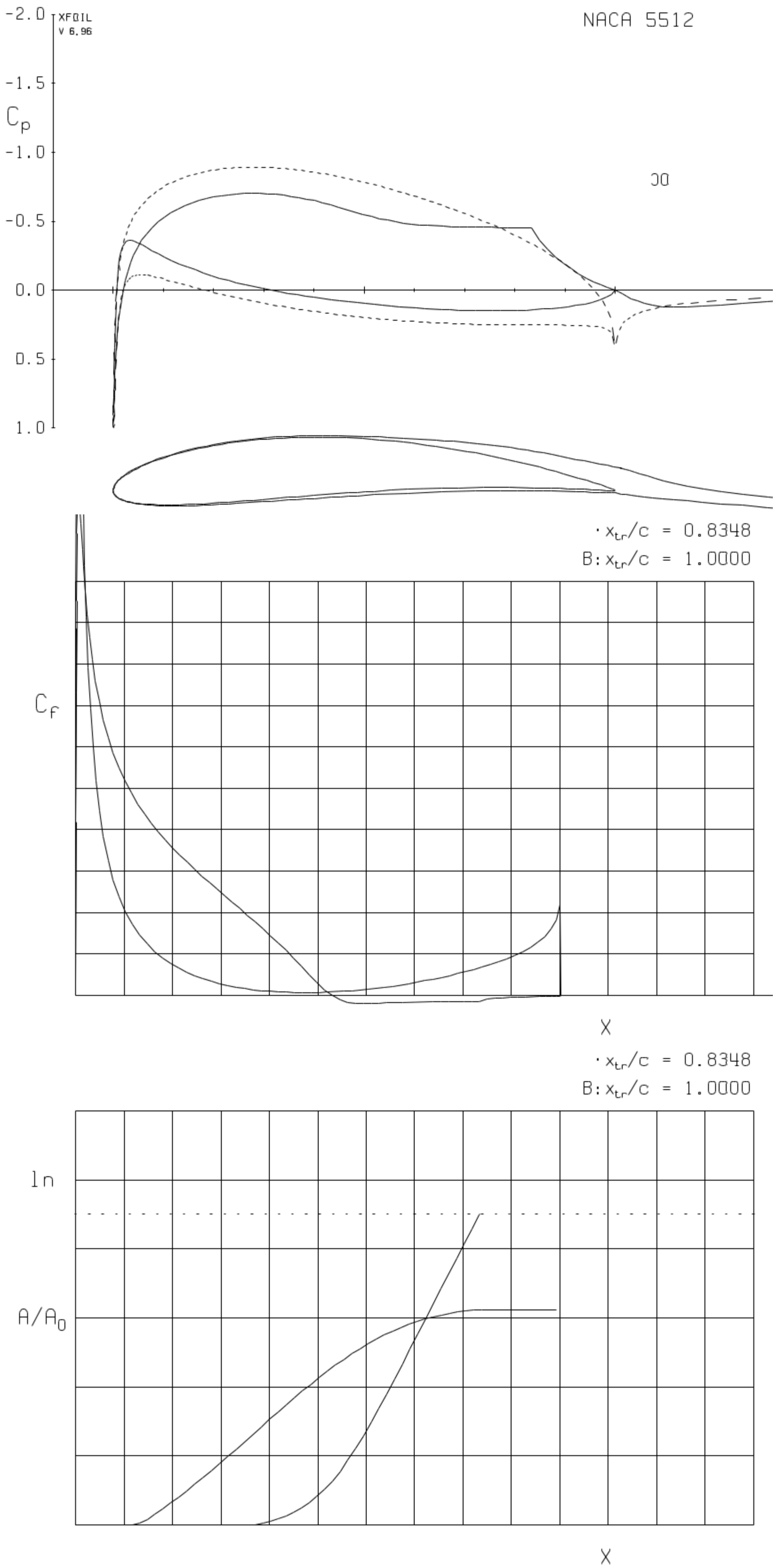

Figure 14.7: NACA 5512 at $\alpha = 0.5^{\circ}$, Re = 10^5, natural transition with $N_{cr} = 9$

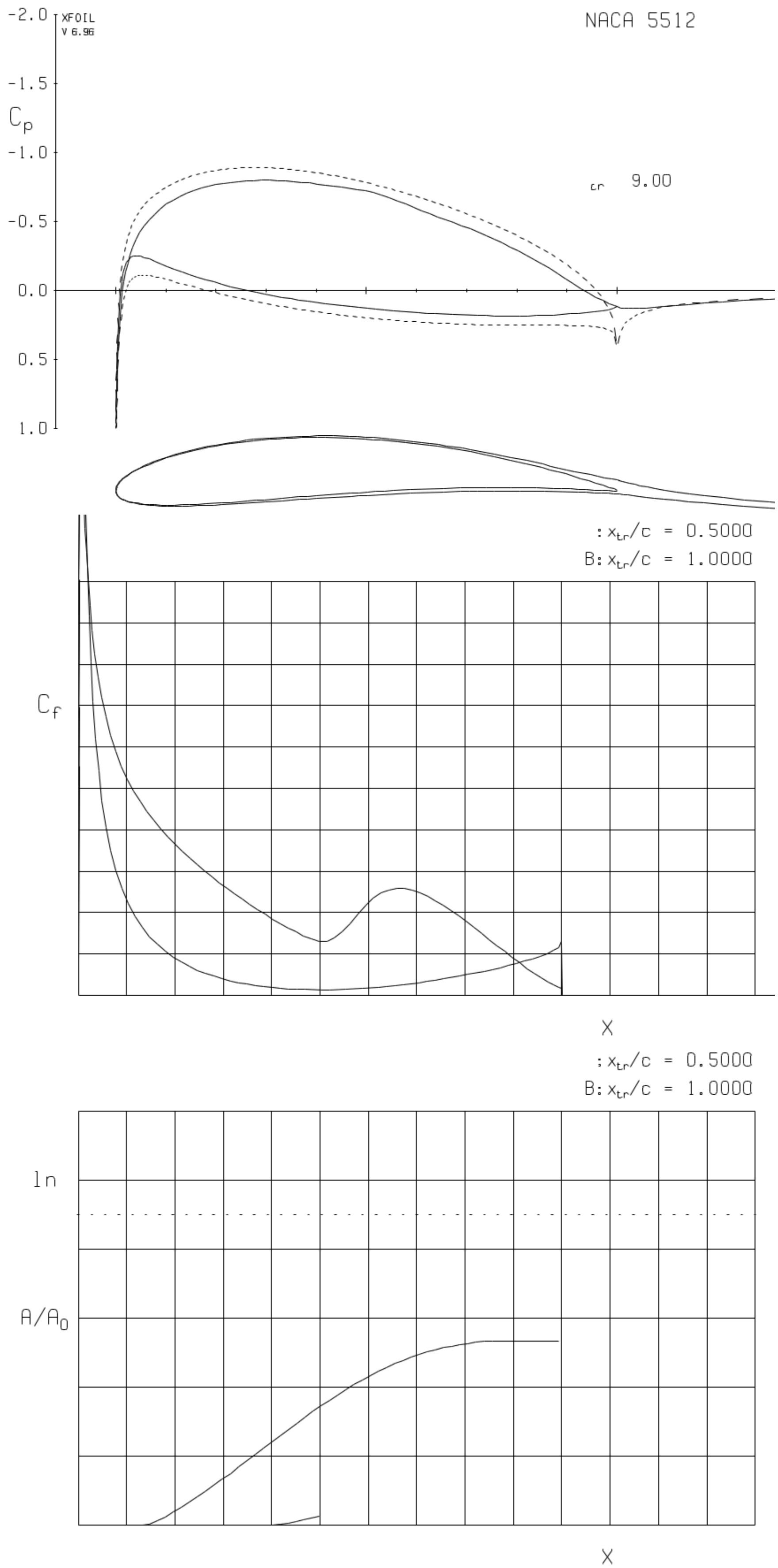

Figure 14.8: NACA 5512 at $\alpha = 0.5^{\circ}$, Re = 10^5, tripped on upper surface at x/c = 0.5

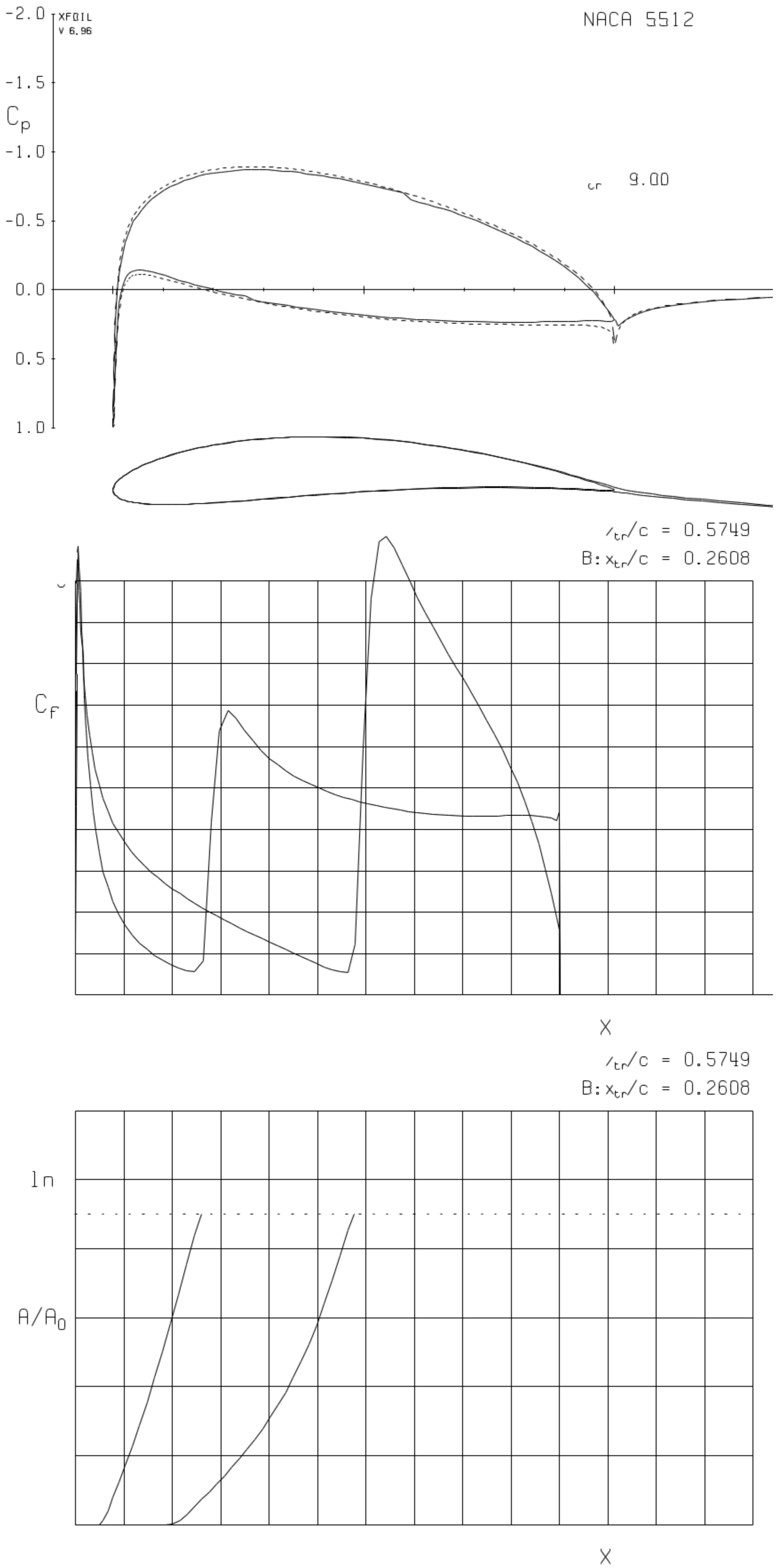

Figure 14.9: NACA 5512 at $\alpha = 0.5^{\circ}$, $Re = 5 \times 10^6$, natural transition with $N_{cr} = 9$

14.4.2 Drag versus Reynolds number behavior for thick and thin airfoils

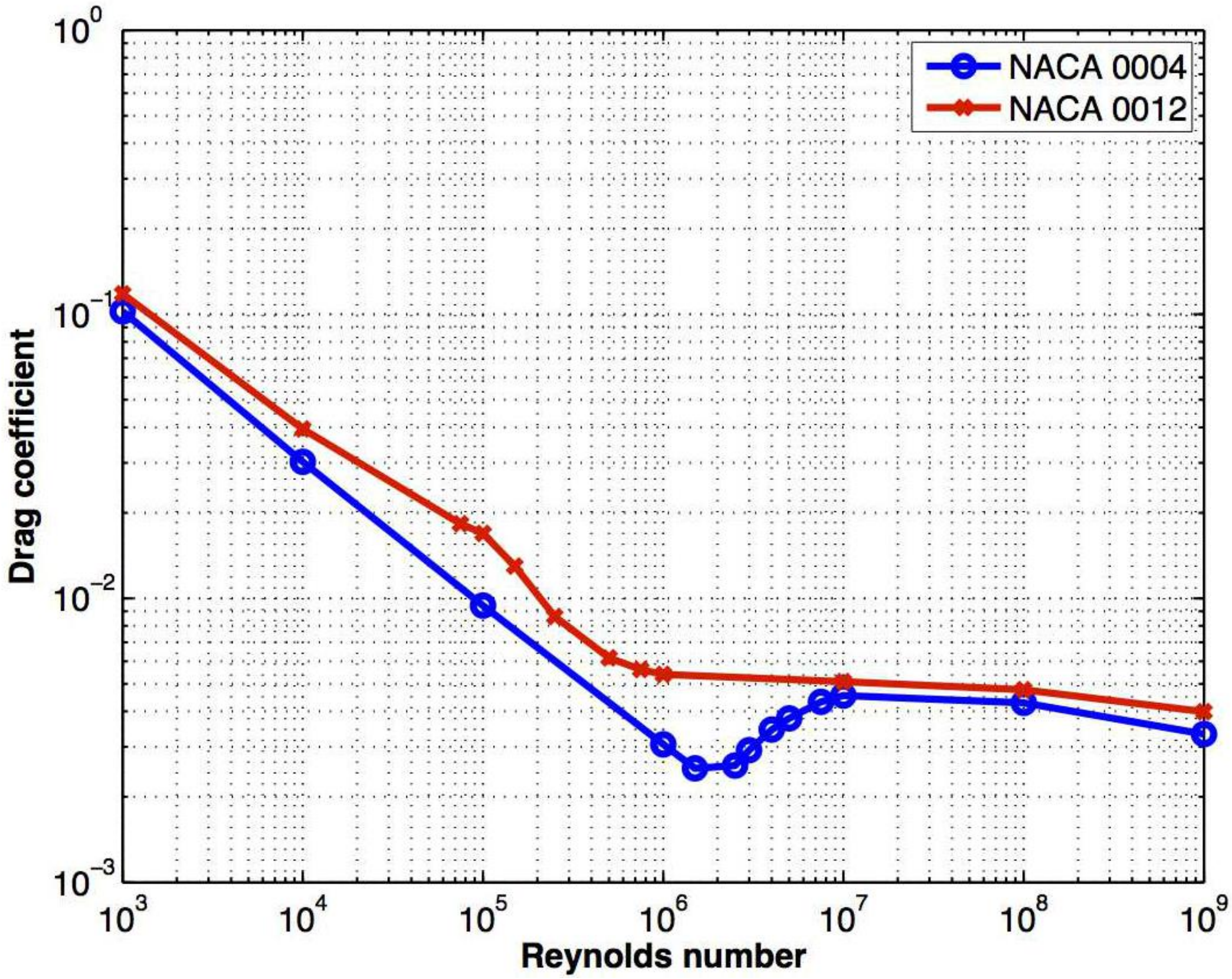

The figure shows the variation of c_d with Re for the NACA 0004 and 0012 airfoils.

- For the NACA 0012 for Re ≤ 10^5, the slope of c_d versus Re is not −1/2 as predicted from flat plate, laminar boundary layer theory. Explain why this is happening by inspecting the boundary layer behavior.

- For Re just greater than 10^5, the drag coefficient on the NACA 0012 drops rapidly. Explain why this is happening by inspecting the boundary layer behavior.

- For the NACA 0004, the drag coefficient changes behavior around Re = 2×10^6. Explain why this is happening by inspecting the boundary layer behavior.

In the additional pages of this problem, you will find C_p, C_f , and N distributions versus x/c at the following conditions:

- NACA 0004: Re = 1e3, 1e4, 1e5, 1e6, 2e6, 5e6, 1e7, 1e9

- NACA 0012: Re = 1e3, 1e4, 1e5, 2e5, 5e5, 1e6, 1e7, 1e9

NACA 0004 plots

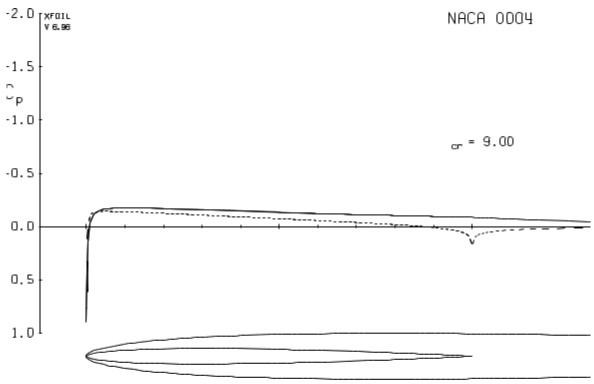

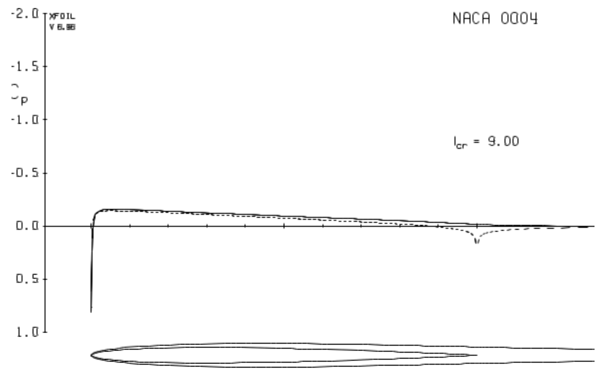

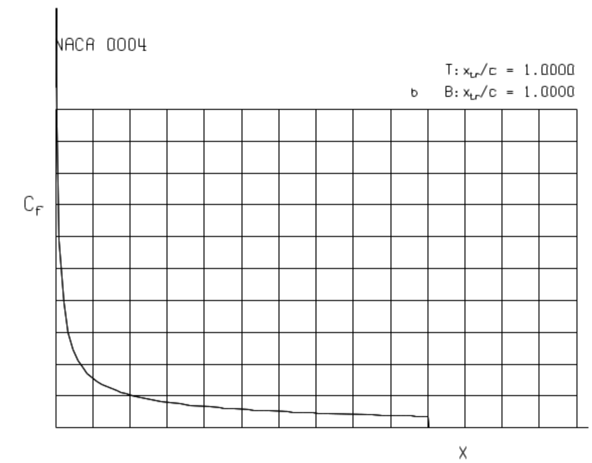

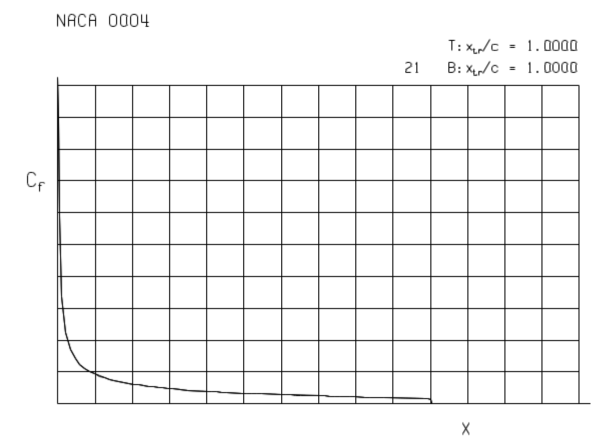

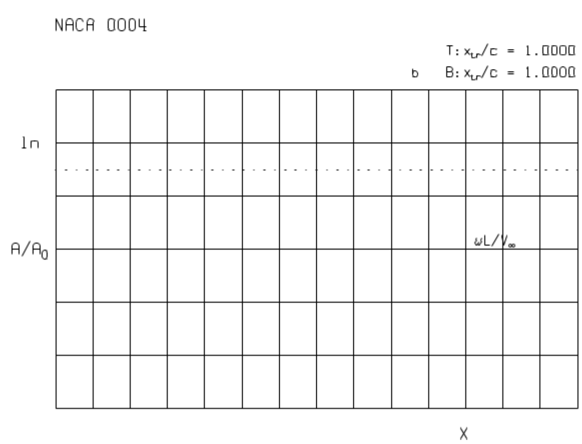

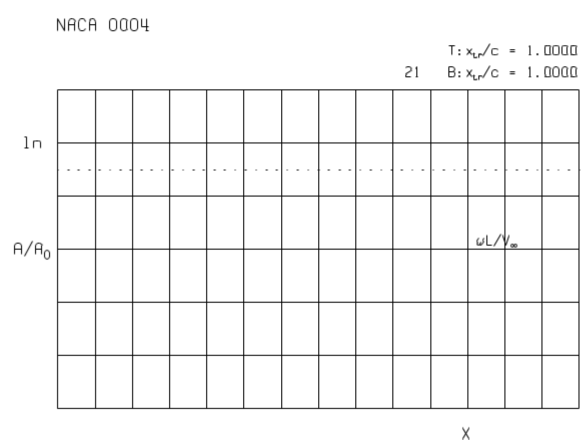

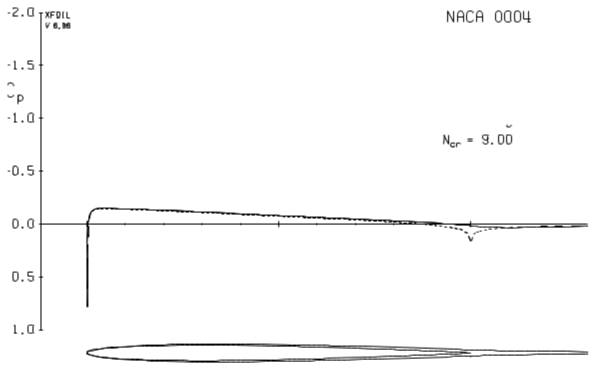

XFOIL
V 6.96
NACA 0004
-2.0
-1.5
Cp
-1.0
Ncr = 9.00
-0.5
0.0
0.5
1.0

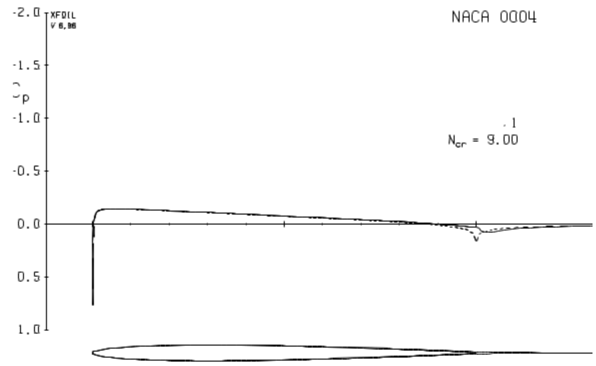

XFOIL
V 6.96
NACA 0004
-2.0
-1.5
Cp
-1.0
Ncr = 9.00
-0.5
0.0
0.5
1.0

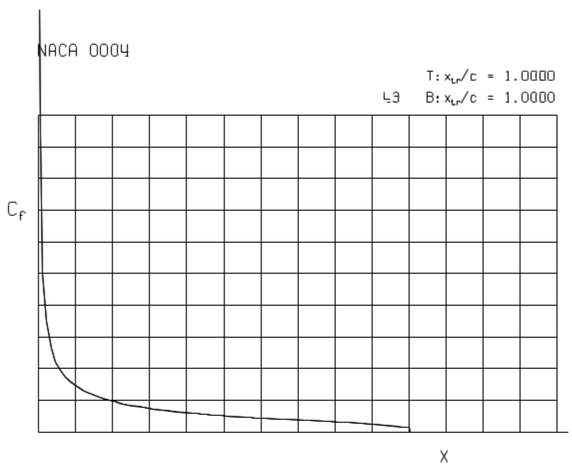

NACA 0004
T: xtr/c = 1.0000
B: xtr/c = 1.0000
Cf
X

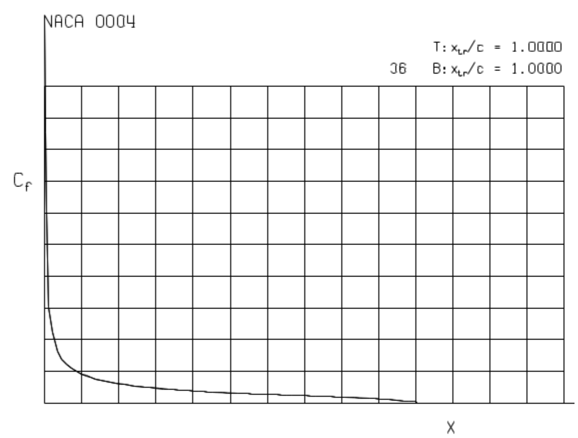

NACA 0004
T: xtr/c = 1.0000
36 B: xtr/c = 1.0000
Cf
X

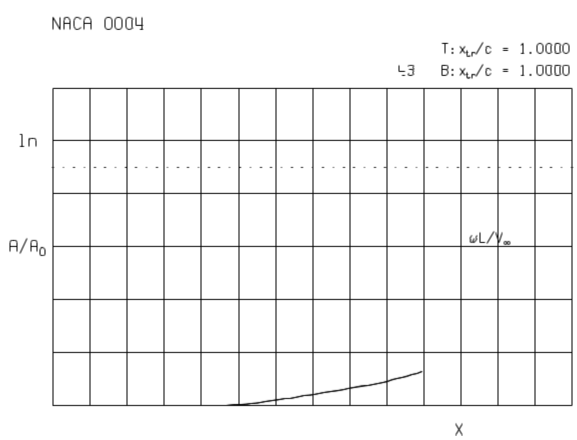

NACA 0004
T: xtr/c = 1.0000
B: xtr/c = 1.0000
ln
A/A0
ωL/V∞
X

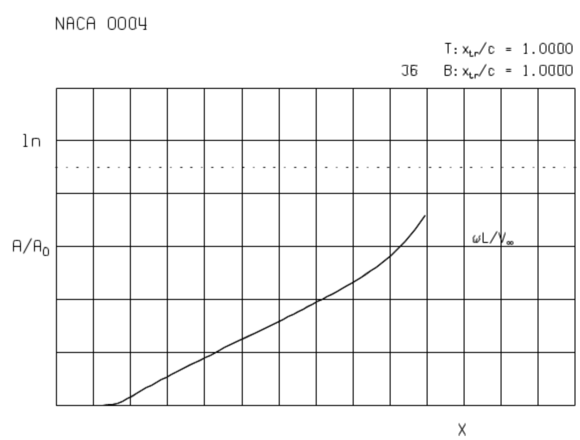

NACA 0004
T: xtr/c = 1.0000
36 B: xtr/c = 1.0000
ln
A/A0
ωL/V∞
X

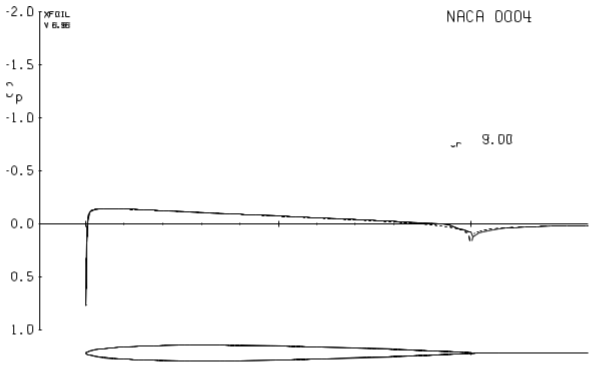
NACA 0004
-2.0
-1.5
Cp
-1.0
-0.5
0.0
0.5
1.0
9.00

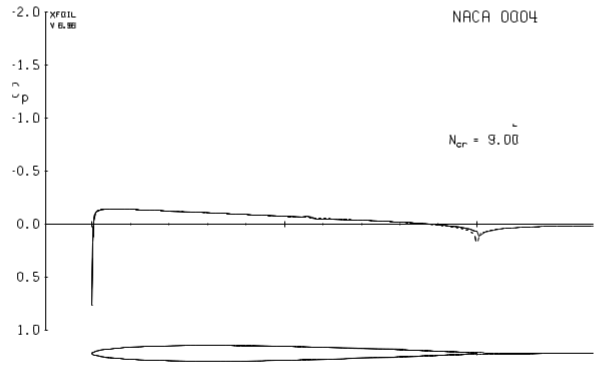
NACA 0004
-2.0
-1.5
Cp
-1.0
-0.5
0.0
0.5
1.0
Ncr = 9.00

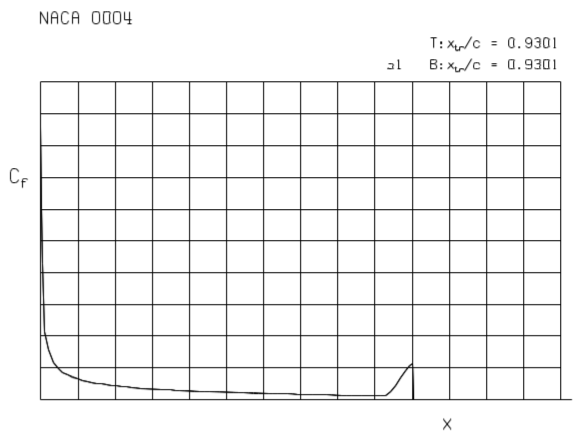
NACA 0004
T: xtr/c = 0.9301
B: xtr/c = 0.9301
Cf
X

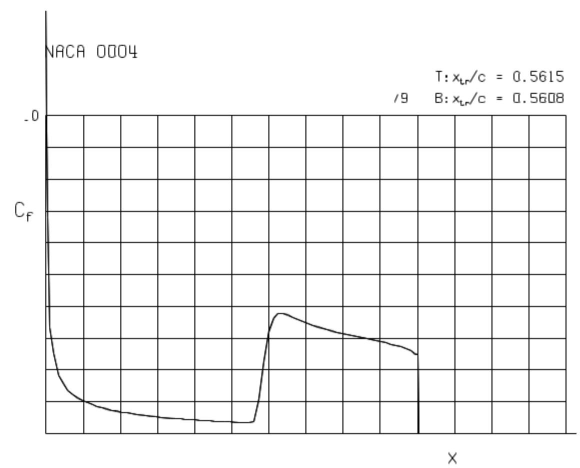
NACA 0004
T: xtr/c = 0.5615
B: xtr/c = 0.5608
Cf
X

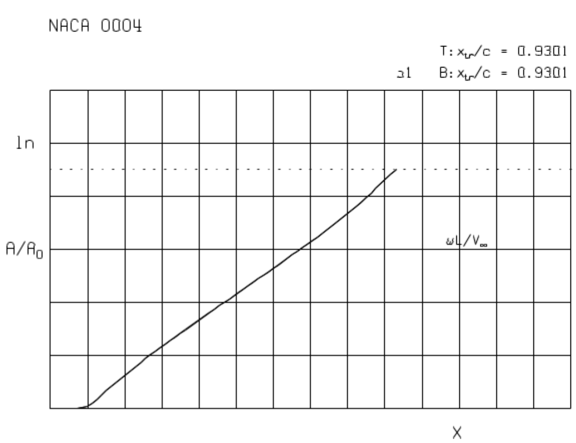
NACA 0004
T: xtr/c = 0.9301
B: xtr/c = 0.9301
ln
A/A0
ωL/V∞
X

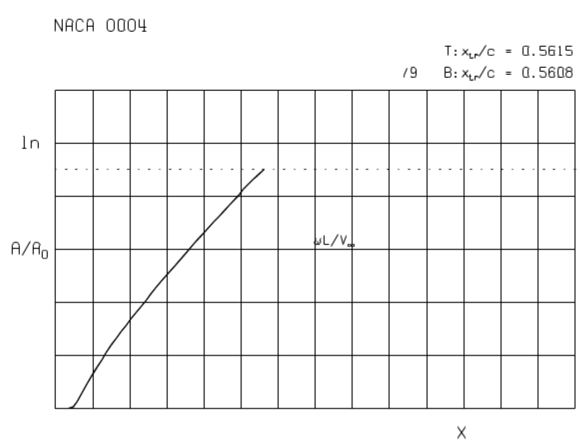
NACA 0004
T: xtr/c = 0.5615
B: xtr/c = 0.5608
ln
A/A0
ωL/V∞
X

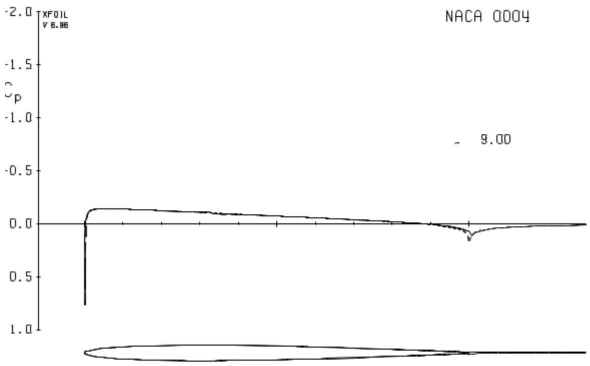
XFOIL
V 6.96
NACA 0004
-2.0
-1.5
-1.0
-0.5
0.0
0.5
1.0
9.00

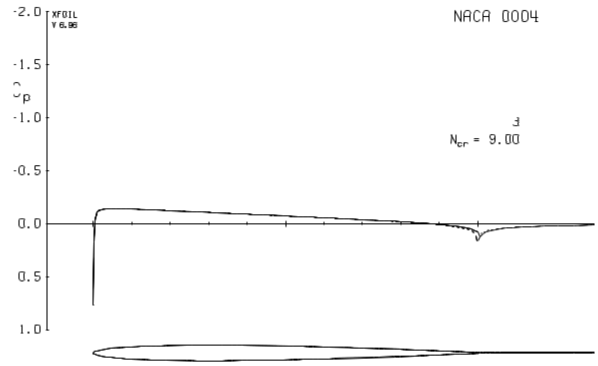
XFOIL
V 6.96
NACA 0004
-2.0
-1.5
-1.0
-0.5
0.0
0.5
1.0
N_{cr} = 9.00

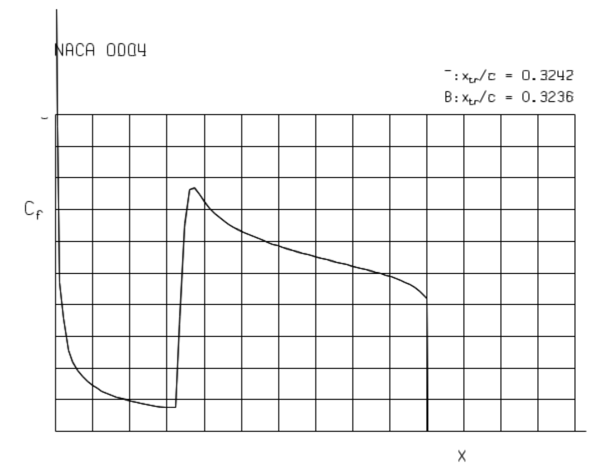
NACA 0004
B: x_{tr}/c = 0.3236
C_f
X

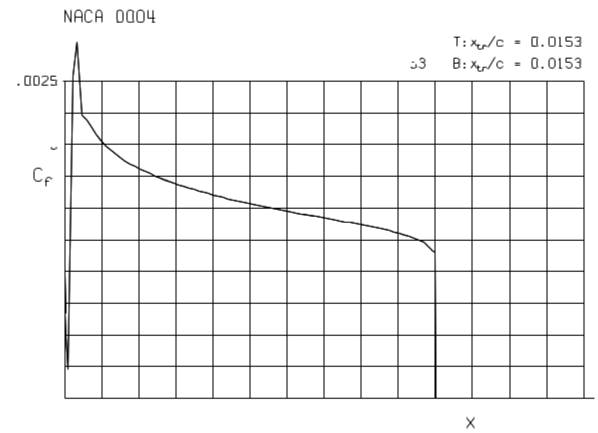
NACA 0004
T: x_{tr}/c = 0.0153
B: x_{tr}/c = 0.0153
.0025
C_f
X

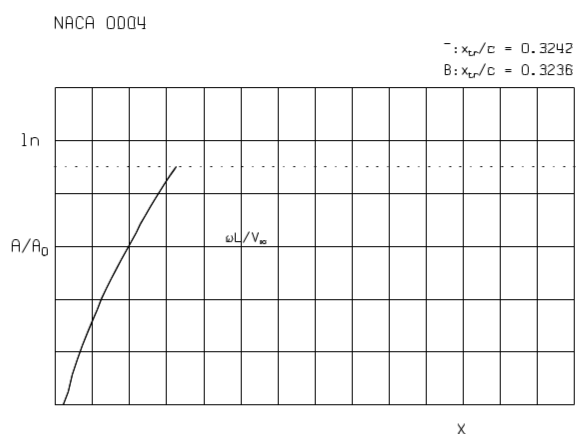
NACA 0004
B: x_{tr}/c = 0.3236
ln
A/A_0
$\omega L/V_\infty$
X

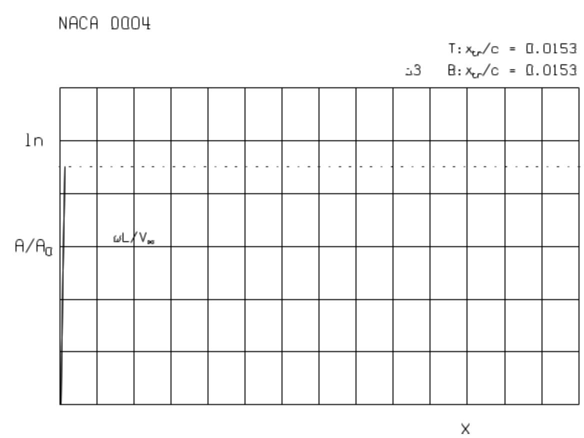
NACA 0004
T: x_{tr}/c = 0.0153
B: x_{tr}/c = 0.0153
ln
A/A_0
$\omega L/V_\infty$
X

NACA 0012 plots

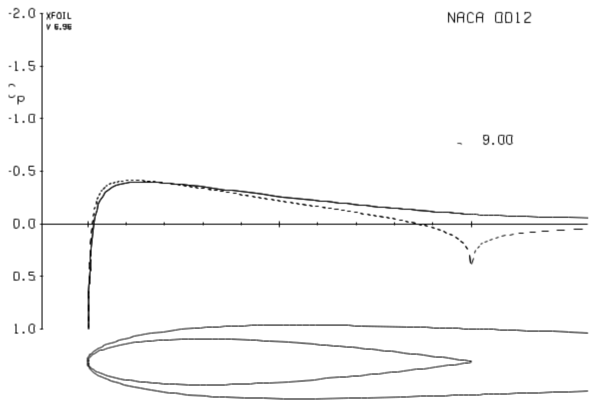

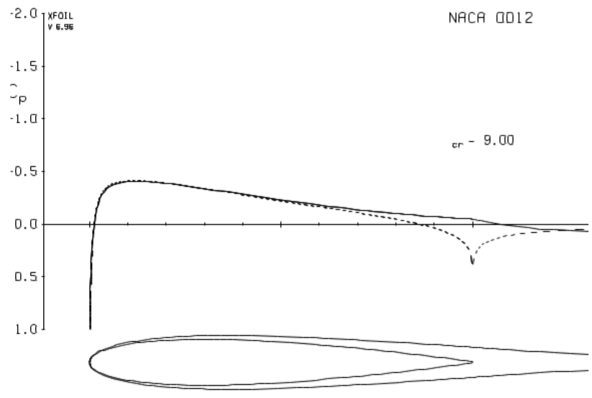

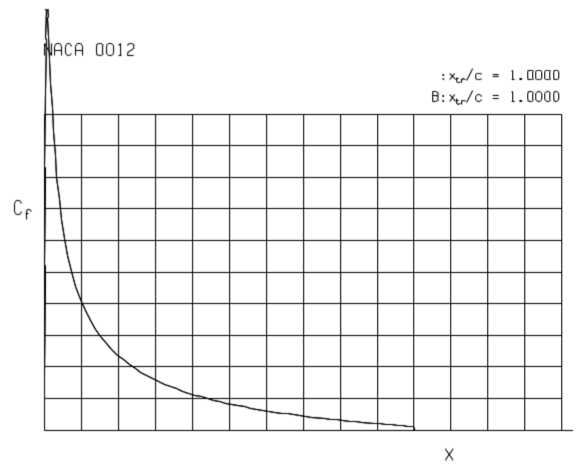

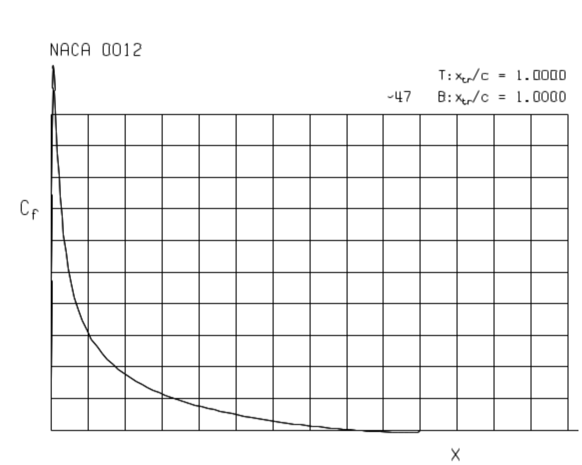

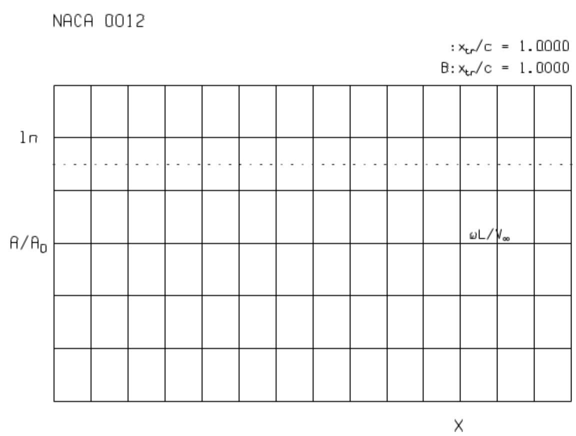

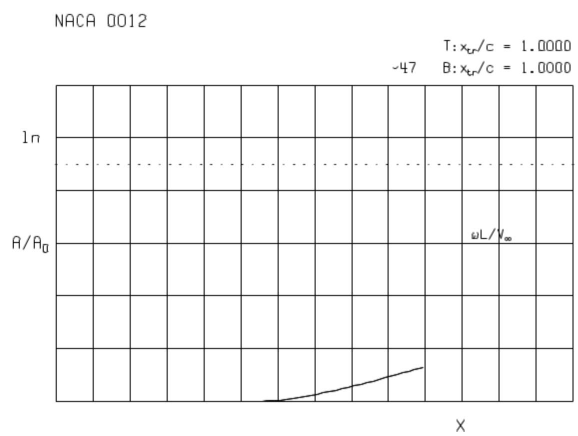

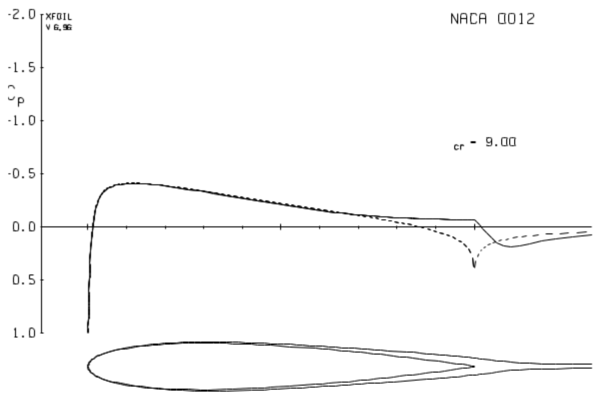
-2.0
XFOIL
V 6.96
NACA 0012
-1.5
Cp
-1.0
cr = 9.00
-0.5
0.0
0.5
1.0

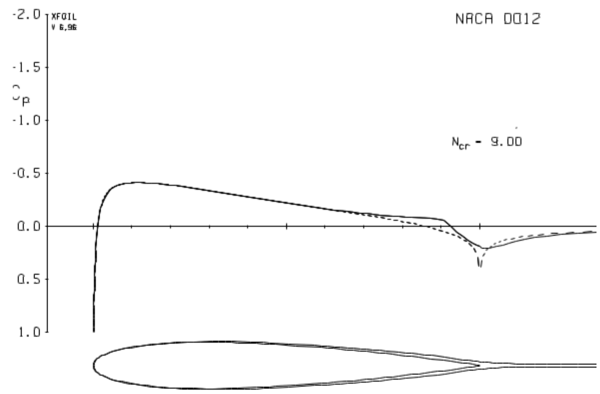
-2.0
XFOIL
V 6.96
NACA 0012
-1.5
Cp
-1.0
Ncr = 9.00
-0.5
0.0
0.5
1.0

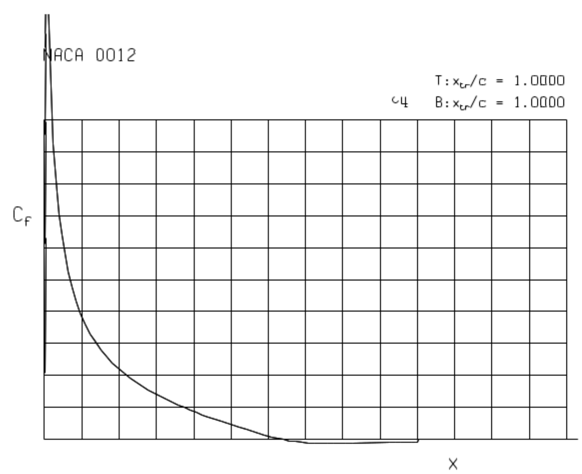
NACA 0012
T: xtr/c = 1.0000
B: xtr/c = 1.0000
Cf
x

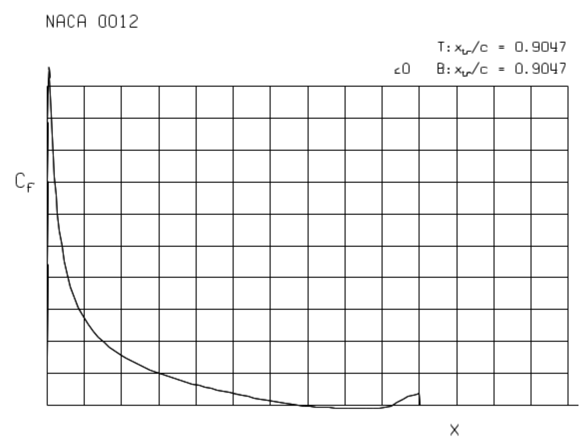
NACA 0012
T: xtr/c = 0.9047
B: xtr/c = 0.9047
Cf
x

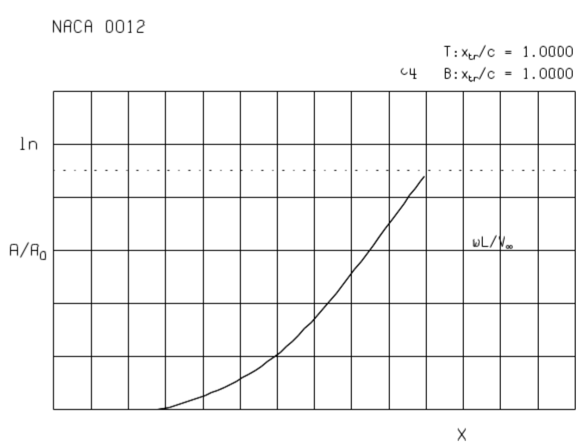
NACA 0012
T: xtr/c = 1.0000
B: xtr/c = 1.0000
ln
A/A0
ωL/V∞
x

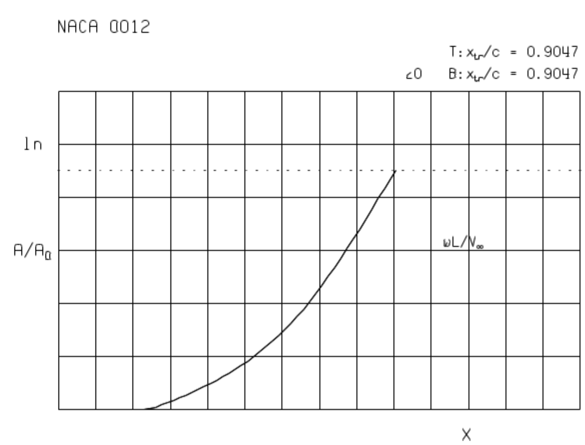
NACA 0012
T: xtr/c = 0.9047
B: xtr/c = 0.9047
ln
A/A0
ωL/V∞
x

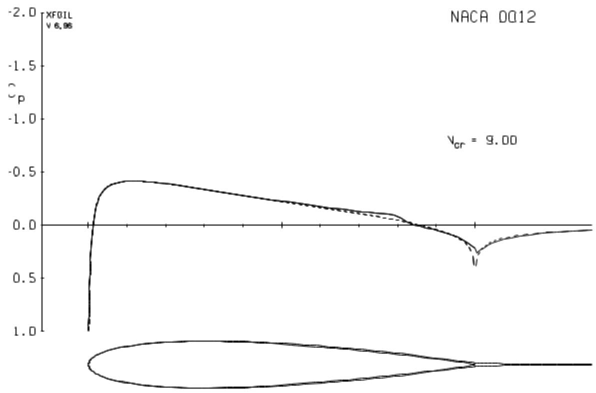
NACA 0012
XFOIL
V 6.96
-2.0
-1.5
-1.0
-0.5
0.0
0.5
1.0
C_p
N_{cr} = 9.00

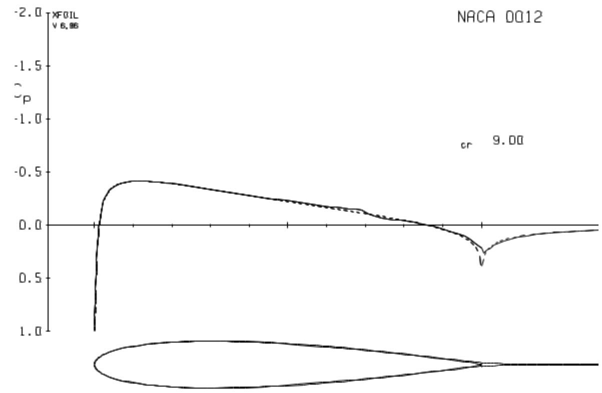
NACA 0012
XFOIL
V 6.96
-2.0
-1.5
-1.0
-0.5
0.0
0.5
1.0
C_p
$_{cr}$ 9.00

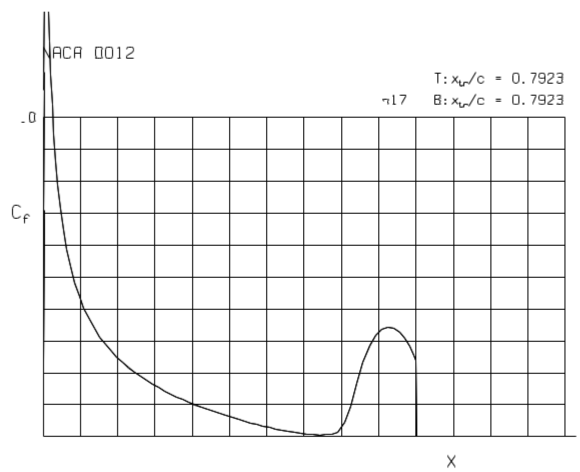
NACA 0012
T: x_{tr}/c = 0.7923
¬17 B: x_{tr}/c = 0.7923
.0
C_f
X

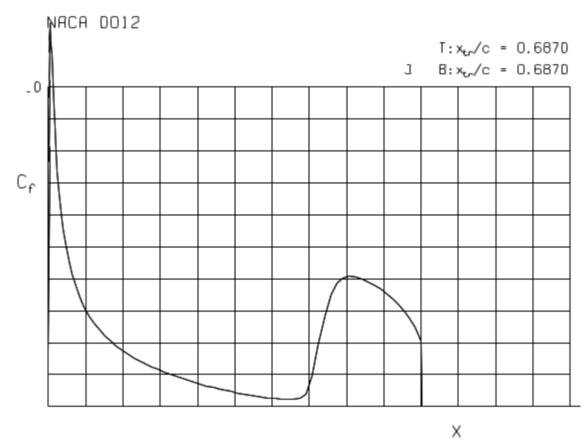
NACA 0012
T: x_{tr}/c = 0.6870
J B: x_{tr}/c = 0.6870
.0
C_f
X

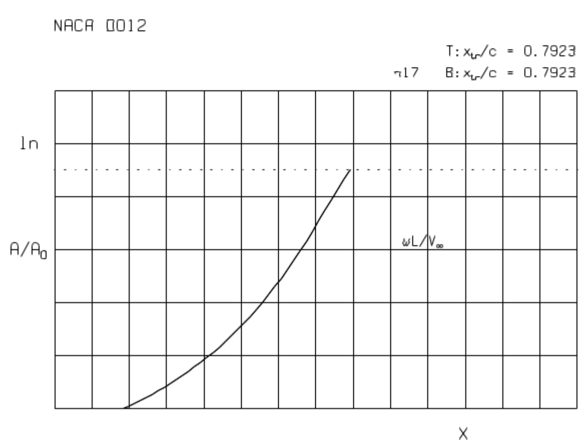
NACA 0012
T: x_{tr}/c = 0.7923
¬17 B: x_{tr}/c = 0.7923
ln
A/A_0
$\omega L/V_\infty$
X

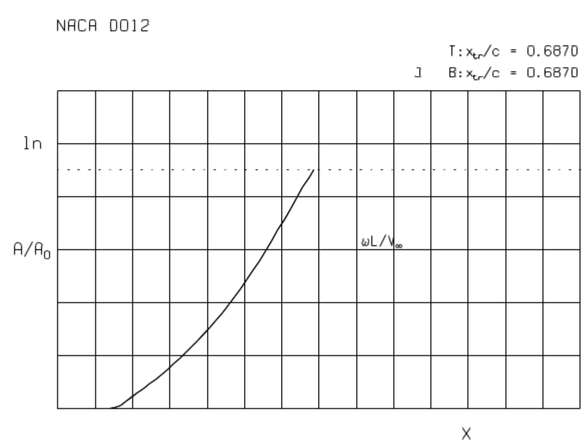
NACA 0012
T: x_{tr}/c = 0.6870
J B: x_{tr}/c = 0.6870
ln
A/A_0
$\omega L/V_\infty$
X

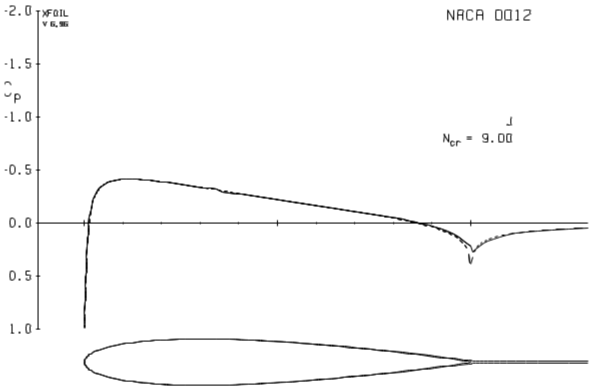
XFOIL
V 6.96
NACA 0012
-2.0
-1.5
-1.0
-0.5
0.0
0.5
1.0
C_p
N_{cr} = 9.00
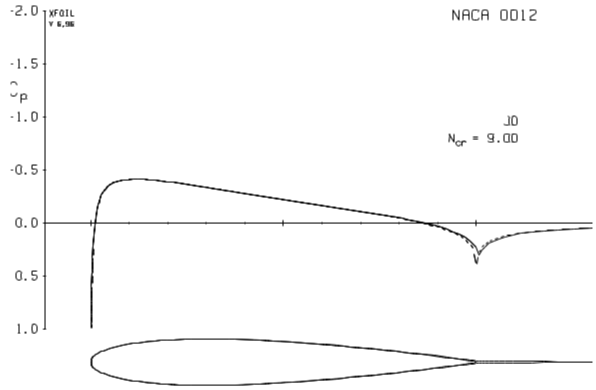
XFOIL
V 6.96
NACA 0012
-2.0
-1.5
-1.0
-0.5
0.0
0.5
1.0
C_p
N_{cr} = 9.00
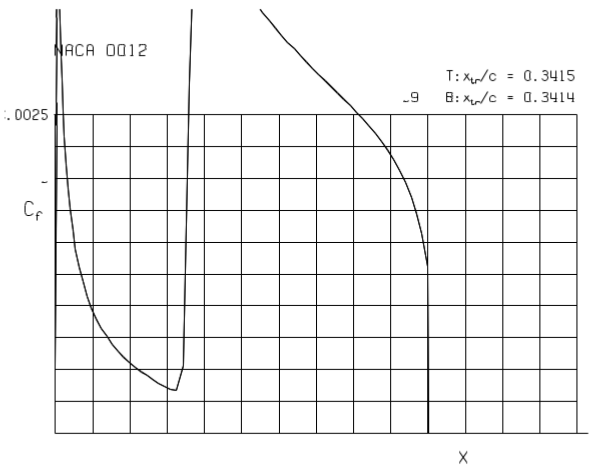
NACA 0012
T: x_{tr}/c = 0.3415
B: x_{tr}/c = 0.3414
.0025
C_f
X
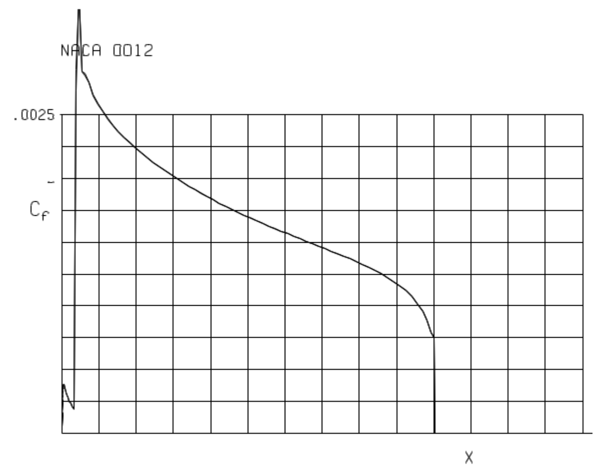
NACA 0012
.0025
C_f
X
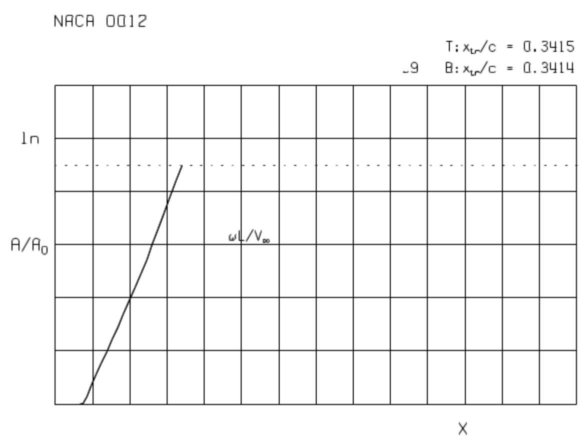
NACA 0012
T: x_{tr}/c = 0.3415
B: x_{tr}/c = 0.3414
ln
A/A_0
$\omega L/V_\infty$
X
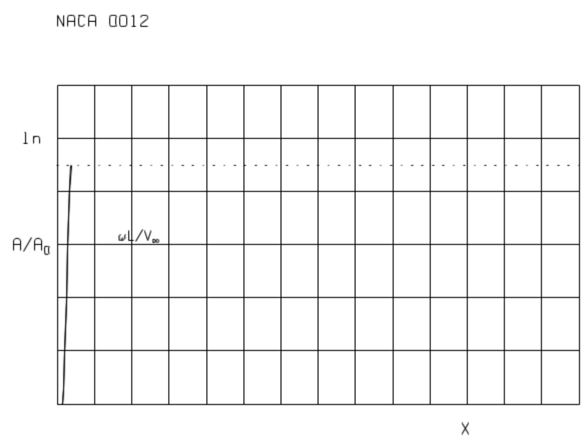
NACA 0012
ln
A/A_0
$\omega L/V_\infty$
X